



Universiteit
Leiden
The Netherlands

Metabolomics assisted with stable-isotope labeling: exploring neuronal metabolism related to Parkinson's disease

Huang, L.

Citation

Huang, L. (2024, January 25). *Metabolomics assisted with stable-isotope labeling: exploring neuronal metabolism related to Parkinson's disease*. Retrieved from <https://hdl.handle.net/1887/3715034>

Version: Publisher's Version

License: [Licence agreement concerning inclusion of doctoral thesis in the Institutional Repository of the University of Leiden](#)

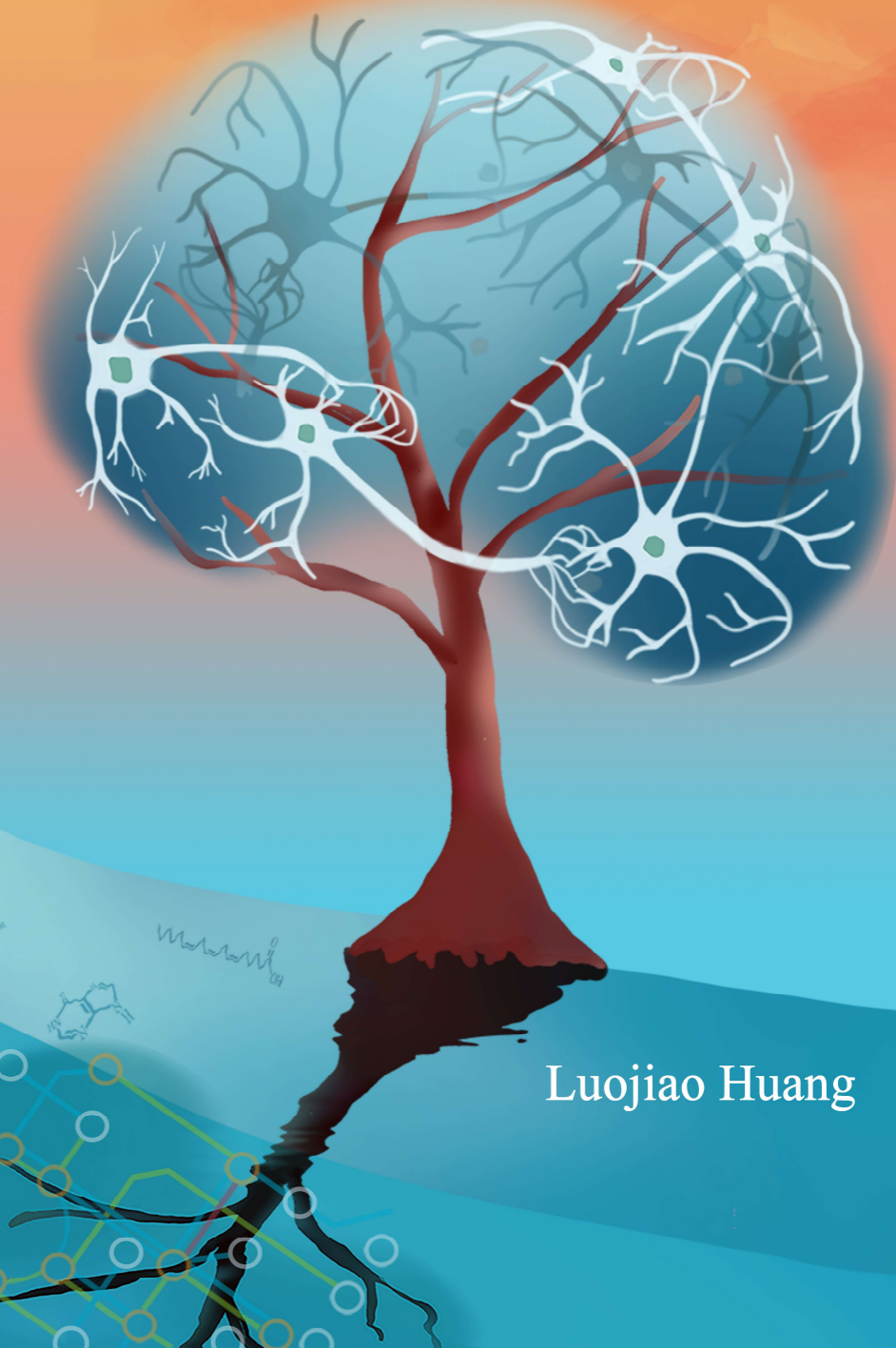
Downloaded from: <https://hdl.handle.net/1887/3715034>

Note: To cite this publication please use the final published version (if applicable).

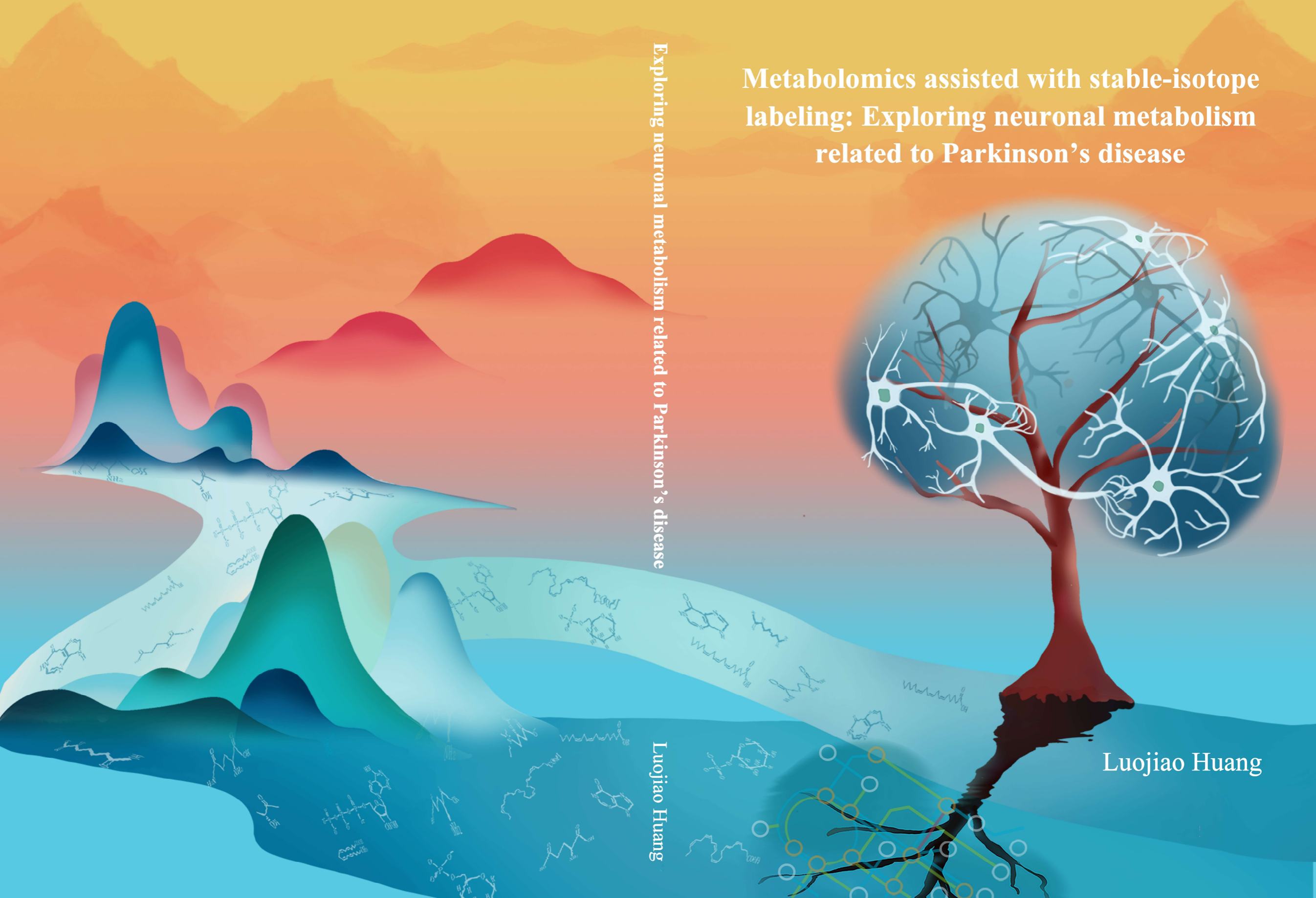
Metabolomics assisted with stable-isotope labeling: Exploring neuronal metabolism related to Parkinson's disease

Exploring neuronal metabolism related to Parkinson's disease

LuoJiao Huang



LuoJiao Huang



**Metabolomics assisted with
stable-isotope labeling:
Exploring neuronal metabolism
related to Parkinson's disease**

Luojiao Huang

黄罗娇

The publication of the thesis was financially supported by:

Leiden University Libraries

SCIEX

Cover design: Luojiao Huang

Thesis layout: Luojiao Huang

Printing: PrintSupport4U

© Copyright, Luojiao Huang, 2024

ISBN: 978-94-93289-38-3

All rights reserved. No part of this book may be reproduced in any form or by any means without permission of the author.

**Metabolomics assisted with stable-isotope
labeling: Exploring neuronal metabolism
related to Parkinson's disease**

Proefschrift

ter verkrijging van
de graad van doctor aan de Universiteit Leiden,
op gezag van rector magnificus prof.dr.ir. H. Bijl,
volgens besluit van het college voor promoties
te verdedigen op donderdag 25 januari 2024
klokke 13:45 uur

door

Luojiao Huang 黄罗娇

Geboren te Zhejiang, China

in 1993

Promotor

Prof. dr. T. Hankemeier

Co-promotor

Dr. A.B. Wegrzyn

Dr. R.M. Fleming

Promotiecommissie

Prof. dr. H. Irth

Prof. dr. E.C.M. de Lange

Prof. dr. J.M.F.G. Aerts

Prof. dr. B.M. Bakker

University of Groningen, the Netherlands

Prof. dr. M. Cascante

Barcelona University, Spain

The research described in this thesis was performed at Metabolomics and Analytics Centre (MAC) of the Leiden Academic Centre for Drug Research (LACDR), Leiden University (Leiden, The Netherlands). The research was financially supported as indicated in each chapter.

To my grandpa, in loving memory.

Contents

Chapter I	General introduction and scope	2
Chapter II	Systematic evaluation of HILIC stationary phases for global metabolomics of human plasma <i>Metabolites (2022)</i>	22
Chapter III	Unraveling the metabolic dysfunction processes fueling parkinsonism pathogenesis in human iPSC-derived mid-brain neurons with PINK1 mutation and rotenone exposure <i>Manuscript in preparation</i>	58
Chapter IV	Reconstruction of glutathione metabolism in neuronal model of rotenone-induced neurodegeneration using mass isotopologue analysis with HILIC-Zeno MRM ^{HR} <i>Analytical chemistry (2023)</i>	94
Chapter V	fluxTrAM: Integration of tracer-based metabolomics data into atomically-resolved genome-scale metabolic networks for metabolic flux analysis; application to human neuronal metabolism <i>Manuscript in preparation</i>	132
Chapter VI	Conclusions and perspectives	182
Appendix	Nederlandse samenvatting	195
	Curriculum vitae	199
	List of publications	200
	Acknowledgements	202

Chapter 1:

General introduction and scope

Introduction

Parkinson's disease

Parkinson's disease (PD) is a common neurodegenerative disorder of the central nervous system that mainly affects the motor system, finally leading to symptoms such as bradykinesia, rigidity, resting tremor, and postural instability. As the disease worsens, patients can further develop cognitive and behavioral problems such as depression, anxiety, apathy, and dementia [1]. It is generally regarded as a disease of old age and affects roughly 1% of the population over the age of 60 and up to 5% of the population over the age of 85 [2]. However, 4% of patients present early-onset PD symptoms before the age of 50 [3]. The majority of these early-onset cases are linked to various forms of genetic mutations, such as dominantly inherited mutations including SNCA, LRRK2, recessively inherited mutations including Parkin, PINK1, DJ-1 and GBA [4,5]. In addition, epidemiological research indicates environmental factors associated with an increased risk of PD, such as herbicides and pesticides (e.g., paraquat, rotenone, and maneb), metals (e.g., manganese and lead), head trauma, and well water [6]. The etiological discoveries have prompted subsequent research questions about how these risk factors contribute to the loss of dopaminergic neurons in the mid-brain, notably targeting the substantia nigra (SN). Two major hypotheses have been proposed regarding the pathogenesis of the disease. One hypothesis claims that neuron demise can be triggered by protein misfolding and aggregation, whereas the other hypothesis proposes this process is provoked by mitochondrial dysfunction and the consequent oxidative stress [7].

To address the underlying pathogenic mechanism, associated PD studies have been carried out using patient biofluids, postmortem tissue, in vitro cell models and animal models. In vitro patient-derived neuronal models using human induced pluripotent stem cells (iPSC) technology are still young, yet they offer unique advantages for studying specific neuronal subtypes represented by human genetics [8]. Disease modeling in either genomic or epigenetic base helps to reveal unique or common routes leading to the consequences of clinical PD symptoms. The convergence and interactions of genetic predispositions, advancing age, and environmental factors on the impairment of metabolism network can play a crucial role in progressive neurodegeneration. I believe investigating the affected metabolism network caused by various individual risk factors and their interactions can provide new insights into disease cause and hint at potential treatment strategies or possible early-intervention therapies (**Figure 1**).

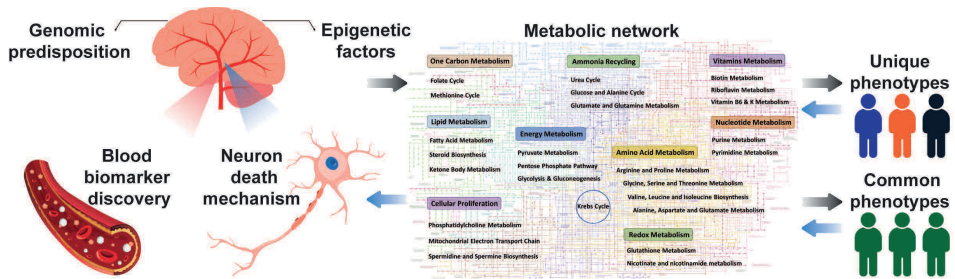


Figure 1. A graphic overview of PD risk factors associated with genomic predispositions and epigenetic factors (due to e.g. environmental stress and aging) that cause unique and common clinical PD symptoms through various metabolism dysregulations. Studies on patient blood or patient-derived neuron analysis can be performed with the goal of identifying disease biomarkers or understanding neuron death mechanisms. Metabolic network adapted from Cao et al [9].

System biology

System biology integrates experimental and computational approaches to perform a comprehensive and systematic analysis and evaluation of complex biological systems [10,11]. Constructing a hierarchical molecular network topology is a fundamental key to understanding cellular function in disease-specific or cell-specific conditions at the molecular level, which also requires knowledge of diverse biological components and sufficient collection of biological data [12,13]. Advanced developments in quantitative measurement technology covering genomics, transcriptomics, proteomics, and metabolomics in a high-throughput manner highly improve the quality and efficiency of metabolic model construction [14,15]. Recon3D is the latest updated and expanded human metabolic network reconstruction, accounting for 3,288 open reading frames, 13,543 metabolic reactions involving 4,140 unique metabolites, and 12,890 protein structures [16]. With multi-layers of biological data integration into a generic human metabolic model, context-specific models at the genome scale can be generated and characterized for a certain cell or tissue type. Applications have been shown for hepatocytes [17], liver cancer stem cells [18], fibroblasts [19], and peripheral blood mononuclear cells [20,21]. This comprehensive modeling approach can also be utilized to help in PD research, thereby, our group generated a comprehensive, high-quality, thermodynamically constrained model named iDopaNeuro, representing the normal metabolism in iPSC-derived human dopaminergic neurons [22]. The iDopaNeuro model can simulate changes in metabolic phenotypes brought on by any neurotoxin or drug intervention, providing directions for new biochemical experiments and insights into a systematic understanding of PD pathogenesis.

The metabolic process involves thousands of metabolites that are exchanged or transformed through biochemical reactions in a metabolic network. It can be greatly influenced by genetic or environmental factors and reflects the global outcomes of gene expression, protein kinetics, and regulations in a biological system [23]. Tracking the changes in the dynamic metabolism pattern is currently of great interest [10]. Metabolomics has emerged as a powerful tool to target the changes in metabolism at its sources, intermediates, and products. Furthermore, it can offer metabolite-relevant data as constraints used for genome-scale modeling analysis; Alternatively, it can also be utilized as a validation dataset to assist biological interpretation and refine the model's predictive fidelity.

Metabolomic analysis

Metabolomics is focused on the systematic analysis of small biochemical molecules in biological organisms [24]. These small molecules, also referred to as metabolites, are characterized by a molecular weight below 1500 Da, diverse physicochemical properties and a broad concentration range from millimolar to picomolar [25,26]. Based on the compound partition coefficient, represented by LogP, metabolites can be categorized into three groups: polar ($\text{LogP} < 0$); medium-polar ($0 < \text{LogP} < 5$); non-polar ($\text{LogP} > 5$) [27]. Polar metabolites generally include amino acids, nucleotides, carbohydrates, and carnitines. Medium-polar metabolites are represented by classes of fatty acids, steroids, benzenes, prenol lipids, ketones, some of the amino acids, and glycerophospholipids. Non-polar metabolites generally include glycerolipids, sphingolipids, steroids, some of the prenol lipids, and glycerophospholipids [27].

Metabolomics measurement is generally achieved using two main analytical techniques: mass spectrometry (MS) and nuclear magnetic resonance (NMR) spectroscopy. MS is more widely used than NMR due to its superior detection sensitivity, wide dynamic range, and capacity for accurate metabolite identification [28]. Recent advancements of mass spectrometry technology in ionization versatility, detector sensitivity and resolution intimately promote high-throughput metabolome analysis [29,30]. MS can be coupled with different chromatography separations. According to the physico-chemical properties of metabolite targets, suitable chromatography among gas chromatography (GC), liquid chromatography (LC), and capillary electrophoresis (CE) can be selected for sufficient metabolite separations. GC is suitable for volatile and thermally stable metabolites (eventually after derivatization), and CE is robust for polar and charged metabolite analysis [31]. Compared to them, LC has the widest metabolite coverage, with a combined utilization of hydrophilic interaction chromatography (HILIC) and reversed-phase liquid chromatography (RPLC). On top of these, a recent innovative technique of coupling ion

mobility spectrometry to mass spectrometry allows supplementary chromatographic separation on the basis of compound size, shape, charge, and mass [32].

A query performed across various human metabolome databases reported that around 3278 metabolites have been detected via LC-MS analysis and collected with experimental spectra. The most frequent biological sample types used in LC-MS-based metabolomics analysis are blood (plasma or serum), tissue, cells, urine, and feces [27]. Blood carries diverse metabolites through vessels and maintains a homeostatic correspondence with tissues and cells in the body [33]. Typically, receiving nutrients or hormones from the blood, tissues and cells release metabolic waste products, organic waste, or send hormone signal regulation to neighboring tissues. This also describes the role of blood as a crucial hub for metabolite exchange throughout the body [34]. The study of paired arterial and venous plasma profiling shows additional benefits for revealing subtle changes related to tissue-specific metabolism [33]. Unsurprisingly, the metabolome composition of plasma and cells was found with considerable overlap, except for the lipids, which are found in higher enrichment in cells due to the need for composing membrane structure [27]. From an analytical perspective, sample preparation and the LC-MS method, with minor tweaks, can be shared between these two sample types. From a biological perspective, global metabolic profiling for plasma and cell samples can offer a data-driven research approach to disease biomarker discovery. While targeted analysis of metabolites belonging to specific compound classes, metabolic pathways, or modules, especially for tissue and cell samples, can provide a hypothesis-driven research approach in disease mechanism study [35]. Selecting the appropriate approach and sample type depends on the biological questions that need to be answered in any metabolomics study.

Use of stable isotopes in metabolite quantification and identification

Stable-isotopes have an unreplacable role in targeted metabolite quantification. Instrumental variations and complex matrix effects are inevitable issues and easily lead to signal suppression during LC-MS analysis. To circumvent this, stable-isotope labeled metabolites possessing with the same retention and ionization behavior can be used as internal standards (**Figure 2.a**). This method is known as the stable-isotope dilution and has already become the gold standard for accurate quantification. However, due to the high cost of stable-isotope labeled standard, it is not practical to get an internal standard for each individual metabolite in targeted metabolomics analysis. Many alternative strategies have been implemented, for instance, 1) select a single or small number of internal standards per metabolite class [36,37] (**Figure 2.b**). 2) generate labeled intracellular metabolome as internal standards reference by culturing with labeled substrates, applicable for

metabolomics study not only in cell level, but also in plant, animal and human level [38–41] (**Figure 2.b**). 3) prepare internal standards by derivatizing standards with isotope labeling reagents, only applicable for the derivatization strategy [42,43] (**Figure 2.c**).

One major challenge that hinders biological interpretation based on global metabolic profiling is metabolite identification. For untargeted MS-based metabolomics analysis, detected features generally consist of biological signals, contaminants, non-metabolite-related noise, and background signals [44,45]. Unique biological features were reported to account for approximately 10% of the signals in the electrospray ionization mode [46,47]. This adds difficulties to the reliable feature extraction and annotation of putative metabolites of biological origin. To tackle this problem, stable-isotope labeling becomes a novel approach for feature identification. The basic principle is a cultivation of an organism group with highly isotopic labeling and a group with isotopic natural abundance. The labeled samples are extracted and mixed into a whole labeled metabolome pool, later divided into aliquots, and added to a non-labeled metabolome extract [48]. The analysis of mixtures of native and labeled metabolome leads to labeling-specific isotopic distributions of both the non-labeled and labeled metabolite ions in the mass spectra, which helps to filter biologically derived metabolites [49–51] (**Figure 2.d**). Studies have reported a comprehensive identification of true metabolite-related features in microorganisms [49,52–54], plants [49–51] with the help of feeding fully ^{13}C labelled nutrients. However, the same approach is not often utilized in mammalian organisms since mammalian cells require a complex mixture of nutrients and rarely reach full ^{13}C labeling. A proof-of-principle study on human cancer cells managed to realize "deep labeling" using a custom growth medium where glucose and all amino acids were fully ^{13}C labeled, while vitamins and serum components were ^{12}C . Due to the fact that the isotopic distributions of metabolites can be in a non-fully carbon-labeled state, there is difficulty in determining the carbon numbers for unknown metabolic features. But more importantly, endogenous metabolic features from de novo synthesis can be fully identified via ^{13}C incorporation [55].

Either through improving metabolite quantification or metabolite identification towards full metabolome annotation in a given cell or tissue type, it can be highly beneficial in gaining a broader and deeper picture of human metabolism. Additionally, it will also help refine a context-specific genome-scale model to achieve more accurate metabolic prediction and comprehension of mechanisms. More effort has to be made to reach this ultimate goal since the analytical challenges still remain. In this thesis, we aim to make efforts focusing on the fundamental evaluation of a robust HILIC-MS method for polar metabolome analysis with high feature coverage and excellent separation that is applicable for global metabolite

profiling and transferable to metabolite quantification, as demonstrated in **Chapter 2** and **Chapter 3**.

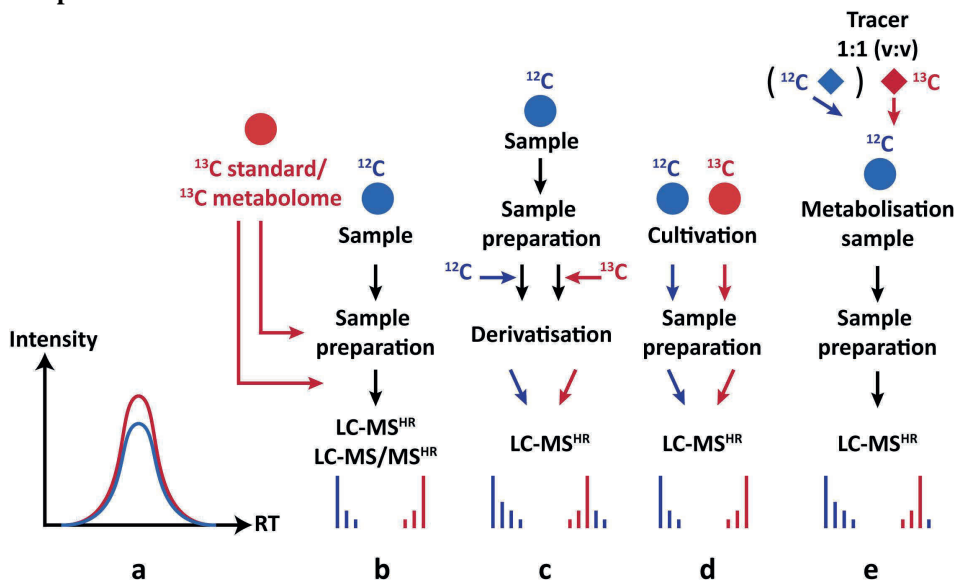


Figure 2. Different strategies for using stable isotopes to assist metabolomics studies. **a.** ^{13}C , ^{15}N , and ^{34}S -enriched substances are not chromatographically separated from the corresponding natural isotopologues, thus the non-labeled (blue) and the labeled isotopologues (red) elute at the same retention time with identical peak profiles. **b.** Absolute compound quantification using an authentic, labeled standard or relative quantification using a stock of globally labeled sample extract of the same organism for inter-experiment comparison. The extracts are subsequently mixed and measured with high resolution LC-MS (LC-MS^{HR}). **c.** Derivatization using non-labeled and labeled derivatization agents enables rapid recovery of many metabolites belonging to the same chemical groups (e.g. alcohols, acids ...). **d.** For non-targeted annotation of an organism's metabolome, the organism can be cultivated in parallel using differently isotopologue-enriched nutrition sources (e.g., ^{12}C and ^{13}C glucose as sole carbon source). The resulting data pattern helps in the extraction of true biological signals. **e.** Metabolism experiment using natural and fully labeled tracer substances enables metabolism studies and greatly helps to separate products of metabolism from other biological signals. In contrast with metabolism studies, fluxomics (tracer-based metabolomics) experiments only spike with the labeled tracer. Referred to Bueschl et al [56].

Stable-isotope labeling in tracing cellular metabolism activity (Tracer-based metabolomics)

Cellular metabolism is a self-maintenance and regulation process that provides energy, generates building blocks, and tunes signaling pathways for cell survival and growth. Metabolism also supports cell-to-cell communication, helping to maintain an active microenvironment and contributing to the whole organism's survival. Due to the intrinsic network feature of metabolic pathways complexity, redundancy and reaction reversibility, metabolite concentrations generally exhibit strong robustness to any genetic or enzymatic changes [57]. Many uncertainties remain for the interpretation of cell metabolism based on the static metabolic phenotype data. Metabolic flux, also known as metabolite turnover over time or metabolic reaction rate, starts to gain more attention because of its ability in representing functional pathway activities. Stable or radioactive isotope labeling shows a unique advantage in studying metabolic fluxes and elucidating the structure of metabolic pathways and networks. A given isotopic tracer fed to living cells can be metabolized via enzymatic reactions. In a reaction process, a number of molecular bonds broken and reformed, the isotopic atoms are rearranged and incorporated into downstream metabolites within the metabolic network [58]. The specific labeling pattern of intermediate metabolites derived from stable isotopic tracer can be measured by mass spectrometry (**Figure 2.e**). Mass isotopologues refers to molecules that differ only by the number of isotopic substitutions [59]. Mass isotopologue distribution (MID) records the relative abundance for all mass isotopologue peaks. Here, we will introduce qualitative and quantitative applications involving metabolite isotopologue data interpretation and modeling for exploring cellular metabolism, as well as the remaining challenges for tracer-based metabolomics.

Probing pathway activity

With stable isotopic labeling, we can quantify the utilization of certain carbon or nitrogen sources in the targeted downstream products. ^{13}C -glucose, ^{13}C -glutamine and $^{15}\text{N}_2$ -glutamine have been frequently used to monitor the nutrient dependence of tumor tissue. Through infusing $^{13}\text{C}_6$ -glucose into human lung cancer patients, higher ^{13}C -enrichment in lactate, alanine, succinate, glutamate, aspartate, and citrate was observed in the tumors compared to non-cancerous tissues, suggesting more active glycolysis and the tricarboxylic acid cycle relying on glucose in the tumor tissues [60]. Glutamine was reported to be an important nutrient for most cancer cells in culture [61]. However, an in-vivo lung tumor study in mice showed low ^{13}C -glutamine utilization by both tumors and normal tissue. Genetic deletion and pharmacological inhibition of glutaminase showed no influence on the tumor growth [62]. ^{13}C labeled substrates can also be used to determine their contribution

to lipogenic acetyl-CoA production by measuring the isotopic enrichment in fatty acids (palmitate, stearate, oleate, etc.) [63].

Specific enzyme activation over certain pathways can be characterized through labeled enrichment analysis of intermediate metabolites or quantification of particular isotopologue. Pyruvate carboxylase (PC) catalyzes an important anaplerotic reaction that creates oxaloacetate from pyruvate. The resulting presence of $^{13}\text{C}_3$ -citrate, $^{13}\text{C}_5$ -citrate, $^{13}\text{C}_3$ -malate, and $^{13}\text{C}_3$ -aspartate from $^{13}\text{C}_6$ -glucose indicates high PC activity in human lung tumors [60,64]. The last step of glycolysis, converting phosphoenolpyruvate to pyruvate, is catalyzed by the M2 isoform of pyruvate kinase (PKM2). By quantifying the labeled abundance of $^{13}\text{C}_6$ -glucose-derived metabolite isotopologues ($^{13}\text{C}_3$ -phosphoenolpyruvate, $^{13}\text{C}_3$ -pyruvate, $^{13}\text{C}_2$ -citrate, $^{13}\text{C}_3$ -serine, $^{13}\text{C}_2$ -glycine, $^{13}\text{C}_3$ -lactate), human colon carcinoma HCT116 cells demonstrated PKM2 silencing in response to serine deprivation, shown with more pyruvate diverted into mitochondria and shifting more carbon flux into serine biosynthesis [65]. Similar approaches were employed for reporting a highly activated phosphoglycerate dehydrogenase in some cancer cells, which largely diverts glycolytic flux carbon into serine and glycine metabolism [66].

Many enzymatic reactions are bidirectional, reaction reversibility adds more flexibility to metabolic network regulation. By feeding cells with a designed tracer, a reversible reaction direction can be identified when the expected labeling pattern is observed in certain reaction products [67]. In addition, stable-isotope tracing shows its advantages in studying compartment-specific pathways. By tracing the isotope labeled hydrogen (^2H) in compartmentalized reactions that use NADPH as a cofactor and produce ^2H -labeled 2-hydroxyglutarate by mutant isocitrate dehydrogenase enzymes, Lewis et al. successfully differentiated pathway-specific NADPH production in the cytosol and mitochondria [68]. Delineating the metabolite labeling pattern associated with two relevant pathways can help determine their relative pathway flux activity. One classical application is determining the relative flux through glycolytic versus pentose phosphate pathway (PPP) catabolism using 1,2- $^{13}\text{C}_2$ -glucose [69]. The ratio of lactate with M+1 labeling and M+2 labeling implies the ratio of PPP overflow to glycolysis. A relative contribution of oxidative PPP to non-oxidative PPP to ribose-5-phosphate and thus nucleotide synthesis can be quantified by a relative comparison of M+1 and M+2 labeling [70]. A similar approach was employed for reporting the flux contribution of glutamine to palmitate synthesis derived from two distinct pathways, the glutaminolysis and reductive carboxylation pathways, in brown adipocyte cells [71].

Discovering novel pathways

Isotope tracing through known pathways or metabolome-wide analysis may facilitate the discovery of novel metabolic flux routes [57,72]. Tracing the carbon conversion of $^{13}\text{C}_6$ -glutamine in the tricarboxylic acid (TCA) cycle resulted in the identification of a novel pathway for tumorigenesis, which is the reductive carboxylation of transforming α -ketoglutarate into citrate, followed by a conversion into acetyl-CoA for lipid synthesis [73,74]. Another breakthrough discovery found in lung and pancreatic cancer studies showed ^{13}C -lactate extensively labels TCA cycle intermediates, indicating a lactate oxidation flux into the TCA cycle [75,76]. However, tracing targeted pathways using specifically designed tracers is generally slow and random in discovering new pathways that have important physiological relevance. Very few studies have performed a metabolome-wide analysis with stable isotope labeling due to the difficulties in complex data analysis and interpretation. Puchalska et al. combined stable isotope tracing with untargeted metabolomics and identified a set of mitochondrial and cytoplasmic metabolic pathways related to the utilization of ketone bodies, acetoacetate in macrophages. They revealed an acetoacetate shuttle that connects the metabolism of hepatocytes to neighboring macrophages and protects the liver from high-fat diet-induced fibrosis [77]. To fully exploit their ability to discover new pathways based on broad-scope metabolomes, ongoing efforts should be made in the areas of unknown feature identification and dedicated data analysis pipelines for labeled data processing [78].

Quantitative metabolic flux analysis

For a metabolic network, metabolite concentrations and metabolic fluxes are regarded as the integrated functional response to the intertwined regulations at the genetic, protein modification, allosteric, and kinetic levels [79]. Quantifying network-flux distributions gives a complementary characterization of metabolic phenotypes in cells under particular conditions. The intracellular reaction rates are not measurable directly but can be inferred computationally using stable-isotopically labeled isotopologue distribution data. ^{13}C -based tracers are most commonly used for experimental flux quantification, known as ^{13}C metabolic flux analysis. The network model scope is basically determined based on specific research hypotheses. Most studies so far have focused on the central carbon metabolism and the related amino acid and fatty acid metabolism. A curated network model including metabolic reactions of interest and the respective carbon atom transitions is needed to be built as a prerequisite. Following an isotope labeling experiment, the isotope labeling distribution of intermediate metabolites, and external rates of substrate uptake and product secretion are measured and used as model constraint inputs. The model flux simulation generally starts with a set of free fluxes with random initial values. The simulated labeling

distribution is then compared with the experimental labeling distribution. This computational fitting step restarts continuously until it reaches the minimized differences between simulated and experimental measurements, thereby, the final simulated flux distribution is approaching the *in vivo* fluxes [80].

Simulation of the ^{13}C metabolic flux is typically based on several assumptions [81]. For example, cultured cells are maintained under a metabolic steady state with constant metabolic fluxes and metabolite pools during the labeling experiment. It is also assumed that enzyme activity displays no kinetic differences between natural substrate and isotopically labeled substrate. When isotopic steady state is reached, the labeling distribution data can be used for stationary metabolic flux analysis. While in many cases, it takes rather long time to reach constant labeling distribution for some metabolites. Isotopically non-stationary metabolic flux analysis can be performed with additional inputs of intracellular metabolite pool size together with dynamic labeling distribution at multiple sampling time points [82,83]. The precision and accuracy of metabolic flux estimation are statistically evaluated by verifying the goodness of fit and determining confidence intervals for the fluxes, also called sensitivity analysis.

Quantitative metabolic flux analysis has helped in characterizing metabolic rewiring and understanding disease phenotypes [84,85]. During the process of detachment from monolayer culture and growth as anchorage-independent tumor spheroids, Jiang et al quantified the reduction in glycolysis, pyruvate dehydrogenase flux, and glucose/glutamine oxidation but enhancement in reductive isocitrate dehydrogenase flux in spheroids [85]. Metabolic flux quantitative analysis also helped guide cell bioengineering to produce valuable products from renewable resources [79]. For instance, ^{13}C flux analysis was performed in Chinese hamster ovary cells to evaluate the effectiveness of a newly designed medium variant in reducing ammonia production. The metabolic effect showed an effective reduction of toxic product (ammonia) production and no significant alteration in the bioenergetic fluxes [86].

Challenges in tracer-based metabolomics

A well-established metabolic pathway for a particular cell type is crucial for compelling interpretation of either metabolite concentrations or MID data toward pathway activity. For a well-studied metabolic pathway, for instance, metabolite connection and transformation in the classical central carbon metabolism are usually taken for granted. New reactions or unknown reaction reversibility can be confirmed using a designed tracer. In other words, this also means the labeling information can help support and validate the metabolic pathway reconstruction. Technically, time-of-flight (TOF) or Orbitrap mass spectrometry

analysis at high mass resolution could obtain the labeling information, including the labeled atom number and total isotopic enrichment, based on the intact structure level. However, the positional labeling information embedded in the metabolite substructure or moiety can be missed. Although a tandem quadrupole-based mass spectrometry analysis using multiple reaction monitoring (MRM) can offer partial substructure information, it has the significant drawback of losing detection sensitivity with increased metabolite targets and paired ion transitions [87–90]. Tandem MS-based approaches via parallel reaction monitoring (PRM/MRM^{HR}) [91], SWATH [92], and all-ion fragmentation techniques (MS^{All}) [93] in high resolution have shown their advantages in terms of recording the entire fragmentation spectrum and increasing sensitivity by reducing the detection cycle time. Application based on ultrahigh-resolution MS^{All} on an Orbitrap Fusion Tribrid MS has been shown to confirm the reconstruction of purine and pyrimidine metabolism using not only the MID of an intact metabolite but also the MID of its moiety [93]. Changes in intact and moiety MIDs could also be collectively used to infer specific enzyme activity [94]. A labeled metabolite containing the same number of isotopes but with different labeling positions can indicate distinct enzyme regulations. This method, however, lost the specific link between fragments and their given precursor isotopologue, making it impossible to distinguish different labeling positions for the same precursor isotopologue. Thereby, further method development is required to improve the part of LC-MS measurement (step 1 in **Figure 3**) in order to fully capture labeled metabolite information at the intact molecule and moiety level with good sensitivity in a single analytical run.

Quantitative metabolic flux analysis into understanding human cellular metabolism still has relatively few applications. One bottleneck can be the tedious work related to tracer-based metabolomics data processing (step 2 in **Figure 3**). The other bottleneck is that the model scope is often limited to the central carbon metabolism with established methods for ¹³C metabolic flux analysis. It is faced with highly challenging computation in order to integrate tracer-based MID data into a larger network model and further to a genome-scale level (step 3 in **Figure 3**). A recently developed mathematical and computational method, named moiety fluxomics, has shown its ability to infer metabolic reaction flux at genome scale, given mass isotopologue distribution data [95]. This remains to be tested in the iDopaNeuro model for human dopaminergic neurons. Flux outputs have to be viewed with skepticism until the model has passed many rounds of flux estimates, flux accuracy assessment, and experimental study validation. This can be a lengthy cycle before finally reaching a compelling biological conclusion.

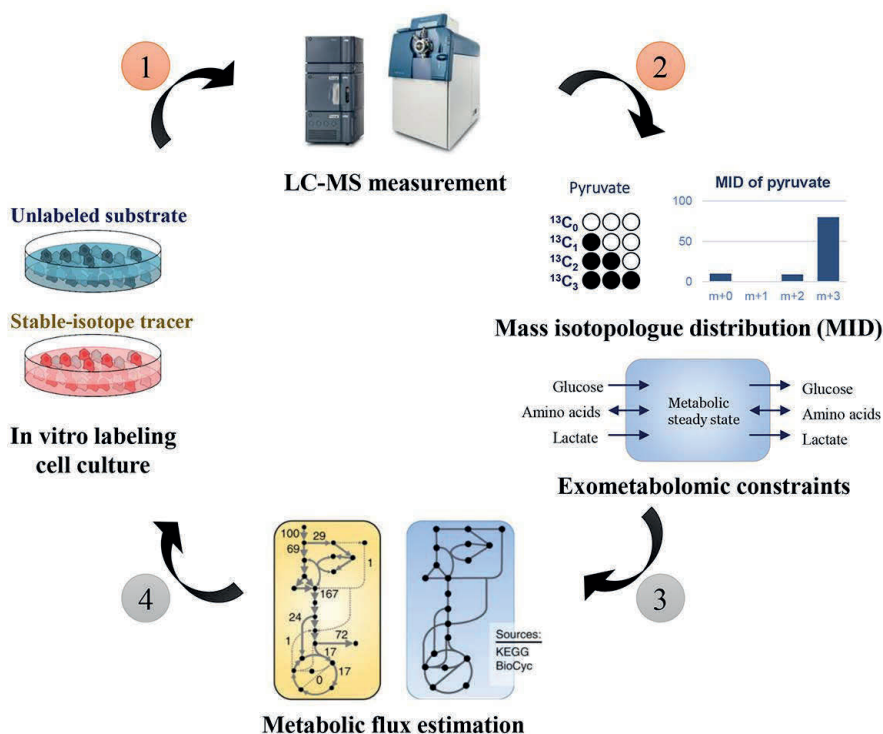


Figure 3. In a typical ^{13}C metabolic flux analysis workflow, in-vitro labeled samples can be measured using LC-MS techniques (step 1), MS raw data needs to be processed metabolite by metabolite (step 2), and the calculated MID data, together with exometabolomic constraints, are next fed into a constructed metabolic model for estimating the optimal flux distribution (step 3). The obtained flux results can guide the next tracer experiment design (step 4). Metabolic network model adapted from Long et al [81].

Scope of this thesis

Based on the hypothesis that mitochondrial dysfunction and the resulting oxidative stress is one of the drivers of Parkinson's disease (PD), the basic goal of our research is to study the role of mitochondrial dysfunction in the onset of Parkinson's disease through monitoring the underlying molecular events. Both variations in metabolite pool size and metabolite transformation or transport (turnover) rate should be taken into account for a comprehensive characterization of metabolic regulation over biochemical pathways. However, as was discussed in the introductory section, there is currently still a lack of suitable analytical measurement, computational processing, and modeling techniques. The study of mitochondrial dysfunction requires (i) the robust measurement of polar metabolites, (ii) the

study of metabolic fluxes at a larger scale. For the latter, sensitive MS/MS analysis coupled with high-resolution MS analysis and a proper computational workflow for tracer-based mass spectrometry data processing and quantitative flux analysis in an atomically resolved genome-scale model are needed.

Therefore, the aim of this thesis was to develop a robust LC-MS method to analyze a wide range of polar metabolites, a tracer-based metabolomics analytical method, and a computational workflow for metabolic flux analysis within a human-specific genome-scale metabolic model. The other aim of this thesis was to apply these methods to investigate metabolic dysregulation of dopaminergic neurons due to genetic and environmental factors. The aim in **Chapter 2** was to systematically evaluate polar stationary phases for global polar metabolome analysis, moreover, to offer valuable guidance on determining an optimal chromatography column for various biological matrices. We compared the neutral phase of the Waters BEH-amide column with the zwitterionic phase of the Merck ZIC-cHILIC column for 9 classes of polar compounds using 54 authentic standards at three pH conditions. The ZIC-cHILIC column outperformed BEH-amide in terms of chromatographic peak performance and selectivity of critical isomers. Investigation into the retention mechanism demonstrated mixed mode interactions in neutral and zwitterionic phases, specifically with a strong electrostatic interaction present in ZIC-c at neutral pH condition. A matrix-related assessment covering matrix effect, salt effect, intra- and inter-batch repeatability was carried out using human plasma, which was followed by a practical metabolomics study using plasma samples with diverse phenotypes. ZIC-c enhanced plasma feature coverage and improved their retention distribution, which is highly advantageous for global profiling of plasma samples and assisting new biomarker discovery. In the following chapters, we validated, adapted, and further applied the established ZIC-c HILIC-MS method to cellular metabolomics analysis.

To achieve a comprehensive picture of metabolic dysregulation related to individual and combined effects of genetic and environmental factors (PINK1 mutation and rotenone) for PD and facilitate the pathogenesis mechanism understanding, **Chapter 3** employed multiple targeted metabolomics platforms covering polar and non-polar metabolomes covering central carbon metabolism, acylcarnitine and polyunsaturated fatty acid metabolism. The patient-specific and isogenic human induced pluripotent stem cell (iPSC)-derived mid-brain neurons with and without PINK mutation were utilized as the in vitro experimental model, which received additional treatments with rotenone exposure or NAD⁺ supplementation. The study revealed overlapping and compensating metabolome disturbances induced by individual factors and their contributions to a broad metabolic dysregulation indicative of neurodegeneration. The supplementation of NAD⁺ to the dual factor-influenced neurons

was evaluated with limited improvement in neuronal energy production relying on the enhanced branched chain amino acid metabolism.

In **Chapter 4**, a new LC-MS method is proposed for stable-isotope labeled mass isotopologue analysis at both MS¹ and MS² level. Given the fact that the detection duty cycles for the orthogonal injection TOF-MS are typically less than 30%, this unavoidable cause of sensitivity loss always exists for current high-resolution tandem TOF-MS method. A recent revolutionary technique, Zeno-pulsing, has been reported to increase the duty cycle up to 100%, thus achieving significant detection improvement [96]. The combination of HILIC separation coupled to high-resolution MRM detection with Zeno trap pulsing allowed for wide coverage of polar metabolome analysis and excellent sensitivity at the MS² level. In comparison with the conventional SWATH and MRM^{HR} methods, the HILIC-Zeno MRM^{HR} method achieved a higher sensitivity gain. Meanwhile, it maintained isotope fidelity for precursor and fragment isotopologue distribution as well as specificity linking a given precursor isotopologue to its generated fragments. Tracing labeled atoms at the moiety level clearly illuminates the reaction connections through metabolite transformation. The method was applied to a human-derived mid-brain neuronal model and revealed a new elucidation of glutathione metabolism regulation in response to rotenone stress via interpreting labeling pattern changes from both intact metabolites and moieties. Aside from capturing the static metabolite level or concentration, dynamic pathway activity provides a complementary perspective for a more complete understanding of metabolic phenotyping. Quantitative flux inference from metabolite labeling patterns remains a big challenge, especially at a genome-scale. Besides, there is still a lack of an automated processing pipeline to make this procedure more efficient and turn it into a standardized workflow. **Chapter 5** aims to construct an automated data processing pipeline for quantitative flux analysis in a genome-scale model, termed *fluxTram*. The pipeline is composed of two essential modules: the processing of tracer-based mass spectrometry data into standardized mass isotopologue distribution and the generation of metabolite structure and reaction databases over a genome-scale model. As a demonstration of the pipeline, *fluxTram* processed ¹³C-labeled metabolomics data collected from an *in vitro* iPSC-derived mid-brain neuron model, which assisted a conventional ¹³C metabolic flux analysis within a central carbon (core) metabolism model. In parallel, *fluxTram* resolved the atom mappings of a genome-scale, dopaminergic neuronal metabolic model (iDopaNeuroC). The combination of the *fluxTram* outputs allowed us to conduct a moiety fluxomics analysis in the iDopaNeuroC model. An integrative metabolic flux analysis involving core model flux solution, moiety flux solution, and results from two other *in silico* genome-scale flux analysis methods: entropy flux solution and flux balance analysis became possible, enabling

a comparison of neuronal metabolic function inference and prediction using competing methods. Furthermore, atom mapping assisted in determining the labeling configuration of a tracer used in a subsequent tracer experiment.

Finally, in **Chapter 6** a general conclusion of the studies described in this thesis is provided. Perspectives and recommendations on future improvements and applications of the proposed LC-MS methods and data processing pipelines are also discussed.

References

1. Kouli A, Torsney KM, Kuan W-L. Parkinson's Disease: Etiology, Neuropathology, and Pathogenesis. Exon Publications. 2018;3–26.
2. Fahn S. Description of Parkinson's disease as a clinical syndrome. *Ann N Y Acad Sci*. 2003;991:1–14.
3. Van Den Eeden SK, Tanner CM, Bernstein AL, Fross RD, Leimpeter A, Bloch DA, et al. Incidence of Parkinson's Disease: Variation by Age, Gender, and Race/Ethnicity. *American Journal of Epidemiology*. 2003;157:1015–22.
4. Reeve A, Simcox E, Turnbull D. Ageing and Parkinson's disease: Why is advancing age the biggest risk factor? *Ageing Research Reviews*. 2014;14:19–30.
5. Farrer MJ. Genetics of Parkinson disease: paradigm shifts and future prospects. *Nature Reviews Genetics*. 2006;7:306–18.
6. Tsuboi Y. Environmental-Genetic Interactions in the Pathogenesis of Parkinson's Disease. *Exp Neurobiol*. 2012;21:123–8.
7. Dauer W, Przedborski S. Parkinson's Disease: Mechanisms and Models. *Neuron*. 2003;39:889–909.
8. Tran J, Anastacio H, Bardy C. Genetic predispositions of Parkinson's disease revealed in patient-derived brain cells. *npj Parkinsons Dis*. Nature Publishing Group; 2020;6:1–18.
9. Cao G, Song Z, Hong Y, Yang Z, Song Y, Chen Z, et al. Large-scale targeted metabolomics method for metabolite profiling of human samples. *Analytica Chimica Acta*. 2020;1125:144–51.
10. Kitano H. Systems Biology: A Brief Overview. *Science*. American Association for the Advancement of Science; 2002;295:1662–4.
11. Kitano H. Computational systems biology. 2002;420:21.
12. Ideker T. Systems biology 101—what you need to know. *Nature Biotechnology*. 2004;22:473–5.
13. Aderem A. Systems Biology: Its Practice and Challenges. *Cell*. Elsevier; 2005;121:511–3.
14. Fischer HP. Towards quantitative biology: Integration of biological information to elucidate disease pathways and to guide drug discovery. *Biotechnology Annual Review [Internet]*. Elsevier; 2005 [cited 2022 Nov 1]. p. 1–68.
15. Pinu FR, Beale DJ, Paten AM, Kouremenos K, Swarup S, Schirra HJ, et al. Systems Biology and Multi-Omics Integration: Viewpoints from the Metabolomics Research Community. *Metabolites*. Multidisciplinary Digital Publishing Institute; 2019;9:76.
16. Brunk E, Sahoo S, Zielinski DC, Altunkaya A, Dräger A, Mih N, et al. Recon3D enables a three-dimensional view of gene variation in human metabolism. *Nat Biotechnol*. Nature Publishing Group; 2018;36:272–81.
17. Mardinoglu A, Agren R, Kampf C, Asplund A, Uhlen M, Nielsen J. Genome-scale metabolic modelling of hepatocytes reveals serine deficiency in patients with non-alcoholic fatty liver disease. *Nat Commun*. Nature Publishing Group; 2014;5:3083.
18. Hur W, Ryu JY, Kim HU, Hong SW, Lee EB, Lee SY, et al. Systems approach to characterize the metabolism of liver cancer stem cells expressing CD133. *Sci Rep*. Nature Publishing Group; 2017;7:45557.
19. Wegrzyn AB, Herzog K, Gerding A, Kwiatkowski M, Wolters JC, Dolga AM, et al. Fibroblast-specific genome-scale modelling predicts an imbalance in amino acid metabolism in Refsum disease. *The FEBS Journal*. 2020;287:5096–113.
20. Zhang X, Mardinoglu A, Joosten LAB, Kuivenhoven JA, Li Y, Netea MG, et al. Identification of Discriminating Metabolic Pathways and Metabolites in Human PBMCs Stimulated by Various Pathogenic Agents. *Frontiers in Physiology [Internet]*. 2018 [cited 2022 Nov 2];9.
21. Cho JS, Gu C, Han TH, Ryu JY, Lee SY. Reconstruction of context-specific genome-scale metabolic models using multiomics data to study metabolic rewiring. *Current Opinion in Systems Biology*. 2019;15:1–11.
22. Preciat G, Moreno EL, Wegrzyn AB, Willacey CCW, Modamio J, Monteiro FL, et al. Mechanistic model-driven exometabolomic characterisation of human dopaminergic neuronal metabolism [Internet]. *bioRxiv*; 2021 [cited 2022 Oct 15]. p. 2021.06.30.450562.
23. Nicholson JK, Lindon JC. Systems biology: Metabonomics. *Nature*. 2008;455:1054–6.
24. Beger RD, Dunn W, Schmidt MA, Gross SS, Kirwan JA, Cascante M, et al. Metabolomics enables precision medicine: "A White Paper, Community Perspective." *Metabolomics*. 2016;12:149.
25. Fiehn O. Metabolomics – the link between genotypes and phenotypes. *Plant Mol Biol*. 2002;48:155–71.

26. Weckwerth W. Metabolomics: an integral technique in systems biology. *Bioanalysis*. 2010;2:829–36.
27. Roca M, Alcoriza MI, Garcia-Cañaveras JC, Lahoz A. Reviewing the metabolome coverage provided by LC-MS: Focus on sample preparation and chromatography-A tutorial. *Analytica Chimica Acta*. 2021;1147:38–55.
28. Pan Z, Raftery D. Comparing and combining NMR spectroscopy and mass spectrometry in metabolomics. *Anal Bioanal Chem*. 2007;387:525–7.
29. Wang S, Blair IA, Mesaros C. Analytical Methods for Mass Spectrometry-Based Metabolomics Studies. In: Woods AG, Darie CC, editors. *Advancements of Mass Spectrometry in Biomedical Research* [Internet]. Cham: Springer International Publishing; 2019 [cited 2021 Aug 24]. p. 635–47.
30. Alves S, Paris A, Rathahao-Paris E. Chapter Four - Mass spectrometry-based metabolomics for an in-depth questioning of human health. In: Makowski GS, editor. *Advances in Clinical Chemistry* [Internet]. Elsevier; 2020 [cited 2021 Aug 24]. p. 147–91.
31. Ren J-L, Zhang A-H, Kong L, Wang X-J. Advances in mass spectrometry-based metabolomics for investigation of metabolites. *RSC Advances*. Royal Society of Chemistry; 2018;8:22335–50.
32. Kanu AB, Dwivedi P, Tam M, Matz L, Hill Jr. HH. Ion mobility–mass spectrometry. *Journal of Mass Spectrometry*. 2008;43:1–22.
33. Ivanisevic J, Elias D, Deguchi H, Averell PM, Kurczy M, Johnson CH, et al. Arteriovenous Blood Metabolomics: A Readout of Intra-Tissue Metabostasis. *Sci Rep*. Nature Publishing Group; 2015;5:12757.
34. Psychogios N, Hau DD, Peng J, Guo AC, Mandal R, Bouatra S, et al. The Human Serum Metabolome. *PLoS One*. 2011;6:e16957.
35. Patti GJ, Yanes O, Siuzdak G. Innovation: Metabolomics: the apogee of the omics trilogy. *Nature Reviews Molecular Cell Biology*. 2012;13:263–9.
36. Cífková E, Holčápek M, Lisa M, Ovčáčiková M, Lyčka A, Lynen F, et al. Nontargeted Quantitation of Lipid Classes Using Hydrophilic Interaction Liquid Chromatography–Electrospray Ionization Mass Spectrometry with Single Internal Standard and Response Factor Approach. *Anal Chem*. American Chemical Society; 2012;84:10064–70.
37. Hines KM, Herron J, Xu L. Assessment of altered lipid homeostasis by HILIC-ion mobility-mass spectrometry-based lipidomics. *J Lipid Res*. 2017;58:809–19.
38. Srivastava A, Kowalski G, Callahan D, Meikle P, Creek D. Strategies for Extending Metabolomics Studies with Stable Isotope Labelling and Fluxomics. *Metabolites*. 2016;6:32.
39. You L, Zhang B, Tang YJ. Application of Stable Isotope-Assisted Metabolomics for Cell Metabolism Studies. *Metabolites*. 2014;4:142–65.
40. Bennett BD, Yuan J, Kimball EH, Rabinowitz JD. Absolute quantitation of intracellular metabolite concentrations by an isotope ratio-based approach. *Nature Protocols*. 2008;3:1299–311.
41. Evers B, Gerding A, Boer T, Heiner-Fokkema MR, Jalving M, Wahl SA, et al. Simultaneous Quantification of the Concentration and Carbon Isotopologue Distribution of Polar Metabolites in a Single Analysis by Gas Chromatography and Mass Spectrometry. *Anal Chem*. 2021;93:8248–56.
42. Willacey CCW, Naaktgeboren M, Lucumi Moreno E, Wegrzyn AB, van der Es D, Karu N, et al. LC–MS/MS analysis of the central energy and carbon metabolites in biological samples following derivatization by dimethylaminophenacyl bromide. *Journal of Chromatography A*. 2019;1608:460413.
43. Guo K, Li L. High-Performance Isotope Labeling for Profiling Carboxylic Acid-Containing Metabolites in Biofluids by Mass Spectrometry. *Anal Chem*. American Chemical Society; 2010;82:8789–93.
44. Covey TR, Thomson BA, Schneider BB. Atmospheric pressure ion sources. *Mass Spectrom Rev*. 2009;28:870–97.
45. Trötzlmüller M, Guo X, Fauland A, Köfeler H, Lankmayr E. Characteristics and origins of common chemical noise ions in negative ESI LC-MS. *J Mass Spectrom*. 2011;46:553–60.
46. Keller BO, Sui J, Young AB, Whittall RM. Interferences and contaminants encountered in modern mass spectrometry. *Anal Chim Acta*. 2008;627:71–81.
47. Sindelar M, Patti GJ. Chemical Discovery in the Era of Metabolomics. *J Am Chem Soc*. American Chemical Society; 2020;142:9097–105.
48. Clendinen CS, Stupp GS, Ajredini R, Lee-McMullen B, Beecher C, Edison AS. An overview of methods using ¹³C for improved compound identification in metabolomics and natural products. *Frontiers in Plant Science*. 2015;6:611.
49. Bueschl C, Kluger B, Lemmens M, Adam G, Wiesenberger G, Maschietto V, et al. A novel stable isotope labelling assisted workflow for improved untargeted LC–HRMS based metabolomics research. *Metabolomics*. 2014;10:754–69.
50. Kluger B, Bueschl C, Neumann N, Stückler R, Doppler M, Chassy AW, et al. Untargeted Profiling of Tracer-Derived Metabolites Using Stable Isotopic Labeling and Fast Polarity-Switching LC–ESI-HRMS. *Analytical Chemistry*. 2014;86:11533–7.
51. Hegeman AD, Schulte CF, Cui Q, Lewis IA, Huttlin EL, Eghbalian H, et al. Stable Isotope Assisted Assignment of Elemental Compositions for Metabolomics. *Anal Chem*. 2007;79:6912–21.
52. Stupp GS, Clendinen CS, Ajredini R, Szewc MA, Garrett T, Menger RF, et al. Isotopic Ratio Outlier Analysis Global Metabolomics of *Caenorhabditis elegans*. *Anal Chem*. American Chemical Society; 2013;85:11858–65.
53. Qiu Y, Moir R, Willis I, Beecher C, Tsai Y-H, Garrett TJ, et al. Isotopic Ratio Outlier Analysis of the *S. cerevisiae* Metabolome Using Accurate Mass Gas Chromatography/Time-of-Flight Mass Spectrometry: A New Method for Discovery. *Anal Chem*. American Chemical Society; 2016;88:2747–54.

54. Mahieu NG, Huang X, Chen Y-J, Patti GJ. Credentialing Features: A Platform to Benchmark and Optimize Untargeted Metabolomic Methods. *Anal Chem*. American Chemical Society; 2014;86:9583–9.
55. Grankvist N, Watrous JD, Lagerborg KA, Lyutvinskiy Y, Jain M, Nilsson R. Profiling the Metabolism of Human Cells by Deep ¹³C Labeling. *Cell Chemical Biology* [Internet]. 2018 [cited 2018 Oct 2];
56. Bueschl C, Krska R, Kluger B, Schuhmacher R. Isotopic labeling-assisted metabolomics using LC–MS. *Analytical and Bioanalytical Chemistry*. 2013;405:27–33.
57. Jang C, Chen L, Rabinowitz JD. Metabolomics and Isotope Tracing. *Cell*. 2018;173:822–37.
58. Hiller K, Metallo C, Stephanopoulos G. Elucidation of cellular metabolism via metabolomics and stable-isotope assisted metabolomics. *Curr Pharm Biotechnol*. 2011;12:1075–86.
59. Trefely S, Ashwell P, Snyder NW. FluxFix: automatic isotopologue normalization for metabolic tracer analysis. *BMC Bioinformatics*. 2016;17:485.
60. Fan TW, Lane AN, Higashi RM, Farag MA, Gao H, Bousamra M, et al. Altered regulation of metabolic pathways in human lung cancer discerned by ¹³C stable isotope-resolved metabolomics (SIRM). *Molecular Cancer*. 2009;8:41.
61. Mayers JR, Vander Heiden MG. Famine versus feast: understanding the metabolism of tumors in vivo. *Trends in Biochemical Sciences*. 2015;40:130–40.
62. Davidson SM, Papagiannakopoulos T, Olenchok BA, Heyman JE, Keibler MA, Luengo A, et al. Environment Impacts the Metabolic Dependencies of Ras-Driven Non-Small Cell Lung Cancer. *Cell Metabolism*. 2016;23:517–28.
63. Tumanov S, Bulusu V, Kamphorst JJ. Analysis of Fatty Acid Metabolism Using Stable Isotope Tracers and Mass Spectrometry. *Methods Enzymol*. 2015;561:197–217.
64. Sellers K, Fox MP, Bousamra M, Slone SP, Higashi RM, Miller DM, et al. Pyruvate carboxylase is critical for non-small-cell lung cancer proliferation. *J Clin Invest*. American Society for Clinical Investigation; 2015;125:687–98.
65. Chaneton B, Hillmann P, Zheng L, Martin ACL, Maddocks ODK, Chokkathukalam A, et al. Serine is a natural ligand and allosteric activator of pyruvate kinase M2. *Nature*. 2012;491:458–62.
66. Locasale JW, Grassian AR, Melman T, Lyssiotis CA, Mattaini KR, Bass AJ, et al. Phosphoglycerate dehydrogenase diverts glycolytic flux and contributes to oncogenesis. *Nat Genet*. 2011;43:869–74.
67. Park JO, Rubin SA, Xu Y-F, Amador-Noguez D, Fan J, Shlomi T, et al. Metabolite concentrations, fluxes and free energies imply efficient enzyme usage. *Nat Chem Biol*. 2016;12:482–9.
68. Lewis CA, Parker SJ, Fiske BP, McCloskey D, Gui DY, Green CR, et al. Tracing Compartmentalized NADPH Metabolism in the Cytosol and Mitochondria of Mammalian Cells. *Molecular Cell*. 2014;55:253–63.
69. Lee WN, Boros LG, Puigjaner J, Bassilian S, Lim S, Cascante M. Mass isotopomer study of the nonoxidative pathways of the pentose cycle with [1,2-¹³C₂]glucose. *Am J Physiol*. 1998;274:E843–851.
70. Ghergurovich JM, Lang JD, Levin MK, Briones N, Facista SJ, Mueller C, et al. Local production of lactate, ribose phosphate, and amino acids within human triple-negative breast cancer. *Med (N Y)*. 2021;2:736–54.
71. Yoo H, Antoniewicz MR, Stephanopoulos G, Kelleher JK. Quantifying Reductive Carboxylation Flux of Glutamine to Lipid in a Brown Adipocyte Cell Line. *J Biol Chem*. 2008;283:20621–7.
72. Chokkathukalam A, Kim D-H, Barrett MP, Breitling R, Creek DJ. Stable isotope-labeling studies in metabolomics: new insights into structure and dynamics of metabolic networks. *Bioanalysis*. 2014;6:511–24.
73. Metallo CM, Gameiro PA, Bell EL, Mattaini KR, Yang J, Hiller K, et al. Reductive glutamine metabolism by IDH1 mediates lipogenesis under hypoxia. *Nature*. 2012;481:380–4.
74. Mullen AR, Wheaton WW, Jin ES, Chen P-H, Sullivan LB, Cheng T, et al. Reductive carboxylation supports growth in tumour cells with defective mitochondria. *Nature*. 2012;481:385–8.
75. Faubert B, Li KY, Cai L, Hensley CT, Kim J, Zacharias LG, et al. Lactate Metabolism in Human Lung Tumors. *Cell*. 2017;171:358–371.e9.
76. Hui S, Ghergurovich JM, Morscher RJ, Jang C, Teng X, Lu W, et al. Glucose feeds the TCA cycle via circulating lactate. *Nature*. 2017;551:115–8.
77. Puchalska P, Martin SE, Huang X, Lengfeld JE, Daniel B, Graham MJ, et al. Hepatocyte-Macrophage Acetoacetate Shuttle Protects against Tissue Fibrosis. *Cell Metab*. 2019;29:383–398.e7.
78. Weindl D, Wegner A, Hiller K. Metabolome-Wide Analysis of Stable Isotope Labeling—Is It Worth the Effort? *Front Physiol* [Internet]. 2015 [cited 2019 Feb 24];6.
79. Sauer U. Metabolic networks in motion: ¹³C-based flux analysis. *Molecular Systems Biology* [Internet]. 2006 [cited 2018 Sep 28];2.
80. Wiechert W, Niedenführ S, Nöh K. A Primer to ¹³C Metabolic Flux Analysis. In: Villadsen J, editor. *Fundamental Bioengineering* [Internet]. Weinheim, Germany: Wiley-VCH Verlag GmbH & Co. KGaA; 2015 [cited 2019 Nov 27]. p. 97–142.
81. Long CP, Antoniewicz MR. High-resolution ¹³C metabolic flux analysis. *Nat Protoc*. 2019;14:2856–77.
82. Wiechert W, Nöh K. Isotopically non-stationary metabolic flux analysis: complex yet highly informative. *Current Opinion in Biotechnology*. 2013;24:979–86.
83. Jazmin LJ, Young JD. Isotopically Nonstationary ¹³C Metabolic Flux Analysis. 2013.
84. Jiang L, Boufersaoui A, Yang C, Ko B, Rakheja D, Guevara G, et al. Quantitative metabolic flux analysis reveals an unconventional pathway of fatty acid synthesis in cancer cells deficient for the mitochondrial citrate transport protein. *Metab Eng*. 2017;43:198–207.

85. Jiang L, Shestov AA, Swain P, Yang C, Parker SJ, Wang QA, et al. Reductive carboxylation supports redox homeostasis during anchorage-independent growth. *Nature*. 2016;532:255–8.
86. Pereira AGM, Walther JL, Hollenbach M, Young JD. ¹³C Flux Analysis Reveals that Rebalancing Medium Amino Acid Composition can Reduce Ammonia Production while Preserving Central Carbon Metabolism of CHO Cell Cultures. *Biotechnology Journal*. 2018;13:1700518.
87. Antoniewicz MR. Tandem mass spectrometry for measuring stable-isotope labeling. *Current Opinion in Biotechnology*. 2013;24:48–53.
88. Choi J, Antoniewicz MR. Tandem mass spectrometry: A novel approach for metabolic flux analysis. *Metabolic Engineering*. 2011;13:225–33.
89. Yuan J, Bennett BD, Rabinowitz JD. Kinetic flux profiling for quantitation of cellular metabolic fluxes. *Nature Protocols*. 2008;3:1328–40.
90. Rühl M, Rupp B, Nöh K, Wiechert W, Sauer U, Zamboni N. Collisional fragmentation of central carbon metabolites in LC-MS/MS increases precision of ¹³C metabolic flux analysis. *Biotechnol Bioeng*. 2012;109:763–71.
91. Mairinger T, Hann S. Implementation of data-dependent isotopologue fragmentation in ¹³C-based metabolic flux analysis. *Anal Bioanal Chem*. 2017;409:3713–8.
92. Jaiswal D, Prasanna CB, Hendry JL, Wangikar PP. SWATH Tandem Mass Spectrometry Workflow for Quantification of Mass Isotopologue Distribution of Intracellular Metabolites and Fragments Labeled with Isotopic ¹³C Carbon. *Analytical Chemistry*. 2018;90:6486–93.
93. Sun Q, Fan TW-M, Lane AN, Higashi RM. An Ion Chromatography–Ultrahigh-Resolution-MS 1 /Data-Independent High-Resolution MS 2 Method for Stable Isotope-Resolved Metabolomics Reconstruction of Central Metabolic Networks. *Anal Chem*. 2021;93:2749–57.
94. Fan TW-M, Sun Q, Higashi RM. Ultrahigh resolution MS1/MS2-based reconstruction of metabolic networks in mammalian cells reveals changes for selenite and arsenite action. *Journal of Biological Chemistry*. 2022;298:102586.
95. Fleming RMT, Haraldsdottir HS, Preciat G, Huang L, Thiele I, Harms A, et al. Conserved moiety fluxomics.
96. Chernushevich IV, Merenbloom SI, Liu S, Bloomfield N. A W-Geometry Ortho-TOF MS with High Resolution and Up to 100% Duty Cycle for MS/MS. *J Am Soc Mass Spectrom*. 2017;28:2143–50.

Chapter 2:

Systematic Evaluation of HILIC Stationary Phases for Global Metabolomics of Human Plasma

Based on:

Farideh Hosseinkhani*, Luojiao Huang*, Anne-Charlotte Dubbelman, Faisa Guled, Amy C. Harms and Thomas Hankemeier

Systematic Evaluation of HILIC Stationary Phases for Global Metabolomics of Human Plasma

Metabolites 2022;12:165.

* Shared first authors

Abstract

Polar hydrophilic metabolites have been identified as important actors in many biochemical pathways. Despite continuous improvement and refinement of hydrophilic interaction liquid chromatography (HILIC) platforms, its application in global polar metabolomics has been underutilized. In this study, we aimed to systematically evaluate polar stationary phases for untargeted metabolomics by using HILIC columns (neutral and zwitterionic) that have been exploited widely in targeted approaches. To do so, high-resolution mass spectrometry was applied to thoroughly investigate selectivity, repeatability and matrix effect at three pH conditions for 9 classes of polar compounds using 54 authentic standards and plasma matrix. The column performance for utilization in untargeted metabolomics was assessed using plasma samples with diverse phenotypes. Our results indicate that the ZIC-c HILIC column operated at neutral pH exhibited several advantages, including superior performance for different classes of compounds, better isomer separation, repeatability and high metabolic coverage. Regardless of the column type, the retention of inorganic ions in plasma leads to extensive adduct formation and co-elution with analytes, which results in ion-suppression as part of the overall plasma matrix effect. In ZIC-c HILIC, the sodium chloride ion effect was particularly observed for amino acids and amine classes. Successful performance of HILIC for separation of plasma samples with different phenotypes highlights this mode of separation as a valuable approach in global profiling of plasma sample and discovering the metabolic changes associated with health and disease.

Introduction

Metabolomics is rapidly becoming a powerful approach in its application to system biology-based studies. It enables characterizing the profile of small molecules in biological samples and thereby discovering metabolites that discriminate across phenotypes [1,2]. In-depth investigations of metabolic pathways highlighted polar and ionic compounds such as amino acids, carboxylic acids, phosphorylated compounds, nucleotides, sugars etc., as key modulators of physiological and pathophysiological processes [3,4]. Metabolomics studies are typically performed using liquid chromatography (LC) hyphenated to mass spectrometry (MS), and reversed-phase (RP) LC is the most widespread choice in bioanalytical separation as it generates reproducible data for a large set of metabolites. However, the analysis of polar and ionic compounds continues to challenge this mode of chromatography as they are poorly retained on the stationary phase of RPLC columns [5]. Even though chemical derivatization of these compounds is an active research area, disadvantages of this approach include partial derivatization and increased sample complexity. Moreover, tedious derivatization steps make it a time-consuming method, and additional experimental steps may influence the recovery rate, accuracy and repeatability of the result [6]. To that end, hydrophilic interaction liquid chromatography (HILIC) has grown in popularity for the chromatographic retention and separation of polar compounds [7]. In HILIC, the high organic content mobile phase prolongs retention time, and improves mass spectral detection of polar metabolites by increasing the ionization efficiency [8]. The separation mechanism includes a combination of various hydrophilic, electrostatic, and ionic interactions; however, the dominant mechanism depends on the physicochemical property of the stationary phase (neutral, charged and zwitterionic) and the structure of the analytes [7]. Among all commercially available stationary phases, the neutral stationary phase of Acquity-Waters (UPLC BEH-amide) and the zwitterionic (ZIC) stationary phases of SeQuant® Merck (HPLC Phosphorylcholine and Sulfobetaine) have often been exploited for the separation and targeted analysis of polar metabolites. For instance, BEH-amide has recently been utilized for effective separation of 24 amino acids from cell culture [9] and could successfully cover key metabolite classes such as sugars, amino acids, nucleotides and organic acids in plasma samples [10]. Arase et al. [11] reported the phosphorylcholine type ZIC-cHILIC as the most appropriate column for the separation of nucleotides. In another study, ZIC-HILIC has been applied for determination of organic acids in plasma and urine for the assessment of acidosis in patients with severe malaria [12]. Despite the increased interest in HILIC in the last decade for targeted profiling of polar metabolites, the potential of HILIC in untargeted metabolomics is underestimated due to low reproducibility, complex retention mechanisms and low peak capacities [13]. Even

though several comparison studies investigated the metabolic coverage and retention mechanisms involved in different HILIC columns, the lack of a practically helpful guide has resulted in no consensus on the utilization of the appropriate column and analytical procedure. In a recent study, Contrepois et al. [14] reported that, at neutral pH, a superior separation and higher metabolic coverage in plasma and urine were achieved by ZIC-HILIC when testing five columns, including BEH-amide and BEH-HILIC (charged). In another study, Sillner et al. [15] observed better performance of BEH-amide at basic pH compared to a zwitterionic column in terms of peak width, isomers separation, and the number of detected features in fecal samples.

In addition to the metabolic coverage, matrix effect and batch repeatability are crucial factors that need to be considered in untargeted metabolomics studies of biological samples. Inorganic ions such as sodium, potassium and chloride are among the major electrolytes in different body fluids. These ions are well known to affect electrospray ionization by promoting adduct ions with sample analyte and cluster ion formation with mobile phase additives, and leading to ion suppression [16]. The use of RP-LC often diminishes these problems as salts generally elute with the void volume. However, when employing HILIC, these inorganic ions can be retained by the chromatographic system and impact the detection of coeluting polar analytes [17]. Most previous studies have only focused on the effect of buffer salt on the retention mechanism [18,19], while far too little attention has been paid to the matrix salt effect on the analysis of diverse polar metabolites.

This study set out to systematically explore the selectivity of HILIC interaction and coverage for two popular HILIC columns; BEH-amide and ZIC-c HILIC. We scored the performance of two stationary phases (zwitterionic and neutral) for nine different classes of compounds at three different pH conditions (acidic, neutral, basic). Parameters were evaluated in terms of number of detected metabolites, peak shape, retention factor, resolution and sensitivity. To assess the intra- and inter-batch column repeatability in measuring biological samples, we monitored the peak area variation and retention time shift using plasma samples. Plasma matrix effect, particularly salt effect on neutral and zwitterionic stationary phases, was also evaluated. Finally, we assessed the column performance for utilization in untargeted metabolomics using plasma samples with diverse phenotypes. Comparison based on the total feature numbers and retention distribution of detected features was carried out to determine the optimal HILIC stationary type. Since plasma matrix contains different polar metabolites, many of which elute close to the solvent front in RP chromatography, HILIC separation can enhance plasma metabolome coverage and provide an enhanced view on plasma composition.

Materials and methods

1. Chemicals and Materials

Analytical grade solvents acetonitrile, methanol, chloroform and formic acid (98%) were purchased from Biosolve (Biosolve BV, Valkenswaard, The Netherlands), whereas ammonium formate ($\geq 99.995\%$), ammonium hydroxide (28–30 wt % solution of ammonia in water) sodium chloride ($\geq 99.0\%$) and sodium hydroxide were obtained from Sigma Aldrich (Sigma-Aldrich, Burlington, WV, USA). MilliQ water was obtained from a Merck Milli-pore A10 purification system (Raleigh, USA). Chemical standards and stable isotope-labelled standards were purchased from Sigma-Aldrich (St. Louis, USA) unless otherwise mentioned. The complete information of the (stable isotope-labelled) standards and suppliers are provided in the supporting information Table S1. An EDTA pooled plasma (June 2020) was used for the column performance, matrix effect, and repeatability evaluation and purchased from Innovative Research (Peary Court Novi, MI, USA). Four diverse EDTA plasma samples (categorized as Dutch, American, fasted and non-fasted) were used for untargeted analysis. American, fasted and non-fasted pooled plasmas were purchased from Innovative Research (Peary Court Novi, MI, USA) and Dutch pooled plasma was purchased from Sanquin (Sanquin, Amsterdam, The Netherlands).

2. Standard Solutions

A total number of 54 authentic standards were used during the experiment covering a wide range of polar metabolic classes including amino acids (17), amines (4), sugars (2), sugar phosphates (3), nucleosides (7), nucleotides (5), acyl-carnitines (2), coenzyme A (1) and organic acids (13). Stock solutions of the analytes were prepared at a concentration of 10mM in milliQ water, except for aspartic acid, adenosine, adenine, uracil which were prepared in methanol and water (1:1, v/v). For certain standards, addition of 0.05% formic acid (aspartic acid, adenosine, adenine, uracil) or 0.1M sodium hydroxide (hypoxanthine, uric acid) was needed to assist dissolution. Stock solutions were stored in Eppendorf tubes at -80°C . A standard mix solution was prepared by mixing 54 individual standard solutions at a final concentration of 160 μM . The standard mix solution was aliquoted in separate Eppendorf tubes and also stored at -80°C . Standard working solutions were prepared at a final concentration of 20 μM by dilution of the standard mix solution in acetonitrile/milliQ water (9:1, v/v).

Stable isotope-labelled standards (SILs) used in the study include U- $^{13}\text{C}_4$, U-D $_3$, ^{15}N -aspartate, U- $^{13}\text{C}_5$ -glutamine, 2,3,3-D $_3$ -leucine, D $_4$ -choline, U- $^{13}\text{C}_6$ -glucose, U- $^{15}\text{N}_2$ -UMP, D $_3$ -carnitine, $^{13}\text{C}_3$ -pyruvate, 2,2,3,3-D $_4$ -succinate, 2,2-D $_2$ -glycine, 2,3-D $_2$ -fumarate, U- $^{13}\text{C}_{11}$, U- $^{15}\text{N}_2$ -tryptophan, U- $^{13}\text{C}_4$, U- $^{15}\text{N}_2$ -asparagine, U- $^{13}\text{C}_5$, U-D $_5$, ^{15}N -glutamate, U- $^{13}\text{C}_5$ -valine, U- $^{13}\text{C}_6$ -lysine and U- $^{15}\text{N}_2$ -UMP. The SILs stock solution was prepared at concentration of

10mM in milliQ water and stored at -80°C . Together with the quality control sample, this mix was used for day-to-day analysis to monitor the process and analytical variation.

3. Sample Preparation

Plasma samples were extracted using chloroform/MeOH/water solvent system (2.6/2.0/2.4, v/v/v) according to Sostare et al. [19]. Briefly, 100 μL of plasma was quenched using 75% ice-cold methanol (400 μL MeOH+132 μL milliQ water) and 200 μL of chloroform. The mixture was subsequently vortexed for 3 min and centrifuged for 10min (13,000 $\times g$, 4°C). The upper layer of supernatant ($\sim 600\mu\text{L}$) was transferred into a new Eppendorf tube and then mixed with 200 μL of chloroform and 230 μL of milliQ water. The mixture was vortex mixed for 3min and centrifuged for 10min (13,000 $\times g$, 4°C) for a second liquid-liquid extraction (LLE). The final upper layer ($\sim 900\mu\text{L}$) was collected and evaporated to dryness in a Labcono SpeedVac (Labcono, Kansas City, MO, United State). The residue was then reconstituted with 100 μL of acetonitrile/ milliQ water (9:1, v/v). In order to increase the quenching and minimize the residual enzymatic activity, all solvents for extraction in this study were used ice-cold. To improve the sensitivity for untargeted analysis, those plasma samples were processed in the same manner only reconstituted in 50 μL of reconstitution solution.

A Quality control (QC) sample was prepared by pooling 50 μL of every study sample, spiked with standard mixture solution and SILs solution at a final concentration of 20 and 40 μM respectively. This QC sample was used for monitoring the stability, precision, random errors and correcting for instrument fluctuations during the analytical run.

4. Instrumentation and LC-MS Acquisitions

HILIC chromatography was performed using a Waters Acquity UPLC Class II (Waters Chromatography Europe BV, Etten-Leur, The Netherlands) with the oven temperature set at 30°C . Two HILIC columns were investigated in this study, the Acquity BEH-amide column (2.1mm x 100mm, 1.7 μm , Waters, Irland) and the SeQuant[®] ZIC[®]-cHILIC column (2.1mm x 100mm, 3.0 μm - Merck, Darmstadt, Germany). The mobile phase composition was the same for both columns. Mobile phase A consisted of 90% acetonitrile and 10% 5mM ammonium formate. Mobile phase B consisted of 10% acetonitrile, 90% 5mM ammonium formate. The acidic and basic pH of the aqueous 5mM ammonium formate were adjusted using formic acid and ammonium hydroxide respectively. The BEH-amide column is composed of neutral ethylene bridge hybrid (BEH) particles which enables the stability of the column over a wide range of pH (2-11). Therefore, BEH-amide column was operated at 3 different pH values of mobile phase; acidic (pH 3), neutral (pH 7) and basic (pH 10). The ZIC-c column is composed of silica-based particles (1:1 charge-balanced

phosphorylcholine functional group) which lose stability in pH above 8. Therefore, the ZIC-c was operated only at acidic and neutral conditions.

For each HILIC column, the gradient and flow rate were optimized based on the standards retention (Table S2). The flow rate used with SeQuant® ZIC®-cHILIC column was 0.25 mL/min and the starting gradient condition was 0% B for 2 min, changing linearly to 40% B over the next 20 min, after which the solvent composition returned to starting condition over 0.1min, followed by re-equilibration for 10min prior to the next injection. The flow rate applied on Acquity BEH-amide column was 0.5 mL/min and the starting gradient condition was 0% B for 1.2min, changing linearly to 40% B over the next 14min, ends up with 0% B from 14.2-18min.

Mass spectrometry experiments were carried out on a quadrupole-TOF (SCIEX 5600 TripleTOF, AB SCIEX, Foster City, CA). Electrospray ionization (ESI) was operating at both positive and negative ion mode. The ESI source parameters were as follows (positive/negative ion mode): spray voltage ± 4.5 kV, capillary temperature 550°C, sheath gas 50, auxiliary gas 65, curtain gas 25. The full scan mode was applied for data acquisition over a m/z range of 50-900Da. The complete compound list with observed mass adducts and m/z ratios is shown in Table S1. In total, five LC conditions were analysed with both positive and negative ESI TOF-MS.

5. Matrix effect

Matrix effect (i.e., suppression and enhancement of metabolite signal in $[M-H]^-$ or $[M+H]^+$) was evaluated by the post extraction addition method which is based on a quantitative signal comparison between a plasma matrix spiked with standard mix solution (20 μ L) after the sample clean-up versus a neat standard. To evaluate the sodium and chlorine influence among the general matrix effect, saline (NaCl) solution in three different concentrations (6.0, 7.5 and 9.0g/L milliQ water) spiked with standard mix solution were used as controls. A schematic workflow of the matrix effect experiment is given in Figure S1. The reported matrix effect values are an average of three replicates obtained from independent sample preparations within each sample group. Matrix effect was calculated according to equation (2) if metabolite was detected with a basal level in plasma, otherwise using equation (1).

$$ME = \frac{\text{Peak area of analyte in spiked plasma matrix}}{\text{Peak area of analyte in neat standard solution}} \quad (1)$$

$$ME = \frac{\text{Peak area of analyte in spiked plasma matrix} - \text{Peak area of analyte in unspiked plasma matrix}}{\text{Peak area of analyte in neat standard solution}} \quad (2)$$

Matrix effect in the range of $\pm 20\%$ ($0.80 < ME < 1.20$) were considered as negligible and labelled as “no matrix effect”, since it is the common variability accepted in bioanalysis

[13]. ME values below 0.80 were considered as ion suppression, and those above 1.20 as ion enhancement.

6. Repeatability

To evaluate the repeatability, intra- and inter-batch analysis were performed at optimal chromatography condition of each column. Therefore, ZIC-c and BEH-amide were operated at pH 7 and 10 respectively coupled with negative ESI-MS. Prior to batch analysis, the column was equilibrated with the initial mobile phase gradient and subsequently conditioned with 20 pooled lab QC plasma injections. The intra-batch analysis included consecutive injection of 200 plasma QC samples. The inter-batch analysis included three batches, comprising injections of 20 plasma QC samples per batch with an interval of two days in between. The inter- and intra-batch variation were assessed by calculating the relative standard deviation.

7. Data analysis

The identification and integration of the analytes from LC-MS raw data was performed using AB Sciex PeakView™ 2.0 and MultiQuant™ 3.0.1. Related chromatographic peak parameters including retention time, peak height, peak width, tailing factor were also calculated by MultiQuant automatically. Predicted logD, charge state and hydrogen bond number under pH 3, 7, 10 for each analyte were calculated using Marvin Sketch software version 20.10.0, ChemAxon (<http://www.chemaxon.com/>) and shown in Table S3. To achieve good comparison between different chromatography conditions over all analytes, a chromatographic performance scoring system was defined to assign a score for each individual metabolite [14,21]. The scoring system was defined based on following parameters: metabolite retention, peak sensitivity (as indicated by natural log of the signal-to-noise ratio), peak sharpness (as indicated by natural log of the peak height), and peak symmetry (as indicated by the tailing factor). Details of scoring parameters are presented in the supporting information Table S4. The total score for each compound was calculated according to the formula (3).

$$\mathbf{Score}_{\text{total}} = \mathbf{Score}_{\text{retention}} + \mathbf{Score}_{\text{sharpness}} + \mathbf{Score}_{\text{symmetry}} + \mathbf{Score}_{\text{sensitivity}} \quad (3)$$

A simple linear regression model was used to analyse the relationship between metabolites polarity at different pH conditions and elution order. The model was built in R (version 3.6.2), and plotted a fitting line across all data points. Based on the linear model, the Pearson's correlation coefficient (r) was calculated. For untargeted analysis, the raw data sets were converted to mzXML files and subsequently centroided using Proteo Wizard MSConvert version 3.0 [21]. Metabolite features were extracted from converted data sets using XCMS package (version 3.10) in R (version 3.6.2) [28]. Data were processed as a multi-group experiment and the parameter settings were as follows: centWave algorithm

for feature detection ($\Delta m/z = 5$ ppm, minimum peak width = 5 s and maximum peak width = 100 s, S/N threshold = 10, $mzdiff = 0.01$, integration method = 1, prefilter peaks = 3, prefilter intensity = 100, noise filter = 100); obiwrap settings for retention time correction (profStep = 1); and parameters for chromatogram alignment, including $mzwid = 0.01$, minfrac = 0.5 and bw = 5. The resulting XCMS peak table was further processed to preserve only peaks that were not present in technical blanks while being present in at least one plasma phenotype. For recognition and removal of erroneous features in the datasets, MS-FLO (<http://msflo.fiehnlab.ucdavis.edu>) was used [29]. To obtain an overview of the metabolic data, abundance profiles of metabolites were \log (generalized logarithm) transformed and subjected to principal component analysis (PCA) using MetaboAnalyst version 5.0 (<https://www.metaboanalyst.ca>) [30]. The retention factor (K) was calculated according to formula (4), where t_R is the retention time of the feature in minutes and the t_0 is the void volume of the column in minutes.

$$K = \frac{t_R - t_0}{t_0} \quad (4)$$

Results and discussion

1. Column selectivity and performance

Two prominent HILIC columns (BEH-amide and ZIC-c) were tested for selectivity and performance for nine classes of compounds comprising 54 polar metabolites (Table S1). Previous studies [14] often utilized the same separation gradient while comparing different HILIC columns. However, the different structure of stationary phases might require different chromatography conditions for obtaining a good performance [20]. Therefore, we used a specified gradient for each column that could retain most of the tested analytes. We aimed at using a scoring approach that allows to compare the performance of different chromatographic conditions for the analytes of interest based on the following parameters: metabolite retention, peak sensitivity, peak sharpness and peak symmetry [14,21]. The metabolite performance was considered as good, acceptable, or bad, based on the calculated total score (see Table S4, supporting information). Metabolites scored as “good” exhibit long retention (void time $\times 4$) and avoid the ion suppression zone. In addition, their narrow peak profile together with minimal tailing and high sensitivity provide more reliable metabolite identification and quantification. Metabolites evaluated as “acceptable” can be used for qualitative purposes, but might introduce problems during quantitative analysis. Metabolites evaluated as “bad” are not recommended to be measured using the corresponding HILIC method due to either broad peak profile, early elution or low peak intensity [14].

Figure 1a shows the performance cumulative score per chromatographic condition for each individual metabolite. The ZIC-c column operated at neutral pH was superior in coverage

and peak performance, as the majority (96%) of tested standards achieved a good or acceptable performance score. In comparison, the BEH-amide showed the best performance at basic condition with 74% of metabolites obtaining good or acceptable score. From the standard working solution (20 μ M), most compounds were detected by ZIC-c at both acidic and neutral pH, except for citric acid, glycerate-3-phosphate and malic acid, which were only detected under the neutral condition. In contrast, BEH-amide resulted in bad performance for the above-mentioned organic acids, as well as for 6-phosphogluconic acid, ribose-5-phosphate, ADP and ATP. Regardless of the pH, both columns exhibited good chromatographic performance for amines, nucleosides and acyl carnitines, but sugar phosphates, nucleotides and coenzyme-A only performed well on ZIC-c.

Figure 1b presents the column selectivity and chromatographic peak performance of representative metabolites from different classes under the five different LC method conditions. Baseline separation of the isomers, leucine and isoleucine, fructose and glucose, glucose 6-phosphate and fructose 6-phosphate could be achieved with the ZIC-c column only.

This finding is consistent with that of Contrepois et al. [14] who reported a superior separation and higher metabolic feature coverage in plasma and urine using a zwitterionic column (ZIC-HILIC) at neutral pH among five tested columns, including BEH-amide and BEH HILIC (charged). Similarly, among six different HILIC stationary phases, Tufi et al. [22] proposed ZIC-c for simultaneous analysis of neurotransmitters in cell extracts. In fecal samples, Sillner et al. [15] also compared the performance of silica, amide, and zwitterionic columns for fecal polar metabolites and concluded that the zwitterionic column (ZIC-c) provided superior coverage and selectivity.

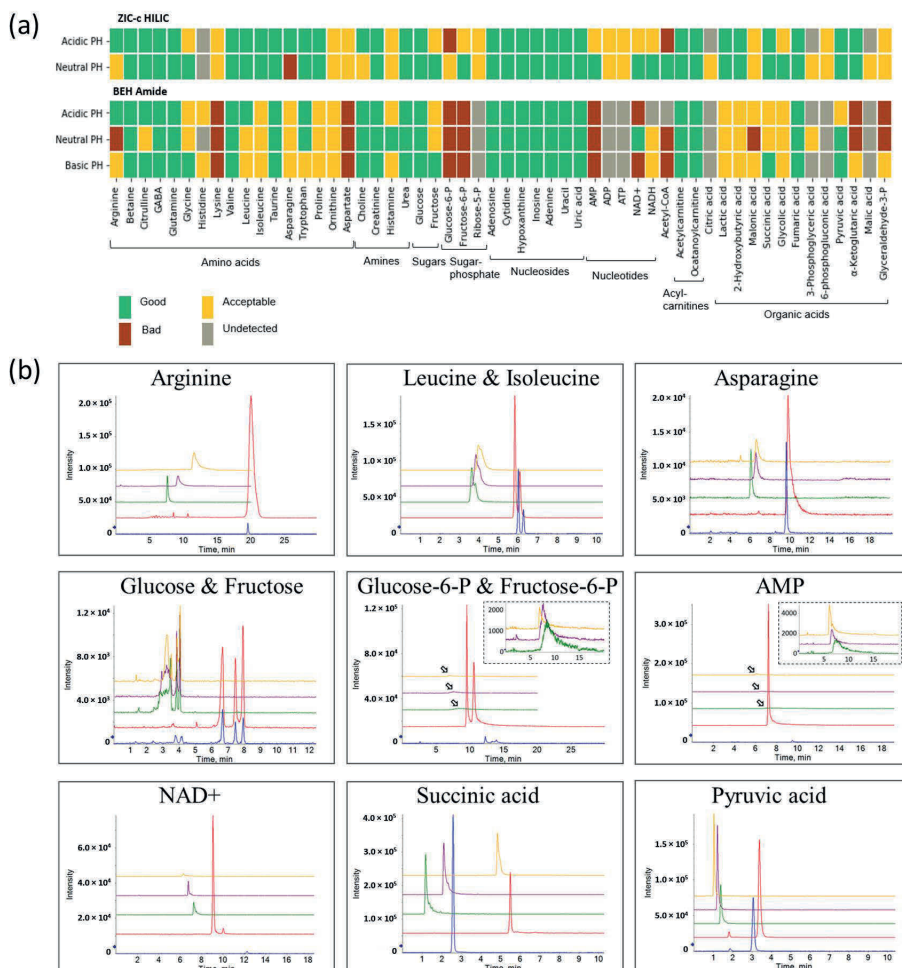


Figure 1. Overview of performance score and selectivity under chromatographic conditions. (a) Individual score of column performance for polar metabolites from different classes of compounds. (b) Column selectivity and chromatographic peak performance of representative metabolites from different classes under five different LC method conditions. Anomer mutarotation causes the glucose signal to split into two separate peaks as shown on both columns. **Blue:** ZIC-c HILIC at pH 3; **Red:** ZIC-c HILIC at pH 7; **Green:** BEH Amide at pH 3; **Purple:** BEH Amide at pH 7; **Yellow:** BEH Amide at pH 10.

2. Retention mechanism

HILIC separation is generally regarded as a mixed-mode mechanism. Partitioning of solutes occurs between the surface aqueous layer and the relatively non-polar organic mobile phase based on the polarity of the solutes. Electrostatic attractions or repulsions are created

between charged solutes and the stationary phase. In addition, molecules with hydrogen-donor or hydrogen-acceptor groups can interact through the hydrogen bonds with the stationary phase [23]. To gain a better insight into the interaction of metabolites with zwitterionic and neutral stationary phases under different pH values, correlation analysis was performed between the physical and chemical properties of a variety of compounds and their retention on each column. Physical and chemical properties including logD value, charged state and hydrogen bonding of 54 metabolites under acidic, neutral and basic pH are listed in Table S3. As depicted in Figure 2, a linear relationship was observed between metabolites polarity (as indicated by logD) at different pH conditions and elution order (as shown by the percentage of water phase). The impact of charge state is displayed as different dot colours, and the size of the dot reflects the influence of hydrogen bonding. At pH 3, both columns showed a relatively high correlation between logD and water fraction, which indicates that under acidic conditions, the separation mechanism is mainly governed by the partitioning of the analytes between the organic-rich bulk and water-rich layer. However, as pH increases, the correlation factor between logD and water fraction decreases. Increasing the pH from 3 to 7 converts the charge of organic acids from neutral to anionic, and nucleotides from zwitterionic to anionic (Table S3). Therefore, in the ZIC-c column at pH 7, anionic compounds such as 2-hydroxybutyric acid and lactic acid provoke more electrostatic attraction with the positively charged quaternary ammonium part of the phosphorylcholine functional group, indicating that a higher percentage of water is needed for elution. However, this effect was minimal for nucleotides such as AMP and NAD⁺ that required a higher percentage of water for elution in pH 3 as well. This can be explained by the fact that although these compounds are zwitterionic at pH 3 and demonstrate no net charge, they are still able to participate in electrostatic interactions with zwitterionic functional groups of the column.

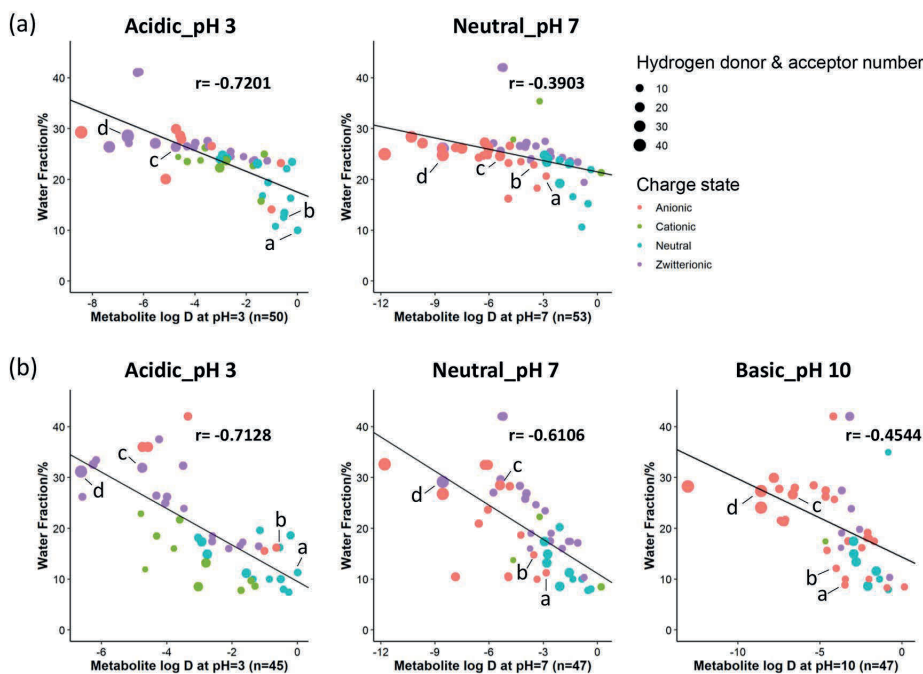


Figure 2. Analysis of the relative contribution to the retention mechanism on different HILIC columns. (a) Correlation analysis on ZIC-cHILIC and (b) Correlation analysis on BEH-amide. Individual metabolites are shown as a: 2-hydroxybutyric acid; b: lactic acid; c: AMP; d: NAD⁺.

Compared to ZIC-c, BEH-amide shows relatively higher involvement of partitioning at neutral pH with a higher correlation coefficient. However, at basic pH, partitioning is decreased by electrostatic interactions due to ionization of residual silanol groups, that causes even less retention or exclusion of anionic compounds [8,13]. In terms of polar interactions, hydrogen bonding also influences compound retention on both BEH-amide and ZIC-c HILIC columns. For each charge group, it was observed that compounds with higher total hydrogen donors and acceptors retain longer on the column. In line with previous studies [23,24], our results also demonstrated the mixed mode of retention mechanisms in neutral and zwitterionic HILIC. Hydrophilic partitioning interaction plays a primary role in separation. In addition, both BEH-amide and ZIC-c columns exhibited hydrogen-bonding interaction, whereas ZIC-c showed stronger electrostatic interactions than BEH-amide.

3. Matrix effect

Inorganic ions such as sodium (Na⁺) and chloride (Cl⁻) are undeniably part of the plasma matrix. These ions are known to interfere with the electrospray ionization and affect the sensitivity in mass spectrometry [25]. This effect can be incremental in HILIC separation since these ions can be retained by the polar stationary phase and interact with the mobile

phase additive [26]. To investigate the effect of matrix inorganic ions in untargeted HILIC-MS analysis, chromatographic separation and ionization of analytes of interest were compared with sodium chloride solution spiked with the standard mix. Blood plasma contains approximately 135-145 mmol/L sodium while the amount in 0.9% saline solution is 154 mmol/L. In order to closely mimic the plasma salt composition, we used sodium chloride solution at three concentrations: 0.6% and 0.75% and 0.9%. A major elution peak of sodium cluster series with the mobile phase component, formate, was detected as $[\text{Na}(n+1) + \text{HCOO}n]^+$ in the positive mode and $[\text{Na}(n) + \text{HCOO}(n+1)]^-$ in the negative mode around the highest water fraction (40%) during the HILIC gradient for both columns (Figure S2). Therefore, the coeluting metabolites arginine and lysine are directly influenced due to competition with the sodium cluster (Table S5-S6). Along with the increasing level of sodium chloride in samples, an increased signal of the $[\text{M}+\text{Na}]^+$ adduct was observed on citrulline, glutamine (eluting around 10mins) and adenosine, ocatanoyl-carnitine, creatinine, which eluted at around 4mins on the ZIC-c column. Similarly, a slight increased $[\text{M}+\text{Na}]^+$ adduct signal was detected for glutamine on the BEH-amide column at around 6mins (Table S7, Figure 3). No chloride ion cluster was directly detected, but a significantly increased adduct signal of $[\text{M}+\text{Cl}]^-$ was detected for the indicated analytes in the sodium chloride sample on the ZIC-c column at around 5.7-6.0, 10 mins, and on the BEH-amide column at around 1.45-1.8, 2.4-2.9 mins (Table S7, Figure 3). Most compounds that eluted around these periods exhibited ion suppression due to adduct formation (Table S5-S6).

In addition to the matrix effect caused by inorganic ions, the overall effect of plasma matrix on ionization was investigated as well. Table 1 summarizes the statistics for the entire plasma matrix and sodium chloride effect on representative metabolite classes. A comparable plasma matrix effect was observed on both columns, with 73% of 51 representative metabolites influenced on ZIC-c, and 68% of 47 representative metabolites influenced on BEH-amide. ZIC-c showed more susceptibility to the effect of sodium chloride than BEH-amide regarding the total number of affected metabolites as well as the measurement precision as shown in Table S5-S6. In particular, amino acids and amines showed more numbers affected by the presence of sodium chloride on ZIC-c. This significant ion suppression or enhancement caused by sodium chloride might be attributed to the constant competition between Na^+ , Cl^- and the zwitterionic amino acids, positively charged amines during the electrostatic interaction at pH 7 condition (Table S3).

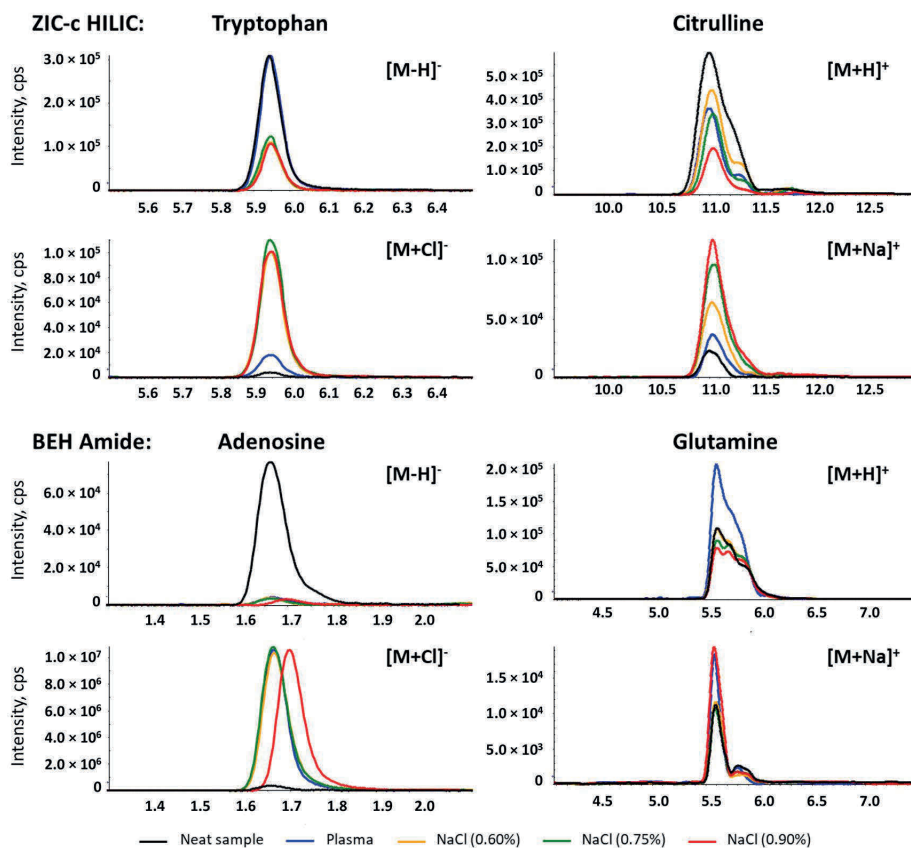


Figure 3. Extracted ion chromatogram of metabolites influenced by sodium chloride on the ZIC-c HILIC and BEH-amide columns. Citrulline and glutamine showed the increased MS responses of sodium adducts in plasma and salt sample (pure sodium chloride solution) versus neat sample (no sodium chloride). Tryptophan and adenosine showed the increased MS responses of chloride adducts in plasma and salt sample (pure sodium chloride solution) versus neat sample (no sodium chloride).

Table 1. Summary of plasma matrix effect and sodium chloride effect on representative metabolite classes.

Metabolite classes	ZIC-c (51 metabolites detected)		BEH (47 metabolites detected)	
	Matrix effect	Salt effect	Matrix effect	Salt effect
Amino acids	11 (16)	11 (16)	14 (17)	4 (17)
Amines	2 (4)	3 (4)	2 (4)	1 (4)
Sugar & Sugar phosphate	5 (5)	4 (5)	4 (4)	2 (4)
Nucleoside & Nucleotide	10 (13)	10 (13)	8 (11)	7 (11)
Acylcarnitines	1 (2)	0 (2)	0 (2)	1 (2)
Organic acids	8 (11)	8 (11)	6 (9)	6 (9)

* Numbers within brackets represent the total metabolite number for each class. Numbers before brackets represent the number of affected metabolites. For metabolites that were measured in both positive and negative modes, matrix/salt effect is marked when either mode showed ion suppression/ enhancement.

For both columns, there was no significant increase in matrix effect value with increased sodium chloride concentration. Ion suppression with low matrix effect value was observed only in 0.9% group for a few metabolites. However, this still suggests that high-salt matrices can have a significant impact. Existing research attempted depletion of salt during sample preparation by methods such as cation and anion solid phase extraction, thereby enhancing the sensitivity [15]. However, repeatability and coverage of such methods needs more validation for biological samples with high concentrations of various salts. Overall, our results indicated that regardless of the column type, inorganic ions have affinity for the polar stationary phase in HILIC chromatography. Further investigation on depletion of these ions during sample preparation while having a high metabolic coverage is needed.

4. Repeatability evaluation

A key prerequisite for obtaining good metabolic profiles is repeatability. In terms of this, HILIC is recognized to be more challenging in long batch analysis than in RP columns due to the complex retention mechanism. Therefore, we further evaluated two HILIC columns for intra- and inter-batch repeatability using retention time (RT) and peak area stability of 42 representative polar compounds in a pooled plasma QC sample. The detailed results are summarized in Table S8, and supplemented by Figure S4 and Figure S5. The distribution of relative standard deviations (RSD) for RT and peak area in intra- and inter-batch analysis are visualized in Figure 4.

4.1. Intra-batch repeatability

RSD values below 30% for peak area define a high-quality dataset for untargeted analysis and reflects good method stability over runs with plasma matrix [27]. The intra-batch peak

area repeatability of both columns was excellent; of 42 tested analytes, all showed an RSD < 20% on the ZIC-c HILIC except for arginine (21%), while for BEH-amide, all metabolites showed an RSD < 20% with exception of arginine (22%), adenosine (34%) and malonic acid (22%). Both columns also exhibited a good RT stability for all tested analytes with variation < 5% RSD, within 200 consecutive injections of pooled plasma QC sample.

4.2. Inter-batch repeatability

Similarly, the inter-batch analysis revealed high RT stability in both columns with RSD < 5% for most of the analytes, with the exception of malonic acid (12%) on BEH-amide. The peak area analysis evaluations also showed satisfactory repeatability; on the ZIC-c HILIC, all metabolites showed an RSD below 20%, with the exception of arginine, lysine, fructose-6-P with relatively high RSD, ranging from 20% to 30%. On the BEH-amide, 40 metabolites showed an RSD below 20% while this value was relatively high for cytidine and uric acid ranging from 20% to 35%.

Although we performed a pre-batch run with 20 QC plasma samples on both HILIC columns, malonic acid showed improved peak shape after more sample injections on BEH-amide (Figure S3). Similarly, increased peak responses were observed for arginine, lysine, fructose-6-P, and adenosine. In contrast, decreased peak responses were observed for cytidine and uric acid on BEH-amide. The accumulated matrix that remained in the ion source might cause changes in the peak response as well. This can be alleviated through MS ion source cleaning between batches. Nucleosides eluting in the early stage of the gradient on the BEH-amide column showed less peak area repeatability than on the ZIC-c HILIC column. Although the chromatographic repeatability has been considered a common challenge in HILIC technology, our results demonstrate that the deviation of peak areas and retention times across inter- and intra-batch analysis did not vary significantly, which reflects good method stability and enables reliable chromatogram alignment and peak matching across different samples.

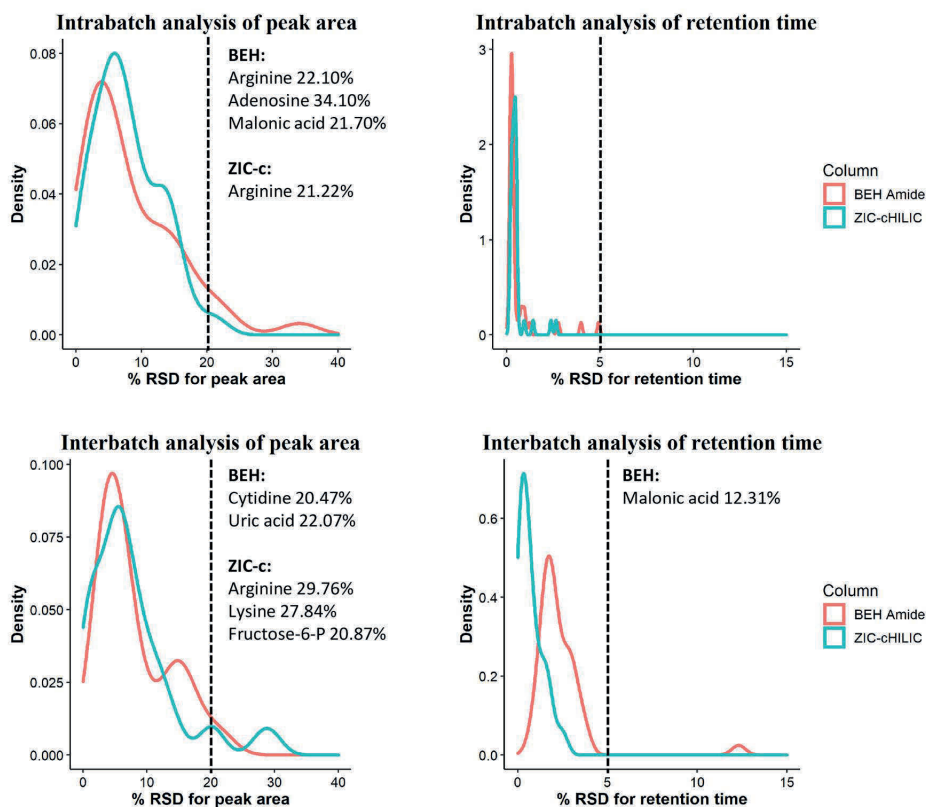


Figure 4. Repeatability evaluation of peak areas and retention times of 42 representative compounds during inter- and intra-batch analysis using ZIC-c HILIC and BEH-amide columns. Metabolite names with an RSD above 20% are listed on the right side of the cut-off line.

5. Untargeted metabolomics analysis for human plasma

Untargeted metabolomics analysis of plasma samples from four different phenotypes were utilized to estimate and compare the metabolic coverage of each column. The quality of generated chromatographic peaks has a great effect on the coverage output. When using HILIC for global metabolomics, one drawback is the presence of poor chromatographic peaks (broad peaks, multiple peaks and tailing peaks). The total ion chromatograms of the plasma samples and some examples of poor peak shapes are presented in supplementary Figure S6 and Figure S7. During data processing of this type of peaks, many features with the same m/z could be generated by the peak extraction algorithm while multiple features are generated by a single metabolite. Therefore, following untargeted HILIC-MS analysis, data were extensively pre-processed using XCMS, MS-FLO and in-house tools, followed by strict rules of feature removal to omit isotopes, background peaks (in procedure blank

per method), and also unreliable retention areas (which restricted the inclusion of peaks with broad tailing). The different steps of the data pre-processing and the feature yield per step are summarized in Table S9. Two-dimensional PCA score plots (Figure 5a) revealed a visible separation in metabolic profiles induced by different plasma phenotypes (Dutch, USA, fasted and non-fasted) on both HILIC columns. The first two principal components respectively explain 47.6% and 25.0% of the total variance of the data for ZIC-c HILIC, while those for BEH-amide explain 45.3% and 26.5% respectively. In addition to the successful separation, replicates of each phenotype are clustered together in the plot showing good repeatability in the HILIC-MS. The lower intra-group variation on BEH-amide can be explained by the lower number of covered features. In total, 720 and 1003 m/z features were detected on the ZIC-c column respectively under negative and positive ESI modes, while a total of 562 and 602 m/z features were detected on the BEH-amide column using negative and positive ESI modes respectively. In addition to the higher coverage, ZIC-c HILIC was more successful in isomer separation which is another necessary evaluation in LC condition optimization for untargeted metabolite profiling. For example, among the negative and positive features, 18 and 39 pairs of putative isomers were detected respectively on ZIC-c column, while 10 and 13 pairs were detected respectively on BEH-amide column. The successful isomer separation by ZIC-c might be attributed to the selectivity of the positively charged stationary phase for acidic isomers, which are negatively charged at neutral pH.

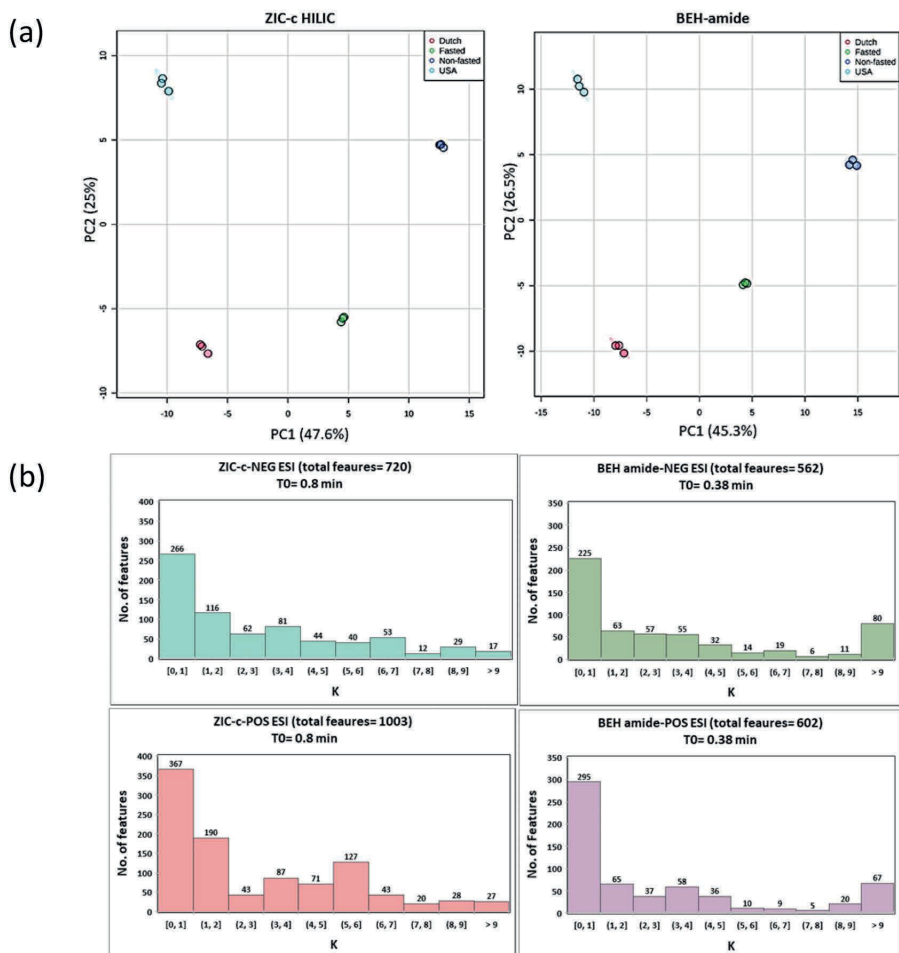


Figure 5. (a) Principal component analysis (PCA) score plot of pre-processed untargeted features in ZIC-c and BEH-amide. Each phenotype was subjected to a triplicate sample analysis; (b) Retention factor (K) distribution of detected features on each column.

Investigation of the column retention mechanisms revealed partitioning as a major retention mechanism in both ZIC-c and BEH-amide columns. This may have resulted in an overall similar retention distribution of plasma features detected in the untargeted analysis in both columns (Figure 5b). Features eluting in the early volume zone are represented in K [0,1]; they accounted for the highest percentage in both columns, with an average 44.5% of total features on BEH-amide, compared to an average of 36.8% on ZIC-c HILIC. In contrast, the number of features with longer retentions, represented in $K \geq 1$, obviously decreases. Due to the presence of strong electrostatic interactions in ZIC-c HILIC, more balanced retention

profiles were observed in the range of $K \geq 2$, which is important for untargeted analysis to reduce co-elution and selectively cover more features.

Conclusions

The performance of two widely used HILIC columns, BEH-amide and ZIC-c HILIC, for global metabolomics were systematically evaluated using metabolite standard solutions and human plasma samples. Mobile phase pH is the most critical parameter since it affects metabolite charge and its retention behaviour, thereby impacting the column selectivity and the quantity of detected metabolic features in untargeted analysis. Our data indicate the highest performance for ZIC-c when operated at pH 7 and for BEH-amide at pH 10. The ZIC-c HILIC column exhibited several advantages, including superior performance for different classes of compounds, better isomer separation, high repeatability and high metabolic coverage. Regardless of the column type, the retention of inorganic ions in plasma leads to extensive adduct formation and co-elution with analytes and, as a result, ion-suppression particularly for amino acids and amine classes on ZIC-c HILIC, while it acts as minor contributing factor to the overall plasma matrix effect. Further investigation on depletion of these ions during sample preparation while maintaining a high metabolic coverage is needed. Our evaluation proved high repeatability in retention time and detected peak area is achieved with the complex plasma matrix. The repeatability test also indicates that adequate equilibration and conditioning of both ZIC-c and BEH-amide columns is required prior to batch analysis, which is essential for the interpretation of untargeted data. Apart from these specific results, this work provides guidance on systematically evaluating a chromatography column performance for global plasma metabolomics studies, which is highly valuable in the future evaluation of (novel) HILIC stationary phases applied to other types of matrices.

Acknowledgments

We would like to thank Mr. Tim N. Kloots and Mr. Gerwin Spijksma for their technical support. This project was co-funded by the ZonMW Memorabel grant 733050814 (Understanding the role of the gut microbiome in the pathogenesis and prevention of dementia). The instrumentation used for this research was part of the Netherlands X-omics Initiative and partially funded by NWO, project 184.034.019. L. Huang would like to thank the financial support from China Scholarship Council (CSC) Grant [No. 201806210057]. F. Hosseinkhani would like to thank the University of Applied Sciences Leiden for financial support.

References

1. Rosato, A.; Tenori, L.; Cascante, M.; Ramon, P.; Carulla, D.A.; Martins, V.A.P.; Saccenti, E. From correlation to causation: analysis of metabolomics data using systems biology approaches. *Metabolomics* 2018, 14, 1–20, doi:10.1007/s11306-018-1335-y.

2. Johnson, C.H.; Ivanisevic, J.; Siuzdak, G. and towards mechanisms. *Nat. Publ. Gr.* 2016, 1–9, doi:10.1038/nrm.2016.25.
3. Coras, R.; Murillo-Saich, J.; Guma, M. Circulating Pro- and Anti-Inflammatory Metabolites and Its Potential Role in Rheumatoid Arthritis Pathogenesis. *Cells* 2020, 9, 827, doi:10.3390/cells9040827.
4. Gallart-Ayala, H.; Konz, I.; Mehl, F.; Teav, T.; Oikonomidi, A.; Peyratout, G.; van der Velpen, V.; Popp, J.; Ivanisevic, J. A global HILIC-MS approach to measure polar human cerebrospinal fluid metabolome: Exploring gender-associated variation in a cohort of elderly cognitively healthy subjects. *Anal. Chim. Acta* 2018, 1037, 327–337, doi:10.1016/j.aca.2018.04.002.
5. Dao-Quan Tang, LJ Zou, Xiao-Xing Yin, and C.N. HILIC-MS FOR METABOLOMICS: AN ATTRACTIVE AND COMPLEMENTARY APPROACH TO RPLC-MS. *Mass Spectrom. Rev.* 2014, 221–235, doi:10.1002/mas.
6. Medvedovici, A.; Bacalum, E.; David, V. Sample preparation for large-scale bioanalytical studies based on liquid chromatographic techniques. *Biomed. Chromatogr.* 2018, 32, doi:10.1002/bmc.4137.
7. Buszewski, B.; Noga, S. Hydrophilic interaction liquid chromatography (HILIC)-a powerful separation technique. *Anal. Bioanal. Chem.* 2012, 402, 231–247, doi:10.1007/s00216-011-5308-5.
8. McCalley, D. V. Study of retention and peak shape in hydrophilic interaction chromatography over a wide pH range. *J. Chromatogr. A* 2015, 1411, 41–49, doi:10.1016/j.chroma.2015.07.092.
9. Li, J.; Wang, Q.L.; Liu, Y.; Ke, Y.; Fan, Q.Q.; Zhou, P.; An, M.C.; Liu, H.M. Simultaneous determination of 24 free amino acids in MGC803 cells by hydrophilic interaction liquid chromatography with tandem mass spectrometry. *J. Chromatogr. B Anal. Technol. Biomed. Life Sci.* 2019, 1132, doi:10.1016/j.jchromb.2019.121792.
10. Virgiliou, C.; Gika, H.G.; Theodoridis, G.A. HILIC-MS-MS Multi-Targeted Method for Metabolomics. *Metab. ProfilingMethods Protoc.* 2018, 1738, 133–147, doi:10.1007/978-1-4939-7643-0.
11. Arase, S.; Kimura, S.; Ikegami, T. Method optimization of hydrophilic interaction chromatography separation of nucleotides using design of experiment approaches I: Comparison of several zwitterionic columns. *J. Pharm. Biomed. Anal.* 2018, 158, 307–316, doi:10.1016/j.jpba.2018.05.014.
12. Sriboonvorakul, N.; Leepipatipboon, N.; Dondorp, A.M.; Pouplin, T.; White, N.J.; Tarning, J.; Lindegardh, N. Liquid chromatographic-mass spectrometric method for simultaneous determination of small organic acids potentially contributing to acidosis in severe malaria. *J. Chromatogr. B Anal. Technol. Biomed. Life Sci.* 2013, 941, 116–122, doi:10.1016/j.jchromb.2013.10.005.
13. Guo, Y. Recent progress in the fundamental understanding of hydrophilic interaction chromatography (HILIC). *Analyst* 2015, 140, 6452–6466, doi:10.1039/c5an00670h.
14. Contrepois, K.; Jiang, L.; Snyder, M. Optimized analytical procedures for the untargeted metabolomic profiling of human urine and plasma by combining hydrophilic interaction (HILIC) and reverse-phase liquid chromatography (RPLC)-mass spectrometry. *Mol. Cell. Proteomics* 2015, 14, 1684–1695, doi:10.1074/mcp.M114.046508.
15. Sillner, N.; Walker, A.; Harrieder, E.M.; Schmitt-Kopplin, P.; Witting, M. Development and application of a HILIC UHPLC-MS method for polar fecal metabolome profiling. *J. Chromatogr. B Anal. Technol. Biomed. Life Sci.* 2019, 1109, 142–148, doi:10.1016/j.jchromb.2019.01.016.
16. Emrgren, I.; Haglöf, J.; Engskog, M.K.R.; Nestor, M.; Hedeland, M.; Arvidsson, T.; Pettersson, C. Adduct formation in electrospray ionisation-mass spectrometry with hydrophilic interaction liquid chromatography is strongly affected by the inorganic ion concentration of the samples. *J. Chromatogr. A* 2019, 1600, 174–182, doi:10.1016/j.chroma.2019.04.049.
17. Elmsjö, A.; Haglöf, J.; Engskog, M.K.R.; Emrgren, I.; Nestor, M.; Arvidsson, T.; Pettersson, C. Method selectivity evaluation using the co-feature ratio in LC/MS metabolomics: Comparison of HILIC stationary phase performance for the analysis of plasma, urine and cell extracts. *J. Chromatogr. A* 2018, 1568, 49–56, doi:10.1016/j.chroma.2018.05.007.
18. West, C.; Auroux, E. Deconvoluting the effects of buffer salt concentration in hydrophilic interaction chromatography on a zwitterionic stationary phase. *J. Chromatogr. A* 2016, 1461, 92–97, doi:10.1016/j.chroma.2016.07.059.
19. Alpert, A.J. Effect of salts on retention in hydrophilic interaction chromatography. *J. Chromatogr. A* 2018, 1538, 45–53, doi:10.1016/j.chroma.2018.01.038.
20. Ahn, J.; Bones, J.; Yu, Y.Q.; Rudd, P.M.; Gilar, M. Separation of 2-aminobenzamide labeled glycans using hydrophilic interaction chromatography columns packed with 1.7 μm sorbent. *J. Chromatogr. B* 2010, 878, 403–408, doi:10.1016/J.JCHROMB.2009.12.013.
21. Bajad, S.U.; Lu, W.; Kimball, E.H.; Yuan, J.; Peterson, C.; Rabinowitz, J.D. Separation and quantitation of water soluble cellular metabolites by hydrophilic interaction chromatography-tandem mass spectrometry. *J. Chromatogr. A* 2006, 1125, 76–88, doi:10.1016/j.chroma.2006.05.019.
22. Tufi, S.; Lamoree, M.; de Boer, J.; Leonards, P. Simultaneous analysis of multiple neurotransmitters by hydrophilic interaction liquid chromatography coupled to tandem mass spectrometry. *J. Chromatogr. A* 2015, 1395, 79–87, doi:10.1016/j.chroma.2015.03.056.
23. Greco, G.; Letzel, T. Main interactions and influences of the chromatographic parameters in HILIC separations. *J. Chromatogr. Sci.* 2013, 51, 684–693, doi:10.1093/chromsci/bmt015.
24. Wang, J.; Guo, Z.; Shen, A.; Yu, L.; Xiao, Y.; Xue, X.; Zhang, X.; Liang, X. Hydrophilic-subtraction model for the characterization and comparison of hydrophilic interaction liquid chromatography columns. *J. Chromatogr. A* 2015, 1398, 29–46, doi:10.1016/j.chroma.2015.03.065.

25. Ekdahl, A.; Johansson, M.C.; Ahnoff, M. Tracing and separating plasma components causing matrix effects in hydrophilic interaction chromatography-electrospray ionization mass spectrometry. *J. Chromatogr. B Anal. Technol. Biomed. Life Sci.* 2013, 923–924, 83–91, doi:10.1016/j.jchromb.2013.02.013.
26. Takayama, N.; Lim, L.W.; Takeuchi, T. Retention behavior of inorganic anions in hydrophilic interaction chromatography. *Anal. Sci.* 2017, 33, 619–625, doi:10.2116/analsci.33.619.
27. Iturraspe, E.; Da Silva, K.M.; Talavera Andújar, B.; Cuykx, M.; Boeckmans, J.; Vanhaecke, T.; Covaci, A.; van Nuijs, A.L.N. An exploratory approach for an oriented development of an untargeted hydrophilic interaction liquid chromatography-mass spectrometry platform for polar metabolites in biological matrices. *J. Chromatogr. A* 2021, 1637, 461807, doi:10.1016/j.chroma.2020.461807.
28. Smith, C.A.; Want, E.J.; O'Maille, G.; Abagyan, R.; Siuzdak, G. XCMS: Processing mass spectrometry data for metabolite profiling using nonlinear peak alignment, matching, and identification. *Anal. Chem.* 2006, 78, 779–787, doi:10.1021/ac051437y.
29. DeFelice, B.C.; Mehta, S.S.; Samra, S.; Čajka, T.; Wancewicz, B.; Fahrmann, J.F.; Fiehn, O. Mass Spectral Feature List Optimizer (MS-FLO): A Tool To Minimize False Positive Peak Reports in Untargeted Liquid Chromatography-Mass Spectroscopy (LC-MS) Data Processing. *Anal. Chem.* 2017, 89, 3250–3255, doi:10.1021/acs.analchem.6b04372.
30. Pang, Z.; Chong, J.; Zhou, G.; De Lima Morais, D.A.; Chang, L.; Barrette, M.; Gauthier, C.; Jacques, P.É.; Li, S.; Xia, J. MetaboAnalyst 5.0: Narrowing the gap between raw spectra and functional insights. *Nucleic Acids Res.* 2021, 49, W388–W396, doi:10.1093/nar/gkab382.
31. Haug, K.; Cochrane, K.; Nainala, V.C.; Williams, M.; Chang, J.; Jayaseelan, K.V.; O'Donovan, C. MetaboLights: A resource evolving in response to the needs of its scientific community. *Nucleic Acids Res.* 2020, 48, D440–D444, doi:10.1093/nar/gkz1019.

Supplementary Materials

Data Availability Statement: The data presented in this study are accessible through EBI Metabolights repository accession number MTBLS4157 (www.ebi.ac.uk/metabolights/MTBLS4157) [31]

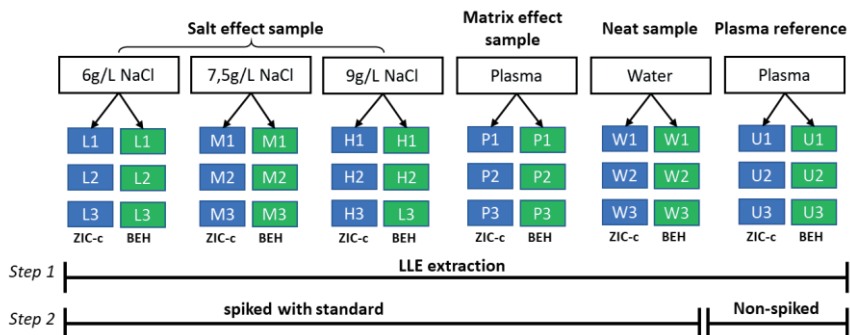


Figure S1. A schematic workflow of the matrix effect evaluation. Each group has three replicates processed independently. L: low concentration; M: medium concentration; H: high concentration; P: plasma spiked with standard; W: water spiked with standard; U: non-spiked plasma.

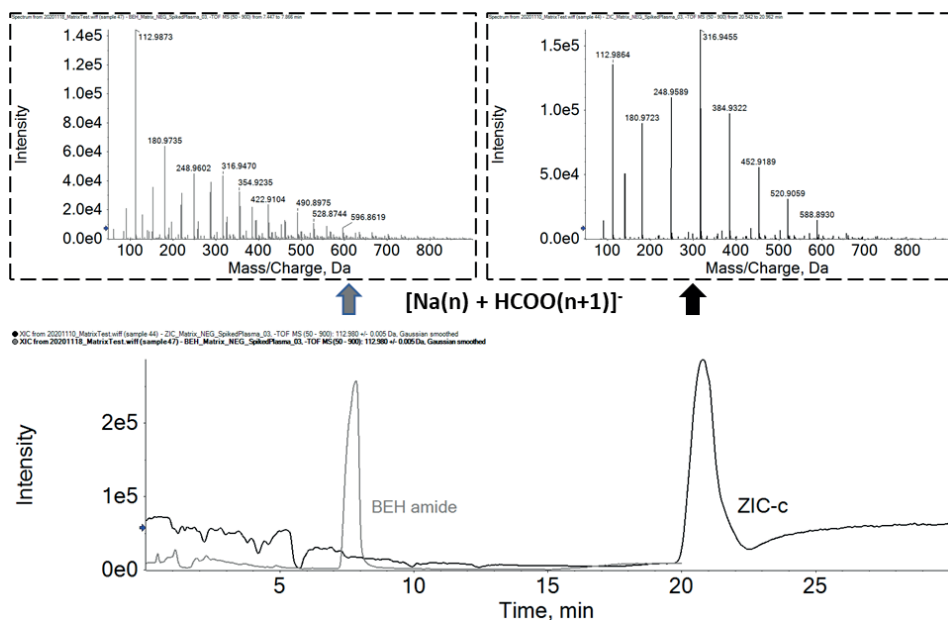


Figure S2. The major elution profile of sodium as a sodium formate cluster on the ZIC-c HILIC column and BEH Amide HILIC column. The extracted ion chromatograms of $[\text{Na}(n) + \text{HCOO}(n+1)]^-$ are shown below. The corresponding mass spectra at the elution time range are shown above.

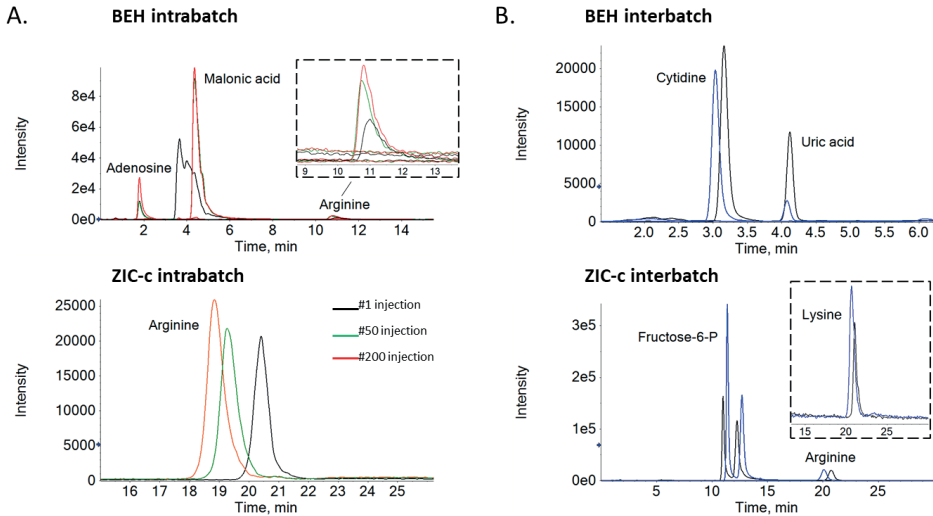


Figure S3. Extracted ion chromatograms of metabolites with a high RSD deviation (above 20%) in peak area reproducibility evaluation.

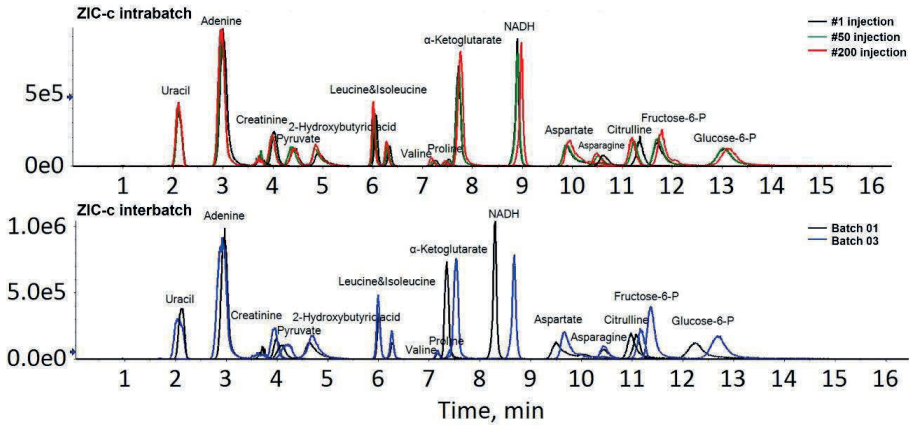


Figure S4. Extracted ion chromatograms of 16 metabolites covering the amino acid, amine, sugar phosphate, nucleoside, nucleotide, and organic acid classes presented for repeatability evaluation of retention time and peak area on the ZIC-c HILIC column.

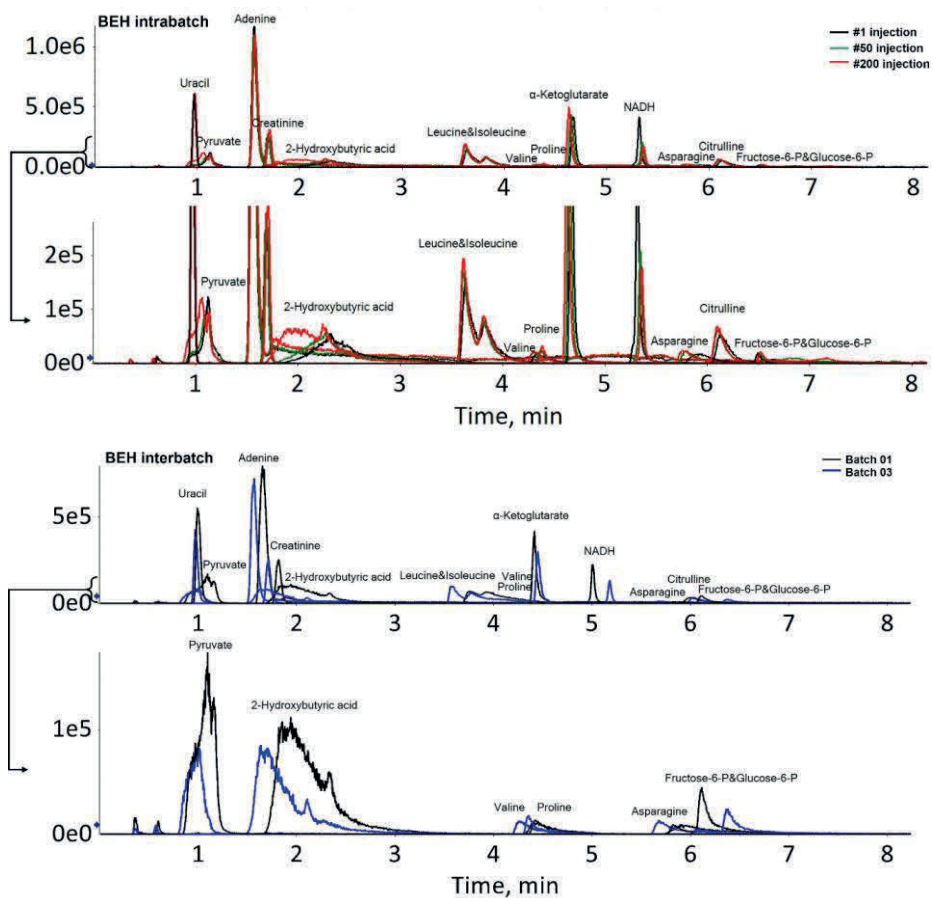


Figure S5. Extracted ion chromatograms of 15 metabolites covering the amino acid, amine, sugar phosphate, nucleoside, nucleotide, and organic acid classes presented for repeatability evaluation of retention time and peak area on the BEH-amide HILIC column.

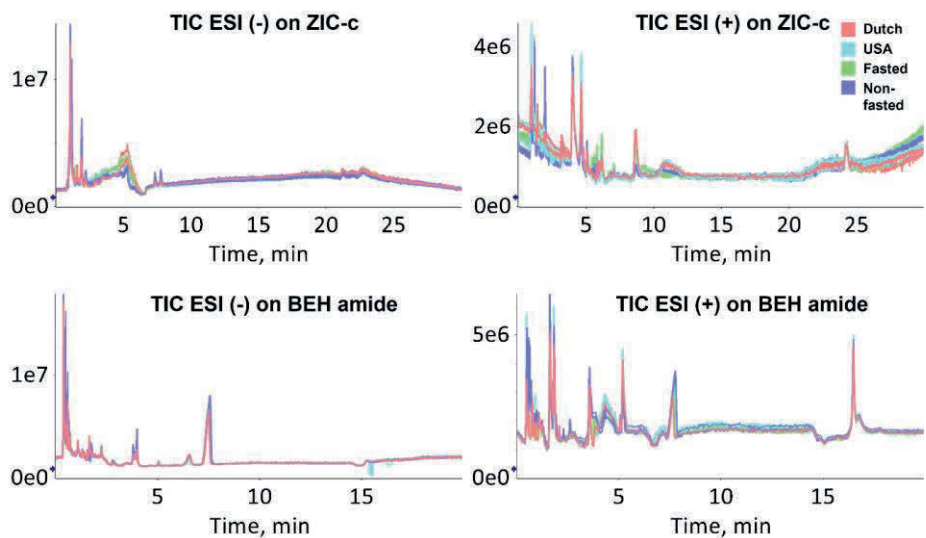


Figure S6. The total ion chromatogram (TIC)s of each plasma sample from four different phenotypes analyzed using the untargeted HILIC-MS method. Each phenotype has three replicates, extracted and measured independently. (Red for Dutch, Blue for USA, Green for fasted, Purple for non-fasted)

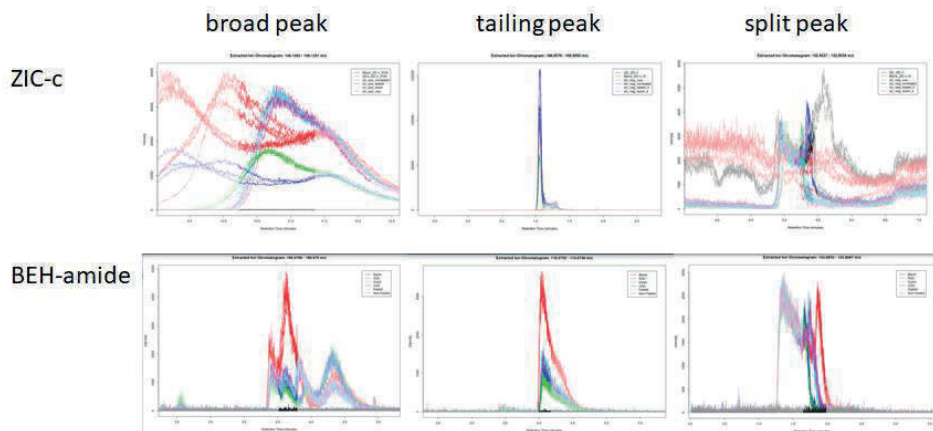


Figure S7. Bad feature showcase from untargeted plasma analysis.

Table S2. Columns and mobile phase conditions for ZIC-c HILIC and BEH Amide column

Column name	SeQuant ZIC-cHILIC	Acquity BEH Amide UPLC Column
Stationary type	Zwitterionic	Neutral
Surface Functional group	Phosphorylcholine	Amide
Dimensions/mm	2.1*100	2.1*100
Particle size/ μm	3	1.7
Column temperature/ $^{\circ}\text{C}$	30	30
Flow rate/ $\mu\text{L} \cdot \text{min}^{-1}$	0.25	0.5
Mobile phase A	90% acetonitrile, 10% water with 5 mM	90% acetonitrile, 10% water with 5 mM
Mobile phase B	10% acetonitrile, 90% water with 5 mM	10% acetonitrile, 90% water with 5 mM
	min – %B	min – %B
	0 – 0	0 – 0
	2 – 0	1.2 – 0
	4 – 15	9.2 – 40
Gradient	10 – 21	14 – 40
	15 – 26	14.2 – 0
	20 – 40	18 – 0
	20.1 – 0	
	30 – 0	
Sample injection volume/ μL	3	3

Table S3. Physical and chemical properties of polar target compound under pH=3, 7, 10

Compound	Log D Value			Charge State (%)			Hydrogen donor Total
	pH3	pH7	pH10	pH3	pH7	pH10	
Arginine	-	-5.21	-3.19	78.00(+++)	98.92(+++)	90.99(+++)	15
Asparagine	-	-4.3	-5.39	90.03(+)	95.06(+)	98.11(-)	12
Aspartic acid	-3.5	-5.37	-7.47	93.85(+)	98.40(++-)	78.32(-)	13
Betaine	-	-3.72	-3.72	65.59(+)	99.98(+)	100.00(+++)	5
Citrulline	-	-3.93	-4.65	83.10(+)	99.13(++-)	89.68(-)	13
GABA	-3.6	-2.89	-3.08	97.09(+)	99.57(++-)	51.80(+)	8
Glutamine	-	-4	-4.67	86.60(+)	99.29(++-)	87.72(-)	12
Glycine	-	-3.41	-4.12	81.82(+)	99.16(++-)	89.36(-)	8
Histidine	-	-3.7	-4.18	92.64(+++)	75.48(+)	84.33(-)	10
Isoleucine	-	-1.51	-2	60.15(+)	99.61(++-)	79.18(-)	8
Leucine	-	-1.59	-2.13	60.35(+)	99.55(++-)	81.75(-)	8
Lysine	-	-5.32	-3.21	62.99(+++)	99.46(+++)	41.77(++-)	11
Ornithine	-	-5.76	-3.66	66.68(+++)	99.45(+++)	41.79(++-)	11
Proline	-2.6	-2.57	-2.59	91.15(++-)	99.99(++-)	93.04(++-)	7
Taurine	-	-2.62	-3.28	100.00(++-)	99.34(++-)	86.93(-)	10
Tryptophan	-	-1.09	-1.7	72.52(++-)	99.41(++-)	85.53(-)	9
Valine	-2.1	-1.95	-2.44	64.08(++-)	99.62(++-)	78.89(-)	8
Choline	-	-4.66	-4.66	-	-	-	3
Creatinine	-1.3	0.21	0.15	99.99(+)	56.91(+)	77.62(-)	7
Histamine	-	-3.2	-0.84	99.99(+++)	50.80(+++)	70.82(0)	5
Urea	-	-1.36	-1.36	-	-	-	6
Glucose	-	-2.93	-2.95	100.00(0)	99.99(0)	94.25(0)	17
Fructose	-	-2.76	-2.94	100.00(0)	99.93(0)	59.82(0)	17
Glucose-6-P	-	-6.24	-7.81	98.08(-)	85.87(-)	94.24(-)	22
Fructose-6-P	-	-6.07	-7.8	98.09(-)	85.85(-)	59.81(-)	22
Ribose-5-P	-	-6.04	-7.78	96.61(-)	76.85(-)	99.97(-)	20
Acetyl-CoA	-	-	-	32.92(++-)	92.47(----)	99.99(----)	40
Adenine	-	-0.53	-0.83	72.65 (+)	99.89 (0)	60.85(0)	7
Adenosine	-	-2.09	-2.09	84.42(+)	99.92(0)	99.51(0)	17
ADP	-	-7.51	-9.56	80.45(+++)	69.83(-)	99.28(-)	27
AMP	-	-5.4	-6.65	82.47(++-)	85.17(-)	99.50(-)	22
ATP	-	-	-	30.5(----)	69.34(---)	99.77(----)	32
Cytidine	-2.8	-2.8	-2.8	93.22(+)	99.86(0)	99.61(0)	17
Hypoxanthine	-	-0.36	-0.91	84.58(0)	99.53(0)	82.35(-)	7
Inosine	-	-1.57	-1.58	66.31 (0)	99.98 (0)	86.63(0)	17
NAD+	-	-8.57	-8.59	77.77(+++)	99.28(++-)	94.72(++-)	37
NADH	-	-8.57	-8.59	77.65(++-)	99.29(-)	100(-)	37
Uracil	-	-0.86	-2.01	100(0)	98.16(0)	93.97(-)	6
Uric acid	-	-2.09	-2.09	99.9(0)	60.45(0)	47.7(-)	10
Acetylcarnitine	-	-3.68	-3.68	92.53(+)	99.8(+)	100 (+)	7
Ocatanoylcarnitine	-	-0.75	-0.75	94.29 (+)	99.84(++-)	100(++-)	7
2-Hydroxybutyric acid	0.01	-2.84	-3.48	96.48(0)	99.73(-)	100(-)	8
3-Phosphoglyceric acid	-	-7.87	-9.89	74.33(-)	78.43(---)	99.93(---)	16
6-phosphogluconic acid	-	-9.69	-	71.34(-)	72.73(---)	99.61(---)	25
Citric acid	-1.6	-8.63	-	53.37(0)	97.46(---)	99.98(---)	18
Fumaric acid	-	-6.06	-7.1	68.61(0)	99.83(-)	100(-)	10
Glyceraldehyde 3-	-	-4.85	-6.53	97.23(-)	80.38(-)	99.98(-)	13
Glycolic acid	-	-4.24	-4.57	77.59(0)	99.97(-)	100(-)	8
Isocitric acid	-	-8.74	-12	54.43(0)	97.56(---)	99.98(---)	18
Lactic acid	-	-3.52	-4	86.15(0)	99.94(-)	100(-)	8
Malic acid	-	-6.33	-8.15	62.02(0)	98.72(-)	99.99(-)	13
Malonic acid	-	-4.94	-7.28	77.73(-)	92.69 (-)	99.99(-)	10
Oxaloacetate	-	-6.72	-7.1	43.51(-)	99.94(-)	96.57(-)	12
Pyruvic acid	-	-3.35	-3.46	72.23(0)	99.97(-)	99.31(-)	7
Succinic acid	-	-4.92	-7.39	78.44(0)	95.55(-)	100(-)	10
α -Ketoglutaric acid	-	-6.58	-7.17	55.12(-)	99.92(-)	100(-)	12

Table S4. Scoring criteria for the evaluation of compound chromatography performance

	Parameter criterion	Score value
Retention	$4.0 \cdot t_0 \leq RT$	1
	$1.5 \cdot t_0 \leq RT < 4.0 \cdot t_0$	0
	$0.5 \cdot t_0 \leq RT < 1.5 \cdot t_0$	-1
	$0 \leq RT < 0.5 \cdot t_0$	-2
Peak sharpness	$W \leq 0.1 \text{ min}$	2
	$0.1 \text{ min} < W \leq 0.2 \text{ min}$	1
	$0.2 \text{ min} < W \leq 0.4 \text{ min}$	0
	$W > 0.4 \text{ min}$	-2
Peak symmetry	$0.85 < TF \leq 1.5$	2
	$1.5 < TF \leq 2.5, 0.6 < TF \leq 0.85$	1
	$2.5 < TF \leq 3.5$	0
	$TF > 3.5$	-2
Peak sensitivity	$100000 \leq H$	2
	$10000 \leq H < 100000$	1
	$1000 \leq H < 10000$	0
	$H < 1000$	-2

*In the table above, H refers to peak height. W refers to peak width at 50% of the maximum peak height. TF means tailing factor, RT means retention time and t_0 refers to time for void volume.

Overall evaluation:

$$\text{Score}_{\text{total}} = \text{Score}_{\text{retention}} + \text{Score}_{\text{sharpness}} + \text{Score}_{\text{symmetry}} + \text{Score}_{\text{sensitivity}}$$

a. Good: Score total ≥ 4

b. Acceptable: $0 \leq$ Score total < 4

c. Bad: Score total < 0

Table S5. Plasma overall matrix effect and particular sodium chloride effect on metabolites analyzed using ZIC-c HILIC column

Class	Component Name	Retention Time ZIC-c	Water fraction % ZIC-c	Matrix effect ZIC-c	Salt effect ZIC-c	ZIC-c spiked_plasma (n=3)	ZIC-c 0.6%_salt (n=3)	ZIC-c 0.6%_salt (n=3) negative detection mode [M-H] ⁻	ZIC-c 0.75%_salt (n=3)	ZIC-c 0.9%_salt (n=3)	ZIC-c spiked_plasma (n=3)	ZIC-c 0.6%_salt (n=3)	ZIC-c 0.75%_salt (n=3)	ZIC-c 0.9%_salt (n=3)	
Amino acids	Arginine*	20.00	40.00	yes	yes	1.09 11%	0.85 19%	1.20%	0.97 14%	0.76 13%	0.76 13%	0.54 27%	0.52 8%	0.43 42%	
	Asparagine	9.75	26.60	no	no	0.75 6%	0.96 1%	1.04 6%	0.64 5%						
	Aspartate	8.51	25.61	yes	yes	0.8 5%	0.81 14%		0.66 1%						
	Betaine*	6.13	23.70	yes	yes	0.58 6%	0.58 14%	0.55 7%	0.64 29%	0.76 8%	1.21 14%	1.3 4%	1.3 4%	1.15 5%	
	Citrulline*	10.43	27.14	yes	yes	0.97 1%	0.97 1%	1.1 2%	1.08 7%	0.76 8%	0.56 24%	0.55 46%	0.55 46%	0.59 22%	
	GABA	10.85	27.48	yes	no	0.29 2%	0.30 2%	0.30 2%	0.28 3%	0.28 3%	0.28 3%	0.28 3%	0.28 3%	0.28 3%	
	Glycine*	9.67	26.55	yes	yes	2.52 16%	0.80 1%	0.87 8%	0.88 3%	0.94 14%	0.31 1%	0.31 1%	0.31 1%	0.31 1%	
	Glycyl-L-Proline	6.08	26.65	yes	yes	2.02 6%	0.93 2%	1.57 5%	0.9 9%	1.31 2%	1.78 12%	1.91 9%	1.91 9%	2.26 10%	
	Isoleucine	5.82	23.66	yes	yes	0.8 2%	0.41 51%	0.32 3%	0.47 61%	0.2 58%	0.07 35%	0.06 24%	0.06 24%	0.06 45%	
	Lysine*	20.30	40.00	yes	yes	1.52 45%	0.53 26%	0.79 61%	0.76 59%	0.2 58%	0.07 35%	0.06 24%	0.06 24%	0.06 45%	
	Omitline*	10.41	27.13	yes	yes	0.92 24%	0.93 20%	1.06 16%	1.21 17%	0.82 7%					
	Proline	7.10	24.48	yes	no	1.7 5%	0.83 2%	0.97 7%	0.82 7%	0.97 2%					
	Taurine	8.28	25.42	yes	yes	1.05 3%	0.9 3%	0.99 2%	0.97 5%	0.97 5%					
	Tryptophan	5.81	23.45	yes	yes	0.43 41%	0.43 41%	0.35 5%	0.45 52%	1.05 7%	0.81 5%	0.82 10%	0.82 10%	0.75 4%	
Valine*	6.90	24.32	yes	yes	2.05 5%	0.69 18%	0.68 4%	0.72 18%	0.93 4%	1.29 5%	1.39 4%	1.39 4%	1.33 3%		
Amines	Choline*	11.31	27.85	no	no	0.89 3%	0.9 3%	0.98 7%	0.88 3%	0.42 18%	0.88 9%	0.86 1%	0.86 1%	0.82 6%	
	Creatinine*	3.89	21.34	yes	no	0.9 9%	0.96 2%	1.05 4%	0.98 4%	0.95 9%	1.29 4%	1.41 2%	1.41 2%	1.34 2%	
	Histamine*	17.05	35.39	no	yes					0.69 7%	0.65 8%	0.66 10%	0.66 10%	0.56 9%	
	Urea*	3.10	16.60	yes	yes	0.45 21%	0.43 10%	0.43 30%	0.32 7%						
	Fructose	6.66	24.13	yes	yes	1.46 5%	0.77 5%	0.71 12%	0.79 31%						
	Glucose	7.46	24.77	yes	no	11.23 6%	0.94 6%	0.91 12%	0.83 7%						
	Fructose-6-P	9.54	26.43	yes	yes	0.61 9%	0.61 9%	0.6 24%	0.44 0.2%						
	Fructose-1,6-bisP	8.60	25.62	yes	yes	0.15 2%	0.15 2%	0.15 2%	0.15 1%						
	Biotin	8.44	25.52	yes	yes	0.45 8%	0.45 8%	0.59 20%	0.59 20%						
	Ascorb-COA	7.24	24.99	yes	yes	0.32 38%	0.42 38%	0.43 61%	0.21 3%						
	Adrenaline	2.87	15.22	no	yes	1.14 10%	1.2 4%	1.29 9%	1.23 2%						
	Adenosine*	3.54	19.24	yes	yes	0.89 4%	0.87 11%	1.04 11%	0.99 5%						
	ADP	9.17	26.14	yes	yes	0.7 11%	0.73 8%	0.76 17%	0.59 2%						
	AMP	7.23	24.58	yes	yes	0.49 15%	0.55 5%	0.57 21%	0.43 2%						
Nucleoside & Nucleotide	ATP	11.98	28.38	no	no	0.97 8%	1.02 2%	1.01 8%	0.92 2%						
	Cytidine*	5.72	23.38	yes	yes	0.4 12%	0.2 46%	0.18 7%	0.31 82%	1.37 3%	1.94 21%	2.21 13%	2.21 13%	1.46 48%	
	Hydroxanthine	3.99	21.94	yes	no	0.84 1%	0.97 7%	1.04 10%	0.85 3%						
	Inosine	5.40	23.12	yes	yes	1.65 6%	1.75 6%	1.89 9%	1.56 5%						
	NADP*	9.10	26.08	yes	yes	0.86 4%	0.86 4%	0.79 17%	0.67 8%						
	NADH	7.49	24.79	yes	yes	0.32 12%	0.39 8%	0.43 33%	0.3 1%						
	Uracil	2.10	10.60	yes	no	0.72 2%	0.92 2%	0.94 6%	0.8 3%						
	Uric acid	6.18	23.74	yes	yes	0.65 6%	0.58 5%	0.59 11%	0.53 10%						
	Acyl/leamlines	Acetyl-leamline*	6.61	24.09	no	no					0.86 5%	1.1 4%	1.18 1%	1.18 1%	1.14 1%
		Oxamoy-leamline*	3.57	19.42	yes	no					0.65 5%	0.84 8%	0.91 1%	0.91 1%	0.83 2%
		2-Hydroxybutyric acid	3.02	10.62	yes	yes	1.93 1%	0.85 4%	0.85 9%	0.7 1%					
		β-phosphoglyceric acid	10.38	24.70	yes	yes	0.31 2%	0.31 2%	0.31 2%	0.30 1%					
		β-phosphoglutamic acid	7.38	24.30	yes	yes	1.05 1%	1.05 1%	1.11 3%	0.98 1%					
		Glycerol-3-P*	9.73	26.58	yes	yes	0.09 12%	0.6 1%	0.63 26%	0.44 0.2%					
Glycerol-3-P*		9.30	26.24	yes	yes	0.63 24%	0.51 19%	0.53 35%	0.33 3%						
Glycerol-3-P		5.85	23.48	no	no	1.17 4%	1.11 1%	1.24 4%	1.15 7%						
Lactate		5.07	22.86	yes	yes	4.3 9%	0.4 13%	0.37 3%	0.44 36%						
Malonic acid		3.04	16.24	yes	yes	0.39 26%	0.39 11%	0.38 38%	0.26 8%						
Pyruvate		3.38	18.28	no	no	0.93 1%	1 6%	1.06 10%	0.87 1%						
Succinic acid		5.50	23.20	yes	yes	0.71 20%	0.68 5%	0.64 20%	0.41 19%						
α-ketoglutarate		6.87	24.30	yes	yes	0.53 19%	0.62 10%	0.64 28%	0.41 10%						

Table S6. Plasma overall matrix effect and particular sodium chloride effect on metabolites analyzed using BEH Amide HILIC

Class	Component Name	Retention Time BEH	Water fraction % BEH	Matrix effector BEH	Salt effect BEH	BEH spiked plasma (n=3)	BEH 0.6% salt (n=3)	BEH 0.75% salt (n=3)	BEH 1.0% salt (n=3)	BEH 0.6% salt (n=3)	BEH 0.75% salt (n=3)	BEH 0.9% salt (n=3)	
Amino acids	Arginine	11.61	40.00	yes	yes	3.39, 14%	2.57, 25%	2.76, 4%	1.82, 13%	1.47, 10%	1.54, 9%	1.28, 13%	
	Asparagine	6.59	28.45	no	no	0.91, 7%	1.06, 4%	1.16, 2%	1.06, 5%				
	Aspartate	6.41	27.73	yes	yes	1.21, 10%	0.89, 4%	0.85, 7%	0.63, 25%				
	Betaine	3.53	16.15	no	no	2.17, 12%	0.99, 4%	0.99, 4%	0.87, 11%	0.83, 3%	0.95, 8%	0.87, 2%	
	Citrulline	6.33	27.41	yes	no	0.7, 2%	0.98, 2%	0.97, 3%	0.99, 13%	1.13, 16%	1.23, 9%	0.98, 17%	
	GABA	5.45	23.87	no	no	0.9, 5%	1.04, 3%	1.05, 3%	0.99, 8%	0.81, 3%	0.93, 5%	0.85, 3%	
	Glutamine	6.04	26.24	yes	no	2.09, 12%	1.06, 4%	1.16, 1%	1.06, 4%	1.64, 2%	1.54, 2%	0.84, 4%	
	Glycine	5.89	25.64	yes	yes	2.26, 9%	0.99, 1%	0.99, 8%	0.92, 6%	1.54, 2%	0.85, 6%	0.76, 6%	
	Histidine	11.07	42.00	yes	no	1.37, 4%	0.86, 5%	0.85, 4%	0.88, 15%				
	Isoleucine	4.00	18.04	no	no	1.21, 9%	0.96, 0.1%	0.95, 4%	0.83, 12%				
	Leucine	4.00	18.04	no	no	1.21, 9%	0.96, 0.1%	0.95, 4%	0.83, 12%				
	Lysine	12.05	40.00	yes	yes	2.71, 16%	1.81, 34%	1.84, 7%	1.44, 17%	2.35, 16%	1.25, 18%	0.93, 16%	
Amines	Ornithine	6.33	27.41	yes	no	0.71, 5%	0.94, 2%	0.93, 2%	0.92, 11%				
	Proline	4.44	19.81	yes	no	2.14, 13%	0.98, 3%	0.98, 3%	0.9, 9%				
	Taurine	3.86	17.48	yes	no	1.92, 12%	0.95, 5%	0.9, 3%	0.82, 14%				
	Tryptophan	3.86	17.48	yes	no	1.55, 9%	1.13, 3%	1.13, 4%	0.92, 10%				
	Valine	3.53	16.15	yes	no	2.17, 12%	0.97, 2%	0.99, 4%	0.87, 11%				
	Choline	3.84	17.40	no	no	0.96, 9%	0.98, 2%	1, 4%	0.94, 7%	1.17, 6%	0.75, 6%	0.87, 22%	
	Creatinine	1.62	8.47	yes	yes	-0.13, -4%	0.1, 4%	0.09, 2%	0.11, 49%	0.68, 7%	0.71, 11%	0.79, 9%	
	Histamine	8.21	34.96	no	no				0.85, 2%	0.85, 2%	0.87, 6%	0.85, 4%	
	Urea	1.10	10.00	yes	no					2.91, 2%		0.86, 5%	0.8, 6%
	Sugar & Sugar phosphate	Fructose	3.24	14.98	yes	no	1.24, 7%	1, 8%	0.96, 5%	0.81, 10%			
		Glucose	3.86	17.48	yes	no	15.08, 10%	1.09, 5%	1.01, 12%	0.93, 4%			
		Fructose-6-P	6.96	29.94	yes	yes	3.32, 29%	1.26, 20%	1.25, 12%	0.86, 26%			
Glucose-6-P		6.96	29.94	yes	yes	3.32, 29%	1.26, 20%	1.25, 12%	0.86, 26%				
Acetyl-CoA		6.54	28.25	no	yes	1.08, 32%	1.12, 15%	1.04, 9%	0.76, 19%				
Adenine		1.49	7.95	yes	yes	0.54, 5%	0.67, 4%	0.65, 5%	0.61, 19%				
Nucleoside & Nucleotide	Adenosine	1.66	8.63	yes	yes	0.07, 6%	0.11, 5%	0.11, 3%	0.14, 47%	2.07, 6%	2.42, 3%	2.02, 48%	
	AMP	6.14	26.64	yes	no	2.93, 17%	1.13, 14%	1.14, 10%	0.92, 24%				
	Cytidine	2.85	13.42	yes	no	0.99, 6%	1, 7%	0.98, 6%	0.96, 10%	0.7, 3%	0.98, 5%	0.95, 3%	
	Hydroxybutyric acid	1.58	8.31	yes	yes	0.7, 6%	0.8, 4%	0.83, 5%	0.76, 10%				
	Inosine	2.40	11.61	no	no	1.02, 8%	1.02, 2%	1.07, 4%	0.96, 6%				
	NAD+	6.31	27.33	yes	yes	2.25, 13%	0.65, 24%	0.6, 13%	0.29, 26%				
	NADH	5.50	24.07	yes	yes	2.32, 19%	0.54, 22%	0.47, 11%	0.18, 56%				
	Uracil	0.95	10.00	no	no	0.89, 5%	0.93, 3%	0.96, 3%	0.9, 3%				
	Uric acid	4.27	19.13	yes	yes	2.44, 40%	0.32, 5%	0.28, 7%	0.25, 11%				
	Acyl/leamitines	Acetyl-leamitine	4.26	19.09	no	no				0.99, 4%	1.17, 8%	1.04, 12%	
		Octanoyl-leamitine	2.09	10.36	no	yes				0.84, 3%	0.78, 5%	0.68, 10%	
		2-Hydroxybutyric acid	1.71	8.83	yes	yes	0.28, 6%	0.22, 10%	0.21, 5%	0.23, 23%			
Fumaric acid		4.90	21.66	yes	no	1.39, 2%	0.89, 4%	0.88, 3%	0.8, 18%				
Glyceraldehyde-3-P		6.46	27.93	yes	yes	0.79, 24%	1.24, 18%	1.27, 9%	0.89, 15%	0.63, 3%	0.76, 7%	0.81, 8%	
Glycolic acid		3.40	15.63	yes	yes	0.7, 9%	0.55, 16%	0.55, 5%	0.58, 22%				
Organic acids	Lactate	2.52	12.09	yes	yes	5.74, 13%	0.63, 27%	0.59, 5%	0.77, 30%				
	Malonic acid	4.78	21.18	yes	yes	1.24, 3%	0.74, 7%	0.78, 3%	0.71, 1%				
	Pyruvate	1.02	10.00	no	no	1.12%	1.03, 2%	0.99, 3%	1.02, 4%				
	Succinic acid	4.86	21.50	no	no	1.15, 10%	1.03, 8%	1, 4%	1.06, 11%				
	α-Ketoglutarate	4.78	21.18	no	yes	1.07, 9%	1.03, 3%	1.03, 5%	0.74, 17%				

* Metabolites were measured under both positive and negative modes. The matrix effect and salt effect are considered as precense where either ionization mode shows ion suppression or enhancement.

Ion enhancement
Ion suppression

Notes: The data in the table is formatted as matrix effect value_RSD value.

Table S7. The ratio of the (de)protonated and adduct species peak area in plasma matrix and pure sodium chloride solution compared to neat solution

Metabolite	Ratio	Column	Retention time/min	Neat sample	Spiked Plasma	NaCl (0.6%)	NaCl (0.75%)	NaCl (0.9%)
Adenine	[M+Cl] ⁻ /[M+H] ⁺	BEH-amide	1.49	0.061 ± 0.0022	0.780 ± 0.0079	0.757 ± 0.0422	0.760 ± 0.0365	0.810 ± 0.0452
Hypoxanthine	[M+Cl] ⁻ /[M+H] ⁺	BEH-amide	1.58	0.032 ± 0.0017	0.596 ± 0.0183	0.589 ± 0.0454	0.552 ± 0.0317	0.532 ± 0.0386
Creatinine	[M+Cl] ⁻ /[M+H] ⁺	BEH-amide	1.62	7.728 ± 1.0990	318.756 ± 27.709	2325.011 ± 300.049	2975.311 ± 351.513	1918.263 ± 706.1848
Adenosine	[M+Cl] ⁻ /[M+H] ⁺	BEH-amide	1.66	4.685 ± 0.0576	1268.875 ± 390.9191	1490.065 ± 18.8154	1489.313 ± 104.5880	1219.608 ± 861.4329
2-Hydroxybutyric acid	[M+Cl] ⁻ /[M+H] ⁺	BEH-amide	1.71	0.011 ± 0.0015	0.072 ± 0.0101	0.082 ± 0.0201	0.090 ± 0.0050	0.091 ± 0.0206
Inosine	[M+Cl] ⁻ /[M+H] ⁺	BEH-amide	2.4	0.037 ± 0.0019	0.049 ± 0.0020	0.137 ± 0.0597	0.130 ± 0.0160	0.122 ± 0.0214
Cytidine	[M+Cl] ⁻ /[M+H] ⁺	BEH-amide	2.85	0.183 ± 0.0034	0.122 ± 0.0174	0.315 ± 0.0807	0.355 ± 0.0434	0.397 ± 0.0631
Cytidine	[M+Cl] ⁻ /[M+H] ⁺	ZIC-e	5.72	1.476 ± 0.0717	11.366 ± 2.8003	73.045 ± 43.7812	80.434 ± 5.8956	48.083 ± 39.4344
Tryptophan	[M+Cl] ⁻ /[M+H] ⁺	ZIC-e	5.81	0.011 ± 0.0012	0.067 ± 0.0073	0.708 ± 0.5442	0.816 ± 0.1290	0.476 ± 0.3846
Citrulline	[M+Cl] ⁻ /[M+H] ⁺	ZIC-e	10.43	0.027 ± 0.0004	0.034 ± 0.0035	0.060 ± 0.0060	0.067 ± 0.0123	0.082 ± 0.0055
Glutamine	[M+Na] ⁺ /[M+H] ⁺	BEH-amide	6.04	0.051 ± 0.0020	0.036 ± 0.0009	0.045 ± 0.0093	0.037 ± 0.0075	0.061 ± 0.0112
Adenosine	[M+Na] ⁺ /[M+H] ⁺	ZIC-e	3.54	0.030 ± 0.0002	0.095 ± 0.0294	0.135 ± 0.0291	0.155 ± 0.0449	0.206 ± 0.0381
Octanoyl carnitine	[M+Na] ⁺ /[M+H] ⁺	ZIC-e	3.57	0.004 ± 0.0001	0.0280 ± 0.0071	0.034 ± 0.0087	0.038 ± 0.0136	0.054 ± 0.0111
Creatinine	[M+Na] ⁺ /[M+H] ⁺	ZIC-e	3.89	0.033 ± 0.0003	0.078 ± 0.0186	0.146 ± 0.0253	0.171 ± 0.0563	0.230 ± 0.0213
Glutamine	[M+Na] ⁺ /[M+H] ⁺	ZIC-e	9.53	0.018 ± 0.0020	0.083 ± 0.0407	0.201 ± 0.1062	0.270 ± 0.1611	0.615 ± 0.1870
Citrulline	[M+Na] ⁺ /[M+H] ⁺	ZIC-e	10.43	0.063 ± 0.0010	0.150 ± 0.0701	0.476 ± 0.2266	0.607 ± 0.3614	1.3245 ± 0.3739

Table S8. Intra-batch and inter-batch reproducibility analysis of peak retention time and peak area

Compounds	BEH amide-%RSD				ZIC-C-%RSD			
	Interbatch		Intrabatch		Interbatch		Intrabatch	
	Area	RT	Area	RT	Area	RT	Area	RT
Arginine	5.29	2.96	22.10	0.79	29.76	1.83	21.22	2.63
Asparagine	2.12	2.44	2.05	0.62	0.60	0.17	1.30	0.48
Aspartic acid	17.41	2.83	10.43	0.94	5.53	0.84	8.98	0.24
Betaine	5.33	2.34	1.43	0.32	3.76	0.05	5.19	0.30
Citrulline	3.30	1.98	3.58	0.17	4.07	0.37	8.67	0.50
GABA	8.40	1.78	4.40	0.20	5.42	0.44	9.06	0.47
Glutamine	4.12	1.99	2.06	0.29	0.59	0.30	1.00	0.47
Glycine	4.65	1.97	3.98	0.28	2.27	0.35	2.55	0.43
Isoleucine	3.31	1.66	0.91	0.29	0.71	0.06	2.06	0.35
Leucine	3.31	1.66	2.13	0.29	0.61	0.06	0.82	0.32
Lysine	5.85	3.15	5.75	0.77	27.84	0.77	4.20	2.37
Ornithine	2.94	1.98	2.66	0.17	4.82	0.37	17.35	0.50
Proline	3.06	1.79	1.65	0.17	2.69	0.13	10.35	0.34
Taurine	6.03	1.36	3.24	0.13	6.05	0.30	7.45	0.41
Tryptophan	7.95	1.67	1.13	0.29	0.48	0.04	2.12	0.30
Valine	2.71	2.34	1.54	0.32	1.70	0.05	4.94	0.40
Choline	4.42	1.78	4.75	0.19	5.33	0.44	7.46	0.47
Creatinine	8.16	1.45	15.88	0.33	10.89	0.36	5.49	0.52
Fructose	7.97	1.11	4.58	0.27	5.75	0.12	12.43	0.35
Glucose	5.02	0.97	5.42	0.18	6.11	0.18	9.03	0.38
Fructose-6-P	14.31	2.85	7.87	0.22	20.87	1.51	11.33	0.18
Glucose-6-P	14.31	2.85	7.87	0.22	8.92	1.52	9.76	0.21
Acetyl-CoA	5.56	3.69	11.96	0.93	11.59	2.60	13.81	0.46
Adenine	2.60	1.69	15.87	0.31	5.24	0.46	6.31	0.46
Adenosine	15.91	1.59	34.10	0.23	14.66	0.54	14.87	0.53
AMP	3.54	2.94	4.35	0.32	7.80	1.18	4.50	0.15
Cytidine	20.47	1.54	15.37	0.20	11.49	0.07	13.56	0.29
Hypoxanthine	12.35	1.3	9.66	0.29	6.17	0.52	4.85	0.58
Inosine	4.66	1.8	14.59	0.23	13.39	0.10	13.94	0.26
NAD+	6.26	2.31	12.75	0.45	19.38	1.27	14.32	0.23
NADH	15.04	2.69	13.32	0.41	11.93	1.85	13.42	0.40
Uracil	14.31	0.8	14.69	0.21	6.95	0.69	6.56	0.24
Uric acid	22.07	1.43	19.14	0.28	8.47	0.49	5.72	0.29
2-Hydroxybutyric acid	11.19	1.63	5.33	3.98	8.30	0.78	7.37	0.50
Fumaric acid	5.50	1.9	4.68	0.26	1.53	1.61	0.94	0.42
Glyceraldehyde 3-phosphate	4.90	3.1	10.92	0.33	5.34	1.62	6.31	0.21
Glycolic acid	4.09	3.12	5.11	2.75	8.95	0.82	5.44	0.45
Lactic acid	17.12	3.53	6.33	2.39	6.97	0.60	5.56	0.32
Malonic acid	14.96	12.31	21.70	4.92	9.01	2.32	14.54	1.40
Pyruvic acid	2.55	1.31	0.90	1.20	0.67	1.19	3.44	0.39
Succinic acid	4.35	3.73	6.61	0.16	3.22	0.81	1.58	0.93
α -Ketoglutaric acid	6.84	2.03	3.98	0.22	4.53	1.04	6.94	0.19

Table S9. Process of untargeted feature filtering

Cleaning process	ZIC-c Neg ESI	ZIC-c POS ESI	BEH-amide Neg ESI	BEH-amide POS ESI
Total features detected by XCMS	1975	2366	1460	1731
Removal of peaks eluted in void-volume time	113	286	280	505
Removal of isotopes	256	280	154	150
Removal of non-biological peaks (by blank)	432	563	360	441
Consolidating features per retention time	454	234	104	33
Final features	720	1003	562	602
Putative isomeric feature	18	39	10	13

Chapter 3:

Unraveling the metabolic dysfunction processes fueling parkinsonism pathogenesis in human iPSC-derived mid-brain neurons with PINK1 mutation and rotenone exposure

Based on:

LuoJiao Huang, Vincent Verschoor, Agnieszka Wegrzyn, Fadhilah Rachmi Rosmasari, Wei Yang, Alida Kindt-Dunjko, Jens C. Schwamborn, Christine Klein, Amy Harms, Ronan Fleming, Thomas Hankemeier

Unraveling the Metabolic Dysfunction Processes Fueling Parkinsonism Pathogenesis in Human iPSC-derived Mid-brain Neurons with PINK1 Mutation and Rotenone Exposure

Manuscript submitted

Abstract

Parkinson's disease (PD) is a complex neurodegenerative disease and can be triggered by multiple risk factors, such as genetic alterations, environmental or occupational exposures, and aging. It is characterized by the loss of dopaminergic neurons. However, until now, no clear molecular mechanism driving neuronal death has been well understood and no intrinsically effective therapy is available. In this study, we used human induced pluripotent stem cell (iPSC)-derived mid-brain neuronal models to investigate the separate and combined effects of a phosphatase and tensin homolog-induced kinase 1 (PINK1) mutation and rotenone exposure by comparative metabolomics of central carbon metabolism, acylcarnitine and polyunsaturated fatty acid metabolism. Neurons with PINK1 mutation or rotenone exposure both revealed varying extents of metabolic disturbances in terms of energy imbalance, mitochondrial respiratory impairment, oxidative stress and neuronal inflammation. Moreover, rotenone negatively impacted antioxidant capacity. These overlapping and compensating disturbances ultimately led to a broad metabolic dysregulation in the mutation model and toxicant exposure. In addition, β -nicotinamide adenine dinucleotide (NAD⁺) supplementation to the rotenone-treated PINK1-mutant neurons improved the branched chain amino acid metabolism, resulting in increased energy production. These results suggest that gene-environmental interactions contribute to the complexity of neurodegeneration from a metabolic perspective. NAD⁺ supplementation for the *in vitro* cellular PD model shows its limitations in ameliorating these disturbances. Overall, our study provides valuable insights into a deeper understanding of parkinsonism pathogenesis.

Introduction

Parkinson's disease (PD), a prevalent neurodegenerative disease in the aging population, is characterized by severe motor symptoms and developing mental health problems [1]. As the worldwide aging population grows and life expectancy increases, the continuously increased prevalence and incidence of PD can pose a big challenge to global health and economics [2]. PD is a complex and multifactorial disease, with genetic alterations, environmental or occupational exposures and aging all playing a role [2,3].

Mutations in phosphatase and tensin homolog-induced kinase 1 (PINK1) have been typically identified in familial early-onset PD cases [4], causing a failure of cellular mitophagy to remove damaged mitochondria. Patients with this monogenic form of PD were reported to have symptoms clinically identical to those of patients with sporadic forms of PD [5,6]. PINK1 deficiency is associated with mitochondrial dysfunction, which is regarded as a hallmark of PD. Elucidating the relevant molecular mechanisms could also help to identify the key mechanism underlying the more prevalent sporadic PD [7]. Besides, PINK1 deficiency was reported incapable to induce neuronal loss, which makes scientists reconsider its role during neurodegeneration [8,9]. On the other hand, environmental toxins have been identified that increase the risk of developing PD, such as pesticides paraquat or rotenone [10]. Rotenone is a classic mitochondrial complex I inhibitor, inducing acute parkinsonian syndrome [11]. Since mitochondrial defects are commonly found in genetic and toxin perturbations, the role of genome-environment interactions becomes highly interesting and generates a possible hypothesis that genetic deficiency involved in mitochondrial-stress pathways could increase the susceptibility towards neurodegeneration in response to environmental toxins [12,13]. Expanding the investigation of the mechanisms from mono-cause to dual-cause intervention can gain more insights into the pathogenesis of sporadic PD.

Complex interactions between genotype, lifestyle, environmental exposure, and drug treatment result in diverse metabolic phenotypes in individuals, which fortunately can be identified and quantified at the level of endogenous metabolites or exogenous small molecules/metabolites [14]. Metabolomic technologies provide unique advantages in systematic measurements of metabolic pathway alterations associated with diseased conditions [15]. In order to probe into the PD pathogenesis mechanism, previous metabolomics studies majorly focused on measuring brain tissues from toxin-induced PD animal models (mouse, rat, goldfish, drosophila) and have revealed abnormal metabolic activities in glycolysis, tricarboxylic acid cycle (TCA), amino acids metabolism, nucleotides synthesis, fatty acids and lipids metabolism [16–21]. Few transgenic animal models have been generated that are implemented for PD metabolomics investigation other

than the alpha-synuclein transgenic mouse model [22,23]. A significant increase of guanosine level was discovered in the aged PD-related alpha-synuclein A53T transgenic mice, indicating a protective mechanism against neurodegeneration [23]. In-vitro cellular models, especially the induced pluripotent stem cell (iPSC)-derived model, give more flexibility in studying metabolomic perturbations caused by selective toxins or inhibitors [24,25], or patient-specific gene deficiency [26]. However, limited metabolomics studies at the cellular level have been carried out, and to our knowledge, there has been no report showing the metabolomic profile of human iPSC-derived neurons with PINK1 deficiency, let alone the interaction with toxin perturbations.

Mitochondria act as a major energy source for maintaining cellular functions and are highly abundant in neurons to support their high-rate energy consumption. Dysfunctional mitochondria are closely linked to disturbed metabolic energy homeostasis and play an important role in neurodegeneration [27]. β -nicotinamide adenine dinucleotide (NAD⁺) is an essential cofactor in cellular energy metabolism and is also a critical signaling pathway regulator in cell survival and neuroprotection [28]. NAD⁺ depletion has been widely reported in many PD-related animal and cellular models [29]. Current PD treatments are primarily dopamine-based and symptomatic in order to improve motor outcomes. No pharmacologic treatments for slowing or ameliorating neuronal degeneration are available. The supplementation of NAD⁺ or its precursors has the potential to become a promising therapeutic strategy [30,31].

In this study, we aimed first to identify metabolic dysregulations in the metabolome of dopaminergic neurons, aroused by PINK1 mutation, rotenone toxicity, and their interactive effects, and second, to assess the efficacy of NAD⁺ supplementation as a treatment for reversing the aforementioned disturbed metabolic phenotypes. We performed targeted metabolic profiling on the iPSC-derived mid-brain neuron models cultured from a PINK1-mutant and its gene-corrected cell line and evaluated changes brought on by rotenone treatment. Our results revealed systemic metabolic pathway alterations from glucose, amino acid, nucleotide, acylcarnitine, and fatty acid metabolism related to neuronal energy failure and oxidative stress. Moreover, for the first time, we showed how impaired mitochondrial homeostasis in PINK1-mutant neurons responded to rotenone perturbation, which contributes to a deeper understanding of potential PD pathogenesis mechanisms. In terms of the identified disturbed metabolism, we further demonstrated the limited ability of NAD⁺ treatment in energy restoration for PINK1 parkinsonism, which provides valuable hints for improving future potential therapies in ameliorating neuronal degeneration.

Materials and methods

1. In vitro cell culture

Information on isogenic pairs of wild-type and mutant human neuroepithelial stem cell (hNESc) lines from an early-onset PD patient with a PINK1-Q456X mutation can be found in details in Table S1. The PINK1-mutant and its isogenic control hNESCs (cell line ID: M826 and GC826) were maintained and generated into midbrain-specific dopaminergic neurons by following an established protocol [32,33], with some adaptations mentioned in the sections below. The same adaptations were also applied in our previous work [34].

1.1 N2B27 medium preparation

The culture medium, denoted N2B27 medium, was used as the basis to prepare both maintenance and differentiation media. N2B27 was prepared by mixing 24 mL Neurobasal medium (Life Technologies, USA), 24 mL of Dulbecco's Modified Eagle Medium: Nutrient Mixture F-12 (DMEM/F12) medium (Life Technologies, USA) supplemented with 1% penicillin and streptomycin (Life Technologies, USA), 0.5 mL of 200 mM L-glutamine (Life Technologies, USA), 0.5 mL of B27 supplement without Vitamin A and 0.25 mL of N2 supplement (Life Technologies, USA) to reach a total volume of 49.25 mL.

1.2 Plate coating and culture group design

New cell-culture treated 6/12-well plates (ThermoFisher scientific, USA) were coated with 1% Matrigel (Corning, USA, Catalogue number: Cat #354277) in 1000/600 μ L of DMEM (1X) medium supplemented with knockout serum replacement (ThermoFisher scientific, USA). Four wells from 6-well plate were used for propagation of each cell line. Each cell line was next cultured on 12-well plates in five conditions including control, dimethyl sulfoxide (DMSO) control, rotenone treatment, NAD⁺ treatment, and combined treatment.

1.3 Cell seeding and maintenance

The medium to maintain the hNESc in culture, denoted maintenance medium, was based on N2B27 medium with 0.5 μ M purmorphamine (PMA, Enzo life sciences, USA), 3 μ M CHIR-99021 (Axon Medchem, The Netherlands) and 150 μ M ascorbic acid (Sigma Aldrich, USA). Each cell line was propagated on 6-well plates till reaching 80-90% confluency and enzymatically passaged with Accutase (ThermoFisher scientific, USA) onto precoated 12-well plates. Recollected cells were seeded in six replicate wells per condition group on 12-well plates. The cell seeding on 12-well plate was done by preparing 4×10^5 million cells/mL in maintenance medium and adding 300 μ L of this preparation together with another 300 μ L of maintenance medium to reach 1.2×10^5 cells per well. The plate was incubated at 37 °C and 5% CO₂ for 48 h.

1.4 Neuronal differentiation and maturation

The differentiation medium with PMA preparation to induce the differentiation of hNESc towards midbrain dopaminergic neurons consisted of N2B27 medium with 200 μ M ascorbic acid, 0.01 ng/ μ L brain-derived neurotrophic factor (BDNF, Peprotech, USA), 0.01 ng/ μ L

glial cell line-derived neurotrophic factor (GDNF, Peprotech, USA), 0.001 ng/ μ L transforming growth factor beta-3 (TGF β -3, Peprotech, USA), 2.5 μ M dibutyryl cyclic adenosine monophosphate (dbcAMP) (Sigma Aldrich, USA) and 1 μ M PMA. This medium preparation was completely replaced every 2 days during the next 6 days of culture in the differentiation process. For the maturation of differentiated neurons, PMA is required to be absent from the differentiation medium. This differentiation medium without PMA was used from day 9 onwards and complete media replacement was done every 2 days for 2 weeks.

1.5 Neuron treatment with rotenone or NAD⁺

After 21 days of neuron differentiation and maturation, neurons in the rotenone group were exposed to 400 nM rotenone (dissolved by DMSO) for 24 hours, and neurons in the NAD⁺ group were supplemented with 2 mM NAD⁺ for 24 hours. Neurons in the combined treatment group were first treated with 400 nM rotenone for 24 hours. After that, neurons were cultured for another 24 hours with medium containing 2 mM NAD⁺ to replace the used rotenone medium. In the control group, the cells were given differentiation medium containing no additional compound. In the DMSO control group, the cells were given differentiation medium with the same amount of DMSO as in the rotenone treatment.

1.6 Cell and medium sample harvest

The spent medium was collected into a 1.5 mL Eppendorf tube. For cell quenching, 200 μ L of ice-cold 80% MeOH in water was used immediately after removing the spent medium and washing with phosphate buffered saline (PBS, Gibco/Life Technologies, USA). Quenched cell lysate was harvested into a new Eppendorf tube. All sample tubes were fast frozen into liquid nitrogen and stored in the -80 °C freezer until LC-MS measurement.

2. Sample preparation and LC-MS measurement

Cell samples were lysed with sonication after one freeze-thaw cycle, vortexed and then centrifuged at 16000 g 4 °C for 10 min. Cell pellets were collected for measuring the total protein content later. Supernatants were transferred into clean 1.5 mL Eppendorf tubes and evaporated to dryness in a Labcono SpeedVac (MO, United State). Each sample was reconstituted with 75 μ L ice cold methanol/water (80%/20%; v/v). 50 μ L of the sample reconstitution volume was collected and transferred into a new Eppendorf tube for polar metabolome measurement. Next, 10 μ L of the sample reconstitution volume was collected and transferred into a new Eppendorf tube for acylcarnitine measurement. The remaining volume per sample was pooled together as a quality control (QC) sample pool. In total, 10 QC samples with 50 μ L were prepared for polar metabolome measurement, and 10 QC samples with 10 μ L were prepared for acylcarnitine metabolome measurement.

Polar metabolome: Cell lysate samples aliquoted for polar metabolome measurement followed a liquid-liquid extraction (LLE) method that was described in our previous work. 5 μ L of polar ISTD solution was added into each sample, which was then followed with LLE extraction by an ice-cold solvent mixed with methanol/water/chloroform. The final upper phase was transferred into a new Eppendorf tube and taken to dryness. The residue was reconstituted with 50 μ L of ice-cold methanol/water (1:1 v/v). Finally, 45 μ L of reconstitution solution was transferred into an autosampler vial with glass insert for LC-MS measurement [35].

Acylcarnitines: Cell lysate samples aliquoted for acylcarnitine measurement were processed using a protein precipitation method. An ice-cold crash solvent was prepared by mixing 20% acylcarnitine ISTD solution with 80% methanol solvent. 30 μ L of the crash solvent was added into each sample, which was then followed with vortexing for 10 mins, centrifuging at 16000 rcf, 4 °C for 10 min. Finally, 35 μ L of the supernatant was transferred into an autosampler vial with glass insert for LC-MS measurement.

Signaling lipids: Medium samples aliquoted for signaling lipids measurement followed a liquid-liquid extraction (LLE) method with minor adaptations that was also described in our previous work [36]. Medium aliquots (100 μ L) were thawed on ice, and then 10 μ L antioxidant (0.2mg/ml butylated hydroxytoluene (BHT) and 0.2 mg/ml ethylenediaminetetraacetic acid (EDTA)) solution and 10 μ L of signaling lipid ISTD solution were added. Samples were briefly vortexed and then acidified with 100 μ L of buffer solution (0.2 M citric acid and 0.4 M disodium hydrogen phosphate buffer at pH 4.5). LLE was accomplished by adding 800 μ L of a butanol (BuOH)/methyl tert-butyl ether (MTBE) (1:1 v/v) solution. Samples in Eppendorf tubes were settled on ice for 20 mins and transferred in the bullet blender to mix for 4 minutes at the speed of level 8. After a subsequent centrifugation at 16000 rcf, 4 °C for 10 min, 700 μ L of the upper organic phase was collected and taken to dryness. The residue was reconstituted with 50 μ L of ice-cold methanol/acetonitrile (7:3 v/v, with 100 nM CUDA). Finally, 45 μ L of reconstitution solution was transferred into an autosampler vial with glass insert for LC-MS measurement.

3. LC-MS measurement

Polar metabolome: Targeted 106 polar metabolites analyses was performed on a SCIEX tripleTOF 5600 MS system (SCIEX, USA) coupled to a Waters Acquity UPLC Class II (Waters, USA) equipped with a SeQuant® ZIC®-cHILIC HPLC column (2.1mm x 100 mm, 3.0 μ m, Merck, Germany). The LC-MS method followed a previously described method. Mobile phase A consisted of 90% acetonitrile, 10% water with 5 mM ammonium formate, and mobile phase B consisted of 10% acetonitrile, 90% water with 5 mM ammonium formate. The injection volume was 3 μ L. The flow rate was 0.5 mL/min and the gradient

was as follows: 0 min-0% B, 2 min-15% B, 5 min-21% B, 7.5 min-26% B, from 10 to 11 min-40% B, from 11.5 to 18 min-0% B. Electrospray ionization (ESI) was operating at negative ion mode. The following ion source parameters were applied, spray voltage 4.5 kV, capillary temperature 400 °C, ion source gas 1 20 psi, ion source gas 2 50 psi, curtain gas 25 psi, CAD gas 7 psi [37].

Acylcarnitines: Targeted 50 acylcarnitine metabolites analyses was performed on a SCIEX QTRAP 6500 MS system (SCIEX, USA) coupled to a Waters Acquity UPLC Class II (Waters, USA) equipped with an AccQ-Tag™ Ultra C18 column (2.1mm x 100 mm, 1.7 µm, Waters, USA). In the LC-MS method, mobile phase A consisted of water with 0.1% formic acid, and mobile phase B consisted of acetonitrile with 0.1% formic acid. The injection volume was 5 µL. Separations were performed at 60 °C at a flow rate of 0.7 mL/min using the following gradient: from 0 to 1.10 min-5% B, from 1.11 to 2 min-11% B, 8 min-70% B, from 8.01 to 9.01 min-100% B, from 9.20 to 11 min-5% B. Electrospray ionization (ESI) was operating at positive ion mode, followed with a multiple reaction monitoring detection method. The applied ion source and compound parameters were shown below, spray voltage 4.5 kV, capillary temperature 350 °C, ion source gas 1 80 psi, ion source gas 2 70 psi, curtain gas 20 psi, CAD gas -2 psi, CXP 10 V, DP 70 V, EP 10 V [38].

Signaling lipids: Targeted 106 signaling lipid mediators were analyzed at low mobile phase pH condition. The analyses was performed on a SCIEX Triple Quad™ 7500 MS system (SCIEX, USA) coupled to a Shimadzu Nexera Prominence LC (Shimadzu, Japan) equipped with an Acquity BEH C18 column (50 × 2.1 mm, 1.7 µm; Waters, USA). In the LC-MS method, mobile phase A consisted of water with 0.1% acetic acid, mobile phase B consisted of a mixture of acetonitrile–methanol (9:1, v/v) with 0.1% acetic acid, mobile phase C consisted of isopropanol with 0.1% acetic acid. The injection volume was 5 µL. Separations were performed at 40 °C at a flow rate of 0.7 mL/min using the following gradient: 20% B and 1% C as starting conditions; changing to 85% B between 0.75 and 14 min and to 15% C between 11 and 14 min; conditions held for 0.5 min prior to column re-equilibration at the starting conditions from 14.8 to 16 min. Electrospray ionization (ESI) was operating at both positive and negative ion mode, followed with a multiple reaction monitoring detection method. The applied ion source parameters were, spray voltage 4.5 kV, capillary temperature 600 °C, ion source gas 1 65 psi, ion source gas 2 65 psi, curtain gas 45 psi, CAD gas 9 psi [36].

4. Immunofluorescence staining

At the end of differentiation stage, immunofluorescence staining was performed on the matured neurons of each cell line, GC826 and M826. Cells were fixed using 4%

formaldehyde in PBS for 20 min at room temperature. After removing the fixative, cells were next permeabilized for 60 min at room temperature with 0.1% Triton X-100 and 10% fetal calf serum (FCS) in PBS. The cells were washed once with PBS containing 1% FCS and then incubated with the primary antibody solution overnight at 4°C. Next day, the cells were washed three times with PBS containing 1% FCS, followed by incubation with Hoechst (1:1000, 33342, Invitrogen, USA), and the secondary antibody solution at room temperature for 1.5 hour, protected from light. The cells were finally washed three times with PBS containing 1% FCS. Primary antibody solution was prepared by diluting mouse anti-tubulin- β III (1:500, Cat #801201, BioLegend, USA) and rabbit anti-tyrosine hydroxylase (1:500, Cat #ab112, Abcam, UK) in PBS containing 1% FCS. Secondary antibody solution was prepared by diluting Alexa Fluor 568-conjugated goat anti-mouse IgG (1:1000, Cat #A11031, Invitrogen, USA) and Alexa Fluor 488-conjugated goat anti-rabbit IgG (1:1000, Cat #A11008, Invitrogen, USA) in PBS containing 1% FCS. Images of the stained cells were acquired using a EVOS™ FL Auto 2 Imaging System (ThermoFisher, USA).

5. Rotenone-induced neuron viability assay

For the neuron viability assay, we started a new neuron culture in a 96-well plate after propagation from 6-well plate culture. Neurons from each cell line were maintained and differentiated by following the same protocol. Matured neurons received rotenone treatment divided in different concentration groups, including 100, 200, 400, 800, 1000 and 4000 nM, together with a control and DMSO-treated group. Treatment groups had three sample replicates. After 24-hour incubation at 37 °C and 5% CO₂, 10 μ L of alamarBlue™ cell viability reagent was directly added to cells in culture medium. The culture plate was then incubated for 3 hours at 37 °C and 5% CO₂, also protected from direct light. The absorbance was measured with a microplate reader Infinite M1000 (Tecan, Switzerland) at 570 nm (detection wavelength) and 600 nm (reference wavelength).

6. Bicinchoninic acid (BCA) assay for protein quantitation

The BCA protein assay was performed on the collected cell pellets according to the manufacturer's protocol (Thermo Fisher Scientific, USA). 15 mL of radio-immunoprecipitation-M (RIPA-M) assay buffer was prepared by mixing 1.5 mL of 500 mM Tris (Sigma Aldrich, USA), 1.5 mL of 1500 mM sodium chloride (NaCl), 1.5 mL 10 mM of EDTA, 0.1 mL 1 % IGEPAL CA-630 (Sigma Aldrich, USA), 30 μ L protease Inhibitor Cocktail (Sigma Aldrich, USA), and compensating with Milli-Q water. 10 mL of UREA-T buffer was prepared by dissolving 4.8 g Urea with 500 μ L of 1500 mM NaCl, 1 mL of 500 mM Tris, and Milli-Q water. 150 μ L of ice-cold RIPA-M buffer was added to each sample pellet, which was then followed with vortexing for 10 mins, centrifuging at 16000 rcf, 4 °C

for 10 min. The supernatant was collected into a new Eppendorf tube. Subsequently, the left-over pellet was resuspended in 75 μ L of UREA-T buffer prior to vortexing, sonication for 5 min, and centrifuging at 16000 rcf and 4 °C for 10 min. The resulting supernatant was collected and combined with the previous supernatant. The final sample supernatant was obtained after vortexing and centrifuging the supernatant mixture at 16000 rcf and 4 °C for 10 min. 25 μ L of standard solution or sample supernatant was added in triplicates to wells of three 96-wells plates and then added with 200 μ L of working reagent in each well. The plates were covered with aluminum foil and incubated at 37 °C for 30 min. The absorbance was measured with a microplate reader Infinite M1000 (Tecan, Switzerland) at 562 nm (detection wavelength). Protein content of each sample was quantified based on a standard curve made from a series concentrations of bovine serum albumin.

7. Data processing and analysis

Metabolite peak integration was carried out using the SCIEX OS Analytics processing tool (version 2.1.6). MzQuality (<https://gitlab.com/lacdr-abs/mzqualr>) was used to evaluate intra-batch variations in which metabolites with a background signal over 40 % or a QC relative standard deviation over 30 % were removed. The relative abundance of the metabolite was represented with the peak area ratio of analyte to its internal standard. The peak area ratio data was first corrected by the sample protein content and normalized using probabilistic quotient method. For univariate analysis, normalized data was further treated with cube-root transformation. For multivariate analysis, normalized data was further processed with cube-root transformation and pareto scaling. Neuron viability assay obtained the sample absorbance from measurement wavelength then normalized to the absorbance from reference wavelength. The percentage of viable cells was then calculated using the sample absorbance against the average absorbance in the control group.

Statistical analysis was performed in R programming software (version 3.6.2). An independent two-tailed unpaired Student's t test was performed to evaluate the statistical difference between two treated groups, in which p-values below 0.05 were considered statistically significant. A standard Benjamini-Hochberg method was applied to control the false discovery rate for multiple hypothesis testing in the volcano analysis. Metabolites found with statistical differences were visualized in heatmap, boxplot and correlation map also implemented in R programming software (version 3.6.2).

Results

1. Mid-brain specific neuronal differentiation and its response to rotenone neurotoxicity

A successful *in vitro* iPSC-derived neuron culture is a prerequisite for our follow-up metabolomics investigation. Identification of neuron differentiation was performed at the end of the culture stage

using optical microscopy observation and immunofluorescent staining (Figure 1A-C). Positive expression of tubulin- β III confirmed the differentiation of neurons, moreover, positive expression of tyrosine hydroxylase confirmed the presence of dopaminergic neurons (Figure 1C). The effect of rotenone concentration to induce neuronal stress but no significant neuronal death was first evaluated in this study using the alamar blue assay. Treatment with rotenone for 24 h showed a concentration-dependent decrease in the viability of mutant neurons in a visual rather than a statistical perspective (Figure 1D). Following experiments used rotenone at a medium concentration of 400 nM because there was no significant viability loss when compared to the no rotenone-treated control level.

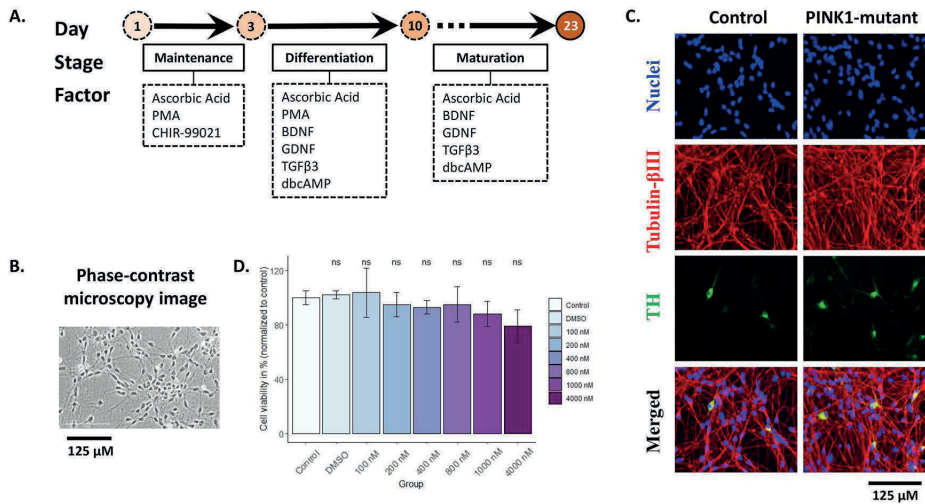


Figure 1. *In vitro* cell culture protocol overview, characterization of neuron differentiation, and viability assay with rotenone exposure. A. Differentiation of human neuroepithelial stem cells (hNESc) into midbrain-specific dopaminergic neurons. The media composition at the various stages of cell culture were shown in the below boxes. B. Neuron colony morphology in the phase-contrast microscopy image acquired on day 23, with a scale bar of 125 μm. C. Immunofluorescence characterization of isogenic PINK1-mutant (M826 cell line) and control (GC826 cell line) mature neurons. Immunofluorescence staining of mutant and isogenic control neurons showed a large percentage of tubulin- β III expression, representing the presence of differentiated neuronal populations (red), including a population of tyrosine hydroxylase (TH) dopaminergic neurons (green), and nuclei were identified with hoechst (blue). A merged image of nuclei, tubulin- β III and TH stains was shown at the bottom, with a scale bar of 125 μm. D. Cell viability quantification for PINK1-mutant neurons with 24-hour exposure to rotenone in a range from 100 nM to 4000 nM. Data represent means \pm SE of three independent experiments, * $p < 0.05$, ns: no significant difference.

2. Metabolic disturbance in control and PINK1-mutant neurons influenced by rotenone

To characterize the individual effect of rotenone exposure or PINK1 mutation, and most importantly their joint impact on dopaminergic neuron metabolism, a combination of multiple analytical platforms was adopted to achieve a broad metabolome coverage. Targeted metabolomics analysis was performed on cell and medium samples from isogenic control groups (control/control_DMSO), a rotenone-treated control group (Rotenone), a PINK1-mutant group (PINK1) and a rotenone-treated PINK1-mutant group (PINK1_Rotenone). Heatmap visualization of individual metabolites was computed based on the relative metabolite abundance change respectively caused by rotenone exposure (Rotenone *versus* control_DMSO), PINK1 mutation (PINK1 *versus* control), or the combined influence of rotenone & PINK1 mutation (PINK1_Rotenone *versus* control_DMSO).

2.1. Central carbon metabolism

The metabolite changes were projected onto the central carbon metabolism pathways, including pathway of glycolysis, pentose phosphate pathway, tricarboxylic acid (TCA) cycle, amino acid metabolism and the connected purine & pyrimidine metabolism (Figure 2).

Lactate (LAC), as a final product of glycolysis, had significantly higher abundance in the rotenone-treated control group, PINK1-mutant group and rotenone-treated PINK1-mutant group than in the control group, suggesting an overall active glycolytic activity with either toxin or mutation influence. Significantly decreased phosphoenolpyruvate (PEP) and increased pyruvate (PYR) were also detected in the PINK1-mutant group. In contrast, increased PEP and decreased PYR were detected in the rotenone-treated control group. The fact that lactate accumulated more in the rotenone-treated group than in the PINK1-mutant group, along with the change of lactate's precursor, showed that the levels of rotenone and the PINK1 mutation's effects on active glycolysis were different, and the mutation influence was relatively minor. The other intermediate metabolites also showed interesting changes, giving a hint of the relevant enzymatic activities. The rate-limiting enzyme phosphofructokinase (PFK) can change fructose-6-phosphate (F6P) into fructose-1,6-phosphate (FDP). The precursor metabolites of F6P, particularly glucose-6-phosphate (G6P), showed a significant decrease, while the downstream metabolites of FDP, dihydroxyacetone phosphate (DHAP), glyceraldehyde 3-phosphate (G3P) showed a significant increase. The results showed an activated PFK enzymatic activity induced by either rotenone exposure or PINK1 mutation. The PINK1-mutant group showed its susceptibility to rotenone exposure reflected in the decreased level of ribose-5-phosphate (R5P), as an important intermediate metabolite of the pentose phosphate pathway. In addition, the ratio plot of NADPH/NADP⁺ in Figure 3 showed a significant decrease in

both rotenone-treated control/PINK1 mutant groups, further indicating an inhibitory role of rotenone on pentose phosphate pathway activity.

Opposite to the accumulation of lactate, the metabolic flux from pyruvate into acetyl coenzyme A (Acetyl-CoA) was found to be significantly decreased in both rotenone-treated control/PINK1 mutant groups. Acetyl-CoA functions as an entry into the tricarboxylic acid cycle (TCA cycle), and its decreased abundance also resulted in a decreased level of cis-aconitate (cis-ACO), α -ketoglutarate (α KG), succinate (SUC) in rotenone-treated control group. Decreased cis-ACO level was also observed in PINK1-mutant group, suggesting a reduced Acetyl-CoA oxidation in mitochondria. However, the levels of α KG, SUC, fumarate (FUM) and malate (MAL) significantly increased in the PINK1-mutant group. Moreover, an elevated α KG level was still maintained under the combined influence of rotenone&PINK1 mutation (Figure S1). We also found a significant decrease in the level of glutamine (GLN), glutamate (GLU), and its derived γ -aminobutyrate (GABA) in both rotenone-treated control/PINK1-mutant groups. Further, by looking at the ratio plot (Figure 3), the ratio of α KG/GLU showed a significant increase in the PINK1-mutant neurons and as well as in the rotenone-treated PINK1-mutant groups. These results might explain the abnormal TCA cycle in PINK1-mutant neurons was caused by an increased nutrient fueling from glutamine except glucose in response to the diversion of pyruvate towards lactate.

Compared to control group, all groups showed a significant energy reduction, reflected in the levels of ATP, UTP, GTP and CTP. Significantly elevated levels in AMP, GMP were also observed within the purine & pyrimidine metabolism. Additionally, with PINK1 mutation or rotenone exposure, elevated levels of nucleosides like guanosine, inosine, adenosine, uridine, and hypoxanthine were partially detected (Figure 2). Taken together, the disturbed neuron is more prone to degrade nucleotides than produce them by de novo synthesis due to inhibition of the pentose phosphate pathway. Strikingly, the NADH/NAD ratio increased more noticeably in the rotenone-treated control/PINK1-mutant groups than in the PINK1-mutant group alone. Overall, rotenone-treated neurons exhibited a very active glycolytic activity and nucleotide degradation, but low pentose phosphate pathway activity and TCA cycle metabolism with potentially inhibited aconitase (ACO2). PINK1-mutant neurons showed an active glycolytic activity, nucleotide degradation and disturbed TCA cycle metabolism with potentially inhibited ACO2. Furthermore, PINK1-mutant neurons showed its high sensitivity to rotenone exposure, resulting in similar metabolome alterations to mere rotenone perturbation. In addition to the major metabolome alterations found in central carbon metabolism, other amino acid changes are also interesting, such as an increased kynurenine level found in the rotenone-treated control group while a decreased

level found in the PINK1 mutant neuron, an increased tyrosine level found in rotenone-treated PINK1-mutant neurons.

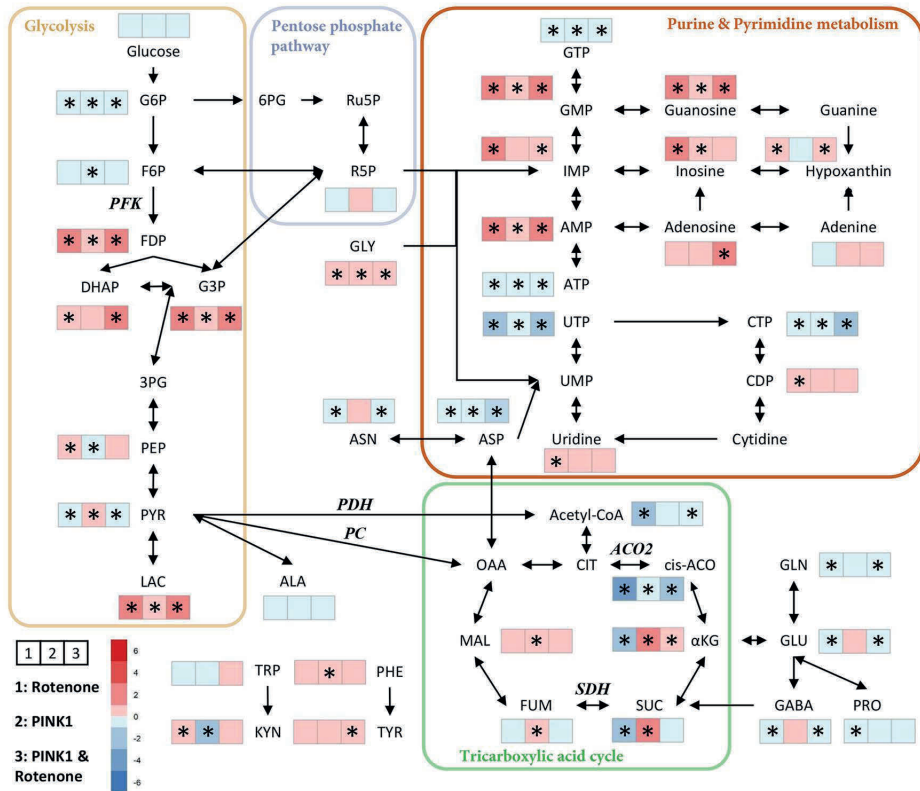


Figure 2. The metabolite alterations within central carbon metabolism, related amino acid and purine & pyrimidine metabolism, which were aroused by rotenone exposure, PINK mutation, or the combined influence of rotenone&PINK1 mutation. The resultant relative changes of each metabolites in the relevant experimental groups compared to its control group (1: rotenone-treated control group *versus* control_DMSO group; 2: PINK1-mutant group *versus* control group; 3: rotenone-treated PINK1-mutant group *versus* control_DMSO group.) were represented in a single heatmap by order from left to right. Increased or decreased change, which was calculated by the \log_2 fold change between the perturbed group versus the control group, was represented in red color or blue color respectively. Significant difference between group comparison was marked by an asterisk*. PFK: phosphofruktokinase; PDH: Pyruvate dehydrogenase; PC: pyruvate carboxylase; SDH: succinate dehydrogenase; ACO2: aconitase.

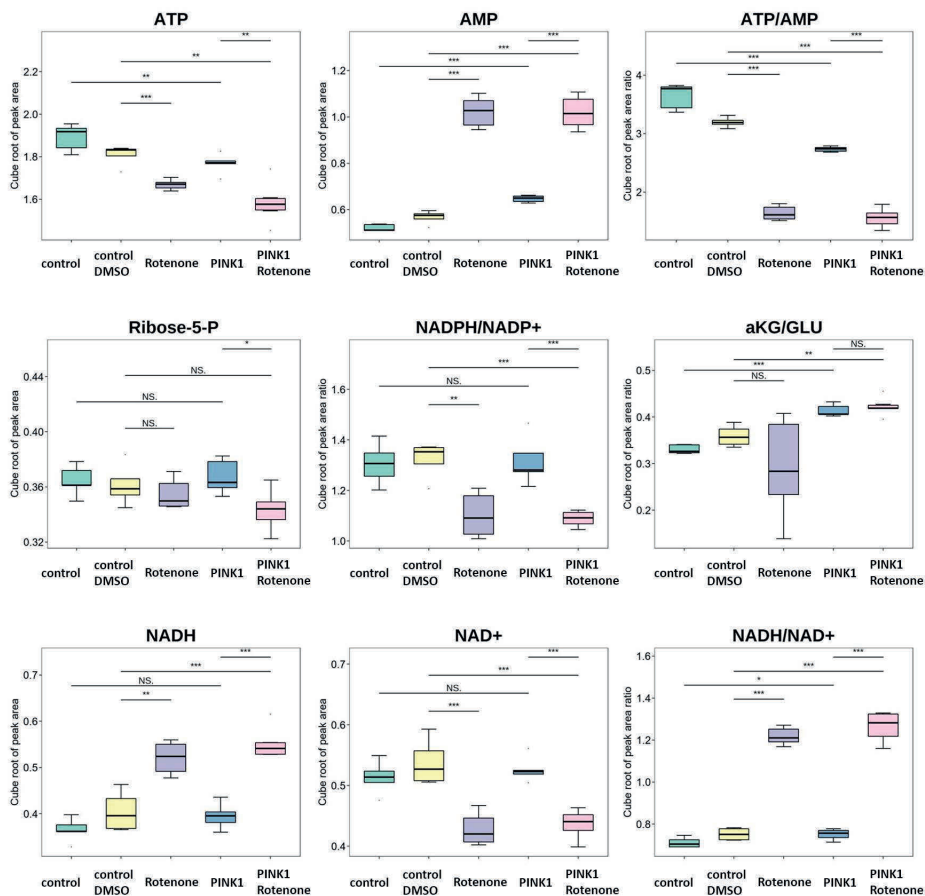


Figure 3. Box plot for showing the metabolite level of ATP, AMP, ribose-5-p, NADH, NAD⁺ and metabolite ratio level of ATP/AMP, NADPH/NADP⁺, α KG/GLU, NADH/NAD⁺ in control groups (control and control_DMSO), rotenone-treated control group (Rotenone), PINK1-mutant group (PINK1) and rotenone-treated PINK1-mutant group (PINK1_Rotenone). Significant difference between group comparison was marked by * ($p < 0.05$), ** ($p < 0.01$), *** ($p < 0.001$). No significant difference was marked by NS.

2.2. Acylcarnitine metabolism

When the glucose-derived energy production is limited, it might trigger neurons to utilize energy supplementation through fatty acid oxidation, which provides the electron donors to feed into the electron transport chain, powering oxidative phosphorylation and maintaining energy homeostasis [39,40]. Carnitine works as a free shuttle by forming into acylcarnitine substrates to assist long-chain fatty acid transport into mitochondria, while medium-chain fatty acid can directly permeate the inner mitochondrial membrane, as illustrated in Figure

4A. To understand more energy substrates and their linked effect to energy metabolism in PD, we also investigated the profile of acylcarnitines in all experimental groups. In total, we found 2 long-chain acylcarnitines (LCAC), 8 short-chain acylcarnitines (SCAC) that showed significant differences under the influence of rotenone or PINK1 mutation. Figure 4B showed an increased level of linoleoyl-carnitine (C18:2-carnitine) observed in rotenone-treated control/PINK1-mutant groups, and increased level of oleoyl-carnitine (C18:1-carnitine) in the PINK1-mutant group and rotenone-treated control/PINK1-mutant groups. However, a decreased free carnitine was only observed in PINK1-mutant group. Malonyl-CoA is a well-known inhibitor of carnitine palmitoyltransferase I (CPT1) [41]. Increased level of malonyl-carnitine (C3:1-2OH-carnitine) was observed along with rotenone exposure. To different extent, all the observed alterations showed an impaired capacity for long-chain fatty acid oxidation with either toxin or mutation influence. On the other hand, we found increased butyryl-carnitine (C4-carnitine) and acetyl-carnitine (C2-carnitine) with toxin or mutation influence. To compensate for the energy deficiency, neurons might have an active medium-chain fatty acid oxidation, forming into increased SCACs. Other intermediate SCACs with odd carbon atoms, such as isovaleryl-carnitine (C4-3M-carnitine), 2-methylbutyryl-carnitine (C4-2M-carnitine), propionyl-carnitine (C3-carnitine), tiglyl-carnitine (C5:1-carnitine), methyl-malonyl-carnitine (C3-DC-M-carnitine) are products derived from branched chain amino acid metabolism. As another nutrient fueling to TCA cycle, branched chain amino acids (leucine, isoleucine and valine) provide carbons to support forming into products of acetyl-CoA and succinate. A significant decreased levels of these SCACs suggested less utilization of branched chain amino acids for energy production (Figure 4C) [42].

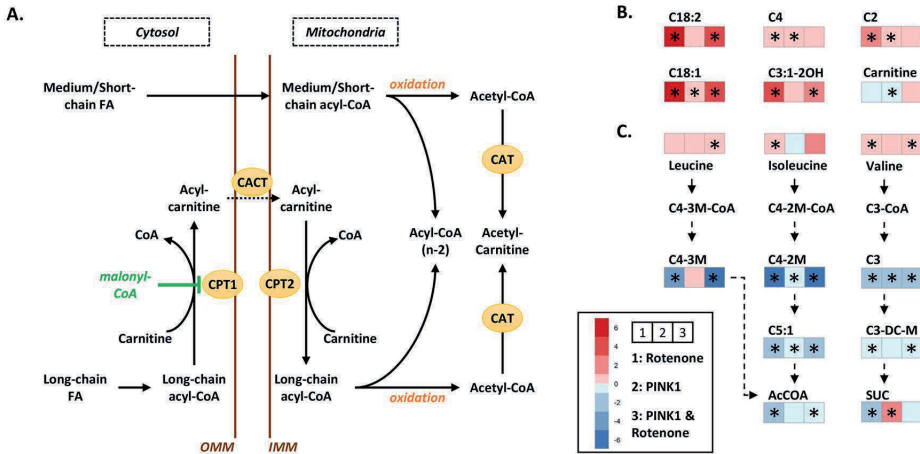


Figure 4. Metabolic disturbances associated with acylcarnitine metabolism in control and PINK1 mutant neurons influenced by rotenone. A. Illustration of mitochondrial fatty acid β -oxidation in neurons. CPT1: carnitine palmitoyltransferase I; CPT2: carnitine palmitoyltransferase II; CACT: carnitine-acylcarnitine translocase. B. Metabolite heatmap showing the relative changes of linoleoyl-carnitine (C18:2-carnitine), oleoyl-carnitine (C18:1-carnitine), malonyl-carnitine (C3:1-2OH-carnitine), butyryl-carnitine (C4-carnitine) and acetyl-carnitine (C2-carnitine) in three experimental groups compared to the control group (1: rotenone-treated control group *versus* control_DMSO group; 2: PINK1-mutant group *versus* control group; 3: rotenone-treated PINK1-mutant group *versus* control_DMSO group.). C. Metabolite heatmap showing the relative change of isovaleryl-carnitine (C4-3M-carnitine), 2-methylbutyryl-carnitine (C4-2M-carnitine), propionyl-carnitine (C3-carnitine), tiglyl-carnitine (C5:1-carnitine), methyl-malonyl-carnitine (C3-DC-M-carnitine) in three experimental groups compared to the control group. Increased or decreased change, which was calculated by the \log_2 fold change between the perturbed group *versus* the control group, was represented in red color or blue color respectively. Significant difference between group comparison was marked by an asterisk*.

3.2.3. Signaling lipid mediators

More than energy balance, fatty acids also play distinct roles in neuroinflammatory regulation, especially poly unsaturated fatty acids (PUFA) and their bioactive eicosanoid and docosanoid metabolites [43]. To investigate further into alterations associated with neuroinflammation in the situation of energy deficiency, we examined PUFAs and signaling lipid mediators secreted into medium samples from all experimental groups. Figure 5A showed an illustrated pathway for the lipid mediators' derivation from the turnover of membrane phospholipids. Among 40 metabolites detected, Figure 5B depicts the metabolite differences observed for PUFAs-n3, PUFAs-n6, PUFAs-n9 and their derived 10 lipid mediators. In the free PUFA group, gamma-linolenic acid (GLA, C18:3, n6), arachidonic acid (AA, C20:4, n6), eicosapentaenoic acid (EPA, C20:5, n3) showed significant increased levels in not only in individual-factor but also in joint-factor group. Interestingly, significantly decreased adrenic acid (AdA, C22:4, n6), docosapentaenoic acid (DPA, C22:5, n6) and increased docosahexaenoic acid (DHA, C22:6, n3) was shown in the PINK1-mutant group. In contrast, the opposite expression of DPA was shown in the rotenone-treated control group. Several signaling lipid mediators were detected with significant alterations from enzymatic-oxidation of linoleic acid (LA, C18:2, n6), AA, EPA and DHA via cytochrome P450 (CYP), cyclooxygenase (COX), lipoxygenase (LOX) or auto-oxidation. A ratio plot can better explain the oxidative metabolism. As can be seen in Figure 6, an increased trend in the ratios of 9,10,13-TriHOME/LA, 9,12,13-TriHOME/LA and 13-HODE/LA, while a decreased level in the ratio of 16-HDoHE/DHA were observed in

individual-factor and joint-factor group. The results suggested an active LOX- and COX-mediated oxidation of LA compared to an inactive DHA oxidation. On the other hand, decreased ratio of 14,15-DiHETrE/AA, 14,15-DiHETE/EPA, 5-HEPE/EPA and 9-HEPE/EPA was only found in rotenone-treated control/PINK1-mutated groups. By analyzing the oxidative stress in neurons with the indicators of glutathione (GSH) and ascorbic acid, we found a similar expression pattern, especially for the rotenone-treated control/PINK1-mutant groups. A correlation analysis between lipid mediators and antioxidant markers (GSH, ascorbic acid, NADPH/NADP⁺) further explored the relationship between oxidative stress and PUFA oxidations (Figure 7). We found a strong positive correlation of antioxidants to AA-, EPA- and DHA-derived oxylipins, while a strong negative correlation to LA-derived oxylipins. Decrease in antioxidants indicates an increased oxidative stress, which may cause an overactive peroxidation of LA in comparison to the other PUFAs.

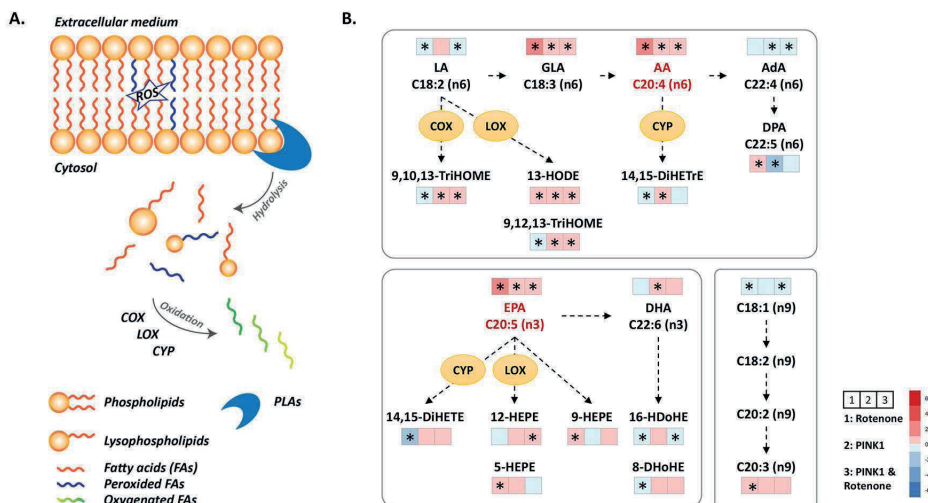


Figure 5. Metabolic disturbances associated with poly unsaturated fatty acid (PUFA) metabolism in control and PINK1 mutant neurons influenced by rotenone. **A.** An illustration of the production of free PUFAs in neurons from membrane phospholipids upon stimulation of the enzyme phospholipase A (PLA) by oxidative stress. Three main enzymatic pathways are responsible for the formation of eicosanoid and docosanoid metabolites, involving cyclooxygenases (COXs), lipoxygenases (LOXs), and epoxygenases of the cytochrome P-450 family (CYPs). ROS: reactive oxygen species. **B.** Metabolite heatmap showing the relative change of PUFAs and their derived lipid mediators in three experimental groups compared to the control group (1: rotenone-treated control group *versus* control_DMSO group; 2: PINK1-mutant group *versus* control group; 3: rotenone-treated PINK1-mutant group *versus* control_DMSO group.). Increased or decreased change, which was calculated

by the \log_2 fold change between the perturbed group versus the control group, was represented in red color or blue color respectively. Significant differences between group comparisons were marked by an asterisk*.

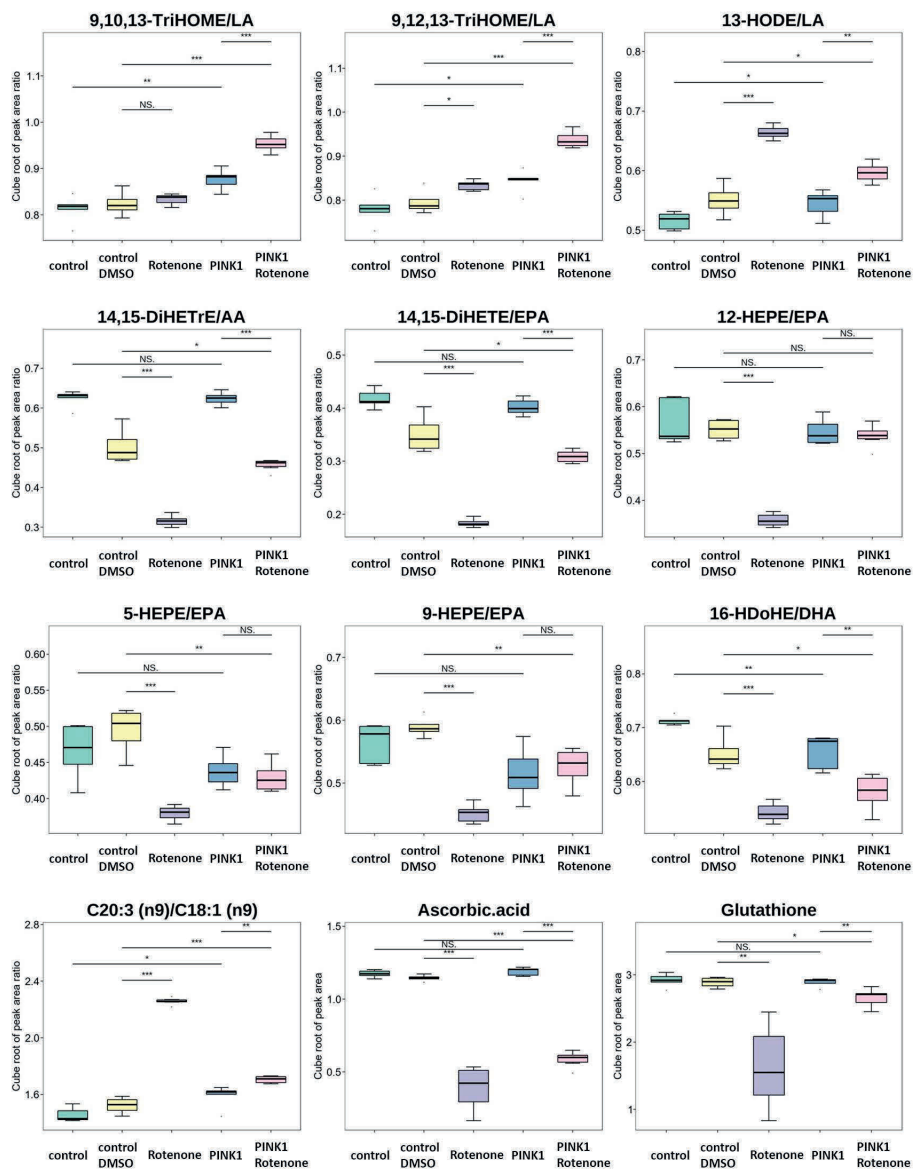


Figure 6. Metabolite ratio changes representing PUFA oxidation, antioxidant metabolite changes in control and PINK1 mutant neurons influenced by rotenone. Box plot for showing the metabolite ratio levels associated with PUFA metabolism in control groups (control and control_DMSO), rotenone-

treated control group (Rotenone), PINK1-mutant group (PINK1) and rotenone-treated PINK1-mutant group (PINK1_Rotenone). Significant difference between group comparison was marked by * ($p < 0.05$), ** ($p < 0.01$), *** ($p < 0.001$). No significant difference was marked by NS.



Figure 7. The correlation heatmap represents pairwise Pearson correlations between the metabolite features from (Figure 6) across all the experimental and control groups. The circle size is proportional to the absolute values of the correlation coefficients. One asterisk was added to encode significance of the correlation. Green indicates a positive correlation, while purple reveals a negative correlation. A darker color indicates a higher degree of positive or negative correlation.

3. Metabolic profiling for showing energy restoration by NAD⁺ treatment

NAD⁺ is reported as an energy supplementing molecule that has been implemented as a PD treatment in many clinical trials so far [44]. To investigate the impact of NAD⁺ treatment on our neurodegenerative models caused by PINK1 mutation or joint factors, we further examined metabolite changes of the energy, acylcarnitines and signaling lipids metabolism in the NAD-treated neurons. In the partial least squares-discriminant analysis (PLS-DA) (Figure 8A), the set of control/control_DMSO, control_rotenone and control_rotenone_NAD groups showed clear separations, similarly, PINK1/PINK1_DMSO/PINK1_NAD, PINK1_rotenone and PINK1_rotenone_NAD groups also revealed clear separations. The rotenone-treated control/PINK1-mutant groups

greatly differed from the control groups. Interestingly, their NAD⁺-treated groups colored in red and grey respectively showed a shift towards their correspondent control groups. The PINK1_NAD group hardly showed separation from the PINK1 group. Based on the volcano analysis between PINK1_NAD and PINK1 group, only one metabolite, hypoxanthine, was found as increased after treatment (Figure 8B). While totally 53 metabolites were found as changed after treating the control_rottenone group. (Figure 8C, Table S5), and 29 metabolites were found to be changed after treating the PINK1_rottenone group (Figure 8D, Table S5). 18 metabolites were found commonly changed in both control_rottenone_NAD group and PINK1_rottenone_NAD group.

To figure out whether the above found metabolite changes were caused by a positive treatment effect or side effect by NAD⁺, we next performed a heatmap analysis for these 18 metabolites in the context also including control groups of control/control_DMSO and PINK1/PINK1_DMSO. As shown in Figure 8E, the level of sorbitol, lactate, AMP, malonylcarnitine, 9,12,13-triHOME, 9,10,13-triHOME and 13-HODE reduced significantly in the NAD⁺ treated-groups, as well as towards the control group level. On the other hand, ascorbic acid, cis-aconitate, NAD⁺, propionylcarnitine, tiglylcarnitine, isovalerylcarnitine, 2-methylbutyrylcarnitine, 14,15-diHETE and 14,15-diHETrE were found increased significantly, also close to the control group level. In addition, ratio box plots in Figure S2 clearly depicted changed LA oxidation and AA oxidation after NAD⁺ treatment, as shown in the decreased level of 9,10,13-TriHOME/LA, 9,12,13-TriHOME/LA and 13-HODE/LA and increased level of 14,15-DiHETrE/AA. The heatmap results suggested NAD⁺ supplementation causes a downregulated glycolytic activity, upregulated branched chain amino acid metabolism and altered fatty acid oxidation. An activated oxidative phosphorylation in mitochondria can be further indicated by the elevated levels of ATP/AMP, GTP/GMP and decreased level of NADH/NAD⁺ observed upon NAD⁺ treatment for rotenone-treated group (Figure 9). Nevertheless, continuously increased IMP and AA (C20:4, n6) in response to NAD⁺ supplementation and a decreased level in the ratio of NADPH/NADP⁺ in NAD⁺-treated PINK1 mutant group might indicate a potential side effect.

A second heatmap analysis was made for those unique metabolites only found to be changed in the PINK1_rottenone_NAD group (Figure 8F). Leucine, betaine, valine, tyrosine, adenosine, oleic acid (C18:1, n9) and 12-HEPE decreased significantly, changing towards the control PINK1/PINK1_DMSO group level, while NADP⁺, mead acid (MA, C20:3, n9), dihomo-gamma-linolenic acid (DGLA, C20:3, n6) and DPA (C22:5, n6) were found increased significantly, but further away from the control level. An increased utilization of branched chain amino acids matched the aforementioned discovery. However, the results

of a further decreased oxidation of EPA into 12-HEPE/5-HEPE and a further increased MA metabolism were unexpected (Figure S2).

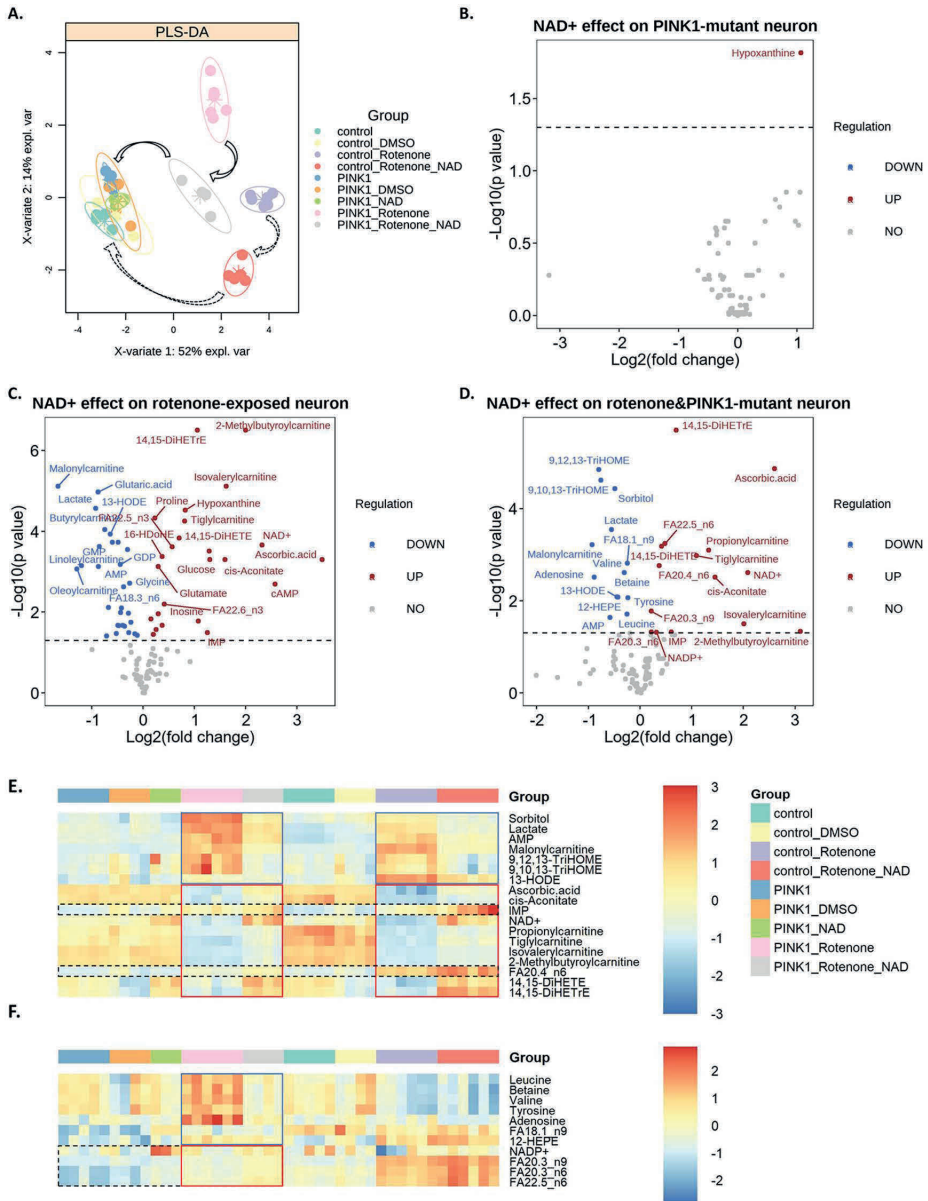


Figure 8. Impacts of NAD⁺ treatment on cellular metabolome in control and PINK1 mutant neurons influenced by rotenone. A. PLS-DA score plot reflecting statistical separation between all perturbation, treatment and control groups. B-D. Volcano plot analysis between PINK1_NAD and PINK1 groups

(B), control_rottenone_NAD and control_rottenone groups (C), PINK1_rottenone_NAD and PINK1_rottenone groups (D) revealing metabolite features increased and decreased by p-value and fold change analysis. Horizontal dashed lines indicate the cutoff p-value of 0.05. Metabolite features marked in red dot represent an increased level, metabolite features marked in blue dot represent a decreased level, and metabolite features marked in grey dot represent no significant difference. E, F. Heatmap profiling for metabolites that were commonly regulated in both NAD⁺-treated control_rottenone group and PINK1_rottenone group (E), and metabolite that were uniquely regulated in NAD⁺-treated PINK1_rottenone group (F).

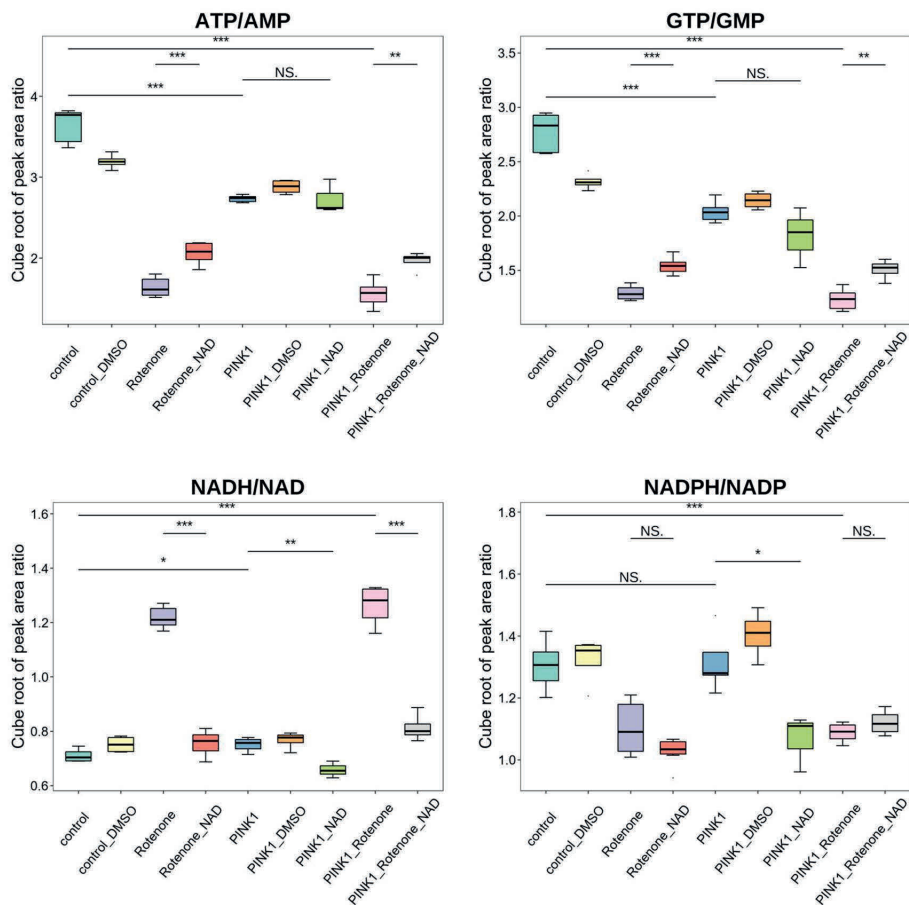


Figure 9. Box plot for showing NAD⁺ treatment regulation on the metabolite ratio level of ATP/AMP, GTP/GMP, NADH/NAD⁺ and NADPH/NADP⁺ for rotenone-treated control group (Rotenone), PINK1-mutant group (PINK1) and rotenone-treated PINK1-mutant group (PINK1_roteneone). Significant differences between groups were marked by * ($p < 0.05$), ** ($p < 0.01$), *** ($p < 0.001$). No significant difference was marked by NS.

Discussion

To date, very few studies were carried out on the human iPSC-derived PD-associated neuron model combined with metabolomic analysis to investigate neurodegenerative metabolism linked to multifactorial etiology. Our study reports the selective metabolomics regulation of human iPSC-derived mid-brain neurons caused by PINK1 mutation, mitochondrial complex I inhibitor (rotenone), and their joint influence. In addition, treatment efficiency via NAD⁺ supplementation was evaluated against in vitro cellular models of mono- and dual-cause interventions. We found similar metabolic dysregulation caused by rotenone and PINK1 mutation seen in reduced energy production and impaired redox balance, as well as differences regarding impaired mitochondrial respiration, anti-oxidative response and neuroinflammation. Neurons with inherent PINK1 mutation showed susceptibility to rotenone stimulation, resulting in more complicated neurodegenerative metabolism. Additionally, they showed insensitive response to NAD⁺ treatment. Considering the common and divergent alterations in metabolic pathways for the rotenone-caused and mutation-caused PD model, dual-cause interventions may play an important role in sporadic PD pathogenesis and might serve as a new strategy for in-vitro drug screening. Energy imbalance has been regarded as a central cause leading to the progression of neurodegeneration and subsequent neuronal death in the brain substantia nigra region [45]. Reflected in the intracellular ATP level from our study, rotenone caused a much more severe and acute shutdown of energy production after 24 h, whereas PINK1 mutation exhibited a long-term and chronic energy deficiency. A high NADH/NAD⁺ ratio can activate pyruvate dehydrogenase kinase (PDK), leading to inhibitory phosphorylation of PDH [46]. Thus, the overall energy supply crisis can be associated with reduced acetyl-CoA utilization in the TCA cycle and an alternation towards upregulated glycolysis. Moreover, the energy deficiency failed to be compensated through branch chain amino acid metabolism and long-chain fatty acid oxidation. Medium-chain fatty acid oxidation might be upregulated for energy supplementation, however, accumulation of acetylcarnitine ultimately reflected its restricted utilization into TCA cycle.

Interestingly, TCA cycle intermediates showed complex disturbances in PINK1 mutation and rotenone-based model. Impaired mitochondrial respiration was revealed by the significantly reduced level found in cis-aconitate, which is a key TCA intermediate converted from citrate by an enzyme of aconitase. Several studies have reported a reduced aconitase activity linking to PINK1 mutation within the striatum of mice, midbrain-specific dopaminergic neurons [47,48]. Our results also found accumulation of several TCA metabolites associated with PINK1 mutation. Accumulated α -ketoglutarate, succinate, fumarate and malate could be fueled by glutamine metabolism in response to the diversion

of pyruvate towards lactate. Similar results were also reported in human iPSC-derived neurons with parkin deficiency, confirmed with ^{13}C -labeled glucose tracing [26]. Besides, an active pyruvate carboxylase through malic enzyme might be triggered by the inhibited PDH activity, which resulted in an elevated level of malate in PINK1-mutant neuron [49]. However, the impact of rotenone completely eliminated the elevated TCA activity in PINK1-mutant neurons (Figure S1). Rotenone is a classic mitochondrial complex I inhibitor that can block the oxidation of NADH to NAD⁺ [50]. To be noted, significantly increased NADH/NAD⁺ ratio levels were observed in both PINK1-mutated and rotenone-treated neurons, though the rotenone effect was more pronounced than the PINK1 mutation (Figure 3). The mitochondrial complex II, also known as succinate dehydrogenase (SDH), catalyzes the oxidation of succinate to fumarate with transferring electrons to the respiratory chain ubiquinone pool [51]. In our study, the increased level of succinate, leading to a consequent decreased ratio of fumarate to succinate, was only observed in the PINK1 mutation-based model, but not in our rotenone-induced neuronal model. Gautier et.al reported a defective functional capacity on mitochondrial complex I and II in PINK1 knockout mice model [47]. Our metabolomics results supported the evidence of complex II deficiencies other than complex I associated with PINK1-mutation in neuronal model. It will be important to better elucidate the mechanism of impaired respiration in both familial and sporadic Parkinson's Disease [52].

The comprehensive metabolic changes measured in energy metabolism subsystems (glycolysis, pentose phosphate pathway, acylcarnitines, and the tricarboxylic cycle, mitochondrial oxidative phosphorylation) strongly explained a mitochondria dysfunction in both rotenone-caused and PINK1 mutation-caused PD neuronal models. Along with impaired mitochondrial respiration, complex I inhibitors also provoke excessive reactive oxygen species (ROS) production [53,54]. Defective antioxidant defense has been reported in many rotenone-induced PD models and leads to severe oxidative damage consequences [55,56]. Our data showed consistent reduced antioxidant levels of glutathione (GSH), ascorbic acid and NADPH/NADP⁺ ratio in the rotenone-affected neuron models, but not in the PINK1 mutant neuronal model. In another study, Testa et.al reported significant increases in oxygen-based free radicals were only observable by a moderate complex I inhibition [57]. Therefore, we believe the effect of PINK1 mutation on complex I inhibition is insufficient to induce severe damage to antioxidant defense. However, the influence of oxidative damage still remained, as supported by the changes found in PUFAs and its oxidized mediators (Figure 5), which could be related to lipid peroxidation shown in both rotenone-caused and PINK1 mutation-caused PD neuronal model. On the one hand, more PUFAs were released from cell membranes through activated phospholipases, as shown in

the significantly increased PUFAs-n3 (GLA, AA) and PUFAs-n6 (EPA). On the other hand, we also observed an increased 13-HODE, which is a reduced hydroxide generated immediately after free-radical-mediated LA oxidation via LOX enzyme and is known for inducing strong pro-inflammatory regulation [58]. In comparison to the overactive peroxidation of LA, the oxidation of other PUFAs (AA, EPA and DHA) generally exhibited a decreased activity in any rotenone-influenced models. Emerging data has demonstrated the beneficial role of 14,15-DiHETrE, an AA-derived oxylipin, in the activation of peroxisome proliferator-activated receptors and exerting anti-inflammatory effects [59,60]. Besides, omega-3 PUFA-derived hydroxy (HEPEs, HDoHEs) and dihydroxy oxylipins (DiHETEs) all showed consistently reduced levels in rotenone-influenced models. Eicosanoids derived from omega-3 PUFA generally have anti-inflammatory effects [61,62]. A recent study demonstrated the ability of EPA/DHA-derived lipid mediators to prevent the reduction in neurogenesis and the increase in neuronal apoptosis and in inflammatory transcription factors induced by pro-inflammatory cytokines [63]. Taken together with our study, these lines of evidence suggest a robust anti-inflammatory and neuroprotective system in the PINK1-mutant model, but a rather severely disturbed system caused by rotenone.

From the metabolomic perspective, NAD⁺ supplementation showed almost no effect on the PINK1 mutant model but wide ameliorations on metabolic dysregulation caused by rotenone toxicity. The mildly boosted mitochondrial biogenesis can be explained by the activated energy compensatory routes through branch chain amino acid metabolism and long-chain fatty acid oxidation, as NAD⁺ is required by both processes as a key cofactor. It also showed ameliorations in the rotenone-induced inflammatory response from pro-inflammatory towards anti-inflammatory. Apart from this, the dual-cause model manifested more unexpected side effects in the PUFAs metabolism, such as decreased EPA-derived HEPEs, increased omega-6 PUFAs and increased oleic acid metabolism into mead acid. To be noted, mead acid is a classic marker for essential fatty acid deficiency in mammalian cell culture [64]. Its presence also suggests an abnormal cell membrane with inadequate supply of AA and DHA, and has the potential consequences of loss of integrity and increased risk of rupture [65]. These unexpected changes can be likely associated with the PINK1 mutation. Overall, the evaluation of NAD treatment proves to have a limited rescuing ability in retrieving energy failure caused by complex I inhibition, but not effective for PINK1 mutant neurons. However, our study has its limitations in exploring NAD⁺ treatment effect only within a 24-hour time range rather than a long-term effect. Future studies can explore the potential prevention benefits for boosting the capacity of neuron against toxin intervention via long-term NAD⁺ or other NAD⁺ precursor supplementation, such as niacin

[66], nicotinamide riboside [67]. In addition, this study was performed based on the PINK1 mutant and gene-corrected hNESc cell lines derived from one patient. A large study involving multiple patients should be performed to validate current discoveries.

Conclusions

In summary, our study elucidated a comprehensive picture of metabolomic dysregulation in an in vitro iPSC-derived neuronal model of PD represented by the PINK1 mutation, mitochondrial complex I inhibitor (rotenone), and joint-factor intervention. Based on the characteristic changes related to energy metabolism and oxidative stress, we clearly address the molecular mechanism of mitochondrial dysfunction in the pathogenesis of PD. Especially with the distinct responses in neuronal antioxidation and inflammation aroused by genome or environmental toxin intervention, the complexity of sporadic PD is further revealed. These findings further support a rising hypothesis, that endogenous PINK1 mutation interacting with exogenous stress can result in converged pathogenetic pathway changes towards parkinsonism. Discoveries in the disturbed pathway changes can help explore more potential therapeutic targets. Moreover, our study targeted the energy decline reflected in the decreased NAD⁺ level. For the first time, our findings showed that supplementing NAD⁺ ameliorated rotenone-related energy defects, but had no effect in the case of PINK1 mutation. Instead, it brought unexpected PUFA dysregulation to the dual-factor group. Future improvements can still be made in regards of utilizing the stable-isotope labeling technique for tracing interesting pathways in order to gain more accurate insights on metabolic flux regulation at a dynamic level.

Acknowledgments

We would like to greatly thank Matthijs Vlasveld and Sylvia Le Dévédec for their support in neuron viability assay. L. Huang would like to thank the financial support from China Scholarship Council (CSC) Grant [No. 201806210057]. This project received funding from the European Union's Horizon 2020 research and innovation programme, for the SysMedPD project, under grant agreement No. 668738, the Dutch National Institutes of Health (ZonMw) TKI-LSH Neuromet project (LSHM18092) and the Dutch Research Council (NWO) 'Investment Grant NWO Large' program, for the 'Building the infrastructure for Exposome re-search: Exposome-Scan' project (No. 175.2019.032).

References

1. Dauer W, Przedborski S. Parkinson's Disease: Mechanisms and Models. *Neuron*. 2003;39:889–909.
2. Kouli A, Torsney KM, Kuan W-L. Parkinson's Disease: Etiology, Neuropathology, and Pathogenesis. Exon Publications. 2018;3–26.
3. Schapira AH, Jenner P. Etiology and pathogenesis of Parkinson's disease. *Movement Disorders*. 2011;26:1049–55.
4. Farrer MJ. Genetics of Parkinson disease: paradigm shifts and future prospects. *Nature Reviews Genetics*. 2006;7:306–18.

5. Bentivoglio AR, Cortelli P, Valente EM, Ialongo T, Ferraris A, Elia A, et al. Phenotypic characterisation of autosomal recessive PARK6-linked parkinsonism in three unrelated Italian families. *Movement Disorders*. 2001;16:999–1006.
6. Valente EM, Brancati F, Caputo V, Graham EA, Davis MB, Ferraris A, et al. PARK6 is a common cause of familial parkinsonism. *Neurol Sci*. 2002;23:s117–8.
7. Reed X, Bandrés-Ciga S, Blauwendraat C, Cookson MR. The role of monogenic genes in idiopathic Parkinson's disease. *Neurobiology of Disease*. 2019;124:230–9.
8. Zhou H, Falkenburger BH, Schulz JB, Tieu K, Xu Z, Xia XG. Silencing of the Pink1 Gene Expression by Conditional RNAi Does Not Induce Dopaminergic Neuron Death in Mice. *Int J Biol Sci*. 2007;3:242–50.
9. Kitada T, Pisani A, Porter DR, Yamaguchi H, Tscherter A, Martella G, et al. Impaired dopamine release and synaptic plasticity in the striatum of PINK1-deficient mice. *Proceedings of the National Academy of Sciences*. Proceedings of the National Academy of Sciences; 2007;104:11441–6.
10. Tanner CM, Kamel F, Ross GW, Hoppin JA, Goldman SM, Korell M, et al. Rotenone, paraquat, and Parkinson's disease. *Environ Health Perspect*. 2011;119:866–72.
11. Martinez TN, Greenamyre JT. Toxin Models of Mitochondrial Dysfunction in Parkinson's Disease. *Antioxid Redox Signal*. 2012;16:920–34.
12. Haque ME, Mount MP, Safarpour F, Abdel-Messih E, Callaghan S, Mazerolle C, et al. Inactivation of Pink1 Gene in Vivo Sensitizes Dopamine-producing Neurons to 1-Methyl-4-phenyl-1,2,3,6-tetrahydropyridine (MPTP) and Can Be Rescued by Autosomal Recessive Parkinson Disease Genes, Parkin or DJ-1. *Journal of Biological Chemistry*. Elsevier; 2012;287:23162–70.
13. Castro IP de, Martins LM, Tufi R. Mitochondrial quality control and neurological disease: an emerging connection. *Expert Reviews in Molecular Medicine*. Cambridge University Press; 2010;12:e12.
14. Holmes E, Wilson ID, Nicholson JK. Metabolic Phenotyping in Health and Disease. *Cell*. Elsevier; 2008;134:714–7.
15. Beger RD, Dunn W, Schmidt MA, Gross SS, Kirwan JA, Cascante M, et al. Metabolomics enables precision medicine: "A White Paper, Community Perspective." *Metabolomics*. 2016;12:149.
16. Lu Z, Wang J, Li M, Liu Q, Wei D, Yang M, et al. (1)H NMR-based metabolomics study on a goldfish model of Parkinson's disease induced by 1-methyl-4-phenyl-1,2,3,6-tetrahydropyridine (MPTP). *Chem Biol Interact*. 2014;223:18–26.
17. Anandhan A, Lei S, Levitsky R, Pappa A, Panayiotidis MI, Cerny RL, et al. Glucose Metabolism and AMPK Signaling Regulate Dopaminergic Cell Death Induced by Gene (α -Synuclein)-Environment (Paraquat) Interactions. *Mol Neurobiol*. 2017;54:3825–42.
18. Tyurina YY, Polimova AM, Maciel E, Tyurin VA, Kapralova VI, Winnica DE, et al. LC/MS analysis of cardiolipins in substantia nigra and plasma of rotenone-treated rats: implication for mitochondrial dysfunction in Parkinson's disease. *Free Radic Res*. 2015;49:681–91.
19. Gao H-C, Zhu H, Song C-Y, Lin L, Xiang Y, Yan Z-H, et al. Metabolic Changes Detected by Ex Vivo High Resolution 1H NMR Spectroscopy in the Striatum of 6-OHDA-Induced Parkinson's Rat. *Mol Neurobiol*. 2013;47:123–30.
20. Shukla AK, Ratnasekhar Ch, Pragya P, Chauhan HS, Patel DK, Chowdhuri DK, et al. Metabolomic Analysis Provides Insights on Paraquat-Induced Parkinson-Like Symptoms in *Drosophila melanogaster*. *Mol Neurobiol*. 2016;53:254–69.
21. Zheng H, Zhao L, Xia H, Xu C, Wang D, Liu K, et al. NMR-Based Metabolomics Reveal a Recovery from Metabolic Changes in the Striatum of 6-OHDA-Induced Rats Treated with Basic Fibroblast Growth Factor. *Mol Neurobiol*. 2016;53:6690–7.
22. Rappley I, Myers DS, Milne SB, Ivanova PT, Lavoie MJ, Brown HA, et al. Lipidomic profiling in mouse brain reveals differences between ages and genders, with smaller changes associated with alpha-synuclein genotype. *J Neurochem*. 2009;111:15–25.
23. Chen X, Xie C, Sun L, Ding J, Cai H. Longitudinal Metabolomics Profiling of Parkinson's Disease-Related α -Synuclein A53T Transgenic Mice. *PLoS One*. 2015;10:e0136612.
24. Baykal AT, Jain MR, Li H. Aberrant regulation of choline metabolism by mitochondrial electron transport system inhibition in neuroblastoma cells. *Metabolomics*. 2008;4:347–56.
25. Lei S, Zavala-Flores L, Garcia-Garcia A, Nandakumar R, Huang Y, Madayiputhiya N, et al. Alterations in energy/redox metabolism induced by mitochondrial and environmental toxins: a specific role for glucose-6-phosphate-dehydrogenase and the pentose phosphate pathway in paraquat toxicity. *ACS Chem Biol*. 2014;9:2032–48.
26. Okarmus J, Havelund JF, Ryding M, Schmidt SI, Bogetoft H, Heon-Roberts R, et al. Identification of bioactive metabolites in human iPSC-derived dopaminergic neurons with PARK2 mutation: Altered mitochondrial and energy metabolism. *Stem Cell Reports*. 2021;16:1510–26.
27. Wang W, Zhao F, Ma X, Perry G, Zhu X. Mitochondria dysfunction in the pathogenesis of Alzheimer's disease: recent advances. *Molecular Neurodegeneration*. 2020;15:30.
28. Fang EF, Lautrup S, Hou Y, Demarest TG, Croteau DL, Mattson MP, et al. NAD⁺ in Aging: Molecular Mechanisms and Translational Implications. *Trends in Molecular Medicine*. 2017;23:899–916.
29. Lautrup S, Sinclair DA, Mattson MP, Fang EF. NAD⁺ in Brain Aging and Neurodegenerative Disorders. *Cell Metabolism*. 2019;30:630–55.
30. Brakedal B, Dölle C, Riemer F, Ma Y, Nido GS, Skeie GO, et al. The NADPARK study: A randomized phase I trial of nicotinamide riboside supplementation in Parkinson's disease. *Cell Metabolism*. 2022;34:396-407.e6.

31. Radenkovic D, Reason, Verdin E. Clinical Evidence for Targeting NAD Therapeutically. Pharmaceuticals (Basel). 2020;13:247.
32. Moreno EL, Hachi S, Hemmer K, Trietsch SJ, Baumuratov AS, Hankemeier T, et al. Differentiation of neuroepithelial stem cells into functional dopaminergic neurons in 3D microfluidic cell culture. *Lab on a Chip*. 2015;15:2419–28.
33. Reinhardt P, Glatza M, Hemmer K, Tsytsyura Y, Thiel CS, Höing S, et al. Derivation and Expansion Using Only Small Molecules of Human Neural Progenitors for Neurodegenerative Disease Modeling. Daadi M, editor. *PLoS ONE*. 2013;8:e59252.
34. Preciat G, Moreno EL, Wegrzyn AB, Willacey CCW, Modamio J, Monteiro FL, et al. Mechanistic model-driven omexometabolic characterisation of human dopaminergic neuronal metabolism [Internet]. *bioRxiv*; 2021 [cited 2022 Oct 15]. p. 2021.06.30.450562.
35. Huang L, Drouin N, Causon J, Wegrzyn A, Castro-Perez J, Fleming R, et al. Reconstruction of Glutathione Metabolism in the Neuronal Model of Rotenone-Induced Neurodegeneration Using Mass Isotopologue Analysis with Hydrophilic Interaction Liquid Chromatography-Zeno High-Resolution Multiple Reaction Monitoring. *Anal Chem*. 2023;95:3255–66.
36. Zazzo A. Signaling lipids as diagnostic biomarkers for ocular surface cicatrizing conjunctivitis. *J Mol Med*. 2020;10.
37. Hosseinkhani F, Huang L, Dubbelman A-C, Guled F, Harms AC, Hankemeier T. Systematic Evaluation of HLIC Stationary Phases for Global Metabolomics of Human Plasma. *Metabolites*. 2022;12:165.
38. Alves RDAM, Dane AD, Harms A, Strassburg K, Seifar RM, Verdijk LB, et al. Global profiling of the muscle metabolome: method optimization, validation and application to determine exercise-induced metabolic effects. *Metabolomics*. 2015;11:271–85.
39. McCann MR, George De la Rosa MV, Rosania GR, Stringer KA. L-Carnitine and Acylcarnitines: Mitochondrial Biomarkers for Precision Medicine. *Metabolites*. 2021;11:51.
40. Jones LL, McDonald DA, Borum PR. Acylcarnitines: role in brain. *Prog Lipid Res*. 2010;49:61–75.
41. Knottnerus SJG, Bleeker JC, Wüst RCI, Ferdinandusse S, IJlst L, Wijburg FA, et al. Disorders of mitochondrial long-chain fatty acid oxidation and the carnitine shuttle. *Rev Endocr Metab Disord*. 2018;19:93–106.
42. Chen W-S, Liu M-H, Cheng M-L, Wang C-H. Decreases in Circulating Concentrations of Short-Chain Acylcarnitines are Associated with Systolic Function Improvement After Decompensated Heart Failure. *International Heart Journal*. 2020;61:1014–21.
43. Liu JJ, Green P, John Mann J, Rapoport SI, Sublette ME. Pathways of polyunsaturated fatty acid utilization: Implications for brain function in neuropsychiatric health and disease. *Brain Research*. 2015;1597:220–46.
44. Radenkovic D, Reason, Verdin E. Clinical Evidence for Targeting NAD Therapeutically. Pharmaceuticals (Basel). 2020;13:247.
45. Blaszczyk JW. The Emerging Role of Energy Metabolism and Neuroprotective Strategies in Parkinson's Disease. *Front Aging Neurosci*. 2018;10:301.
46. Houten SM, Wanders RJA. A general introduction to the biochemistry of mitochondrial fatty acid β -oxidation. *Journal of Inherited Metabolic Disease*. 2010;33:469–77.
47. Gautier CA, Kitada T, Shen J. Loss of PINK1 causes mitochondrial functional defects and increased sensitivity to oxidative stress. *Proceedings of the National Academy of Sciences*. 2008;105:11364–9.
48. Bus C, Zizmare L, Feldkaemper M, Geisler S, Zarani M, Schaedler A, et al. Human Dopaminergic Neurons Lacking PINK1 Exhibit Disrupted Dopamine Metabolism Related to Vitamin B6 Co-Factors. *iScience*. 2020;23:101797.
49. Hassel B. Pyruvate carboxylation in neurons. *Journal of Neuroscience Research*. 2001;66:755–62.
50. Alam M, Schmidt WJ. Rotenone destroys dopaminergic neurons and induces parkinsonian symptoms in rats. *Behavioural Brain Research*. 2002;136:317–24.
51. Rustin P, Munnich A, Rötig A. Succinate dehydrogenase and human diseases: new insights into a well-known enzyme. *Eur J Hum Genet*. Nature Publishing Group; 2002;10:289–91.
52. Plun-Favreau H, Hardy J. PINK1 in mitochondrial function. *Proceedings of the National Academy of Sciences*. 2008;105:11041–2.
53. Sipos I, Tretter L, Adam-Vizi V. Quantitative relationship between inhibition of respiratory complexes and formation of reactive oxygen species in isolated nerve terminals. *J Neurochem*. 2003;84:112–8.
54. Lambert AJ, Brand MD. Inhibitors of the Quinone-binding Site Allow Rapid Superoxide Production from Mitochondrial NADH:Ubiquinone Oxidoreductase (Complex I) *. *Journal of Biological Chemistry*. Elsevier; 2004;279:39414–20.
55. Neely MD, Davison CA, Aschner M, Bowman AB. From the Cover: Manganese and Rotenone-Induced Oxidative Stress Signatures Differ in iPSC-Derived Human Dopamine Neurons. *Toxicol Sci*. 2017;159:366–79.
56. Sherer TB, Betarbet R, Testa CM, Seo BB, Richardson JR, Kim JH, et al. Mechanism of Toxicity in Rotenone Models of Parkinson's Disease. *J Neurosci*. 2003;23:10756–64.
57. Testa CM, Sherer TB, Greenamyre JT. Rotenone induces oxidative stress and dopaminergic neuron damage in organotypic substantia nigra cultures. *Molecular Brain Research*. 2005;134:109–18.
58. Petrovic S, Arsic A, Ristic-Medic D, Cvetkovic Z, Vucic V. Lipid Peroxidation and Antioxidant Supplementation in Neurodegenerative Diseases: A Review of Human Studies. *Antioxidants*. Multidisciplinary Digital Publishing Institute; 2020;9:1128.

59. Gervois P, Fruchart J-C, Delerive P, Staels B. Induction of I κ B α Expression as a Mechanism Contributing to the Anti-inflammatory Activities of Peroxisome Proliferator-activated Receptor- α Activators*. *Journal of Biological Chemistry*. 2000;275:36703–7.
60. Fang X, Hu S, Xu B, Snyder GD, Harmon S, Yao J, et al. 14,15-Dihydroxyecosatrienoic acid activates peroxisome proliferator-activated receptor- α . *American Journal of Physiology-Heart and Circulatory Physiology*. American Physiological Society; 2006;290:H55–63.
61. Kopecky J, Rossmeisl M, Flachs P, Kuda O, Brauner P, Jilkova Z, et al. n-3 PUFA: bioavailability and modulation of adipose tissue function: Symposium on 'Frontiers in adipose tissue biology.' *Proceedings of the Nutrition Society*. Cambridge University Press; 2009;68:361–9.
62. Echeverría F, Ortiz M, Valenzuela R, Videla LA. Long-chain polyunsaturated fatty acids regulation of PPARs, signaling: Relationship to tissue development and aging. *Prostaglandins, Leukotrienes and Essential Fatty Acids*. 2016;114:28–34.
63. Borsini A, Nicolaou A, Camacho-Muñoz D, Kendall AC, Di Benedetto MG, Giacobbe J, et al. Omega-3 polyunsaturated fatty acids protect against inflammation through production of LOX and CYP450 lipid mediators: relevance for major depression and for human hippocampal neurogenesis. *Mol Psychiatry*. Nature Publishing Group; 2021;26:6773–88.
64. Ichi I, Kono N, Arita Y, Haga S, Arisawa K, Yamano M, et al. Identification of genes and pathways involved in the synthesis of Mead acid (20:3n-9), an indicator of essential fatty acid deficiency. *Biochimica et Biophysica Acta (BBA) - Molecular and Cell Biology of Lipids*. 2014;1841:204–13.
65. Crawford MA, Golfetto I, Ghebremeskel K, Min Y, Moodley T, Poston L, et al. The potential role for arachidonic and docosahexaenoic acids in protection against some central nervous system injuries in preterm infants. *Lipids*. 2003;38:303–15.
66. Alisky JM. Niacin improved rigidity and bradykinesia in a Parkinson's disease patient but also caused unacceptable nightmares and skin rash—A case report. *Nutritional Neuroscience*. Taylor & Francis; 2005;8:327–9.
67. Schöndorf DC, Ivanyuk D, Baden P, Sanchez-Martinez A, De Cicco S, Yu C, et al. The NAD⁺ Precursor Nicotinamide Riboside Rescues Mitochondrial Defects and Neuronal Loss in iPSC and Fly Models of Parkinson's Disease. *Cell Reports*. 2018;23:2976–88.

Supplementary Materials

Table S1. Basic information of the control and diseased neural stem cell lines derived from two isogenic iPSC lines

Cell line ID	Cell type	Genotype	Study ID	Clinical diagnosis
GC826	neural stem cell	PINK1, wt/wt	Control (PINK1 gene corrected)	n/a
M826	neural stem cell	PINK1, Q456X/Q456X	PINK1 mutant	affected with Parkinson's disease

Table S2. Detected polar metabolites with ChEBI identifier, retention time and corresponding internal standards

Metabolite	Retention Time (min)	ChEBI ID	Internal standard
Leucine	2.87	25017	DL-LEUCINE-2,3,3-D3
Isoleucine	2.98	24898	DL-LEUCINE-2,3,3-D3
Taurine	3.99	15891	L-ALANINE-d3
Betaine	3.38	17750	Betaine-d9
Asparagine	4.59	22653	L-ASPARAGINE H2O (U-13C4, U15N2)
Tryptophan	2.86	27897	L-TRYPTOPHAN (U-13C11, U15N2)
Glutamine	4.48	28300	L-GLUTAMIC ACID (1,2-13C2)
GABA	3.91	16865	L-2-Aminobutyric acid-d6
Valine	3.35	27266	DL-VALINE-2,3,4,4,5,5-D8
Proline	3.56	26271	DL-VALINE-2,3,4,4,5,5-D8
Histidine	6.70	27570	GLYCINE-2,2-D2
Glycine	4.64	15428	GLYCINE-2,2-D2
Aspartate	4.16	22660	L-ASPARTIC ACID (13C4, 97-99%; D3, 97-99%; 15N, 97-99%)
Threonine	4.29	26986	L-GLUTAMIC ACID (1,2-13C2)
Glutamic acid	4.20	18237	L-GLUTAMIC ACID (1,2-13C2)

Metabolic dysfunction in neurons with PINK1 mutation and rotenone exposure

Alanine	4.33	16449	L-ALANINE-d3
Tyrosine	3.56	18186	DL-VALINE-2,3,4,4,5,5-D8
serine	4.87	17822	GLYCINE-2,2-D2
methionine	3.04	16811	DL-LEUCINE-2,3,3-D3
phenylalanine	2.78	28044	Phenylalanine-d5
Kynurenine	2.77	28683	Phenylalanine-d5
4-hydroxyproline	4.19	20392	DL-VALINE-2,3,4,4,5,5-D8
Glycylglycine	4.57	17201	GLYCINE-2,2-D2
Creatinine	1.80	16737	Creatinine-Nmethyl-D3
Glucose	3.76	17234	D-GLUCOSE-13C6, 99% 13C
Sorbitol	3.56	30911	D-GLUCOSE-13C6, 99% 13C
Glucose-6-P	5.66	14314	D-GLUCOSE-13C6, 99% 13C
Fructose-6-P	4.86	88003	D-GLUCOSE-13C6, 99% 13C
Glucose-1-P	4.84	29042	D-GLUCOSE-13C6, 99% 13C
Ribose-5-P	4.67	78679	D-GLUCOSE-13C6, 99% 13C
Ribulose-5-P	4.24	37455	D-GLUCOSE-13C6, 99% 13C
Fructose-1,6-P2	7.90	78682	D-GLUCOSE-13C6, 99% 13C
Lactate	2.56	42111	13C3-lactate
Pyruvate	1.74	32816	13C3-Pyruvate
α -Ketoglutarate	3.56	30915	SUCCINIC ACID (D4)
2-Hydroxybutyric acid	1.86	1148	13C3-Pyruvate
Malic acid	3.82	25115	AMP-13C10,15N5
Succinic acid	2.84	15741	SUCCINIC ACID (D4)
Fumaric acid	4.06	18012	SUCCINIC ACID (D4)
Ascorbic acid	3.56	22651	AMP-13C10,15N5
cis-Aconitate	3.60	32805	ATP-13C10
Glyceraldehyde-3-P	7.20	17138	UTP-13C9,15N2
Dihydroxyacetone phosphate	4.09	16108	L-ALANINE-d3
glutaric acid	3.51	17859	SUCCINIC ACID (D4)
2-aminoadipic acid	3.46	37024	L-GLUTAMIC ACID (1,2-13C2)
phosphoenolpyruvate	4.88	18021	UTP-13C9,15N2
6-phosphogluconic acid	6.38	48928	ATP-13C10
Acetyl-CoA	4.25	15351	L-GLUTAMIC ACID (1,2-13C2)
AMP	3.89	16027	AMP-13C10,15N5
ADP	5.08	16761	ATP-13C10
ATP	6.55	15422	ATP-13C10
IMP	4.16	17202	AMP-13C10,15N5
GMP	4.78	17345	AMP-13C10,15N5
GDP	6.64	17552	UTP-13C9,15N2
GTP	8.69	15996	ATP-13C10
CTP	7.82	17677	UTP-13C9,15N2
UDP	5.53	17659	UTP-13C9,15N2
UTP	7.12	15713	UTP-13C9,15N2
cAMP	2.84	17489	13C3-lactate
NAD+	4.55	15846	AMP-13C10,15N5
NADH	3.85	16908	AMP-13C10,15N5
NADP+	6.00	18009	UTP-13C9,15N2
NADPH	5.49	16474	UTP-13C9,15N2
Xanthine	1.99	15318	Hypoxanthine-2,8,9-D3
Guanosine	3.00	16750	Hypoxanthine-2,8,9-D3
Adenine	1.32	16708	Creatinine-Nmethyl-D3
Uracil	1.06	17568	Hypoxanthine-2,8,9-D3
Hypoxanthine	1.94	17368	Hypoxanthine-2,8,9-D3
Inosine	2.66	17596	Hypoxanthine-2,8,9-D3
Adenosine	4.23	16335	AMP-13C10,15N5
Uridine	2.13	16704	Hypoxanthine-2,8,9-D3
Glutathione	3.92	16856	L-GLUTAMIC ACID (1,2-13C2)
Oxiglutathione	6.27	167606	ATP-13C10

Table S3. Detected acylcarnitines with ChEBI identifier, retention time and corresponding internal standards

Component Name	Retention Time (min)	ChEBI ID	Internal standard
Acetylcarnitine	0.29	73024	Acetylcarnitine-d3
Butyrylcarnitine	1.22	7676	Butyrylcarnitine-d3
Carnitine	0.39	17126	Carnitine-d3
Choline	0.28	15354	Choline-d3
Deoxycarnitine	0.34	16244	Deoxycarnitine-d3
Linoleylcarnitine	7.77	73072	Octadecanoylcarnitine-d3
Malonylcarnitine	0.30	73028	Acetylcarnitine-d3
Methylmalonylcarnitine	0.31	73031	Butyrylcarnitine-d3
Oleoylecarnitine	8.25	72689	Octadecanoylcarnitine-d3
Propionylcarnitine	0.52	28867	Acetylcarnitine-d3
Tiglylcarnitine	1.75	71179	Butyrylcarnitine-d3
Isovalerylcarnitine	2.05	73025	Butyrylcarnitine-d3
2-Methylbutyrylcarnitine	1.98	73026	Butyrylcarnitine-d3

Table S4. Detected signaling lipids with ChEBI identifier, retention time and corresponding internal standards

Metabolite	Retention time (min)	ChEBI ID	Internal standard
ASL_FA18.0	14.08	28842	BSL_d17_FA18.1_w9_ISTD
BSL_FA18.1_w9	13.81	16196	BSL_d17_FA18.1_w9_ISTD
BSL_FA18.2_w6	13.48	17351	BSL_d4_FA18.2_w6_ISTD_2
BSL_FA18.3_w3	13.17	27432	BSL_d5_FA22.6_w3_ISTD
BSL_FA20.4_w6	13.42	15843	BSL_d8_FA20.4_w6_ISTD
BSL_FA20.5_w3	13.13	28364	BSL_d5_FA22.6_w3_ISTD
BSL_FA22.4_w6	13.73	53487	BSL_d17_FA18.1_w9_ISTD
BSL_FA22.5_w3	13.48	61204	BSL_d5_FA22.6_w3_ISTD
BSL_FA22.6_w3	13.35	28125	BSL_d5_FA22.6_w3_ISTD
BSL_FA18.3_w6	13.21	28661	BSL_d5_FA22.6_w3_ISTD
BSL_FA20.3_w6	13.6	53486	BSL_d4_FA18.2_w6_ISTD_2
BSL_FA20.3_w9	13.68	72865	BSL_d17_FA18.1_w9_ISTD
BSL_FA22.5_w6	13.58	61204	BSL_d4_FA18.2_w6_ISTD_2
BSL_a_LEA	11.57	89605	BSL_d4_LEA_ISTD
BSL_POEA	12.06	71465	BSL_d4_OEA_ISTD
BSL_LEA	12.73	64032	BSL_d4_LEA_ISTD
BSL_PEA	13.12	71464	BSL_d4_PEA_ISTD
BSL_1_OG_2_OG	13.55	30916	BSL_d4_OEA_ISTD
BSL_SEA	13.67	85299	BSL_d3_SEA_ISTD
BSL_OEA	13.27	71466	BSL_d4_OEA_ISTD
BSL_9_12_13_TriHOME	3.68	34506	BSL_d4_PGF2a_ISTD
BSL_9_10_13_TriHOME	3.87	34499	BSL_d4_PGF2a_ISTD
BSL_14_15_DiHETE	8.72	88459	BSL_d11_14_15-DiHETrE_ISTD
BSL_12_13_DiHOME	8.95	72665	BSL_d4_12_13_DiHOME_ISTD
BSL_14_15_DiHETrE	9.5	63966	BSL_d11_14_15-DiHETrE_ISTD
BSL_11_12_DiHETrE	9.8	63969	BSL_d11_14_15-DiHETrE_ISTD
BSL_9_HOTrE	9.97	72625	BSL_d4_9_HODE_ISTD
BSL_20_HETE	10.35	34306	BSL_d6_20_HETE_ISTD
BSL_12_HEPE	10.48	72645	BSL_d8_12_HETE_ISTD
BSL_9_HEPE	10.56	89570	BSL_d8_12_HETE_ISTD
BSL_13_HODE	10.7	72639	BSL_d4_9_HODE_ISTD
BSL_12_13_EpOME	11.95	38229	BSL_d4_12_13_DiHOME_ISTD
BSL_5_HEPE	10.73	72627	BSL_d4_9_HODE_ISTD
BSL_9_HODE	10.78	72651	BSL_d4_9_HODE_ISTD
BSL_9_10_EpOME	12.32	34494	BSL_d4_9_10_DiHOME_ISTD
BSL_16_HDoHE	11.08	72613	BSL_d8_12_HETE_ISTD
BSL_8_HDoHE	11.72	72610	BSL_d8_12_HETE_ISTD
BSL_5_HETrE	12.89	88359	BSL_d8_5_HETE_ISTD

Table S5. Metabolites found with regulation after NAD⁺ treatment

5.1 Comparison of control_Rotenone_NAD versus control_Rotenone group			
Metabolite	Log2_FoldChange	-Log10 (p value with Bonferroni correction)	Relative regulation
GABA	0.30	1.96	UP
Proline	0.23	4.33	UP
Glycine	-0.26	2.72	DOWN
Aspartate	0.15	1.83	UP
Glutamate	0.30	3.13	UP
4-Hydroxyproline	-0.11	1.43	DOWN
Glycylglycine	-0.16	1.46	DOWN
Glucose	1.30	3.30	UP
Sorbitol	-0.30	3.55	DOWN
Fructose-1,6-P2	-0.42	2.10	DOWN
Lactate	-0.92	4.57	DOWN
2-Hydroxybutyric.acid	-0.52	1.47	DOWN
Ascorbic.acid	3.49	3.30	UP
AMP	-0.87	3.13	DOWN
ADP	-0.40	1.67	DOWN
IMP	1.25	1.50	UP
GMP	-0.85	3.62	DOWN
GDP	-0.44	3.18	DOWN
CTP	0.26	1.57	UP
cAMP	2.57	2.70	UP
Xanthine	-0.36	1.65	DOWN
Guanosine	-0.71	1.41	DOWN
Hypoxanthine	0.82	4.53	UP
Inosine	1.07	1.78	UP
Uridine	-0.44	1.99	DOWN
cis-Aconitate	1.60	3.30	UP
Glyceraldehyde-3-P	-0.49	1.67	DOWN
Glutaric.acid	-0.87	4.97	DOWN
UDP	-0.47	1.67	DOWN
NAD ⁺	2.32	3.66	UP
Acetylcarnitine	-0.28	1.49	DOWN
Butyrylcarnitine	-0.75	4.05	DOWN
Choline	-0.24	1.75	DOWN
Malonylcarnitine	-1.66	5.12	DOWN
Oleoylcarnitine	-1.29	3.07	DOWN
Propionylcarnitine	1.29	3.51	UP
Tiglylcarnitine	0.81	4.25	UP
Isovalerylcarnitine	1.62	5.12	UP
2-Methylbutyroylcarnitine	2.00	6.50	UP
Deoxycarnitine	-0.67	2.12	DOWN
Linoleylcarnitine	-1.20	3.15	DOWN
FA20.4_n6	0.37	1.67	UP
FA20.5_n3	0.20	1.45	UP
FA22.5_n3	0.57	3.61	UP

FA22.6_n3	0.41	2.20	UP
FA18.3_n6	-0.38	2.63	DOWN
9,12,13-TriHOME	-0.60	3.73	DOWN
9,10,13-TriHOME	-0.49	3.73	DOWN
14,15-DiHETE	0.70	3.83	UP
14,15-DiHETrE	1.06	6.50	UP
20-HETE	-0.28	1.97	DOWN
13-HODE	-0.64	3.93	DOWN
16-HDoHE	0.37	3.37	UP

5.2 Comparison of PINK1_Rotenone_NAD versus PINK1_Rotenone group

Metabolite	Log2_FoldChange	-Log10 (p value with Bonferroni correction)	Relative regulation
Leucine	-0.25	1.71	DOWN
Betaine	-0.30	2.61	DOWN
Valine	-0.31	2.61	DOWN
Tyrosine	-0.23	2.07	DOWN
Sorbitol	-0.49	4.43	DOWN
Lactate	-0.55	3.54	DOWN
Ascorbic.acid	2.60	4.86	UP
AMP	-0.58	1.64	DOWN
IMP	0.60	1.32	UP
Adenosine	-0.88	2.51	DOWN
cis-Aconitate	1.45	2.51	UP
NAD+	2.09	2.61	UP
NADP+	0.32	1.32	UP
Malonylcarnitine	-0.93	3.22	DOWN
Propionylcarnitine	1.33	3.10	UP
Tiglylcarnitine	1.10	2.98	UP
Isovalerylcarnitine	2.01	1.50	UP
2-Methylbutyroylcarnitine	3.10	1.34	UP
FA18.1_n9	-0.25	2.81	DOWN
FA20.4_n6	0.37	2.76	UP
FA20.3_n9	0.22	1.77	UP
FA20.3_n6	0.22	1.32	UP
FA22.5_n6	0.48	3.24	UP
9,12,13-TriHOME	-0.80	4.84	DOWN
9,10,13-TriHOME	-0.75	4.61	DOWN
14,15-DiHETE	0.42	3.18	UP
14,15-DiHETrE	0.70	5.70	UP
13-HODE	-0.45	2.08	DOWN
12-HEPE	-0.43	2.08	DOWN

5.3 Comparison of PINK1_NAD versus PINK1 group

Metabolite	Log ₂ FoldChange	-Log ₁₀ (p value with Bonferroni correction)	Relative regulation
Hypoxanthine	1.06	1.82	UP

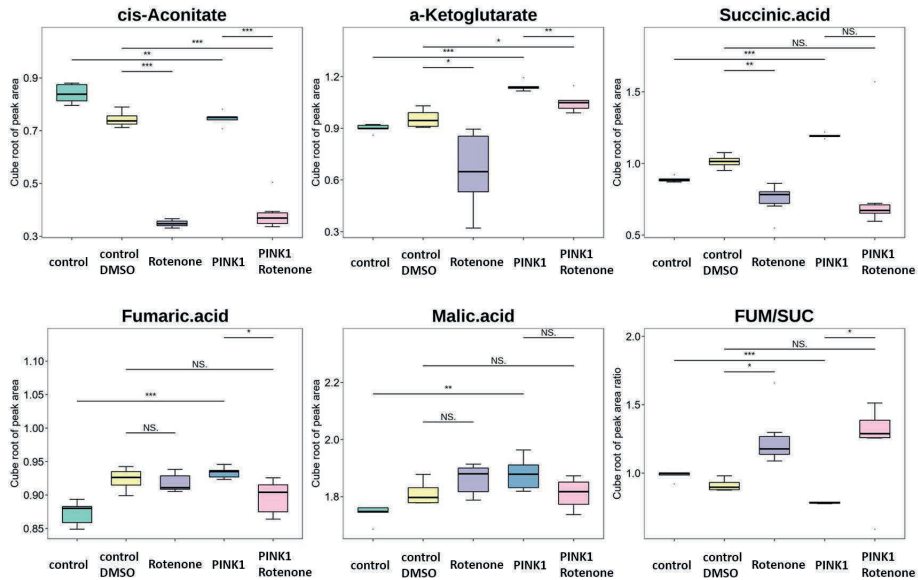


Figure S1. Metabolite changes representing TCA cycle metabolism changes in control and PINK1 mutated neuron influenced by rotenone. Box plot for showing the levels of TCA cycle intermediates in control groups (control and control_DMSO), rotenone-treated control group (Rotenone), PINK1-mutated group (PINK1) and rotenone-treated PINK1-mutated group (PINK1_Rotenone). Significant difference between group comparison was marked by * ($p < 0.05$), ** ($p < 0.01$), *** ($p < 0.001$). No significant difference was marked by NS.

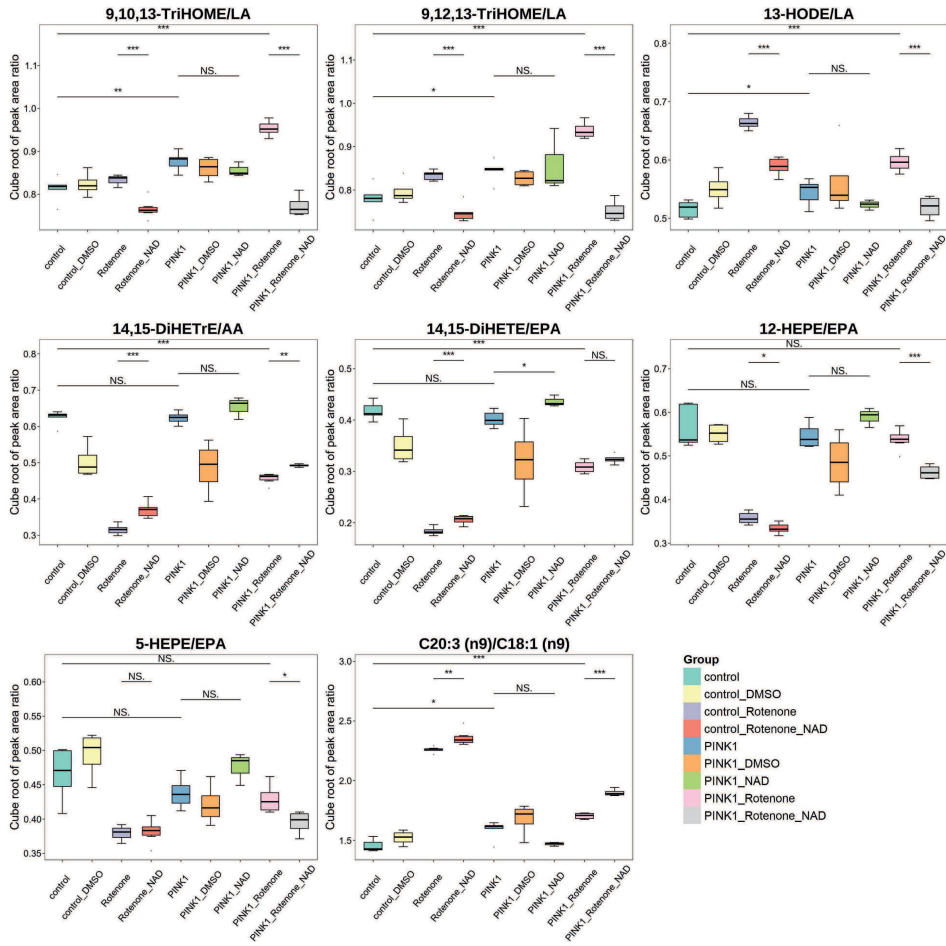


Figure S2. Box plot for showing NAD⁺ treatment regulation on the metabolite ratio level of poly unsaturated fatty acid oxidation for rotenone-treated control group (Rotenone), PINK1-mutated group (PINK1) and rotenone-treated PINK1-mutated group (PINK1_rotenone). Significant difference between group comparison was marked by * (p < 0.05), ** (p < 0.01), *** (p < 0.001). No significant difference was marked by NS.

Chapter 4:

Reconstruction of glutathione metabolism in neuronal model of rotenone-induced neurodegeneration using mass isotopologue analysis with HILIC-Zeno MRM^{HR}

Based on:

Luojiao Huang, Nicolas Drouin, Jason Causon, Agnieszka Wegrzyn, Jose Castro-Perez, Ronan Fleming, Amy Harms, and Thomas Hankemeier*

Reconstruction of Glutathione Metabolism in the Neuronal Model of Rotenone-Induced Neurodegeneration Using Mass Isotopologue Analysis with Hydrophilic Interaction Liquid Chromatography-Zeno High-Resolution Multiple Reaction Monitoring

Analytical Chemistry 2023; DOI: 10.1021/acs.analchem.2c04231

Abstract

Accurate reconstruction of metabolic pathways is an important prerequisite for interpreting metabolomics changes and understanding the diverse biological processes in disease models. A tracer-based metabolomics strategy utilizes stable isotope-labeled precursors to resolve complex pathways by tracing the labeled atom(s) to downstream metabolites through enzymatic reactions. Isotope enrichment analysis is informative and achieved by counting total labeled atoms and acquiring the mass isotopologue distribution (MID) of the intact metabolite. However, quantitative analysis of labeled metabolite substructures/moieties (MS^2 fragments) can offer more valuable insights into the reaction connections through measuring metabolite transformation. In order to acquire the isotopic labeling information at the intact metabolite and moiety level simultaneously, we developed a method that couples hydrophilic interaction liquid chromatography (HILIC) to Zeno trap-enabled high-resolution multiple reaction monitoring (MRM^{HR}). The method enabled accurate and reproducible MID quantification for intact metabolites as well as their fragmented moieties, with notably high sensitivity in the MS^2 fragmentation mode based on the measurement of ^{13}C or ^{15}N -labeled cellular samples. The method was applied to human induced pluripotent stem cell-derived neurons to trace the fate of $^{13}C/^{15}N$ atoms from $D-^{13}C_6$ -glucose/ $L-^{15}N_2$ -glutamine added to the media. With the MID analysis of both intact metabolites and fragmented moieties, we validated the pathway reconstruction of de novo glutathione synthesis in mid-brain neurons. We discovered increased glutathione oxidization from both basal and newly synthesized glutathione pools under neuronal oxidative stress. Furthermore, the significantly decreased de novo glutathione synthesis was investigated and associated with altered activities of several key enzymes, as evidenced by suppressed glutamate supply via glucose metabolism and a diminished flux of glutathione synthetic reaction in the neuronal model of rotenone-induced neurodegeneration.

Introduction

A metabolic network is a (sub)set of metabolic biochemical reactions known to take place in a living organism.¹ Metabolomics studies quantitative changes in metabolite levels and can provide valuable insights into the understanding of disease origin, progression and prognosis, as well as the effects and mechanism of pharmacological interventions.^{2,3} Metabolomics studies of Parkinson's disease (PD) have suggested that energetic failure and increased oxidative stress are significant metabolic hallmarks in the neurodegeneration process.^{4,5} However, metabolic network robustness poses a challenge to the identification of pathway activities in response to perturbations^{6,7} because changes in metabolite consumption and production may not be accompanied by metabolite concentration changes. It is also difficult to distinguish between de novo synthesis and recycling of the existing metabolite pool, which reflects the activity of different metabolic pathways.

Isotope tracing techniques allow one to trace the incorporation of heavy atoms (stable or radioactive⁸) into downstream intermediates from a given labeled precursor. It is an excellent way to monitor pathway activity and has been successfully applied to different levels of organism studies, such as ex-vivo tissues,^{9,10} in-vivo animal models⁹⁻¹¹ and in-vitro cellular culture¹². Mass spectrometry (MS) has become the principal technique used for the analysis of stable isotope-labeled metabolites. It requires only a small amount of sample, manifests excellent detection sensitivity, and can provide structural information on multiple compounds simultaneously. Labeled distributions of intact molecules can be obtained via MS measurements, which consist of a set of mass isotopologue abundances. Mass isotopologue distribution (MID) analysis at the MS¹ level has been generally used in tracer-based metabolomics studies for tracing labeled enrichment through intermediates and probing pathway activity.¹³⁻¹⁶ Subsequently, more attention has been paid to acquiring substructural information on labeled isotopologues and improving metabolic flux interpretation.^{17,18}

Tandem MS-based approaches, using multiple reaction monitoring (MRM), can reveal the isotope labeling states of selected precursor and product ions by including all possible combinations in the transition pairs.^{9,19-21} This method is popular for achieving good performance in metabolite quantification. However, it still shows technical drawbacks in measuring stable isotope-labeled metabolites in a broader metabolomic scope. The number of transition pairs considerably increases with an increasing metabolite atom number, leading to a longer cycle time and fewer data points per peak, as well as less accurate quantification and lower sensitivity for low-abundance isotopologues. In the case for phosphorylated metabolites, compared to PO₃⁻ or H₂PO₄⁻ ions, carbon-containing product ions carry more structural information and are more useful for atom tracing over intersecting

pathways. However, they are generally in very low abundance, which requires a longer dwell time for each transition pair to reach good sensitivity.²²

To overcome these difficulties, advanced tandem MS-based approaches have been developed recently. The MRM methods on triple quadrupole instruments with dynamic modification of the mass filter resolution for precursor or product ions can effectively minimize total MRM transitions, enabling the detection of intact and fragmented metabolite isotopologues with good quantification accuracy in two separate runs.²² Based on a quadrupole linear ion trap instrument, a new liquid chromatography (LC)–mass spectrometry (MS)/MS acquisition method, and a novel isotope recapitulation algorithm (MID Max), the coverage of intact and fragmented metabolite isotopologues has been further extended by combining MRM and an enhanced data-dependent product ion scan type in a single run.²³ Parallel reaction monitoring (PRM) based on high-resolution MS was able to obtain intact and fragmented isotopologue distributions in high resolution within a single analytical run, resulting in a significantly lower cycle time compared to MID Max.²⁴ Other tandem MS-based approaches in high resolution via data-independent acquisition techniques are also available, such as SWATH fragmentation over stacked mass isolation windows on a QqTOF MS²⁵⁻²⁷ and all-ion fragmentation within a wide, predefined mass window on an Orbitrap Fusion Tribrid MS²⁸. When using the SWATH technique, erroneous MID quantification was found for precursors positioned on the margins of two neighboring windows.²⁶ This requires special attention to properly design Q1 isolation windows for target metabolite quantification. Jaiswal et al. suggested employing two different SWATH programs to achieve good MID quantifications corresponding to 19 intermediate metabolites by ensuring all precursor isotopologues fall into a single window in one of the programs.^{26,29} Compared to PRM, the co-fragmentation of all isotopologues of certain metabolite in a single mass window showed higher sensitivity in quantifying precursor and fragment isotopologues of low abundance.²⁹ However, there is no direct spectral connection between a precursor and its corresponding fragments, making it difficult to determine the detailed positioning of labeled atoms within a particular precursor isotopologue. This type of tandem isotopologue distribution, to be noted, has shown strong benefits for improving metabolic flux analysis.^{30,31}

Metabolic pathway reconstruction of central carbon metabolism and its connected *de novo* synthesis pathways is critical for understanding the consecutive reaction changes from energy failure towards oxidative stress in Parkinson's disease. Therefore, to facilitate reconstructing metabolite transformations along these pathways and offer a comprehensive picture of metabolic regulation using both intact and fragmented metabolite isotopologues, we need high-sensitivity detection, but also high data quality for structural elucidation of

the MS² spectra. In this work, we present hydrophilic interaction liquid chromatography (HILIC)–multiple reaction monitoring (MRM^{HR}) using Zeno trap pulsing, a recently introduced system of trapping fragment ions prior to the time-of-flight (TOF) injection. This method combines the advantages of HILIC for wide coverage of polar metabolome analysis and the Zeno trap-enabled technique for duty cycle improvement.³² We compared the performance of the Zeno method to that of the SWATH method and MRM^{HR} (general PRM) with regards to the aspects of sensitivity, accuracy, and fragmentation reproducibility in MID analysis. We further applied the HILIC-Zeno MRM^{HR} method to a classic neuronal model of rotenone-induced neurodegeneration and revealed diverse flux regulations via glucose and glutamine metabolism into glutathione metabolism related to neurodegeneration.

Materials and methods

1. Chemicals and reagents

Standards were purchased from Sigma-Aldrich (Zwijndrecht, The Netherlands) and Fluka (Seelze, Germany). The tracer substances D-¹³C₆-Glucose (99% isotopic purity) and L-¹⁵N₂-glutamine (98% isotopic purity) were purchased from Cambridge Isotope Laboratories (Tewksbury, MA, USA). Acetonitrile in LC-MS grade and chloroform in HPLC grade were purchased from Biosolve B.V. (Valkenswaard, The Netherlands). Methanol in Ultra-LC-MS grade was purchased from ActuaAll (Oss, The Netherlands). Milli-Q Ultra-pure water was obtained from a Merck Milli-pore A10 purification system (Raleigh, USA). Ammonium formate (≥99.995% trace metals basis) and rotenone were purchased from Sigma-Aldrich (Zwijndrecht, The Netherlands). Ammonium hydroxide (28-30 wt% solution of ammonia in water) was purchased from Acros Organics (Geel, Belgium).

2. Standard solutions and cell culture medium

Individual stock solutions of 40 standards were made with 50% MeOH or pure water in 1 mg/mL and stored in -80 °C (Table S1). Mixed standard solutions were prepared at the concentrations of 20, 15, 10, 7.5, 5.0, 2.5, 1.25, 0.5 and 0.1 µg/mL with 50% MeOH as the dilution solution. According to an adapted protocol from Reinhardt,^{33,34} a basal neuron culture medium, N2B27, was made by mixing equal amounts of neurobasal medium (Invitrogen/Life Technologies) and Dulbecco's modified Eagle's medium/F12 medium (Invitrogen/Life Technologies) and adding with 1% penicillin/streptomycin (Life Technologies), 2 mM L-glutamine (Life Technologies), 1:100 B27 supplement without vitamin A (Life Technologies) and 1:200 N2 supplement (Life Technologies). Maintenance medium was made of high-glucose N2B27 medium supplemented with 150 µM ascorbic acid (Sigma Aldrich), 0.5 µM PMA (Enzo Life Sciences) and 3 µM CHIR (Axon Medchem). Differentiation medium was made of high-glucose N2B27 medium supplemented with 200

μM ascorbic acid, 0.01 ng/ μL BDNF (PeproTech), 0.01 ng/ μL GDNF (PeproTech), 0.001 ng/ μL TGF β -3 (PeproTech), 2.5 μM dbcAMP (Sigma-Aldrich), and 1 μM PMA (absent after 6 days of differentiation).

^{13}C labeled maintenance medium and differentiation medium were made by replacing 20.4 mM glucose with the same amount of D- $^{13}\text{C}_6$ -glucose so that the pool size of glucose remains the same. ^{15}N labeled maintenance medium and differentiation medium were made by replacing 2 mM glutamine with the same amount of L- $^{15}\text{N}_2$ -glutamine so that the pool size of glutamine remains the same.

3. Cell culture

For method development and evaluation, the iPSCs-derived human neuroepithelial stem cells (hNESCs) were cultured on a 12-well plate at a density of 300,000 cells/well. Five wells of hNESCs were incubated with maintenance medium containing D- $^{13}\text{C}_6$ -glucose, and another five wells of hNESCs were incubated with maintenance medium containing L- $^{15}\text{N}_2$ -glutamine. Two wells of hNESCs were incubated with normal maintenance medium. The incubation time was 24 h. The ^{13}C and ^{15}N -labeled cellular samples were used as labeled reference samples for method evaluation.

Next, for method application, hNESCs were cultured and differentiated into mid-brain neurons on a 12-well plate at a density of 180,000 cells/well by following the established protocol.^{33,34} After 21 days of neuron differentiation and maturation, we switched the normal differentiation medium into ^{13}C or ^{15}N -labeled differentiation medium. In the ^{13}C -labeling culture with D- $^{13}\text{C}_6$ -glucose ($^{13}\text{C}_6$ -Gluc), five replicates of labeled neuron culture were designed for the healthy group and the rotenone (200 nM) exposure group, respectively, and were accompanied by one unlabeled neuron culture within each group. The same sample design was applied in the ^{15}N labeling culture with L- $^{15}\text{N}_2$ -glutamine ($^{15}\text{N}_2$ -Gln). Differentiated neurons were under incubation with tracers for 24 h and reached isotopic labelling stationarity in metabolites. For cell quenching, ice cold 200 μL of 80% MeOH was added immediately after removing the spent medium and washing with phosphate buffered saline (Gibco/Life Technologies). The quenched cell samples were harvested into a new Eppendorf tube. Cellular samples were fast frozen into liquid nitrogen and stored in the $-80\text{ }^\circ\text{C}$ freezer until LC-MS measurement. Results from unlabeled neurons were used for qualitative peak confirmation during data analysis.

4. Sample preparation

Cell samples were lysed with sonication after one freeze-thaw cycle, vortexed and then centrifuged at 16000 g $4\text{ }^\circ\text{C}$ for 10 min. Cell pellets were collected to measure the protein content using a bicinchoninic acid assay (Thermo Fisher Scientific Inc, United State). Supernatants were transferred into clean 1.5 mL Eppendorf tubes and evaporated to dryness

in a Labcono SpeedVac (MO, United State). Each sample was reconstituted with 60 μL ice-cold methanol/water (80%/20%; v/v). 50 μL of the reconstitution volume was collected and transferred into a new Eppendorf tube. The leftover volume was pooled together as a quality control (QC) sample for each group. Next the reconstituted samples and QC samples were processed with liquid-liquid extraction by adding 40 μL of ice-cold methanol/water (80%/20%; v/v), 45 μL of ice-cold Milli-Q water, and 65 μL of ice-cold chloroform, then followed with mixing and vortexing for 5 min and centrifuging at 16000 g 4 °C for 10 min. 130 μL of the aqueous phase was transferred into a new Eppendorf tube and extracted again by adding 25 μL of ice-cold methanol/water (50%/50%; v/v) and 65 μL of ice-cold chloroform, then followed with mixing and vortexing for 5 min and centrifuging at 16000 ref, 4 °C for 10 min. Finally, 140 μL of the aqueous phase was transferred and taken to dryness. The residue was reconstituted with 50 μL of ice-cold methanol/water (50%/50%; v/v) as the final injection solution for LC-MS measurement. A series of diluted reference samples was prepared by diluting the ^{13}C -labeled reference sample twofold (DF_2x) and threefold (DF_3x) with the injection solvent of methanol/water (50%/50%; v/v).

5. LC-MS measurement

Chromatographic separation was performed using the SeQuant ZIC-c HILIC HPLC column (2.1mm x 100 mm, 3.0 μm , Merck, Darmstadt, Germany) on a Shimadzu Nexera Ultra high-performance liquid chromatograph (LC) (Duisburg, Germany). The LC method was adapted from a previously described method.³⁵ Mobile phase A consists of 90% acetonitrile, 10% water with 5 mM ammonium formate, and mobile phase B consists of 10% acetonitrile, 90% water with 5 mM ammonium formate. The injection volume was 3 μL . The flow rate was 0.5 mL/min and the gradient was as follows: 0 min-0% B, 2 min-15% B, 5 min-21% B, 7.5 min-26% B, from 10 to 11 min-40% B, from 11.5 to 18 min-0% B. The MS analyses were performed on a SCIEX ZenoTOF 7600 system (Darmstadt, Germany) with TwinSpray Turbo V ion source and operated in negative electrospray ionization. The following ion source parameters were applied: a spray voltage of 4.5 kV, a capillary temperature of 400 °C, ion source gas 1 of 20 psi, ion source gas 2 of 50 psi, curtain gas of 25 psi, CAD gas of 7 psi.

A SWATH acquisition method was able to fragment all isotopologues within stacked mass windows over the chromatographic run. Each MS cycle starts with a survey TOF MS scan in 100 ms from 50 to 700 Da using declustering potential (DP) at -80 eV and collision energy (CE) at -5 eV, followed by a fixed Q1 isolation window setting. The Q1 isolation strategy covered a mass range of m/z 60-690 with a 40 Da window width for Q1 isolation (overlap 1 Da). It allowed all possible isotopologues of each target metabolite to be fragmented in the same window. The SWATH scan accumulation time was 85 ms and each

cycle time was 1.576 s, using DP at -80 eV and CE at -30 eV \pm 20 eV. We also tested additional SWATH window settings where the targeted isotopologues fell in two adjacent windows. The curated window settings can be seen in the supporting information, Table S2 and Figure S1.

The MRM^{HR} acquisition method consisted of the same TOF MS scan applied in the SWATH acquisition method, followed by MS/MS scans of the inclusion precursors with unit Q1 isolation and scheduled retention times. The targeted precursors are different for ¹³C and ¹⁵N-labeled sample analysis. Based on the measurement of ¹³C and ¹⁵N-labeled reference cell samples, in total, 180 precursor ions from 25 metabolites were targeted in the ¹³C-labeling MRM^{HR} acquisition method, and 55 precursor ions from 15 metabolites were targeted in the ¹⁵N-labeling MRM^{HR} acquisition method (Table S3-4). DP at -80 eV and CE at -30 eV \pm 20 eV were applied to all precursor ions to have a fair comparison to SWATH acquisition. The Zeno MRM^{HR} acquisition method was designed based on the MRM^{HR} acquisition method and set with the Zeno-trap on-demand above the collision-induced dissociation intensity threshold of 2000 cps.

6. Data analysis

Qualitative data analysis was performed using the SCIEX OS Explorer processing tool. The fragmentation behavior analysis used the online database Metlin³⁶ and mzCloud (<https://www.mzcloud.org/>) as references and was confirmed with our in-house MS² database using analytical standards (see supporting information). Quantitative data analysis was performed using the SCIEX OS Analytics processing tool. The peak areas of metabolite isotopologues in the MS¹ and MS² levels were integrated and further corrected for the natural stable isotope abundance using software IsoCor.³⁷ MID represent the relative abundance of different mass isotopologues and are reported as isotopologue fractions. The ¹³C/¹⁵N enrichment refers to the mean content of isotopic tracer in the metabolite. It was calculated by the formula $ME = (\sum_{i=1}^n Mi * i)/n$, where Mi is the proportion of isotopologues with i ¹³C atoms for a metabolite containing n carbon atoms. Tandem MID analysis was calculated based on the primary MID and further applied with the secondary distribution ratio of isotopomers.

Results and discussion

To meet the study goal of capturing both intact and fragment-labeled isotopologue distributions of metabolites, we developed a MS/MS quantification method based on Zeno MRM^{HR} acquisition coupled to a HILIC separation method. Given the fact that a high number of transitions results in fewer scan points for each transition in the same retention time window, we first optimized the mobile phase gradient of a previously developed HPLC method utilizing a ZIC-c HILIC column for polar metabolite analysis.

1. HILIC-Zeno MRM^{HR} method development

In total, 40 polar metabolites derived from primary carbon metabolism, glutathione metabolism, and purine and pyrimidine metabolism achieved good chromatographic separation for standard solutions (Table S1, Figure S2). For the HILIC-Zeno MRM^{HR} method, 25 selected metabolites including all possible isotopic states were included in the ¹³C-labeling MS² fragmentation method, and 15 metabolites including all possible isotopic states were included in the ¹⁵N-labeling MS² fragmentation method. The selected metabolites were critical intermediates in their relevant metabolic pathway and were detected in labeled states with a TOF MS scan in the reference ¹³C (¹⁵N) cellular sample set. Finally, for metabolites eluting at retention times between 4 and 6 min, where the peak density is the highest, the method ensured a minimum of eight scan points across chromatographic peaks at the base (Figure S3). Under both MS¹ and MS² levels, the method exhibited good linearity for targeted metabolites, with correlation coefficients mostly above 0.99 (Table S5).

With proper isolation window settings, SWATH methods have been reported for MID quantification of targeted metabolites and their fragments with good sensitivity and small error.²⁶ To confirm the impact of entire or partial isotopologue coverage in one Q1 window, as well as the impact of overlapping windows offering partial isotopologue coverage, several SWATH acquisition methods with various mass window settings were evaluated. Our results showed that the quantification of isotopologues that span two windows suffers from peak intensity loss and reduced fidelity (Figure S1). As a reference method for our subsequent method comparisons, we selected a SWATH method with a fixed Q1 isolation window to encompass the intact MID of target metabolites.

2. Evaluation of sensitivity and isotope fidelity

Next, we evaluated the HILIC-Zeno MRM^{HR} method on the quantification performance for precursor and fragment isotopologues and compared these to the HILIC-MRM^{HR} and HILIC-SWATH methods. As shown in **Figure 1**, in the MS¹ TOF level, minor differences in the peak area were detected because of the slight differences in MS scan cycle duration between SWATH, Zeno MRM^{HR} and MRM^{HR} methods. Whereas in the MS² level, a significant signal improvement with the Zeno MRM^{HR} method was observed for all fragment and residual precursor isotopologues in comparison to SWATH and MRM^{HR} methods. The Zeno trap enables almost 100% duty cycle in MS/MS, resulting in signal gains without loss of mass accuracy or resolution.³⁸ The Zeno trap method improved the signal for fragment ions more than for their precursor ion, mostly because of a higher Zeno pulsing gain for lower masses. In comparison to SWATH, the ¹³C-glutamate precursor increased 4.9-fold, while its fragment increased 7.8-fold; the ¹³C-glutathione precursor

increased 4.7-fold, and its fragment increased 7.9-fold with the Zeno trap enabled. Significant sensitivity increases were also seen using the test results for ^{15}N -labeled reference cell samples (Figure S4). Precursor ions of ^{15}N -glutamate showed an increase of 6.6-fold, and fragment ions of ^{15}N -glutamate showed an increase of 8.4-fold compared to the SWATH method.

Moreover, the sensitivity gain still maintains an accurate MID. For metabolites containing 5 carbons (glutamate), or 10 carbons (glutathione), shown in **Figure 2**, the SWATH, Zeno MRM^{HR} and MRM^{HR} methods shared the same TOF MID results; in addition, the precursor MID was in line with the TOF MID. This provided confidence for further investigation of fragment MID. At the MS² fragment level, the Zeno MRM^{HR} method preserved identical ^{13}C isotopologue distributions as the other methods. No artefacts were introduced during Zeno trap pulsing in the Zeno trap. Likewise, for metabolites with one nitrogen (glutamate) or three nitrogens (glutathione) at both MS¹ and MS² levels, the Zeno MRM^{HR} results maintained identical ^{15}N isotopologue distribution as the other two methods (Figure S5). Overall, the HILIC-Zeno MRM^{HR} demonstrated its strong advantages in labeled mass isotopologue analysis in terms of detection sensitivity and isotope fidelity at the MS² level.

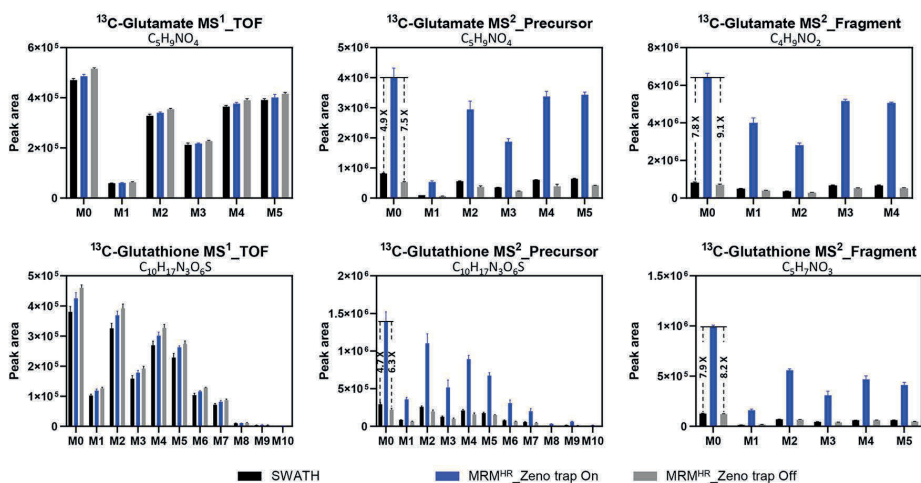


Figure 1. Sensitivity comparison at MS¹ TOF level and MS² fragmentation level among SWATH, MRM^{HR} and Zeno MRM^{HR} acquisition for ^{13}C labeled isotopologue analysis ($n=3$). At the MS² level, each precursor isotopologue was quantified using the peak area of residual precursor ion extracted from its MS/MS scan window. Each fragment isotopologue was quantified by summing the peak areas of the same fragment ion extracted from multiple MS/MS scan windows.

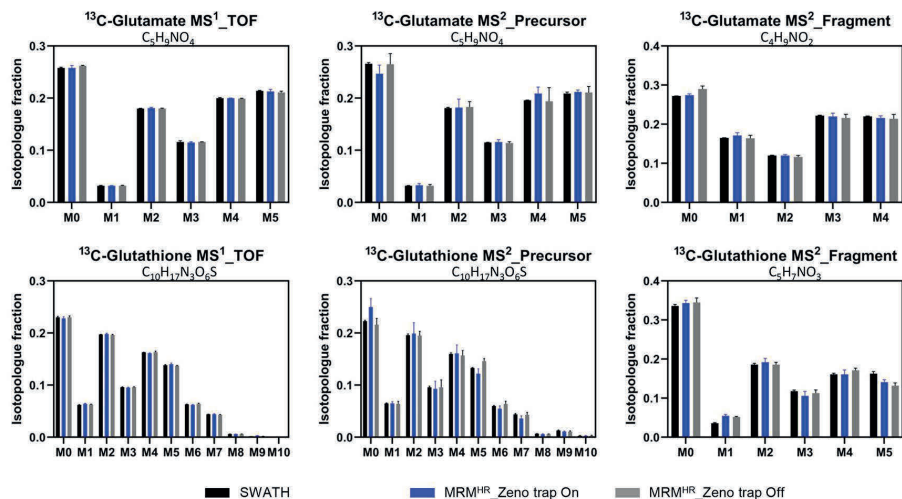


Figure 2. Accuracy comparison at MS¹ TOF level and MS² fragmentation level among SWATH, MRM^{HR} and Zeno MRM^{HR} acquisition for ¹³C labeled isotopologue distribution analysis (n=3).

3. Evaluation of MID quantification reproducibility

In a typical cell culture, the harvested quantity of cells often varies between replicated culture wells. Nonetheless, regardless of variations in total cellular content, isotopologues in fractions should be constant among replicates of a group assuming a consistent metabolic state. We further evaluated the HILIC-Zeno MRM^{HR} method reproducibility in MID quantification for inter-sample analysis. A set of ¹³C reference samples in undiluted form (DF_1x), twofold-dilution (DF_2x) and threefold dilution (DF_3x) was evaluated to imitate the effect of varied metabolite concentrations across samples. The average protein content corresponding to DF_1x, DF_2x and DF_3x samples was 38.0 μ g, 19.0 μ g and 12.7 μ g respectively. As shown in Figure 3, for the metabolites glutamate, ketoglutarate, and glutathione, precursor MIDs had relative standard deviations (RSDs) between 6.7%-21.2%, and fragment MIDs had RSDs between 2.8%-10.1% across DF_1x, DF_2x and DF_3x samples. Fragment MID exhibited better quantification reproducibility than precursor MID. The corresponding MID data in detail can be found in Table S6. Overall, the MID quantification of the HILIC-Zeno MRM^{HR} method over inter-sample analysis demonstrated a reproducibility RSD of less than 25%. The performance of MS/MS fragmentation with the Zeno trap enabled showed good robustness to varied sample concentrations.

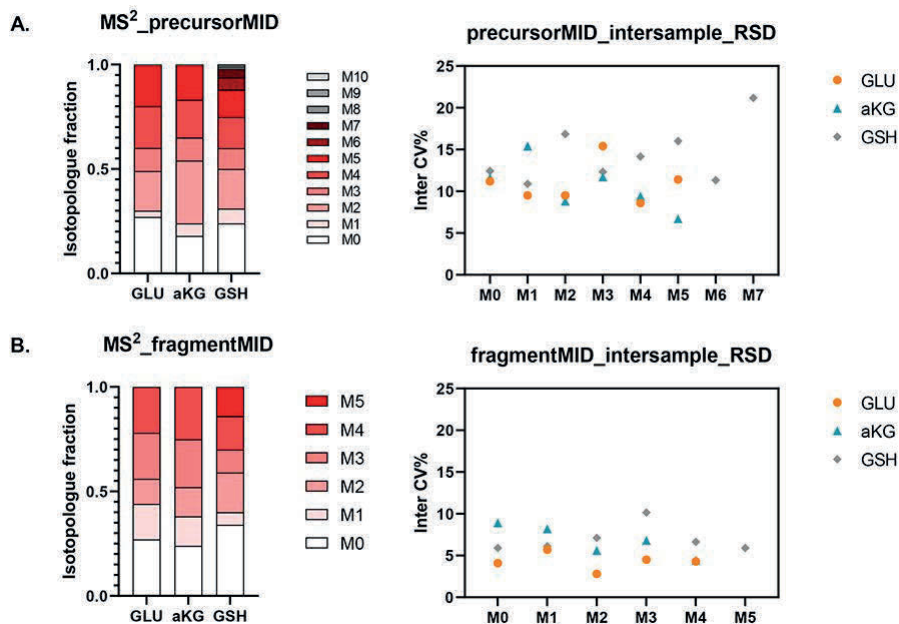


Figure 3. Inter-sample reproducibility of ^{13}C MIDs based on one reference sample set, including no dilution, twofold dilution, and threefold dilution. Each sample was injected three times. (A) Isotopologue fractions for precursor ions on average (left, $n=9$) and their corresponding RSD (right, $n=9$). (B) Isotopologue fractions for fragment ions on average (left, $n=9$) and their corresponding RSD (right, $n=9$). Glutamate: GLU; ketoglutarate: aKG; glutathione: GSH.

4. Tandem mass isotopologue distribution analysis of glutamate

One unique advantage of the HILIC-Zeno MRM^{HR} method is its capacity to resolve the labeling positional information for a particular isotopologue. To exemplify this, we used this method to distinguish two sets of ^{13}C labeling positions in the $^{13}\text{C}_2$ -glutamate isotopologue derived from D- $^{13}\text{C}_6$ -glucose. Figure 4A shows the detected M+0 precursor ion of glutamate and its produced fragments labeled in black, and the M+2 precursor ion and its produced fragments labeled in blue. Fragment₂ produced from M+2 isotopologue showed no labeled m+2 peak, indicating that simultaneous labeling of two ^{13}C atoms at the C4 and C5 positions was impossible. As illustrated in Figure 4B, glutamate derived from $^{13}\text{C}_6$ -glucose after one round of ^{13}C incorporation via the tricarboxylic acid (TCA) cycle can result in two ^{13}C atoms at the C1 and C2 positions via pyruvate anaplerosis (PDH) and two ^{13}C atoms at the C3 and C4 positions via pyruvate carboxylase (PC) pathway.^{39,40} By analyzing the corrected peak area ratio between the m+1 and m+2 peaks of fragment₁, we

could further determine the distribution ratio between 1,2- $^{13}\text{C}_2$ -glutamate and 3,4- $^{13}\text{C}_2$ -glutamate and generate a tandem MID of ^{13}C -glutamate in Figure 4C (Table S7). Healthy mid-brain neurons exhibited a relatively higher flux via PDH activity than PC activity.

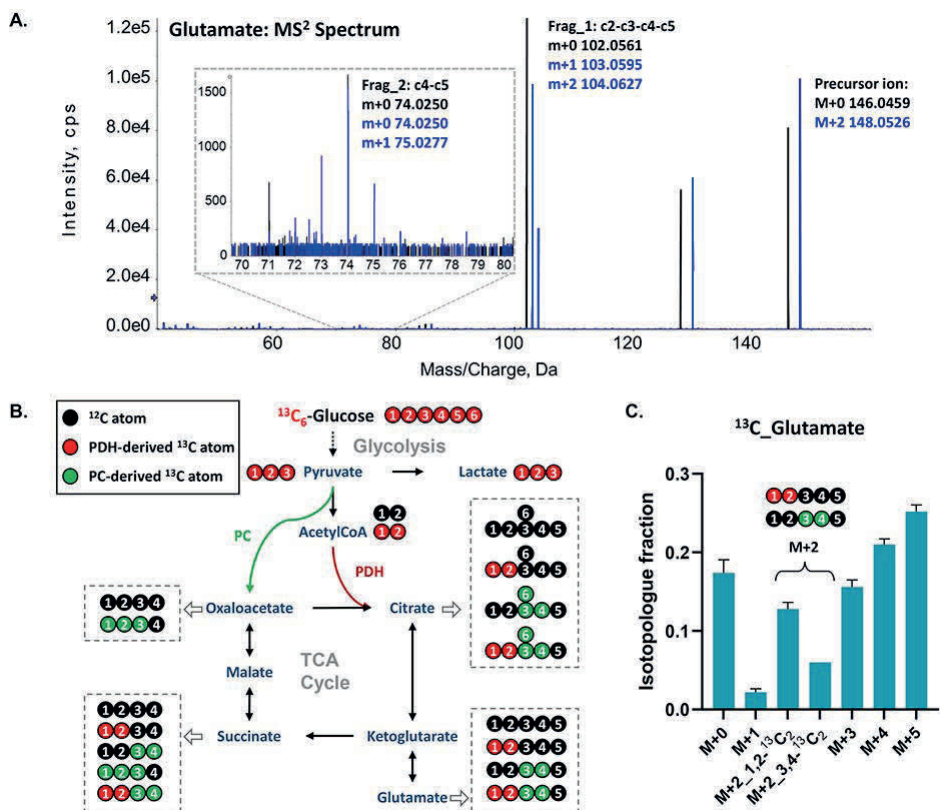


Figure 4. Structural elucidation of $^{13}\text{C}_2$ -glutamate through analyzing the labeling pattern of annotated moiety fragment_1 (Frag_1: c2-c3-c4-c5) and fragment_2 (Frag_2: c4-c5) at the MS² level. (A) MS² spectrum of monoisotopic and $^{13}\text{C}_2$ isotopologue peak of ^{13}C -glutamate. (B) ^{13}C atom tracking derived from D- $^{13}\text{C}_6$ -Glucose into glycolysis and the TCA cycle. The expected ^{13}C labeling patterns for the intermediates, acetylCoA, citrate, glutamate, succinate and oxaloacetate, via PDH and PC pathways were deduced and depicted in red and green, respectively. The first turn of PDH-initiated and PC-initiated ^{13}C labeling results were displayed. (C) Tandem MID of ^{13}C -glutamate measured in healthy neurons.

5. Reconstruction of glutathione metabolism in mid-brain neurons

Glutathione (GSH), one of the intracellular antioxidants, can protect cells by neutralizing reactive oxygen species and converting itself into its oxidized form (GSSG).⁴¹ In modulating redox homeostasis, de novo GSH synthesis was reported to play a more critical

role than recycling GSSG.^{42,43} Rotenone is known as a classic toxin for causing dopaminergic degeneration by inducing oxidative stress. To better distinguish the metabolic change of glutathione metabolism via de novo synthesis among intersecting pathways, the HILIC-Zeno MRM^{HR} method was applied to measure the polar ¹³C/¹⁵N-metabolome from healthy and rotenone-treated mid-brain neurons with D-¹³C₆-glucose/L-¹⁵N₂-glutamine as a tracer.

The analyzed intact isotopologues of key intermediate metabolites from healthy neurons were first used to decipher the key pathway connection associated with de novo glutathione synthesis. In Figure 5A, for healthy mid-brain neurons, intermediates of ketoglutarate and glutamate, and serine and glycine were detected at 62 and 60%, and 11 and 7% levels of ¹³C enrichment, respectively. GSH, GSSG showed 21 and 20% of ¹³C enrichment originating from D-¹³C₆-glucose, respectively. The incorporation of ¹³C atoms from D-¹³C₆-glucose into ketoglutarate and glutamate could be derived from the TCA cycle, and the ¹³C incorporation into serine and glycine could be derived from the de novo serine synthetic branch of glycolysis. The deciphered pathway reconstruction based on the ¹³C-enrichment of intermediates is shown in Figure 5B. Similarly, Figure 5C-D describes the pathway via ¹⁵N atom flow into de novo GSH synthesis. By tracing the ¹⁵N atoms from L-¹⁵N₂-glutamine, 23 and 5% of ¹⁵N enrichment were found in glutamate and serine, while no ¹⁵N enrichment was detected in glycine. GSH, GSSG ultimately showed 5 and 4% of ¹⁵N enrichment originated from L-¹⁵N₂-glutamine, respectively. To be noted, neither ¹³C nor ¹⁵N labeling was found in cysteine, which suggested its independent supply from glucose or glutamine and instead a possible dependence on the essential uptake from the extracellular environment.

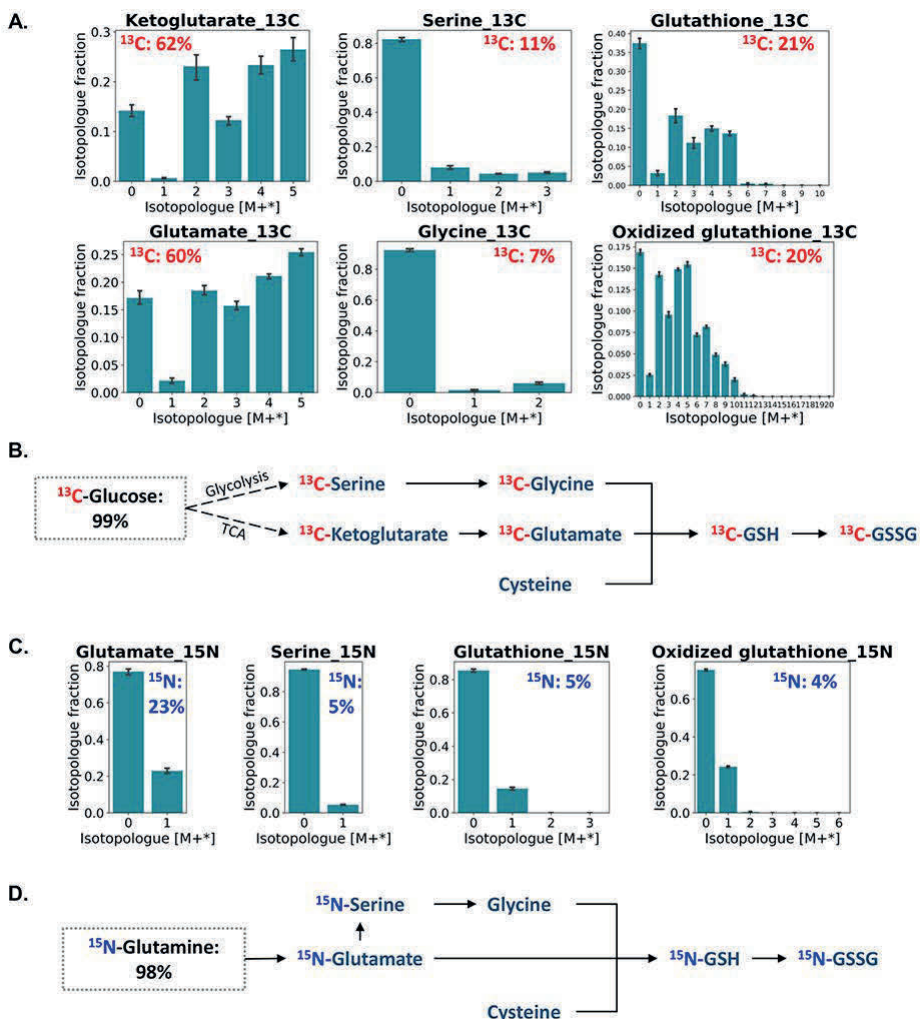


Figure 5. Tracing the de-novo glutathione synthesis pathway via $^{13}\text{C}/^{15}\text{N}$ atom enrichments of intermediate metabolites. The proportion of $^{13}\text{C}/^{15}\text{N}$ enrichment was denoted in red or blue. (A) ^{13}C labeled isotopologue distribution of intact metabolites. (B) ^{13}C atom flow in the de-novo glutathione synthesis pathway using D- $^{13}\text{C}_6$ -glucose as a carbon tracer. (C) ^{15}N labeled isotopologue distribution of intact metabolites. (D) ^{15}N atom flow in the de-novo glutathione synthesis pathway using L- $^{15}\text{N}_2$ -glutamine as a nitrogen tracer.

Based on the intact isotopologues of ^{13}C -GSH in M+1-7, we further investigated its fragment isotopologues (Figure 6), F1, indicating a glutamate moiety, was detected with a labeled distribution from m+0 to m+5 with 39% ^{13}C enrichment, which is similar to the

observed precursor glutamate MID pattern. In addition, F2, indicating a glycine-cysteine moiety, was detected with a labeled distribution from m+0 to m+2 and a ^{13}C enrichment of just 4%. This was consistent with the corresponding patterns of the precursors glycine and cysteine. ^{15}N -GSH was shown in M+1 via the intact isotopologue analysis. The ^{15}N enrichment is further observed only in the glutamate moiety (^{15}N -GSH F1) with its MID shown from m+0 to m+1. This moiety labeling pattern also matched the precursor glutamate MID. Besides the fact that the precursor serine was detected with certain ^{15}N enrichment, the level of ^{15}N -glycine and its incorporation as ^{15}N -GSH F2 could be too low to be detected. The fragment isotopologue distribution further validated the utilization of amino acid moieties derived from D- $^{13}\text{C}_6$ -glucose/L- $^{15}\text{N}_2$ -glutamine in the reconstructed pathway from Figure 5. Therefore, with the help of intact and fragment isotopologue analysis, we confirmed and highlighted the de novo synthesis of GSH in mid-brain neurons requires both glucose and glutamine for providing de novo-synthesized glutamate, serine, or glycine.

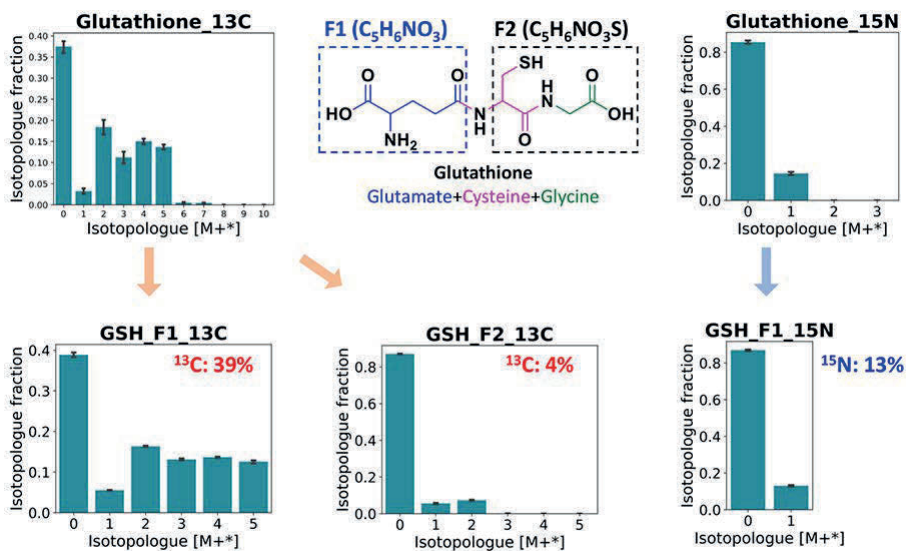


Figure 6. Structural elucidation of $^{13}\text{C}/^{15}\text{N}$ -labeled glutathione via fragment isotopologue analysis. Ionized glutathione could produce a mass spectrum of fragments by collision-induced dissociation, from which fragment 1 (F1) indicated a glutamate moiety, fragment 2 (F2) indicated a glycine-cysteine moiety.

Rotenone inhibits mitochondrial complex I, impairing oxidative phosphorylation and resulting in a dramatic reduction of ATP production. It also produces excess generation of reactive oxygen species and leads to decreased GSH levels.⁴⁴ For mid-brain neurons with

rotenone treatment, we detected decreased ^{12}C -GSH and increased ^{12}C -GSSG compared to controls (Figure 7A). Apart from the ^{12}C -GSH pool, ^{13}C -GSH and ^{13}C -GSSG are synthesized de novo and both showed down-regulation. However, either the peak area ratio of ^{12}C -GSH/ ^{12}C -GSSG or the ratio of ^{13}C -GSH/ ^{13}C -GSSG was significantly decreased below 10 due to rotenone-induced oxidative stress (Figure 7B), which is consistent with a previous report.⁴⁵ Reduced peak area ratios of ^{14}N -GSH/ ^{14}N -GSSG and ratios of ^{15}N -GSH/ ^{15}N -GSSG were also found in ^{15}N labeled neurons (Figure 7D-E). A low GSH/GSSG ratio, as a result of antioxidant defense, may act as a critical factor in the neuroinflammatory and neurodegenerative processes in Parkinson's disease.⁴⁶ Interestingly, rotenone treatment also resulted in a significantly decreased labeled ($^{13}\text{C}/^{15}\text{N}$) fraction of the combined GSH+GSSG (Figure 7C and 7F), further implying defective GSH biosynthesis in rotenone-treated neurons.

To figure out the cause of low glutathione synthesis through de novo regulation, we next analyzed the $^{13}\text{C}/^{15}\text{N}$ -labeling patterns of both the intact molecule and its moieties for GSH and the associated intermediates (Figure 8). Rotenone induced significant depletion in both 1,2- $^{13}\text{C}_2$ -glutamate and 3,4- $^{13}\text{C}_2$ -glutamate, which pointed to inhibition of PDH and PC-mediated TCA cycle activity. Additionally, the ^{13}C -glutamate moiety of GSH (^{13}C -GSH F1) showed decreased ^{13}C fraction. This confirmed that rotenone reduced glutamate production by inhibiting the entry flux into upstream TCA cycle, rather than increasing its consumption for downstream synthesis. No significant depletion was observed in ^{13}C -glycine, while the ^{13}C -glycine moiety of GSH (^{13}C -GSH F2) showed a significantly decreased ^{13}C fraction after rotenone treatment. Based on the distribution ratio between m+0, m+1 and m+2 of F1 isotopologues (Table S8), a tandem analysis of ^{13}C -GSH including three positional isotopomers for M+2 isotopologue was obtained, as shown in Figure 8A. In line with the reduced ^{13}C enrichment found in GSH moieties F1 and F2, the abundance of two major isotopomers, $^{13}\text{C}_2$ -GSH: M+2_Glu+ $^{13}\text{C}_2$ -Gly and M+2_ $^{13}\text{C}_2$ -Glu+Gly, decreased significantly in rotenone-treated conditions. Similar to the alterations of ^{13}C -glycine and ^{13}C -GSH F2, no change was found in ^{15}N -glutamate in the rotenone-treated group, while the ^{15}N -glutamate moiety of GSH (^{15}N -GSH F1) showed a significantly decreased ^{15}N fraction, and ^{15}N -GSH showed corresponding decreases in abundance (Figure 8B).

The results of mass isotopologue analysis showed that, in addition to suppressing glucose metabolism, which directly limits the source of glutamate supplied for de novo GSH synthesis, rotenone may also cause an inhibitory effect on the synthetic reaction of GSH production from glutamate, cysteine, and glycine. The sequential reactions are catalyzed by the ATP-dependent enzymes γ -glutamylcysteine synthetase (γ -GCS) and GSH synthetase (GS). Perceived flux reduction of reactions catalyzed by PDH, PC, γ -GCS and GS may be

a subsequent effect of mitochondrial complex I inhibition, which will need future validation to better understand the metabolic dysfunction during rotenone-induced neurodegeneration. Overall, our results suggest that in this neuronal model of rotenone-induced neurodegeneration, deficient *de novo* GSH synthesis and an increased oxidation into GSSG together resulted in a decreased GSH level under oxidative stress.

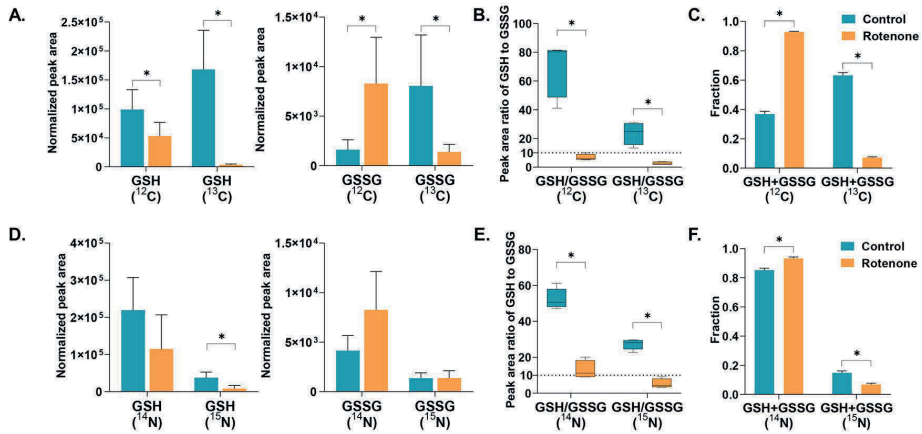


Figure 7. Metabolite abundance changes of glutathione (GSH) and oxidized glutathione (GSSG) under healthy and rotenone-treated conditions. (A) Bar plot representing the normalized peak area of ¹²C/¹³C GSH and GSSG. (B). Box plot representing the peak area ratio of ¹²C-GSH to ¹²C-GSSG and ¹³C-GSH to ¹³C-GSSG. (C) Bar plot representing the unlabeled (¹²C) and labeled (¹³C) fractions of combined GSH+GSSG. (D) Bar plot representing the normalized peak area of ¹⁴N/¹⁵N GSH and GSSG. (E) Box plot representing the peak area ratio of ¹⁴N-GSH to ¹⁴N-GSSG and ¹⁵N-GSH to ¹⁵N-GSSG. (F) Bar plot representing the unlabeled (¹⁴N) and labeled (¹⁵N) fractions of combined GSH+GSSG. Peak area was normalized using the corresponding sample protein content. An asterisk indicates a significant difference, with a p-value below 0.05.

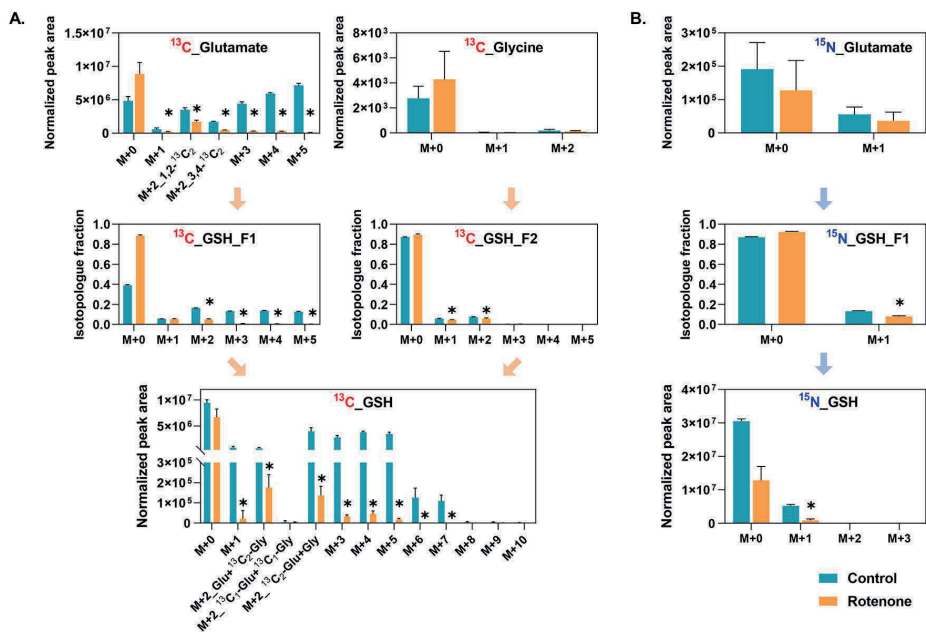


Figure 8. Mass isotopologue analysis of intact and fragmented metabolites for healthy and rotenone-perturbed mid-brain neurons. (A) ^{13}C labeled isotopologue analysis of glutamate, GSH and its moieties F1 and F2. The M+2 isotopologue of ^{13}C -glutamate was identified in two isotopomers. The M+2 isotopologue of ^{13}C -GSH was identified in three isotopomers. (B). ^{15}N -labeled isotopologue analysis of glutamate, GSH and its moiety F1. An asterisk indicates a significant difference, with a p-value below 0.05.

Conclusions

In this study, we developed a HILIC-Zeno MRM^{HR} method that can be used in tracer-based metabolomics studies for structurally-resolved MID analysis. This method allows the simultaneous acquisition at MS¹ and MS² levels in one single run. Labeled isotopologue distributions for intact metabolites can be obtained from the MS¹ level. Meanwhile, labeled isotopologue distributions for both the intact metabolite and its fragmented moieties can be obtained from the MS² level with higher sensitivity due to Zeno trap pulsing. The relationship between the labeled precursor and fragment ions was preserved to accurately identify the same labeled isotopologue with differential labeling positions. For future work, intensity-dependent selection of precursor ions can be combined with Zeno trap to trigger MS² for only present isotopologues, thus achieving even higher sensitivity. Furthermore, including additional target metabolites would provide more insight into pathway regulation, such as for γ -glutamylcysteine.

The method was successfully applied to analyze $^{13}\text{C}/^{15}\text{N}$ -labeled polar extracts of human-derived mid-brain neurons under healthy and oxidatively stressed states using D- $^{13}\text{C}_6$ -glucose/L- $^{15}\text{N}_2$ -glutamine as tracers. By tracing the labeled $^{13}\text{C}/^{15}\text{N}$ atoms in the moieties of metabolite isotopologues, we were able to reconstruct the cell-type and condition-specific pathways of glutathione metabolism in healthy and perturbed mid-brain neurons. The quantitative isotopologue analysis greatly contributed to the new elucidation of glutathione metabolism regulation in response to rotenone perturbation. It is worth mentioning that quantitative isotopologue analysis highlights altered metabolic fluxes, providing guidance for the subsequent targeted analysis of changes in enzymatic activities, which expands our understanding of disease mechanisms at the enzyme level. Although we only present the application of our approach to glutathione metabolism, it can also be applied to study other pathways including central carbon metabolism and de novo nucleotide metabolism. Thereby, more accurate biological interpretations could be achieved within a cell-specific metabolic network.

Acknowledgments

This project received funding from the China scholarship coun-cil (No.201806210057), the European Union's Horizon 2020 research and innovation programme, for the SysMedPD project, under grant agreement No. 668738, the Dutch National Institutes of Health (ZonMw) TKI-LSH Neuromet project (LSHM18092) and the Dutch Research Council (NWO) 'In-vestment Grant NWO Large' program, for the 'Building the infrastructure for Exposome research: Exposome-Scan' project (No. 175.2019.032). Additionally, we acknowledge Vincent Verschoor from Leiden University and Edinson Lucumi Moreno from Harvard University for their invaluable advice and assistance with neuron culture.

References

1. Grüning, N.-M.; Lehrach, H.; Ralser, M. Regulatory Crosstalk of the Metabolic Network. *Trends in Biochemical Sciences* 2010, 35 (4), 220–227.
2. Urbanczyk-Wochniak, E.; Luedemann, A.; Kopka, J.; Selbig, J.; Roessner-Tunali, U.; Willmitzer, L.; Fernie, A. R. Parallel Analysis of Transcript and Metabolic Profiles: A New Approach in Systems Biology. *EMBO Rep* 2003, 4 (10), 989–993.
3. Kell, D. B.; Brown, M.; Davey, H. M.; Dunn, W. B.; Spasic, I.; Oliver, S. G. Metabolic Footprinting and Systems Biology: The Medium Is the Message. *Nat Rev Microbiol* 2005, 3 (7), 557–565.
4. Shao, Y.; Le, W. Recent Advances and Perspectives of Metabolomics-Based Investigations in Parkinson's Disease. *Molecular Neurodegeneration* 2019, 14 (1), 3.
5. Anandhan, A.; Jacome, M. S.; Lei, S.; Hernandez-Franco, P.; Pappa, A.; Panayiotidis, M. I.; Powers, R.; Franco, R. Metabolic Disorder Dysfunction in Parkinson's Disease: Bioenergetics, Redox Homeostasis and Central Carbon Metabolism. *Brain Res Bull* 2017, 133, 12–30.
6. Watson, E.; Yilmaz, L. S.; Walhout, A. J. M. Understanding Metabolic Regulation at a Systems Level: Metabolite Sensing, Mathematical Predictions, and Model Organisms. *Annu Rev Genet* 2015, 49, 553–575.
7. Ma, W.; Trusina, A.; El-Samad, H.; Lim, W. A.; Tang, C. Defining Network Topologies That Can Achieve Biochemical Adaptation. *Cell* 2009, 138 (4), 760–773.
8. Truscott, R. J.; Malegan, D.; McCairns, E.; Halpern, B.; Hammond, J.; Cotton, R. G.; Mercer, J. F.; Hunt, S.; Rogers, J. G.; Danks, D. M. Two New Sulphur-Containing Amino Acids in Man. *Biomed Mass Spectrom* 1981, 8 (3), 99–104.

9. Yuan, M.; Kremer, D. M.; Huang, H.; Breitkopf, S. B.; Ben-Sahra, I.; Manning, B. D.; Lyssiotis, C. A.; Asara, J. M. Ex Vivo and In Vivo Stable Isotope Labelling of Central Carbon Metabolism and Related Pathways with Analysis by LC-MS/MS. *Nat Protoc* 2019, 14 (2), 313–330.
10. Ma, E. H.; Verway, M. J.; Johnson, R. M.; Roy, D. G.; Steadman, M.; Hayes, S.; Williams, K. S.; Sheldon, R. D.; Samborska, B.; Kosinski, P. A.; Kim, H.; Griss, T.; Faubert, B.; Condotta, S. A.; Krawczyk, C. M.; DeBerardinis, R. J.; Stewart, K. M.; Richer, M. J.; Chubukov, V.; Roddy, T. P.; Jones, R. G. Metabolic Profiling Using Stable Isotope Tracing Reveals Distinct Patterns of Glucose Utilization by Physiologically Activated CD8+ T Cells. *Immunity* 2019, 51 (5), 856–870.e5.
11. Berry, D.; Loy, A. Stable-Isotope Probing of Human and Animal Microbiome Function. *Trends in Microbiology* 2018, 26 (12), 999–1007.
12. Fernández-García, J.; Altea-Manzano, P.; Pranzini, E.; Fendt, S.-M. Stable Isotopes for Tracing Mammalian-Cell Metabolism In Vivo. *Trends in Biochemical Sciences* 2020, 45 (3), 185–201.
13. Peterson, A. L.; Walker, A. K.; Sloan, E. K.; Creek, D. J. Optimized Method for Untargeted Metabolomics Analysis of MDA-MB-231 Breast Cancer Cells. *Metabolites* 2016, 6 (4), 30.
14. Hui, S.; Ghergurovich, J. M.; Morscher, R. J.; Jang, C.; Teng, X.; Lu, W.; Esparza, L. A.; Reya, T.; Le Zhan; Yanxiang Guo, J.; White, E.; Rabinowitz, J. D. Glucose Feeds the TCA Cycle via Circulating Lactate. *Nature* 2017, 551 (7678), 115–118.
15. Creek, D. J.; Mazet, M.; Achcar, F.; Anderson, J.; Kim, D.-H.; Kamour, R.; Morand, P.; Millerioux, Y.; Biran, M.; Kerkhoven, E. J.; Chokkathukalam, A.; Weidt, S. K.; Burgess, K. E. V.; Breitling, R.; Watson, D. G.; Bringaud, F.; Barrett, M. P. Probing the Metabolic Network in Bloodstream-Form Trypanosoma Brucei Using Untargeted Metabolomics with Stable Isotope Labelled Glucose. *PLOS Pathogens* 2015, 11 (3), e1004689.
16. Creek, D. J.; Chokkathukalam, A.; Jankevics, A.; Burgess, K. E. V.; Breitling, R.; Barrett, M. P. Stable Isotope-Assisted Metabolomics for Network-Wide Metabolic Pathway Elucidation. *Analytical Chemistry* 2012, 84 (20), 8442–8447.
17. Feith, A.; Teleki, A.; Graf, M.; Favilli, L.; Takors, R. HILIC-Enabled 13C Metabolomics Strategies: Comparing Quantitative Precision and Spectral Accuracy of QTOF High- and QQQ Low-Resolution Mass Spectrometry. *Metabolites* 2019, 9 (4), 63.
18. Alves, T. C.; Pongratz, R. L.; Zhao, X.; Yarrowborough, O.; Sereida, S.; Shirihai, O.; Cline, G. W.; Mason, G.; Kibbey, R. G. Integrated, Step-Wise, Mass-Isotopomeric Flux Analysis of the TCA Cycle. *Cell Metabolism* 2015, 22 (5), 936–947.
19. Antoniewicz, M. R. Tandem Mass Spectrometry for Measuring Stable-Isotope Labeling. *Current Opinion in Biotechnology* 2013, 24 (1), 48–53.
20. Choi, J.; Antoniewicz, M. R. Tandem Mass Spectrometry: A Novel Approach for Metabolic Flux Analysis. *Metabolic Engineering* 2011, 13 (2), 225–233.
21. Yuan, J.; Bennett, B. D.; Rabinowitz, J. D. Kinetic Flux Profiling for Quantitation of Cellular Metabolic Fluxes. *Nature Protocols* 2008, 3 (8), 1328–1340.
22. Rühl, M.; Rupp, B.; Nöh, K.; Wiechert, W.; Sauer, U.; Zamboni, N. Collisional Fragmentation of Central Carbon Metabolites in LC-MS/MS Increases Precision of 13C Metabolic Flux Analysis. *Biotechnol. Bioeng.* 2012, 109 (3), 763–771.
23. McCloskey, D.; Young, J. D.; Xu, S.; Palsson, B. O.; Feist, A. M. MID Max: LC-MS/MS Method for Measuring the Precursor and Product Mass Isotopomer Distributions of Metabolic Intermediates and Cofactors for Metabolic Flux Analysis Applications. *Anal. Chem.* 2016, 88 (2), 1362–1370.
24. Mairinger, T.; Hann, S. Implementation of Data-Dependent Isotopologue Fragmentation in 13C-Based Metabolic Flux Analysis. *Anal Bioanal Chem* 2017, 409 (15), 3713–3718.
25. Gillet, L. C.; Navarro, P.; Tate, S.; Röst, H.; Selevsek, N.; Reiter, L.; Bonner, R.; Aebersold, R. Targeted Data Extraction of the MS/MS Spectra Generated by Data-Independent Acquisition: A New Concept for Consistent and Accurate Proteome Analysis. *Mol Cell Proteomics* 2012, 11 (6), O111.016717.
26. Jaiswal, D.; Prasanna, C. B.; Hendry, J. I.; Wangikar, P. P. SWATH Tandem Mass Spectrometry Workflow for Quantification of Mass Isotopologue Distribution of Intracellular Metabolites and Fragments Labeled with Isotopic 13 C Carbon. *Analytical Chemistry* 2018, 90 (11), 6486–6493.
27. Siegel, D.; Meinema, A. C.; Permentier, H.; Hopfgartner, G.; Bischoff, R. Integrated Quantification and Identification of Aldehydes and Ketones in Biological Samples. *Anal. Chem.* 2014, 86 (10), 5089–5100.
28. Sun, Q.; Fan, T. W.-M.; Lane, A. N.; Higashi, R. M. An Ion Chromatography-Ultrahigh-Resolution-MS 1 /Data-Independent High-Resolution MS 2 Method for Stable Isotope-Resolved Metabolomics Reconstruction of Central Metabolic Networks. *Anal. Chem.* 2021, 93 (5), 2749–2757.
29. Jaiswal, D.; Wangikar, P. P. SWATH: A Data-Independent Tandem Mass Spectrometry Method to Quantify 13C Enrichment in Cellular Metabolites and Fragments. In *Metabolic Flux Analysis in Eukaryotic Cells: Methods and Protocols*; Nagrath, D., Ed.; Methods in Molecular Biology; Springer US: New York, NY, 2020; pp 189–204.
30. Choi, J.; Antoniewicz, M. R. Tandem Mass Spectrometry: A Novel Approach for Metabolic Flux Analysis. *Metabolic Engineering* 2011, 13 (2), 225–233.
31. Mairinger, T.; Steiger, M.; Nocon, J.; Mattanovich, D.; Ko-ellensperger, G.; Hann, S. Gas Chromatography-Quadrupole Time-of-Flight Mass Spectrometry-Based Determination of Isotopologue and Tandem Mass Isotopomer Fractions of Primary Metabolites for 13 C-Metabolic Flux Analysis. *Anal. Chem.* 2015, 87 (23), 11792–11802.

32. Chernushevich, I. V.; Merenbloom, S. I.; Liu, S.; Bloomfield, N. A W-Geometry Ortho-TOF MS with High Resolution and Up to 100% Duty Cycle for MS/MS. *J. Am. Soc. Mass Spectrom.* 2017, 28 (10), 2143–2150.
33. Reinhardt, P.; Glatza, M.; Hemmer, K.; Tsytsyura, Y.; Thiel, C. S.; Höing, S.; Moritz, S.; Parga, J. A.; Wagner, L.; Bruder, J. M.; Wu, G.; Schmid, B.; Röpke, A.; Klingauf, J.; Schwamborn, J. C.; Gasser, T.; Schöler, H. R.; Sternecker, J. Derivation and Expansion Using Only Small Molecules of Human Neural Progenitors for Neurodegenerative Disease Modeling. *PLoS ONE* 2013, 8 (3), e59252.
34. Moreno, E. L.; Hachi, S.; Hemmer, K.; Trietsch, S. J.; Baumuratov, A. S.; Hankemeier, T.; Vulto, P.; Schwamborn, J. C.; Fleming, R. M. T. Differentiation of Neuroepithelial Stem Cells into Functional Dopaminergic Neurons in 3D Microfluidic Cell Culture. *Lab on a Chip* 2015, 15 (11), 2419–2428.
35. Hosseinkhani, F.; Huang, L.; Dubbelman, A.-C.; Guled, F.; Harms, A. C.; Hankemeier, T. Systematic Evaluation of HILIC Stationary Phases for Global Metabolomics of Human Plasma. *Metabolites* 2022, 12 (2), 165.
36. Guijas, C.; Montenegro-Burke, J. R.; Domingo-Almenara, X.; Palermo, A.; Warth, B.; Hermann, G.; Koellensperger, G.; Huan, T.; Uritboonthai, W.; Aisporna, A. E.; Wolan, D. W.; Spilker, M. E.; Benton, H. P.; Siuzdak, G. METLIN: A Technology Platform for Identifying Knowns and Unknowns. *Anal Chem* 2018, 90 (5), 3156–3164.
37. Millard, P.; Delépine, B.; Guionnet, M.; Heuillet, M.; Bellvert, F.; Létisse, F. IsoCor: Isotope Correction for High-Resolution MS Labeling Experiments. *Bioinformatics* 2019, 35 (21), 4484–4487.
38. Loboda, A. V.; Chernushevich, I. V. A Novel Ion Trap That Enables High Duty Cycle and Wide m/z Range on an Orthogonal Injection TOF Mass Spectrometer. *Journal of the American Society for Mass Spectrometry* 2009, 20 (7), 1342–1348.
39. Yang, Y.; Fan, T. W.-M.; Lane, A. N.; Higashi, R. M. Chloroformate Derivatization for Tracing the Fate of Amino Acids in Cells and Tissues by Multiple Stable Isotope Resolved Metabolomics (MSIRM). *Analytica chimica acta* 2017, 976, 63–73.
40. Fan, T. W.-M.; Sun, Q.; Higashi, R. M. Ultrahigh Resolution MS1/MS2-Based Reconstruction of Metabolic Networks in Mammalian Cells Reveals Changes for Selenite and Arsenite Action. *Journal of Biological Chemistry* 2022, 298 (12), 102586.
41. Kurutas, E. B. The Importance of Antioxidants Which Play the Role in Cellular Response against Oxidative/Nitrosative Stress: Current State. *Nutr J* 2016, 15, 71.
42. Townsend, D. M.; Tew, K. D.; Tapiero, H. The Importance of Glutathione in Human Disease. *Biomed Pharmacother* 2003, 57 (3–4), 145–155.
43. Lian, G.; Gnanaprakasam, J. R.; Wang, T.; Wu, R.; Chen, X.; Liu, L.; Shen, Y.; Yang, M.; Yang, J.; Chen, Y.; Vasiliou, V.; Cassel, T. A.; Green, D. R.; Liu, Y.; Fan, T. W.; Wang, R. Glutathione de Novo Synthesis but Not Recycling Process Coordinates with Glutamine Catabolism to Control Redox Homeostasis and Directs Murine T Cell Differentiation. *eLife* 7, e36158.
44. Testa, C. M.; Sherer, T. B.; Greenamyre, J. T. Rotenone Induces Oxidative Stress and Dopaminergic Neuron Damage in Organotypic Substantia Nigra Cultures. *Molecular Brain Research* 2005, 134 (1), 109–118.
45. Wu, G.; Fang, Y.-Z.; Yang, S.; Lupton, J. R.; Turner, N. D. Glutathione Metabolism and Its Implications for Health. *The Journal of Nutrition* 2004, 134 (3), 489–492.
46. Bjørklund, G.; Peana, M.; Maes, M.; Dadar, M.; Severin, B. The Glutathione System in Parkinson's Disease and Its Progression. *Neuroscience & Biobehavioral Reviews* 2021, 120, 470–478.

Supplementary Materials

1. Optimal mass isolation window setting for SWATH acquisition method

When optimizing a SWATH acquisition method, considerations need to be made defining scan time, window size and total number of windows. Additional considerations need to be made in tracer-based studies especially when analyzing diverse metabolites. In this case, for accurate quantitation, all isotopologues of a certain metabolite need to be in the same Q1 window and care should be taken to prevent the underestimated integration of the mass isotopologue located on the edge of a SWATH window.¹ This experiment was designed to test the effect of complete or partial isotopologue coverage in one Q1 window, as well as the influence of overlapping windows giving partial isotopologue coverage. In total four SWATH methods were created with varied Q1 isolation windows and window overlap, as shown in Table S2. Each SWATH method starts with a survey TOF MS scan in 100 ms

from 50 to 700 Da, followed by sixteen Q1 isolation windows covering a mass range of m/z 60-690. The relevant Q1 isolation windows in each SWATH method targeting ^{13}C labeled glutamate were listed in Figure S1, also recorded in cycleID of 2 and 3 from Table S2. SWATH_Win1 and Win4 methods allow glutamate isotopologues of M0-M5 to be measured and quantified in the same window, but SWATH_Win2 and Win3 methods measured and quantified isotopologues across the two neighboring windows.

As a result, SWATH_Win1 and Win4 methods shared similar isotopologue quantification on both isotopologue peak area and isotopologue fraction which was also comparable to the results of general MRM^{HR} acquisition. However, the SWATH_Win2 method had lower signal for the M0-M2 isotopologues and this led to a change in their mass isotopologue fractions. The increased window overlapping width of 3.0 Da in the SWATH_Win3 method showed no improvement in isotopologue quantification combining neighboring windows. The results indicated a big drawback for the quantification of isotopologues of metabolites that span multiple windows, which would also cause subsequent inaccuracies in the quantification of fragment isotopologues. For targeted labeled metabolite analysis, it is strongly recommended to refine the Q1 window setting to include all possible isotopologues of precursor ions, even with the demand of making a custom SWATH window program or creating variable Q1 isolation windows.^{1,2} In this study, the SWATH_Win1 method with fixed Q1 isolation window was finally selected for the formal comparison with general MRM^{HR}, and Zeno MRM^{HR} acquisition.

SWATH method	CycleID	Overlap window width	m/z begin	m/z end	Quantified mass isotopologue
SWATH_Win1	2	1.0 Da	99	140	\
	3		139	180	M0,M1,M2,M3,M4,M5
SWATH_Win2	2	1.0 Da	99	149	M0,M1,M2
	3		148	180	M3,M4,M5
SWATH_Win3	2	3.0 Da	97	149	M0
	3		146	180	M1,M2,M3,M4,M5
SWATH_Win4	2	5.0 Da	95	149	\
	3		144	180	M0,M1,M2,M3,M4,M5

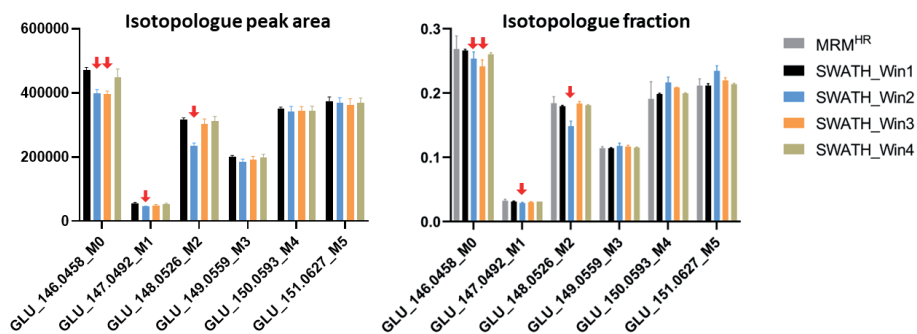


Figure S1. Peak integration influence on target metabolite isotopologues spanning across two neighboring SWATH mass isolation windows compared to complete isotopologues detection within a single window.

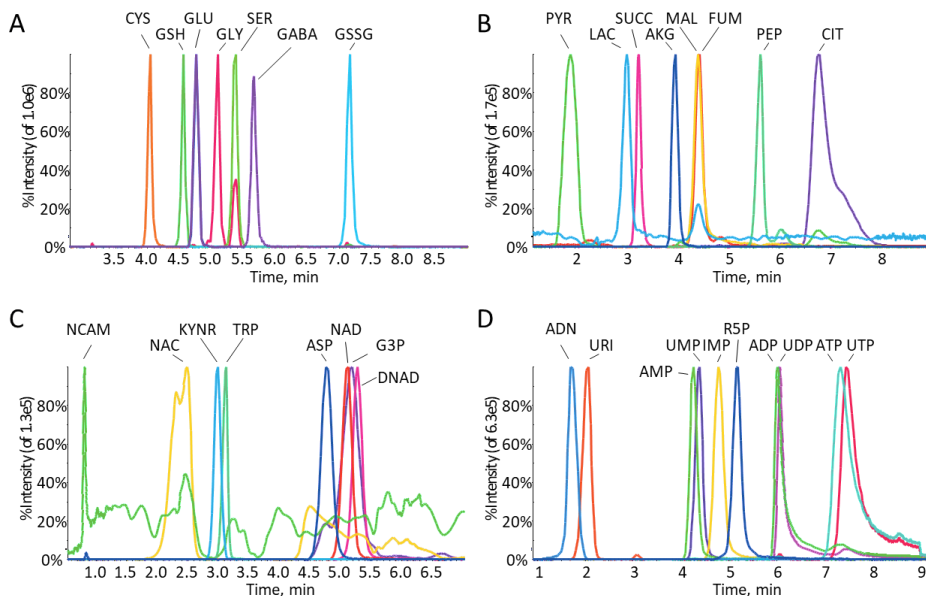


Figure S2. Extracted ion chromatography of target metabolites from de novo glutathione synthesis (A), primary carbon metabolism (B), de novo NAD synthesis (C), purine and pyrimidine metabolism (D). The metabolite abbreviations were introduced in Table S1.

Reconstruction of glutathione metabolism with HILIC-Zeno MRM

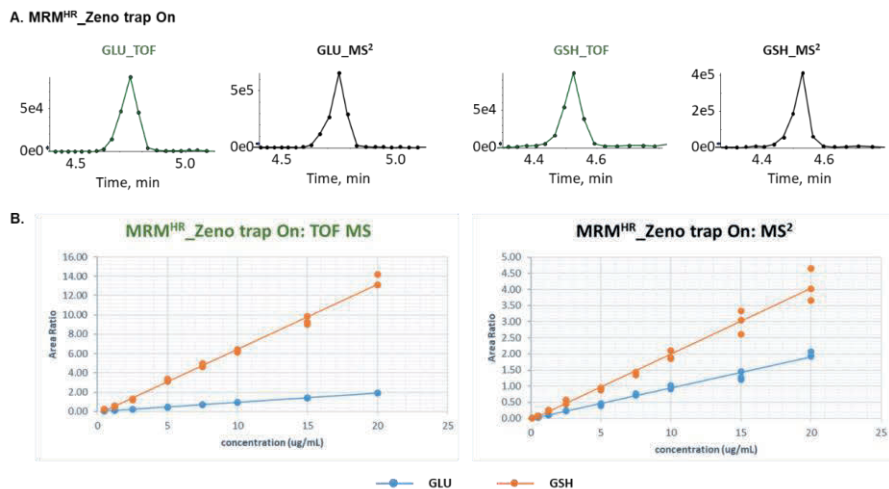


Figure S3. A. Illustration of peak scan points for metabolites glutamate (GLU) and glutathione (GSH) eluting between 4 and 6 mins, using ¹³C labeling Zeno MRM^{HR} acquisition method; B. Linearity test of glutamate (GLU) and glutathione (GSH) based on the quantification for TOF-MS and MS/MS level.

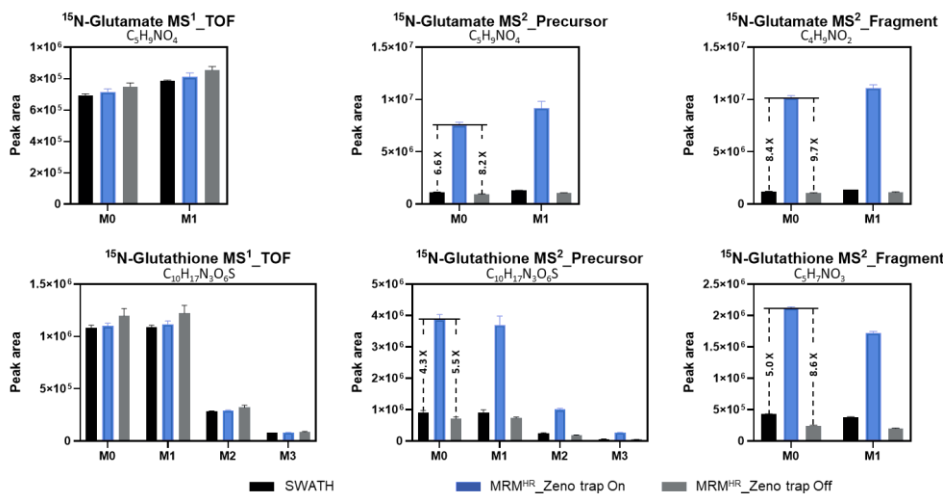


Figure S4. Sensitivity comparison at MS¹ TOF level and MS² fragmentation level among SWATH, MRM^{HR} and Zeno MRM^{HR} acquisition for ¹⁵N labeled isotopologue analysis (n=3). At the MS² level, each precursor isotopologue was quantified using the peak area of residual precursor ion extracted from its MS/MS scan window. Each fragment isotopologue was quantified by summing the peak areas of the same fragment ion extracted from multiple MS/MS scan windows.

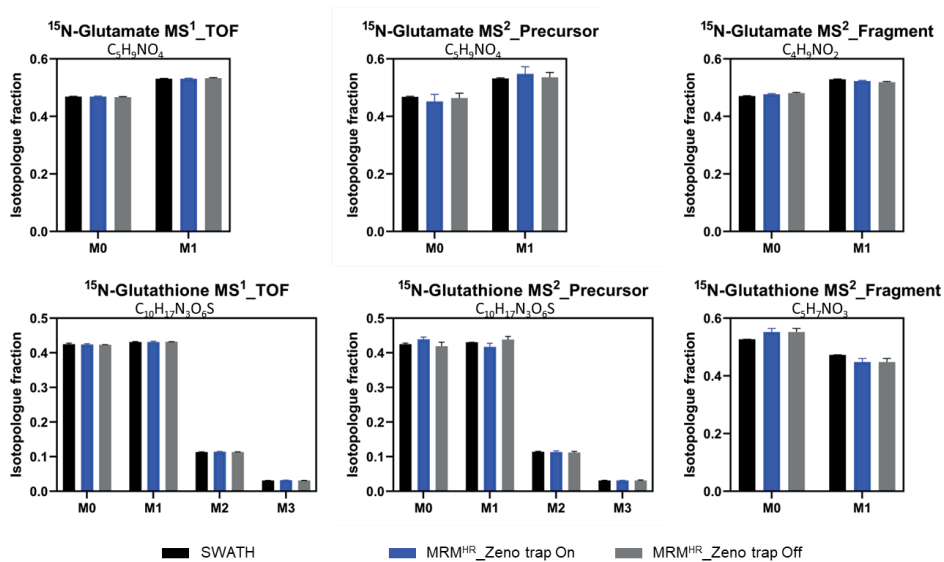


Figure S5. Accuracy comparison at MS¹ TOF level and MS² fragmentation level between SWATH, MRM^{HR} and Zeno MRM^{HR} acquisition for ^{15}N labeled isotopologue distribution analysis (n=3).

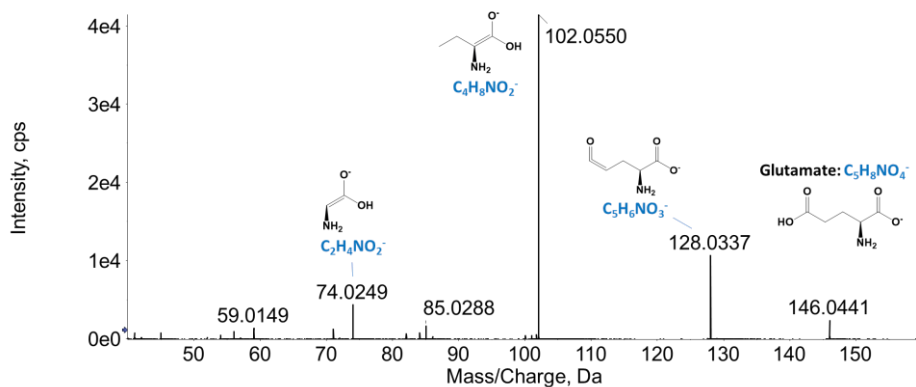


Figure S6. Product ion fragment annotation of glutamate.

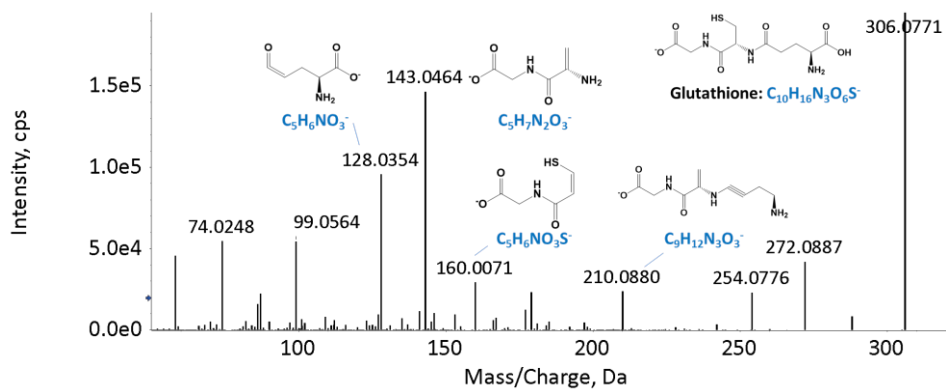


Figure S7. Product ion fragment annotation of glutathione.

References

- Jaiswal, D.; Prasannan, C. B.; Hendry, J. I.; Wangikar, P. P. SWATH Tandem Mass Spectrometry Workflow for Quantification of Mass Isotopologue Distribution of Intracellular Metabolites and Fragments Labeled with Isotopic ^{13}C Carbon. *Analytical Chemistry* 2018, 90 (11), 6486–6493.
- Zhang, Y.; Bilbao, A.; Bruderer, T.; Luban, J.; Strambio-De-Castillia, C.; Lisacek, F.; Hopfgartner, G.; Varesio, E. The Use of Variable Q1 Isolation Windows Improves Selectivity in LC–SWATH–MS Acquisition. *J. Proteome Res.* 2015, 14 (10), 4359–4371.

Table S1: Target metabolite list prepared in individual stock solution

CHEBI ID	Metabolite Name	Abbreviation	Compound Formula	Mono-isotopic Mass/Da	Solvent	Retention time /min
16015	L-Glutamic acid	GLU	C5H9NO4	147.0532	50%MeOH (0.5M NaOH)	4.8
16865	gamma-Aminobutyric acid	GABA	C4H9NO2	103.0633	50%MeOH	5.7
15428	Glycine	GLY	C2H5NO2	75.0320	50%MeOH (0.5M NaOH)	5.1
17561	Cysteine	CYS	C3H7NO2S	121.0197	50%MeOH	4.1
17115	Serine	SER	C3H7NO3	105.0426	50%MeOH	5.4
16856	Glutathione	GSH	C10H17N3O6S	307.0838	50%MeOH	4.6
17858	Oxidized glutathione	GSSG	C20H32N6O12S2	612.1520	50%MeOH	7.1
17053	L-Aspartic acid	ASP	C4H7NO4	133.0375	50%MeOH (0.5M NaOH)	4.8
29052	Glyceraldehyde 3-Phosphate	G3P	C3H7O6P	169.9980	50%MeOH	5.2
16675	Quinolinic acid	QULN	C7H5NO4	167.0219	50%MeOH (0.1M NaOH)	4.6
18304	Nicotinic acid adenine dinucleotide	DNAD	C21H27N6O15P2	665.1010	50%MeOH	5.2
15846	Nicotinamide adenine dinucleotide	NAD	C21H27N7O14P2	663.1091	50%MeOH	5.1
15940	Nicotinic acid	NAC	C6H5NO2	123.0320	50%MeOH	2.5
17154	Niacinamide	NCAM	C6H6N2O	122.0480	50%MeOH	0.9
16828	L-Tryptophan	TRP	C11H12N2O2	204.0899	50%MeOH	3.2
16946	L-Kynurenine	KYNR	C10H12N2O3	208.0848	50%MeOH	3
52742	D-Ribose 5-phosphate	R5P	C5H11O8P	230.0192	50%MeOH	5.1
16695	Uridine 5'-monophosphate	UMP	C9H13N2O9P	324.0359	50%MeOH	4.3
17659	Uridine 5'-diphosphate	UDP	C9H14N2O12P2	404.0022	50%MeOH	5.8
15713	Uridine triphosphate	UTP	C9H15N2O15P3	483.9685	50%MeOH	7.2
16704	Uridine	URI	C9H12N2O6	244.0695	50%MeOH	2
18050	L-Glutamine	GLN	C5H10N2O3	146.0691	50%MeOH	5
17202	Inosine monophosphate	IMP	C10H13N4O8P	348.0470	50%MeOH (0.5M NaOH)	4.7
17596	Inosine	INS	C10H12N4O5	268.0808	50%MeOH	2.9
16027	Adenosine monophosphate	AMP	C10H14N5O7P	347.0631	50%MeOH	4.2
16761	Adenosine diphosphate	ADP	C10H15N5O10P2	427.0294	50%MeOH	5.8
15422	Adenosine triphosphate	ATP	C10H16N5O13P3	506.9957	50%MeOH	7
16335	Adenosine	ADN	C10H13N5O4	267.0968	50%MeOH (12M 37% HCL)	1.7
17345	Guanosine monophosphate	GMP	C10H14N5O8P	363.0580	50%MeOH	5.3
17552	Guanosine diphosphate	GDP	C10H15N5O11P2	443.0243	50%MeOH	7.2
15996	Guanosine triphosphate	GTP	C10H16N5O14P3	522.9906	50%MeOH	8.3

Reconstruction of glutathione metabolism with HILIC-Zeno MRM

16750	Guanosine	GSN	C10H13N5O5	283.0917	50%MeOH (12M 37% HCL)	3.3
30915	Oxoglutaric acid	AKG	C5H6O5	146.0215	50%MeOH	3.9
30769	Citric acid	CIT	C6H8O7	192.0270	50%MeOH	6.7
15741	Succinic acid	SUCC	C4H6O4	118.0266	50%MeOH	3.1
18012	Fumaric acid	FUM	C4H4O4	116.0110	50%MeOH	4.3
30797	L-Malic acid	MAL	C4H6O5	134.0215	MiliQ water	4.2
32816	Pyruvic acid	PYR	C3H4O3	88.0160	50%MeOH	1.8
44897	Phosphoenolpyruvic acid	PEP	C3H5O6P	167.9824	50%MeOH	5.5
422	L-Lactic acid	LAC	C3H6O3	90.0317	50%MeOH	2.9

Table S2: Q1 mass isolation window setting design for different SWATH MS acquisition methods

CycleID	Type	SWATH_Win1		SWATH_Win2		SWATH_Win3		SWATH_Win4	
		m/z begin	m/z end	m/z begin	m/z end	m/z begin	m/z end	m/z begin	m/z end
0	SCAN	50	700	50	700	50	700	50	700
1	SWATH	60	100	60	100	60	100	60	100
2	SWATH	99	140	99	149	97	149	95	149
3	SWATH	139	180	148	180	146	180	144	180
4	SWATH	179	220	179	233	177	233	175	233
5	SWATH	219	260	232	260	230	260	228	260
6	SWATH	259	300	259	312	257	312	255	312
7	SWATH	299	340	311	340	309	340	307	340
8	SWATH	339	380	339	380	337	380	335	380
9	SWATH	379	420	379	420	377	420	375	420
10	SWATH	419	460	419	460	417	460	415	460
11	SWATH	459	500	459	511	457	511	455	511
12	SWATH	499	540	510	540	508	540	506	540
13	SWATH	539	580	539	580	537	580	535	580
14	SWATH	579	620	579	620	577	620	575	620
15	SWATH	619	660	619	672	617	672	615	672
16	SWATH	659	690	671	690	669	690	667	690

Table S3: Inclusion precursors covered in the ¹³C labeling MRM_{HR} acquisition method

Compound ID	Group Name	Precursor Ion (Da)	TOF Start Mass (Da)	TOF Stop Mass (Da)	Accumulation Time (sec)	DP (V)	CE (V)	CE Spread (V)	Retention Time (min)	Retention time tolerance(±, sec)	Fragmentation mode	Time Bins to Sum	Channel1	Channel2	Channel3	Channel4
Glutamate	Carbon	146.05	40	160	0.03	-80	-30	20	4.75	20	CID	4	True	True	True	True
Glutamate C1	Carbon	147.05	40	160	0.03	-80	-30	20	4.75	20	CID	4	True	True	True	True
Glutamate C2	Carbon	148.05	40	160	0.03	-80	-30	20	4.75	20	CID	4	True	True	True	True
Glutamate C3	Carbon	149.06	40	160	0.03	-80	-30	20	4.75	20	CID	4	True	True	True	True
Glutamate C4	Carbon	150.06	40	160	0.03	-80	-30	20	4.75	20	CID	4	True	True	True	True
Glutamate C5	Carbon	151.06	40	160	0.03	-80	-30	20	4.75	20	CID	4	True	True	True	True
GABA	Carbon	102.06	40	110	0.06	-80	-30	20	5.7	20	CID	4	True	True	True	True
GABA C1	Carbon	103.06	40	110	0.06	-80	-30	20	5.7	20	CID	4	True	True	True	True
GABA C2	Carbon	104.06	40	110	0.06	-80	-30	20	5.7	20	CID	4	True	True	True	True
GABA C3	Carbon	105.07	40	110	0.06	-80	-30	20	5.7	20	CID	4	True	True	True	True
GABA C4	Carbon	106.07	40	110	0.06	-80	-30	20	5.7	20	CID	4	True	True	True	True
Glycine	Carbon	74.02	40	80	0.06	-80	-30	20	5.11	20	CID	4	True	True	True	True
Glycine C1	Carbon	75.03	40	80	0.06	-80	-30	20	5.11	20	CID	4	True	True	True	True
Glycine C2	Carbon	76.03	40	80	0.06	-80	-30	20	5.11	20	CID	4	True	True	True	True
Cysteine	Carbon	120.01	40	125	0.06	-80	-30	20	4.06	20	CID	4	True	True	True	True
Cysteine C1	Carbon	121.02	40	125	0.06	-80	-30	20	4.06	20	CID	4	True	True	True	True
Cysteine C2	Carbon	122.02	40	125	0.06	-80	-30	20	4.06	20	CID	4	True	True	True	True
Cysteine C3	Carbon	123.02	40	125	0.06	-80	-30	20	4.06	20	CID	4	True	True	True	True
Serine	Carbon	104.04	40	110	0.06	-80	-30	20	5.39	20	CID	4	True	True	True	True
Serine C1	Carbon	105.04	40	110	0.06	-80	-30	20	5.39	20	CID	4	True	True	True	True
Serine C2	Carbon	106.04	40	110	0.06	-80	-30	20	5.39	20	CID	4	True	True	True	True
Serine C3	Carbon	107.05	40	110	0.06	-80	-30	20	5.39	20	CID	4	True	True	True	True
GSH	Carbon	306.08	50	320	0.03	-80	-30	20	4.56	20	CID	4	True	True	True	True
GSH C1	Carbon	307.08	50	320	0.03	-80	-30	20	4.56	20	CID	4	True	True	True	True
GSH C2	Carbon	308.08	50	320	0.03	-80	-30	20	4.56	20	CID	4	True	True	True	True
GSH C3	Carbon	309.09	50	320	0.03	-80	-30	20	4.56	20	CID	4	True	True	True	True
GSH C4	Carbon	310.09	50	320	0.03	-80	-30	20	4.56	20	CID	4	True	True	True	True
GSH C5	Carbon	311.09	50	320	0.03	-80	-30	20	4.56	20	CID	4	True	True	True	True
GSH C6	Carbon	312.10	50	320	0.03	-80	-30	20	4.56	20	CID	4	True	True	True	True
GSH C7	Carbon	313.10	50	320	0.03	-80	-30	20	4.56	20	CID	4	True	True	True	True
GSH C8	Carbon	314.10	50	320	0.03	-80	-30	20	4.56	20	CID	4	True	True	True	True
GSH C9	Carbon	315.11	50	320	0.03	-80	-30	20	4.56	20	CID	4	True	True	True	True
GSH C10	Carbon	316.11	50	320	0.03	-80	-30	20	4.56	20	CID	4	True	True	True	True
Aspartate	Carbon	132.03	50	140	0.03	-80	-30	20	4.76	25	CID	4	True	True	True	True
Aspartate C1	Carbon	133.03	50	140	0.03	-80	-30	20	4.76	25	CID	4	True	True	True	True
Aspartate C2	Carbon	134.04	50	140	0.03	-80	-30	20	4.76	25	CID	4	True	True	True	True
Aspartate C3	Carbon	135.04	50	140	0.03	-80	-30	20	4.76	25	CID	4	True	True	True	True
Aspartate C4	Carbon	136.04	50	140	0.03	-80	-30	20	4.76	25	CID	4	True	True	True	True
Glyceraldehyde-3-P	Carbon	168.99	50	175	0.03	-80	-30	20	5.15	30	CID	4	True	True	True	True
Glyceraldehyde-3-P C1	Carbon	169.99	50	175	0.03	-80	-30	20	5.15	30	CID	4	True	True	True	True
Glyceraldehyde-3-P C2	Carbon	171.00	50	175	0.03	-80	-30	20	5.15	30	CID	4	True	True	True	True
Glyceraldehyde-3-P C3	Carbon	172.00	50	175	0.03	-80	-30	20	5.15	30	CID	4	True	True	True	True
NAD	Carbon	662.10	80	700	0.03	-80	-30	20	5.1	30	CID	4	True	True	True	True
NAD C1	Carbon	663.11	80	700	0.03	-80	-30	20	5.1	30	CID	4	True	True	True	True
NAD C2	Carbon	664.11	80	700	0.03	-80	-30	20	5.1	30	CID	4	True	True	True	True
NAD C3	Carbon	665.11	80	700	0.03	-80	-30	20	5.1	30	CID	4	True	True	True	True
NAD C4	Carbon	666.12	80	700	0.03	-80	-30	20	5.1	30	CID	4	True	True	True	True

Reconstruction of glutathione metabolism with HILIC-Zeno MRM

NAD C5	Carbon	667.12	80	700	0.03	-80	-30	20	5.1	30	CID	4	True	True
NAD C6	Carbon	668.12	80	700	0.03	-80	-30	20	5.1	30	CID	4	True	True
NAD C7	Carbon	669.13	80	700	0.03	-80	-30	20	5.1	30	CID	4	True	True
NAD C8	Carbon	670.13	80	700	0.03	-80	-30	20	5.1	30	CID	4	True	True
NAD C9	Carbon	671.13	80	700	0.03	-80	-30	20	5.1	30	CID	4	True	True
NAD C10	Carbon	672.14	80	700	0.03	-80	-30	20	5.1	30	CID	4	True	True
NAD C11	Carbon	673.14	80	700	0.03	-80	-30	20	5.1	30	CID	4	True	True
NAD C12	Carbon	674.14	80	700	0.03	-80	-30	20	5.1	30	CID	4	True	True
NAD C13	Carbon	675.15	80	700	0.03	-80	-30	20	5.1	30	CID	4	True	True
NAD C14	Carbon	676.15	80	700	0.03	-80	-30	20	5.1	30	CID	4	True	True
NAD C15	Carbon	677.15	80	700	0.03	-80	-30	20	5.1	30	CID	4	True	True
NAD C16	Carbon	678.16	80	700	0.03	-80	-30	20	5.1	30	CID	4	True	True
NAD C17	Carbon	679.16	80	700	0.03	-80	-30	20	5.1	30	CID	4	True	True
NAD C18	Carbon	680.16	80	700	0.03	-80	-30	20	5.1	30	CID	4	True	True
NAD C19	Carbon	681.17	80	700	0.03	-80	-30	20	5.1	30	CID	4	True	True
NAD C20	Carbon	682.17	80	700	0.03	-80	-30	20	5.1	30	CID	4	True	True
NAD C21	Carbon	683.17	80	700	0.03	-80	-30	20	5.1	30	CID	4	True	True
Ribiose-5P	Carbon	229.01	50	240	0.03	-80	-30	20	5.02	30	CID	4	True	True
Ribiose-5P C1	Carbon	230.02	50	240	0.03	-80	-30	20	5.02	30	CID	4	True	True
Ribiose-5P C2	Carbon	231.02	50	240	0.03	-80	-30	20	5.02	30	CID	4	True	True
Ribiose-5P C3	Carbon	232.02	50	240	0.03	-80	-30	20	5.02	30	CID	4	True	True
Ribiose-5P C4	Carbon	233.03	50	240	0.03	-80	-30	20	5.02	30	CID	4	True	True
Ribiose-5P C5	Carbon	234.03	50	240	0.03	-80	-30	20	5.02	30	CID	4	True	True
UTP	Carbon	482.96	70	500	0.1	-80	-30	20	7.2	40	CID	4	True	True
UTP C1	Carbon	483.96	70	500	0.1	-80	-30	20	7.2	40	CID	4	True	True
UTP C2	Carbon	484.97	70	500	0.1	-80	-30	20	7.2	40	CID	4	True	True
UTP C3	Carbon	485.97	70	500	0.1	-80	-30	20	7.2	40	CID	4	True	True
UTP C4	Carbon	486.97	70	500	0.1	-80	-30	20	7.2	40	CID	4	True	True
UTP C5	Carbon	487.98	70	500	0.1	-80	-30	20	7.2	40	CID	4	True	True
UTP C6	Carbon	488.98	70	500	0.1	-80	-30	20	7.2	40	CID	4	True	True
UTP C7	Carbon	489.99	70	500	0.1	-80	-30	20	7.2	40	CID	4	True	True
UTP C8	Carbon	490.99	70	500	0.1	-80	-30	20	7.2	40	CID	4	True	True
UTP C9	Carbon	491.99	70	500	0.1	-80	-30	20	7.2	40	CID	4	True	True
Uridine	Carbon	243.06	50	260	0.1	-80	-30	20	2.02	20	CID	4	True	True
Uridine C1	Carbon	244.07	50	260	0.1	-80	-30	20	2.02	20	CID	4	True	True
Uridine C2	Carbon	245.07	50	260	0.1	-80	-30	20	2.02	20	CID	4	True	True
Uridine C3	Carbon	246.07	50	260	0.1	-80	-30	20	2.02	20	CID	4	True	True
Uridine C4	Carbon	247.08	50	260	0.1	-80	-30	20	2.02	20	CID	4	True	True
Uridine C5	Carbon	248.08	50	260	0.1	-80	-30	20	2.02	20	CID	4	True	True
Uridine C6	Carbon	249.08	50	260	0.1	-80	-30	20	2.02	20	CID	4	True	True
Uridine C7	Carbon	250.09	50	260	0.1	-80	-30	20	2.02	20	CID	4	True	True
Uridine C8	Carbon	251.09	50	260	0.1	-80	-30	20	2.02	20	CID	4	True	True
Uridine C9	Carbon	252.09	50	260	0.1	-80	-30	20	2.02	20	CID	4	True	True
IMP	Carbon	347.04	70	370	0.03	-80	-30	20	4.65	30	CID	4	True	True
IMP C1	Carbon	348.04	70	370	0.03	-80	-30	20	4.65	30	CID	4	True	True
IMP C2	Carbon	349.05	70	370	0.03	-80	-30	20	4.65	30	CID	4	True	True
IMP C3	Carbon	350.05	70	370	0.03	-80	-30	20	4.65	30	CID	4	True	True
IMP C4	Carbon	351.05	70	370	0.03	-80	-30	20	4.65	30	CID	4	True	True
IMP C5	Carbon	352.06	70	370	0.03	-80	-30	20	4.65	30	CID	4	True	True
IMP C6	Carbon	353.06	70	370	0.03	-80	-30	20	4.65	30	CID	4	True	True

IMP C7	Carbon	354.06	70	370	0.03	-80	-30	20	4.65	30	CID	4	True	True
IMP C8	Carbon	355.07	70	370	0.03	-80	-30	20	4.65	30	CID	4	True	True
IMP C9	Carbon	356.07	70	370	0.03	-80	-30	20	4.65	30	CID	4	True	True
IMP C10	Carbon	357.07	70	370	0.03	-80	-30	20	4.65	30	CID	4	True	True
Inosine	Carbon	267.07	50	280	0.06	-80	-30	20	2.87	20	CID	4	True	True
Inosine C1	Carbon	268.08	50	280	0.06	-80	-30	20	2.87	20	CID	4	True	True
Inosine C2	Carbon	269.08	50	280	0.06	-80	-30	20	2.87	20	CID	4	True	True
Inosine C3	Carbon	270.08	50	280	0.06	-80	-30	20	2.87	20	CID	4	True	True
Inosine C4	Carbon	271.09	50	280	0.06	-80	-30	20	2.87	20	CID	4	True	True
Inosine C5	Carbon	272.09	50	280	0.06	-80	-30	20	2.87	20	CID	4	True	True
Inosine C6	Carbon	273.09	50	280	0.06	-80	-30	20	2.87	20	CID	4	True	True
Inosine C7	Carbon	274.10	50	280	0.06	-80	-30	20	2.87	20	CID	4	True	True
Inosine C8	Carbon	275.10	50	280	0.06	-80	-30	20	2.87	20	CID	4	True	True
Inosine C9	Carbon	276.10	50	280	0.06	-80	-30	20	2.87	20	CID	4	True	True
Inosine C10	Carbon	277.11	50	280	0.06	-80	-30	20	2.87	20	CID	4	True	True
ATP	Carbon	505.99	70	600	0.1	-80	-30	20	7.1	40	CID	4	True	True
ATP C1	Carbon	506.99	70	600	0.1	-80	-30	20	7.1	40	CID	4	True	True
ATP C2	Carbon	508.00	70	600	0.1	-80	-30	20	7.1	40	CID	4	True	True
ATP C3	Carbon	509.00	70	600	0.1	-80	-30	20	7.1	40	CID	4	True	True
ATP C4	Carbon	510.00	70	600	0.1	-80	-30	20	7.1	40	CID	4	True	True
ATP C5	Carbon	511.01	70	600	0.1	-80	-30	20	7.1	40	CID	4	True	True
ATP C6	Carbon	512.01	70	600	0.1	-80	-30	20	7.1	40	CID	4	True	True
ATP C7	Carbon	513.01	70	600	0.1	-80	-30	20	7.1	40	CID	4	True	True
ATP C8	Carbon	514.02	70	600	0.1	-80	-30	20	7.1	40	CID	4	True	True
ATP C9	Carbon	515.02	70	600	0.1	-80	-30	20	7.1	40	CID	4	True	True
ATP C10	Carbon	516.02	70	600	0.1	-80	-30	20	7.1	40	CID	4	True	True
Adenosine	Carbon	266.09	50	280	0.06	-80	-30	20	1.72	20	CID	4	True	True
Adenosine C1	Carbon	267.09	50	280	0.06	-80	-30	20	1.72	20	CID	4	True	True
Adenosine C2	Carbon	268.10	50	280	0.06	-80	-30	20	1.72	20	CID	4	True	True
Adenosine C3	Carbon	269.10	50	280	0.06	-80	-30	20	1.72	20	CID	4	True	True
Adenosine C4	Carbon	270.10	50	280	0.06	-80	-30	20	1.72	20	CID	4	True	True
Adenosine C5	Carbon	271.11	50	280	0.06	-80	-30	20	1.72	20	CID	4	True	True
Adenosine C6	Carbon	272.11	50	280	0.06	-80	-30	20	1.72	20	CID	4	True	True
Adenosine C7	Carbon	273.11	50	280	0.06	-80	-30	20	1.72	20	CID	4	True	True
Adenosine C8	Carbon	274.12	50	280	0.06	-80	-30	20	1.72	20	CID	4	True	True
Adenosine C9	Carbon	275.12	50	280	0.06	-80	-30	20	1.72	20	CID	4	True	True
Adenosine C10	Carbon	276.12	50	280	0.06	-80	-30	20	1.72	20	CID	4	True	True
Glutamine	Carbon	145.06	40	155	0.03	-80	-30	20	5.01	20	CID	4	True	True
Glutamine C1	Carbon	146.07	40	155	0.03	-80	-30	20	5.01	20	CID	4	True	True
Glutamine C2	Carbon	147.07	40	155	0.03	-80	-30	20	5.01	20	CID	4	True	True
Glutamine C3	Carbon	148.07	40	155	0.03	-80	-30	20	5.01	20	CID	4	True	True
Glutamine C4	Carbon	149.08	40	155	0.03	-80	-30	20	5.01	20	CID	4	True	True
Glutamine C5	Carbon	150.08	40	155	0.03	-80	-30	20	5.01	20	CID	4	True	True
α -Ketoglutarate	Carbon	145.01	50	155	0.06	-80	-30	20	3.88	25	CID	4	True	True
α -Ketoglutarate C1	Carbon	146.02	50	155	0.06	-80	-30	20	3.88	25	CID	4	True	True
α -Ketoglutarate C2	Carbon	147.02	50	155	0.06	-80	-30	20	3.88	25	CID	4	True	True
α -Ketoglutarate C3	Carbon	148.02	50	155	0.06	-80	-30	20	3.88	25	CID	4	True	True
α -Ketoglutarate C4	Carbon	149.03	50	155	0.06	-80	-30	20	3.88	25	CID	4	True	True
α -Ketoglutarate C5	Carbon	150.03	50	155	0.06	-80	-30	20	3.88	25	CID	4	True	True
Citrate	Carbon	191.02	40	200	0.03	-80	-30	20	6.4	40	CID	4	True	True

Reconstruction of glutathione metabolism with HILIC-Zeno MRM

Citrate C1	192.02	40	200	0.03	-80	-30	20	6.4	40	CID	4	True	True
Citrate C2	195.03	40	200	0.03	-80	-30	20	6.4	40	CID	4	True	True
Citrate C3	194.03	40	200	0.03	-80	-30	20	6.4	40	CID	4	True	True
Citrate C4	195.03	40	200	0.03	-80	-30	20	6.4	40	CID	4	True	True
Citrate C5	196.04	40	200	0.03	-80	-30	20	6.4	40	CID	4	True	True
Citrate C6	197.04	40	200	0.03	-80	-30	20	6.4	40	CID	4	True	True
Succinate	117.02	40	125	0.06	-80	-30	20	3.13	25	CID	4	True	True
Succinate C1	118.02	40	125	0.06	-80	-30	20	3.13	25	CID	4	True	True
Succinate C2	119.03	40	125	0.06	-80	-30	20	3.13	25	CID	4	True	True
Succinate C3	120.03	40	125	0.06	-80	-30	20	3.13	25	CID	4	True	True
Succinate C4	121.03	40	125	0.06	-80	-30	20	3.13	25	CID	4	True	True
Fumarate	115.00	20	125	0.06	-80	-30	20	4.3	25	CID	4	True	True
Fumarate C1	116.01	20	125	0.06	-80	-30	20	4.3	25	CID	4	True	True
Fumarate C2	117.01	20	125	0.06	-80	-30	20	4.3	25	CID	4	True	True
Fumarate C3	118.01	20	125	0.06	-80	-30	20	4.3	25	CID	4	True	True
Fumarate C4	119.02	20	125	0.06	-80	-30	20	4.3	25	CID	4	True	True
Malate	133.01	40	140	0.07	-80	-30	20	4.2	25	CID	4	True	True
Malate C1	134.02	40	140	0.07	-80	-30	20	4.2	25	CID	4	True	True
Malate C2	135.02	40	140	0.07	-80	-30	20	4.2	25	CID	4	True	True
Malate C3	136.02	40	140	0.07	-80	-30	20	4.2	25	CID	4	True	True
Malate C4	137.03	40	140	0.07	-80	-30	20	4.2	25	CID	4	True	True
Pyruvate	87.01	40	95	0.06	-80	-30	20	1.85	35	CID	4	True	True
Pyruvate C1	88.01	40	95	0.06	-80	-30	20	1.85	35	CID	4	True	True
Pyruvate C2	89.02	40	95	0.06	-80	-30	20	1.85	35	CID	4	True	True
Pyruvate C3	90.02	40	95	0.06	-80	-30	20	1.85	35	CID	4	True	True
Phosphoenolpyruvate	166.98	50	175	0.03	-80	-30	20	5.4	25	CID	4	True	True
Phosphoenolpyruvate C1	167.98	50	175	0.03	-80	-30	20	5.4	25	CID	4	True	True
Phosphoenolpyruvate C2	168.98	50	175	0.03	-80	-30	20	5.4	25	CID	4	True	True
Phosphoenolpyruvate C3	169.99	50	175	0.03	-80	-30	20	5.4	25	CID	4	True	True
Lactate	89.02	40	95	0.06	-80	-30	20	2.92	35	CID	4	True	True
Lactate C1	90.03	40	95	0.06	-80	-30	20	2.92	35	CID	4	True	True
Lactate C2	91.03	40	95	0.06	-80	-30	20	2.92	35	CID	4	True	True
Lactate C3	92.03	40	95	0.06	-80	-30	20	2.92	35	CID	4	True	True

Table S4: Inclusion precursors covered in the ¹⁵N labeling MRM^{HR} acquisition method

Compound ID	Group Name	Precursor Ion (Da)	TOF Start Mass (Da)	TOF End Mass (Da)	Accumulation Time (sec)	DP (V)	CE (V)	CE Spread (V)	Fragmentation mode	Retention Time (min)	Retention time tolerance (+/-sec)	Time Bins to Scan	Channel1	Channel2	Channel3	Channel4
Glutamate	Nitrogen	146.05	40	160	0.08	-80	-30	20	4.75	20	CID	4	True	True	True	True
Glutamate N1	Nitrogen	147.04	40	160	0.08	-80	-30	20	4.75	20	CID	4	True	True	True	True
GABA	Nitrogen	102.06	40	110	0.1	-80	-30	20	5.7	20	CID	4	True	True	True	True
GABA N1	Nitrogen	103.05	40	110	0.1	-80	-30	20	5.7	20	CID	4	True	True	True	True
Glycine	Nitrogen	74.02	40	80	0.1	-80	-30	20	5.11	20	CID	4	True	True	True	True
Glycine N1	Nitrogen	75.02	40	80	0.1	-80	-30	20	5.11	20	CID	4	True	True	True	True
Cysteine	Nitrogen	120.01	40	125	0.1	-80	-30	20	4.06	20	CID	4	True	True	True	True
Cysteine N1	Nitrogen	121.01	40	125	0.1	-80	-30	20	4.06	20	CID	4	True	True	True	True
Serine	Nitrogen	144.04	40	160	0.08	-80	-30	20	4.59	20	CID	4	True	True	True	True
Serine N1	Nitrogen	145.03	40	160	0.08	-80	-30	20	4.59	20	CID	4	True	True	True	True
GSH	Nitrogen	306.08	50	320	0.08	-80	-30	20	4.56	20	CID	4	True	True	True	True
GSH N1	Nitrogen	307.07	50	320	0.08	-80	-30	20	4.56	20	CID	4	True	True	True	True
GSH N2	Nitrogen	308.07	50	320	0.08	-80	-30	20	4.56	20	CID	4	True	True	True	True
GSH N3	Nitrogen	309.07	50	320	0.08	-80	-30	20	4.56	20	CID	4	True	True	True	True
Aspartate	Nitrogen	132.03	50	140	0.08	-80	-30	20	4.76	25	CID	4	True	True	True	True
Aspartate N1	Nitrogen	133.03	50	140	0.08	-80	-30	20	4.76	25	CID	4	True	True	True	True
NAD	Nitrogen	662.10	80	700	0.08	-80	-30	20	5.1	30	CID	4	True	True	True	True
NAD N1	Nitrogen	663.10	80	700	0.08	-80	-30	20	5.1	30	CID	4	True	True	True	True
NAD N2	Nitrogen	664.10	80	700	0.08	-80	-30	20	5.1	30	CID	4	True	True	True	True
NAD N3	Nitrogen	665.09	80	700	0.08	-80	-30	20	5.1	30	CID	4	True	True	True	True
NAD N4	Nitrogen	666.09	80	700	0.08	-80	-30	20	5.1	30	CID	4	True	True	True	True
NAD N5	Nitrogen	667.09	80	700	0.08	-80	-30	20	5.1	30	CID	4	True	True	True	True
NAD N6	Nitrogen	668.08	80	700	0.08	-80	-30	20	5.1	30	CID	4	True	True	True	True
NAD N7	Nitrogen	669.08	80	700	0.08	-80	-30	20	5.1	30	CID	4	True	True	True	True
UTP	Nitrogen	482.96	70	500	0.1	-80	-30	20	7.2	40	CID	4	True	True	True	True
UTP N1	Nitrogen	483.96	70	500	0.1	-80	-30	20	7.2	40	CID	4	True	True	True	True
UTP N2	Nitrogen	484.96	70	500	0.1	-80	-30	20	7.2	40	CID	4	True	True	True	True
Uridine	Nitrogen	243.06	50	260	0.1	-80	-30	20	2.02	20	CID	4	True	True	True	True
Uridine N1	Nitrogen	244.06	50	260	0.1	-80	-30	20	2.02	20	CID	4	True	True	True	True
Uridine N2	Nitrogen	245.06	50	260	0.1	-80	-30	20	2.02	20	CID	4	True	True	True	True
UMP	Nitrogen	347.04	70	370	0.1	-80	-30	20	4.65	30	CID	4	True	True	True	True
UMP N1	Nitrogen	348.04	70	370	0.1	-80	-30	20	4.65	30	CID	4	True	True	True	True
UMP N2	Nitrogen	349.03	70	370	0.1	-80	-30	20	4.65	30	CID	4	True	True	True	True
UMP N3	Nitrogen	350.03	70	370	0.1	-80	-30	20	4.65	30	CID	4	True	True	True	True
IMP	Nitrogen	351.03	70	370	0.1	-80	-30	20	4.65	30	CID	4	True	True	True	True
IMP N1	Nitrogen	352.03	70	370	0.1	-80	-30	20	4.65	30	CID	4	True	True	True	True
Inosine	Nitrogen	267.07	50	280	0.1	-80	-30	20	2.87	20	CID	4	True	True	True	True
Inosine N1	Nitrogen	268.07	50	280	0.1	-80	-30	20	2.87	20	CID	4	True	True	True	True
Inosine N2	Nitrogen	269.07	50	280	0.1	-80	-30	20	2.87	20	CID	4	True	True	True	True
Inosine N3	Nitrogen	270.06	50	280	0.1	-80	-30	20	2.87	20	CID	4	True	True	True	True
Inosine N4	Nitrogen	271.06	50	280	0.1	-80	-30	20	2.87	20	CID	4	True	True	True	True
ATP	Nitrogen	505.99	70	600	0.1	-80	-30	20	7.1	40	CID	4	True	True	True	True
ATP N1	Nitrogen	506.99	70	600	0.1	-80	-30	20	7.1	40	CID	4	True	True	True	True
ATP N2	Nitrogen	507.98	70	600	0.1	-80	-30	20	7.1	40	CID	4	True	True	True	True
ATP N3	Nitrogen	508.98	70	600	0.1	-80	-30	20	7.1	40	CID	4	True	True	True	True
ATP N4	Nitrogen	509.98	70	600	0.1	-80	-30	20	7.1	40	CID	4	True	True	True	True
ATP N5	Nitrogen	510.98	70	600	0.1	-80	-30	20	7.1	40	CID	4	True	True	True	True
Adenosine	Nitrogen	246.09	50	280	0.1	-80	-30	20	1.72	20	CID	4	True	True	True	True
Adenosine N1	Nitrogen	247.09	50	280	0.1	-80	-30	20	1.72	20	CID	4	True	True	True	True
Adenosine N2	Nitrogen	248.08	50	280	0.1	-80	-30	20	1.72	20	CID	4	True	True	True	True
Adenosine N3	Nitrogen	249.08	50	280	0.1	-80	-30	20	1.72	20	CID	4	True	True	True	True
Adenosine N4	Nitrogen	250.08	50	280	0.1	-80	-30	20	1.72	20	CID	4	True	True	True	True
Adenosine N5	Nitrogen	251.07	50	280	0.1	-80	-30	20	1.72	20	CID	4	True	True	True	True
Glutamine	Nitrogen	145.06	40	155	0.08	-80	-30	20	5.01	20	CID	4	True	True	True	True
Glutamine N1	Nitrogen	146.06	40	155	0.08	-80	-30	20	5.01	20	CID	4	True	True	True	True
Glutamine N2	Nitrogen	147.06	40	155	0.08	-80	-30	20	5.01	20	CID	4	True	True	True	True

Table S5: Analysis of calibration curves by linear regression for targeted polar metabolites

Metabolite Name & Abbreviation		Monoisotopic peak quantification based on HILIC-Zeno MRM ^{HR} : MS ¹ TOF			Monoisotopic peak quantification based on HILIC-Zeno MRM ^{HR} : MS ² precursor ion		
		Range (µg/mL)	linear regression equation y=ax+b	Correlation coefficient r ²	Range (µg/mL)	linear regression equation y=ax+b	Correlation coefficient r ²
L-Glutamic acid	GLU	0.5-20	y = 0.09408x - 0.00654	0.9993	0.1-20	y = 0.09423x - 0.00184	0.99231
gamma-Aminobutyric acid	GABA	0.5-20	y = 0.01376x - 0.00321	0.9970	0.5-20	y = 0.02498x - 0.00722	0.98887
Glycine	GLY	2.5-20	y = 0.06750x - 0.02796	0.9705	0.1-20	y = 0.06265x - 0.00114	0.99284
Cysteine	CYS	0.5-20	y = 1.62624x - 0.13405	0.9849	0.5-20	y = 0.04268x - 0.00511	0.98631
Serine	SER	0.5-20	y = 1.85033x - 0.21612	0.9842	0.1-20	y = 0.15519x - 0.00468	0.99099
Glutathione	GSH	0.5-20	y = 0.65298x - 0.17207	0.9963	0.1-20	y = 0.19961x - 0.01335	0.99042
Oxidized glutathione	GSSG	1.25-20	y = 0.13221x - 0.07497	0.9957			
L-Aspartic acid	ASP	0.5-20	y = 0.06897x - 0.01162	0.9971	0.5-20	y = 0.08353x - 0.01169	0.98414
Glyceraldehyde 3-Phosphate	G3P	2.5-20	y = 0.13459x - 0.17471	0.9951	2.5-20	y = 0.05708x - 0.04520	0.97976
Quinolinic acid	QULN	0.5-10	y = 1.99410x - 0.56754	0.9932			
Nicotinic acid adenine dinucleotide	DNAD	0.1-20	y = 0.11626x - 0.00329	0.9993			
Nicotinamide adenine dinucleotide	NAD	0.1-20	y = 0.04911x + 0.00214	0.9978	0.1-20	y = 0.00661x - 0.00028	0.99223
Nicotinic acid	NAC	1.25-20	y = 0.49684x - 0.25695	0.9976			
Niacinamide	NCAM	0.5-7.5	y = 0.03137x + 0.46290	0.9783			
L-Tryptophan	TRP	0.1-15	y = 1.11278x - 0.02141	0.9969			
L-Kynurenine	KYNR	1.25-20	y = 0.25099x + 0.14489	0.9922			
D-Ribose 5-phosphate	R5P	1.25-20	y = 0.12687x + 0.05947	0.9959	0.5-20	y = 0.03181x + 0.00376	0.99025
Uridine 5'-monophosphate	UMP	1.25-20	y = 0.30577x + 0.14279	0.9924			
Uridine 5'-diphosphate	UDP	1.25-15	y = 0.18212x - 0.10722	0.9824			
Uridine triphosphate	UTP	0.5-20	y = 0.04053x - 0.00746	0.9972	0.5-20	y = 0.04263x - 0.00326	0.99768
Uridine	URI	1.25-20	y = 5.07060x + 2.06304	0.9936	1.25-20	y = 10.44443x + 4.55296	0.99138
L-Glutamine	GLN	2.5-20	y = 0.34789x - 0.45254	0.9916	1.25-20	y = 0.12971x - 0.07467	0.99017

Chapter IV

Inosinic acid	IMP	0.5-20	$y = 0.17864x + 0.04607$	0.9974	0.5-20	$y = 0.13977x + 0.03870$	0.99557
Inosine	INS	0.5-20	$y = 2.29697x + 0.53440$	0.9964	0.5-20	$y = 13.48598x + 3.15770$	0.99449
Adenosine monophosphate	AMP	0.5-20	$y = 0.21048x + 0.03594$	0.9983			
Adenosine diphosphate	ADP	1.25-20	$y = 0.19175x - 0.11881$	0.9918			
Adenosine triphosphate	ATP	0.5-20	$y = 0.07104x - 0.00830$	0.9990	0.5-20	$y = 0.07631x + 0.00275$	0.99854
Adenosine	ADN	0.5-20	$y = 0.53435x - 0.04505$	0.9985	0.5-20	$y = 0.77803x + 0.04799$	0.99665
Guanosine monophosphate	GMP	0.5-20	$y = 0.30406x + 0.02837$	0.9973			
Guanosine diphosphate	GDP	1.25-20	$y = 0.09374x - 0.04450$	0.9898			
Guanosine triphosphate	GTP	1.25-20	$y = 0.04653x - 0.01220$	0.9972			
Guanosine	GSN	1.25-20	$y = 1.49311x + 0.92908$	0.9949			
Oxoglutaric acid	AKG	0.5-20	$y = 0.37209x - 0.07267$	0.9962	0.5-20	$y = 0.07988x + 0.01483$	0.99109
Citric acid	CIT	2.5-15	$y = 0.0000112459x - 0.000020919$	0.9885	2.5-15	$y = 0.39052x - 0.68461$	0.98252
Succinic acid	SUCC	0.5-20	$y = 0.21359x - 0.01799$	0.9994	0.1-20	$y = 0.19293x + 0.00388$	0.99613
Fumaric acid	FUM	0.5-15	$y = 0.21057x - 0.01543$	0.9937	0.5-15	$y = 0.05153x + 0.00507$	0.98513
L-Malic acid	MAL	0.5-15	$y = 0.58386x - 0.21395$	0.9922	0.5-15	$y = 0.45951x - 0.16564$	0.99381
Pyruvic acid	PYR	0.5-20	$y = 0.12035x - 0.00952$	0.9986	0.1-20	$y = 0.14188x - 0.00227$	0.995
Phosphoenolpyruvic acid	PEP	1.25-20	$y = 0.06405x - 0.04292$	0.9871	0.5-20	$y = 0.01273x - 0.00236$	0.9869
L-Lactic acid	LAC	0.5-20	$y = 0.01475x + 0.00845$	0.9953	0.5-20	$y = 0.01674x + 0.00646$	0.99327

Table S6. Reproducibility evaluation of ^{13}C mass isotopologue distribution for one sample set with no dilution (n = 3), twofold dilution (n = 3), and threefold dilution (n = 3) measured by HILIC-Zeno MRM^{HR} method

Isotopologue	DF_1x (n=3)	DF_2x (n=3)	DF_3x (n=3)	Mean \pm SD	Inter CV %
	protein content: 38.0ug	protein content: 19.0ug	protein content: 12.7ug		
GLU_C ₅ H ₉ NO ₄ _M0	0.25 \pm 0.016	0.26 \pm 0.019	0.29 \pm 0.035	0.27 \pm 0.030	11.2
GLU_C ₅ H ₉ NO ₄ _M1	0.03 \pm 0.003	0.03 \pm 0.003	0.03 \pm 0.001	0.03 \pm 0.003	9.5
GLU_C ₅ H ₉ NO ₄ _M2	0.18 \pm 0.016	0.18 \pm 0.024	0.20 \pm 0.009	0.19 \pm 0.018	9.5
GLU_C ₅ H ₉ NO ₄ _M3	0.12 \pm 0.004	0.12 \pm 0.010	0.11 \pm 0.033	0.12 \pm 0.018	15.4
GLU_C ₅ H ₉ NO ₄ _M4	0.21 \pm 0.012	0.20 \pm 0.016	0.19 \pm 0.021	0.20 \pm 0.017	8.6
GLU_C ₅ H ₉ NO ₄ _M5	0.21 \pm 0.004	0.21 \pm 0.016	0.18 \pm 0.025	0.20 \pm 0.023	11.4
aKG_C ₃ H ₆ O ₃ _M0	0.20 \pm 0.010	0.18 \pm 0.019	0.16 \pm 0.015	0.18 \pm 0.021	11.6
aKG_C ₃ H ₆ O ₃ _M1	0.05 \pm 0.007	0.06 \pm 0.004	0.06 \pm 0.001	0.06 \pm 0.009	15.4
aKG_C ₃ H ₆ O ₃ _M2	0.28 \pm 0.017	0.30 \pm 0.034	0.32 \pm 0.011	0.30 \pm 0.027	8.8
aKG_C ₃ H ₆ O ₃ _M3	0.11 \pm 0.013	0.11 \pm 0.010	0.10 \pm 0.019	0.11 \pm 0.013	11.7
aKG_C ₃ H ₆ O ₃ _M4	0.19 \pm 0.022	0.18 \pm 0.018	0.18 \pm 0.010	0.18 \pm 0.017	9.4
aKG_C ₃ H ₆ O ₃ _M5	0.17 \pm 0.002	0.16 \pm 0.019	0.17 \pm 0.005	0.17 \pm 0.011	6.7
GSH_C ₁₀ H ₁₇ N ₃ O ₆ S_M0	0.25 \pm 0.016	0.24 \pm 0.046	0.23 \pm 0.03	0.24 \pm 0.03	12.4
GSH_C ₁₀ H ₁₇ N ₃ O ₆ S_M1	0.06 \pm 0.003	0.06 \pm 0.009	0.07 \pm 0.008	0.07 \pm 0.007	10.9
GSH_C ₁₀ H ₁₇ N ₃ O ₆ S_M2	0.20 \pm 0.021	0.19 \pm 0.042	0.18 \pm 0.039	0.19 \pm 0.032	16.8
GSH_C ₁₀ H ₁₇ N ₃ O ₆ S_M3	0.09 \pm 0.015	0.10 \pm 0.011	0.10 \pm 0.014	0.09 \pm 0.012	12.3
GSH_C ₁₀ H ₁₇ N ₃ O ₆ S_M4	0.16 \pm 0.016	0.14 \pm 0.033	0.16 \pm 0.016	0.15 \pm 0.022	14.2
GSH_C ₁₀ H ₁₇ N ₃ O ₆ S_M5	0.12 \pm 0.009	0.13 \pm 0.026	0.13 \pm 0.028	0.13 \pm 0.020	16.0
GSH_C ₁₀ H ₁₇ N ₃ O ₆ S_M6	0.06 \pm 0.005	0.07 \pm 0.005	0.06 \pm 0.004	0.06 \pm 0.007	11.3
GSH_C ₁₀ H ₁₇ N ₃ O ₆ S_M7	0.04 \pm 0.005	0.04 \pm 0.008	0.05 \pm 0.008	0.04 \pm 0.009	21.2
GSH_C ₁₀ H ₁₇ N ₃ O ₆ S_M8	0.01 \pm 0.001	0.01 \pm 0.002	0.01 \pm 0.002	0.01 \pm 0.002	24.2
GSH_C ₁₀ H ₁₇ N ₃ O ₆ S_M9	0.01 \pm 0.001	0.01 \pm 0.003	0.01 \pm 0.002	0.01 \pm 0.002	15.6
GSH_C ₁₀ H ₁₇ N ₃ O ₆ S_M10	0 \pm 0	0 \pm 0	0 \pm 0	0 \pm 0	15.4
GLU_FragC ₄ H ₉ NO ₂ _M0	0.27 \pm 0.004	0.27 \pm 0.019	0.27 \pm 0.010	0.27 \pm 0.011	4.1
GLU_FragC ₄ H ₉ NO ₂ _M1	0.17 \pm 0.007	0.17 \pm 0.012	0.18 \pm 0.004	0.17 \pm 0.010	5.7
GLU_FragC ₄ H ₉ NO ₂ _M2	0.12 \pm 0.003	0.12 \pm 0.005	0.12 \pm 0.003	0.12 \pm 0.003	2.8
GLU_FragC ₄ H ₉ NO ₂ _M3	0.22 \pm 0.008	0.22 \pm 0.015	0.21 \pm 0.002	0.22 \pm 0.010	4.5
GLU_FragC ₄ H ₉ NO ₂ _M4	0.22 \pm 0.005	0.22 \pm 0.010	0.22 \pm 0.012	0.22 \pm 0.009	4.3
aKG_FragC ₄ H ₆ O ₃ _M0	0.26 \pm 0.020	0.24 \pm 0.021	0.23 \pm 0.024	0.24 \pm 0.022	8.9
aKG_FragC ₄ H ₆ O ₃ _M1	0.14 \pm 0.009	0.15 \pm 0.020	0.15 \pm 0.008	0.14 \pm 0.012	8.2
aKG_FragC ₄ H ₆ O ₃ _M2	0.13 \pm 0.005	0.14 \pm 0.013	0.13 \pm 0.003	0.13 \pm 0.008	5.6
aKG_FragC ₄ H ₆ O ₃ _M3	0.23 \pm 0.015	0.23 \pm 0.006	0.23 \pm 0.026	0.23 \pm 0.015	6.8
aKG_FragC ₄ H ₆ O ₃ _M4	0.24 \pm 0.015	0.25 \pm 0.009	0.25 \pm 0.009	0.25 \pm 0.011	4.4
GSH_FragC ₃ H ₆ NO ₃ _M0	0.34 \pm 0.008	0.34 \pm 0.037	0.34 \pm 0.012	0.34 \pm 0.020	5.9
GSH_FragC ₃ H ₆ NO ₃ _M1	0.06 \pm 0.003	0.06 \pm 0.002	0.05 \pm 0.005	0.06 \pm 0.003	6.1
GSH_FragC ₃ H ₆ NO ₃ _M2	0.19 \pm 0.010	0.18 \pm 0.0106	0.19 \pm 0.017	0.19 \pm 0.013	7.1
GSH_FragC ₃ H ₆ NO ₃ _M3	0.11 \pm 0.012	0.12 \pm 0.016	0.12 \pm 0.005	0.11 \pm 0.011	10.1
GSH_FragC ₃ H ₆ NO ₃ _M4	0.16 \pm 0.011	0.17 \pm 0.010	0.15 \pm 0.009	0.16 \pm 0.011	6.6
GSH_FragC ₃ H ₆ NO ₃ _M5	0.14 \pm 0.006	0.14 \pm 0.010	0.15 \pm 0.012	0.14 \pm 0.008	5.9

Table S7. Determination of isotopomers distribution of $^{13}\text{C}_2$ -glutamate according to the labeling pattern of specific fragments in MS² spectrum

sample	Ratio			Ratio		Fraction		
	Frag_1 m+0	Frag_1 m+1	Frag_1 m+2	M+2_ 1,2- $^{13}\text{C}_2$ - Glutamate	M+2_ 3,4- $^{13}\text{C}_2$ - Glutamate	M+2	M+2_ 1,2- $^{13}\text{C}_2$ - Glutamate	M+2_3,4- $^{13}\text{C}_2$ - Glutamate
	Control_C13_1	0	0.67	0.33	0.67	0.33	0.18	0.12
Control_C13_2	0	0.68	0.32	0.68	0.32	0.19	0.13	0.06
Control_C13_3	0	0.69	0.31	0.69	0.31	0.18	0.13	0.06
Control_C13_4	0	0.66	0.34	0.66	0.34	0.18	0.12	0.06
Control_C13_5	0	0.68	0.32	0.68	0.32	0.2	0.14	0.06
Rotenone_C13_1	0.01	0.79	0.21	0.79	0.21	0.17	0.14	0.04
Rotenone_C13_2	0.01	0.79	0.2	0.79	0.2	0.19	0.15	0.04
Rotenone_C13_3	0.01	0.78	0.21	0.78	0.21	0.21	0.16	0.04
Rotenone_C13_4	0.01	0.78	0.21	0.78	0.21	0.2	0.16	0.04
Rotenone_C13_5	0.01	0.79	0.2	0.79	0.2	0.17	0.13	0.03

Table S8. Determination of isotopomers distribution of $^{13}\text{C}_2$ -glutathione according to the labeling pattern of specific fragments in MS² spectrum

sample	Ratio			Fraction			
	Frag_1 m+0 (M+2_ $^{13}\text{C}_2$ -Gly)	Frag_1 m+1 (M+2_ $^{13}\text{C}_1$ -Gly+ $^{13}\text{C}_1$ -Glu)	Frag_1 m+2 (M+2_ $^{13}\text{C}_2$ -Glu)	M+2	M+2_ $^{13}\text{C}_2$ -Gly	M+2_ $^{13}\text{C}_1$ - Gly+ $^{13}\text{C}_1$ -Glu	M+2_ $^{13}\text{C}_2$ -Glu
	Control_C13_1	0.16	0	0.84	0.2	0.03	0
Control_C13_2	0.17	0	0.83	0.21	0.03	0	0.17
Control_C13_3	0.15	0	0.85	0.19	0.03	0	0.16
Control_C13_4	0.15	0	0.85	0.16	0.02	0	0.13
Control_C13_5	0.14	0	0.85	0.17	0.02	0	0.14
Rotenone_C13_1	0.61	0.01	0.39	0.04	0.03	0	0.02
Rotenone_C13_2	0.57	0.01	0.42	0.05	0.03	0	0.02
Rotenone_C13_3	0.53	0.01	0.47	0.04	0.02	0	0.02
Rotenone_C13_4	0.53	0.01	0.46	0.04	0.02	0	0.02
Rotenone_C13_5	0.55	0.01	0.44	0.05	0.02	0	0.02

Chapter 5:

fluxTrAM: Integration of tracer-based metabolomics data into atomically resolved genome-scale metabolic networks for metabolic flux analysis

Based on:

Luojiao Huang[†], German Preciat[†], Jesus Alarcon-Gil[†], Edinson L. Moreno, Agnieszka Wegrzyn, Ines Thiele, Emma Schymanski, Amy Harms, Ronan M.T. Fleming, Thomas Hankemeier

fluxTrAM: Integration of tracer-based metabolomics data into atomically resolved genome-scale metabolic networks for metabolic flux analysis

Manuscript submitted

[†] Shared first authors

Abstract

Quantitative inference of intracellular reaction rates is essential for characterizing metabolic phenotypes. The classical experimental method for measuring metabolic fluxes makes use of stable-isotope tracing of metabolites through the metabolic network, followed by mass spectrometry analysis. Established ^{13}C -based metabolic flux analysis requires multidisciplinary knowledge in analytical chemistry, cell biology, and mathematical modelling, as well as the use of multiple independent software tools for handling mass spectrometry data and integration with a metabolic model. This approach is usually carried out within a small network rather than at genome-scale. To overcome interdisciplinary barriers and extend flux interpretation towards genome-scale, we developed fluxTrAM, a semi-automated pipeline for processing tracer-based metabolomics data and integrating it with atomically resolved genome-scale metabolic networks to enable flux predictions at genome-scale. fluxTrAM integrates several external software packages with the COBRA Toolbox enabling the generation of metabolite structure and reaction databases for a genome-scale model, processing of labelled mass spectrometry data into standardised mass isotopologue distribution data (MID), and metabolic flux inference. To demonstrate the utility of this pipeline, we generated ^{13}C -labeled metabolomics data on an *in vitro* human induced pluripotent stem cell (iPSC)-derived dopaminergic neuronal culture and processed ^{13}C -labeled MID datasets. In parallel, we generated a chemoinformatic database of standardised metabolite structures and atom-mapped reactions for a genome-scale dopaminergic neuronal metabolic model. MID data were integrated into an atomically resolved metabolic model for flux inference at genome-scale using a novel moiety fluxomics method. Inferred fluxes were compared with the MID data exported to established flux inference software for conventional flux inference with a central metabolic model. Flux vectors inferred by conventional and moiety fluxomic approaches were comparable but not identical. Further analysis are necessary with a genome-scale model that is suitable for both conventional and moiety fluxomic approaches to flux inference. Nevertheless, fluxTrAM enables the automation of labelled liquid chromatography (LC)-mass spectrometry (MS) data processing into MID datasets and atom mapping for any given genome-scale metabolic model. It contributes to the standardization and high throughput of metabolic flux analysis towards a genome-scale.

Introduction

Fluxomics aims for quantification of reaction flux at a genome-scale to comprehensively characterise cellular metabolism. Quantification of reaction flux is challenging as, unlike molecular species abundance, intracellular fluxes cannot be directly measured but must be indirectly inferred from measurements of labelled molecular species [1]. A typical in vitro fluxomic workflow proceeds from experimental design and cell culture implementation, to mass spectrometric data generation and processing, and finally to inference of reaction flux by computational modelling [2]. Therefore, progress in fluxomics is dependent on overcoming challenges in a set of complementary fields, including cell biology, analytical chemistry, and mathematical modelling. Herein, we focus on overcoming challenges in automated data handling, processing of mass spectrometry data and preparing an atom mapped model, which ultimately enables computational inference of metabolic flux.

Metabolomics allows a broad profiling of metabolites that connect diverse biochemical reactions in a metabolic network. Given a chromatographic co-elution of metabolite isotopologue peaks, reliable measurement of stable isotopically labeled metabolites requires a high capacity for analytical technology in molecule separation or peak resolution. Recent developments in mass spectrometry (MS) coupled with separation chromatography (gas chromatography, GC, or liquid chromatography, LC) improve the measurement accuracy of metabolite labelling patterns, as well as increase the coverage of metabolite classes [3,4]. In this way, metabolic flux profiling within a large-scale model becomes possible and can have the advantage of providing a systematic view of metabolism. Along with this, an advanced flux profiling approach at a genome-scale level is required.

By measuring a complex biological sample, high resolution (HR) LC-MS generates a large volume of MS raw data especially with a long analytical run for sufficient chromatographic separation. With the challenges of increased targeted metabolites, co-elution adding to the mass spectral complexity and multiple biological replicates in a tracer experiment, it becomes more difficult to process isotopologue labelling data. Manual peak integration to obtain the mass isotopologue distribution (MID) of each target metabolite becomes increasingly time-consuming and error-prone. To improve data quality and reproducibility, several automated peak detection and extraction packages have been developed for LC-HRMS [5–8], that enable automation of tracer-based metabolomics data processing. For instance, X¹³CMS provides unbiased retrieval of isotopologue groups from isotopically labelled compounds between experimental conditions. MetExtract focuses on identifying the entire labelled metabolome and annotating unknown metabolites from mixtures of uniformly highly isotope-enriched and native biological samples. mzMatch-ISO offers its functionality in both automated untargeted metabolite annotation and relative quantification

of metabolite isotopologues. For our goal of targeted MID analysis, a pre-evaluation of each tool's suitability for incorporation into a standardised workflow is indispensable.

The advancement of high-throughput experimental technology has increased the demand for computational approaches to integrate complementary sources of omics data [9–11]. One such approach is integration of omics data with genome-scale computational models of biochemical networks, which are reconstructed from experimental data on molecular species and biochemical reactions [12]. Genome-scale models are especially useful for predicting metabolic reaction flux [13]. However, quantitative inference of intracellular metabolic reaction flux by integration of MID data with a genome-scale metabolic model is challenging and typically is done with a subnetwork model [14].

Integration of experimental MID data with metabolic modelling is currently challenging. On the one hand, the input of experimental MID data always needs external pre-processing including correction of naturally occurring isotopes and tracer purity, which involves intense user manipulation. On the other hand, currently available ^{13}C flux analysis programs implement non-linear optimization by minimizing the difference between measured and iteratively simulated MIDs to compute an optimal flux solution within a specified metabolic network [15–18]. Context-specific omics data supported by literature curation as well as modelling expertise are required to generate an organism-specific network model. Furthermore, for flux inference, a metabolic model must be atomically resolved such that the atom mapping from substrate to product atoms is obtained, manually for small networks or automatically for larger models. Automating the MID data processing and atom transitions resolving into a continuous workflow would be beneficial to accelerate metabolic modelling at genome-scale.

A reaction in a genome-scale metabolic network can be represented by a set of atom transitions, each of which connects an atom in a substrate metabolite to this atom in a product metabolite, forming an atom mapping for a reaction. Atom-mappings can be algorithmically predicted at genome-scale [19] and when compared with manually curated biochemical reactions, accurately predict atom mapping for ~90% of human metabolic reactions [20]. Connecting sets of atom mappings for a metabolic network enables one to atomically resolve a metabolic network at genome-scale [13]. Based on this approach, automated workflows for atom mapping have been developed for several species, including human [20] and *Arabidopsis thaliana* metabolism [21]. However, to have atomically balanced metabolic reactions, it is necessary to identify the structures for each metabolite in a genome-scale model. By including external chemoinformatics software such as Open Babel [22], CXCALC [23] and the Reaction Decoder Tool (RDT) [24] it is possible to convert between chemical formats, identify the pH required to balance the number of

hydrogens in the substrates and products, and thereby atom-map balanced metabolic reactions.

Graph theoretical analysis of an atomically resolved metabolic network enables identification of conserved moieties, each of which is a set of atoms that remains invariant with respect to all metabolic transformations in a given network [25]. The existence of conserved moieties means that a biochemical network is a special type of hypergraph [25], in the sense that the underlying stoichiometric matrix has special mathematical properties not shared with a general rectangular matrix corresponding to a general hypergraph. Fundamentally, this special property arises because one can represent a biochemical network at an atomic level [26]. In a companion paper [27], we exploited this property to develop a new mathematical and computational method that linearly relates metabolic reaction flux to the rate at which each labelled or unlabelled conserved moiety transitions between metabolites. Given mass isotopologue distribution data, this *moiety fluxomics* method enables inference of metabolic reaction flux at genome-scale.

Herein, we present fluxTrAM, a novel pipeline for flux inference with tracer-based metabolomics data and atomically resolved genome-scale model. fluxTrAM is an extension to the COBRA Toolbox v3.4 [13] that also takes advantage of existing third-party packages to achieve automated atom mappings and processing of labelled LC-MS data. It generates a chemoinformatic database of standardised and context-specific metabolite structures based on their InChI string and atom-mapped reactions for a given genome-scale metabolic reconstruction. In parallel, wrapper functions interface with third-party packages to enable processing of LC-MS raw data to generate standardised labelling data. This standardised MID data was subsequently used for established approaches to flux inference as well as a novel moiety fluxomics approach to flux inference where MID data was integrated with an atomically resolved metabolic model to infer the internal fluxes at genome-scale [27]. The utility of the pipeline was demonstrated by using stable-isotope labelled LC-MS data from a human dopaminergic neuronal culture, where conventional ^{13}C metabolic flux analysis was compared with fluxes inferred using moiety fluxomics and also genome scale flux predictions that were independent of labelling data. Based on inferred fluxes, the pipeline also enabled prediction of moieties to be considered for labelling when designing a new labelling experiment to further explore dopaminergic neuron metabolism.

Materials and methods

An overview of the methodology is given in **Figure 1** and described in detail below.

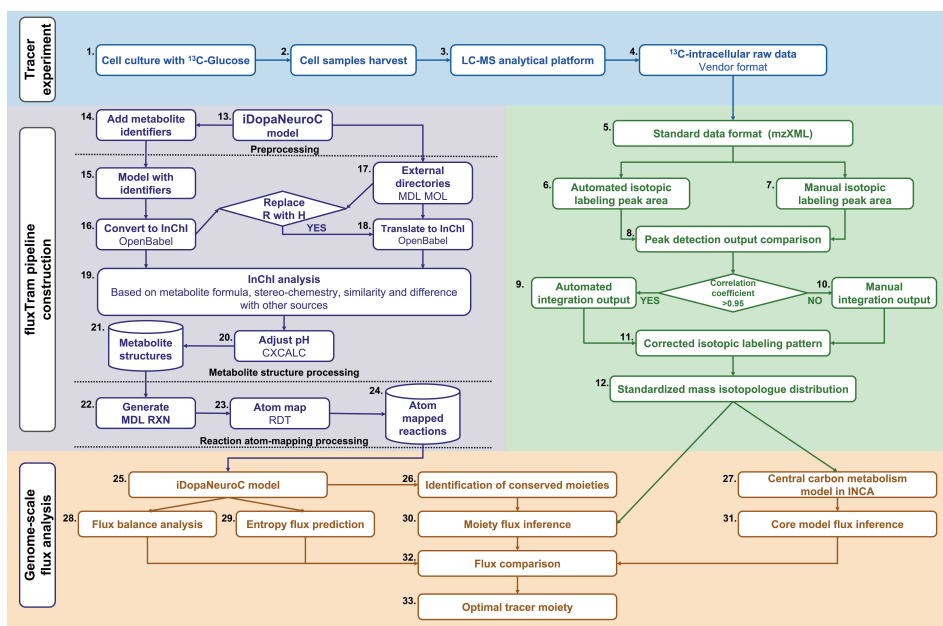


Figure 1. Methodological overview.

In vitro cell culture was fed with fully ^{13}C labelled glucose (1). Labelled cellular samples were collected after certain exposure time (2). A validated LC-MS platform [28] was established to measure labelled intracellular samples (3). Labelled intracellular raw mass spectral data were converted into a standard format (4, 5) and automated peak integration was used to obtain an isotopic labelling pattern (6, 9), unless it showed low correlation (8) to that obtained by manual peak integration (7, 10). Isotopic labelling patterns were converted to mass isotopologue distribution data in a standard format (11, 12). In parallel, atom mapping data was obtained from a genome-scale metabolic network by adding structural chemoinformatic data for each metabolite in the network if required (13-15), or using existing external data (17). The structural chemoinformatic data for each source in the model was used to generate an InChI (16, 18) where any R group in a metabolite structure was replaced by a hydrogen atom. The InChI strings obtained were compared to select the most representative structure for the genome-scale model (19). The number of hydrogen atoms of the highest-scoring metabolite structures was adjusted to match the number of hydrogens at which the metabolite is represented in the metabolic model of dopaminergic neuronal metabolism (iDopaNeuroC) (20), resulting in a database of standardised metabolite structures (21). The metabolic network stoichiometry and metabolite structure database were used to express each reaction in an atomically resolved reaction format (22), which was then atom-mapped (23) to generate an atom-mapped reaction database (24). Atom mapping data was used to identify the conserved moieties in the iDopaNeuroC model (25, 26). The standardised mass isotopologue distributions together with conserved moieties were used as constraints on the

iDopaNeuroC model to infer fluxes using the moiety fluxomic method (30). Fluxes inferred using the moiety fluxomic method were compared with predictions of fluxes without any isotopologue constraints on the iDopaNeuroC using flux balance analysis (FBA, 28) and entropic flux balance analysis [29] (29). Furthermore, the standardised mass isotopologue distribution data was imported established flux inference software (INCA [16,30]) using a central carbon metabolism model (27, 31). We compared inferred fluxes generated from the four different approaches: moiety flux inference, FBA flux prediction, entropy flux prediction and central carbon metabolism flux inference using INCA (32). Optimal genome-scale flux solutions were selected and used to further screen candidate tracer moieties for a new labelling culture experiment (33).

1. Tracer experiment

1.1 In vitro cell culture

Generation of an *in vitro* culture of midbrain-specific dopaminergic neurons followed an established protocol [31,32], with the adaptations described below. This culture method was the same as that used for generation of iDopaNeuroC model [29] a context-specific model of dopaminergic neuronal metabolism.

N2B27 medium preparation

The culture medium, denoted N2B27 medium, was used as the basis to prepare both maintenance and differentiation media. 49.25 mL of culture medium was obtained by mixing 24 mL Neurobasal medium (Invitrogen/Life Technologies), 24 mL of Dulbecco's modified Eagle's medium (DMEM)/F12 medium (Invitrogen/Life Technologies) supplemented with 1% penicillin and streptomycin (Life Technologies), 0.5 mL of 200 mM L-glutamine (Life Technologies), 0.5 mL of B27 supplement without Vitamin A (Life Technologies) and 0.25 mL of N2 supplement (Life Technologies). Glucose-free N2B27 medium was made in the same way, but with the Neurobasal medium replaced with Neurobasal medium with no D-glucose (Invitrogen/Life Technologies), and the DMEM/F12 medium replaced with stable isotope labeling with amino acids in cell culture (SILAC) advanced DMEM/F-12 Flex medium with no glucose (Invitrogen/Life Technologies).

Plate coating

Cell-culture treated 12-well plates (ThermoFisher scientific) were coated with 1% Matrigel (Discovery Labware, Inc., USA, Catalogue number 354277) in 600 μ L of DMEM (1X) medium supplemented with knockout serum replacement (ThermoFisher scientific).

Cell seeding and maintenance

At the time of cell seeding, the knockout DMEM (1X) medium from the coating step was removed from each well and the K7 hNESc line was seeded in three replicate wells. The medium to maintain the hNESc in culture, denoted maintenance medium, was based on

N2B27 medium with 0.5 μM PMA (Enzo life sciences), 3 μM CHIR (Axon Medchem) and 150 μM ascorbic acid (Sigma Aldrich). The cell seeding was done by preparing 1.8×10^6 million cells/mL in maintenance medium and adding 300 μL of this preparation together with another 300 μL of maintenance medium to reach 4×10^5 cells per well. The plate was incubated at 37 $^\circ\text{C}$ and 5% CO_2 for 48 h.

Neuronal differentiation and maturation

The differentiation medium with PMA was prepared to induce the differentiation of hNESc towards midbrain dopaminergic neurons and consisted of N2B27 medium with 200 μM ascorbic acid, 0.01 ng/ μL BDNF (Peprotech), 0.01 ng/ μL GDNF (Peprotech), 0.001 ng/ μL TGF β 3 (Peprotech), 2.5 μM dbcAMP (Sigma Aldrich) and 1 μM PMA. This medium was completely replaced every 2 days during the next 6 days of culture in the differentiation process. For the maturation of differentiated neurons, PMA is required to be absent from the differentiation medium [31,32]. This differentiation medium without PMA was used from day 9 onwards and complete media replacement was done every 2 days for 2 weeks.

^{13}C -labelled neuron culture and sample collection

^{13}C -labelled differentiation medium without PMA was prepared using glucose-free N2B27 medium, supplemented with 20.4 mM fully carbon labelled U- $^{13}\text{C}_6$ -glucose (Cambridge Isotope Laboratories, USA), 200 μM ascorbic acid, 0.01 ng/ μL BDNF, 0.01 ng/ μL GDNF, 0.001 ng/ μL TGF β 3, 2.5 μM dbcAMP. For the pilot stable isotopic labelling study set, differentiated neurons were maintained in two groups separately with ^{13}C labelled and unlabelled medium. Three replicate wells of neurons from each group were incubated under 37 $^\circ\text{C}$ and 5% CO_2 condition for 4 hours before quenching. For the formal stable isotopic labelling study set, dopaminergic neurons were cultured in labelled medium at 37 $^\circ\text{C}$ and 5% CO_2 conditions with different incubation times, from 0min, 5min, 10min, 20min, 40min, 1h, 2h, 3h, 5h, 8h, 12h to 24h. Each condition group was run in triplicates. The spent medium was collected into a 1.5 mL Eppendorf tube. Neurons in each well were immediately quenched by using ice-cold 80% MeOH in water and harvested into a 1.5 mL Eppendorf tube as cell lysate. All samples were fast frozen into liquid nitrogen and stored in the -80 $^\circ\text{C}$ freezer until measurement.

1.2 Sample measurement

Labelled cellular samples were measured on a liquid chromatography-mass spectrometry (LC-MS) platform to obtain the mass isotopologue distribution (MID) of target metabolites (SM4. Table S1) [28]. The concentrations of U- $^{13}\text{C}_6$ -glucose in cell and medium were quantified using the same platform. The cell lysate was sonicated, vortexed and then centrifuged at 16000 relative centrifugal force (rcf), at 4 $^\circ\text{C}$ for 10 min. Cell pellets were collected to measure the protein content using a bicinchoninic acid (BCA) assay (Thermo

Fisher Scientific Inc, USA). Supernatants were transferred into clean 1.5 mL Eppendorf tubes and evaporated to dryness in a Labcono SpeedVac (MO, United State). Each sample was reconstituted with 60 μL ice cold methanol/water (80%/20%; v/v). 50 μL of the reconstitution volume was collected and transferred into a new Eppendorf tube as a cell supernatant sample. Next, 50 μL (5 μL) of each cell supernatant (medium) sample was treated with liquid-liquid extraction by adding 40 μL of ice-cold methanol/water (80%/20%; v/v), 45 μL of ice cold milliQ water and 65 μL of ice-cold chloroform, followed with mixing and vortexing for 5 min and centrifuging at 16000 rcf 4 °C for 10 min. 130 μL of the aqueous phase was transferred into a new Eppendorf tube and extracted again by adding 25 μL of ice-cold methanol/water (50%/50%; v/v) and 65 μL of ice-cold chloroform, followed with mixing and vortexing for 5 min and centrifuging at 16000 rcf, 4 °C for 10 min. 140 μL of the upper aqueous phase was collected and taken to dryness. The residue was reconstituted with 50 μL of methanol/water (50%/50%; v/v), vortex-mixed, and centrifuged to remove debris. The supernatants were finally transferred to vials for LC-MS analysis.

LC-MS analysis was performed on a SCIEX tripleTOF 5600 MS system (SCIEX, USA) coupled to a Waters Acquity UPLC Class II (Waters, USA) equipped with a SeQuant® ZIC®-cHILIC HPLC column (2.1 mm x 100 mm, 3.0 μm , Merck, Germany). The LC-MS method was previously reported [28]. Mobile phase A was 90% acetonitrile, 10% water with 5 mM ammonium formate, and mobile phase B was 10% acetonitrile, 90% water with 5 mM ammonium formate. LC elution followed a nonlinear gradient that starts from 0% B (0-2 min) to 40% B (20 min), ends up with 0% B (20.1-35 min). The flow rate was 0.25 mL/min and the injection volume was 3 μL . The MS detection was set for a scan range of 50-900 m/z . Acquired raw LC-MS data files were stored in vendor-specific formats (.wiff and .wiff.scan).

2. Tracer-based metabolomics data processing

A pipeline for processing of tracer-based metabolomic data was developed, which takes raw mass spectrometry data as input and ultimately generates mass isotopologue distribution data in standard format as output (**Figure 2**). This pipeline is implemented in MATLAB (Mathworks Inc, USA), but calls several established external software tools for (i) LC-MS raw data conversion, (ii) Peak detection and extraction, (iii) Isotopologue peak correction, (iv) Isotopologue peak summary.

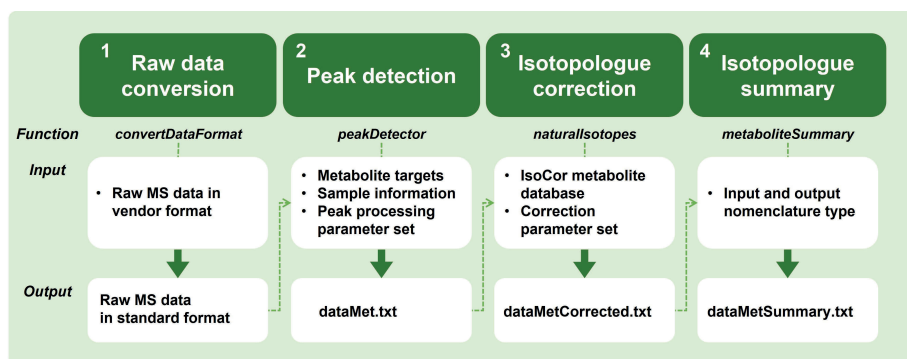


Figure 2. The schematic representation of tracer-based metabolomics data processing pipeline.

In step 1, 'Raw data conversion', raw LC-MS data was processed by the function '*convertDataFormat*' into MS data in standard format. In step 2, 'Peak detection', standardized MS data used additional inputs for running function '*peakDetector*' to generate a result table of metabolite integration in a text file 'dataMet.txt'. At step 3, 'Isotopologue correction', the dataMet.txt file, the isoCor metabolite database, and the correction parameter set were used as inputs for running the function '*naturalIsotopes*' to remove the isotopic impurity of tracer and the naturally occurring isotopic abundance. This created a 'dataMetCorrected.txt' file with a corrected integration table. In step 4, 'Isotopologue summary', the dataMetCorrected.txt file was used as an input together with the entered nomenclature types for running function '*metaboliteSummary*', which finally generated a 'dataMetSummary.txt' file with an integration table including interconverted metabolite nomenclatures and summarized MID results shown in mean and standardized deviation.

LC-MS raw data conversion

A wrapper function (*convertDataFormat*, *MATLAB*) was created based on ProteoWizard msconvert tool [33] for the pipeline to run 'msconvert.exe' externally and automatically but still within a MATLAB environment. It is used to convert vendor-specific formats to standard formats (mzML, mzXML, MGF, MS2/CMS2/BMS2, mzIdentML). The specific output format for fluxTrAM is centroid mode in mzXML with zlib compression.

Peak detection and extraction

To select one automated peak extraction software package, two candidate packages (mzMatch-ISO [7] and X¹³CMS [6]) were compared with two manual peak picking software packages (EIMAVEN [34], Skyline [35]). The two manual peak integration software packages (Skyline and EIMAVEN) utilised a common target metabolite list with exact molecular formula and expected retention time for peak detection. A threshold of 10 ppm was applied so that interferences from ions with close masses could be eliminated during peak extraction. In a first step of applying automated packages, XCMS [5] was used for the initial peak detection and alignment. The optimal values for the parameter settings

used in XCMS, mzMatch-ISO and X¹³CMS analysis were tested in R (*as supplementary files*: X¹³CMS_src.R, mzmatch_install.R). Five types of metabolite classes from the pilot stable isotopic labelling experiment were analysed, which included three amino acids (alanine, aspartate, glutamate), three organic acids (phosphoenolpyruvate, ketoglutarate, fumarate), one sugar phosphate (fructose 1,2-biphosphate), one tripeptide (glutathione), and one nucleotide (ATP). Pearson correlation was used to evaluate the normalised integrated peak area in automated and manual ways, and finally select one package for the automated data processing.

A wrapper function (*peakDetector*, **MATLAB**) was created based on (XCMS [5], mzMatch-ISO [7]) packages for the pipeline to execute R packages still within the MATLAB environment. Converted LC-MS data was first analysed using XCMS to extract peaks. All detected peak features were then processed by mzMatch-ISO for aligning, noise filtering, gap-filling peaks, and later forming into a combined PeakML file containing all samples. Based on the input of a targeted metabolite list, automated profiling could be performed to extract relevant isotopologue peaks.

Isotopologue peak correction

For the correction of incomplete labeling of the isotopic tracer and naturally isotopic abundance in metabolites, a wrapper function (*naturalIsotopes*, **MATLAB**) was created based on IsoCor [36] for the pipeline to excute the Python module within a MATLAB environment. Relying on the experimental inputs, such as MS resolution, isotopic tracer type, isotopic purity, the extracted isotopologue peaks for each metabolite were corrected to only preserve the isotopic abundance resulting from the isotopic tracer. The final output was the corrected MID data of each metabolite in each sample.

Isotopologue peak summary

The function *metaboliteSummary* was created to summarize the MID data from each individual sample into the average MID and corresponding standard deviation. In addition, it also recognises and converts between different possible metabolite nomenclatures (such as Virtual Metabolic Human [37] (VMH) Abbreviation or Full Name, the Kyoto Encyclopaedia of Genes and Genomes database [38] (KEGG), the Human Metabolome Database [39] (HMDB), the International Union of Pure and Applied Chemistry (IUPAC), the International Chemical Identifier (InChI) String and InChIKey [40], the Simplified Molecular-Input Line-Entry System (SMILES) [41]) through the VMH database [37].

3. Atomically resolving genome-scale models

A parallel novel software pipeline was developed to atomically resolve any given genome-scale metabolic model, where the result is a chemoinformatic database of metabolite structures and atom mapped reactions. This pipeline is implemented in MATLAB, but calls

several optional external software tools, such as Open Babel [22] and CXCALC [23] for chemoinformatic data processing and the RDT [24] to atom map metabolic reactions (Java SE Development Kit is required). Installation of these external software tools is optional but recommended to obtain metabolites with higher confidence score. An overview of the methodology to generate an atomically resolved genome-scale model is given in **Figure 1** (13-24) and further described below.

3.1 Metabolite structures

Metabolites were represented with database identifiers, e.g., Virtual Metabolic Human [37] (VMH), PubChem [42], the Kyoto Encyclopaedia of Genes and Genomes database [38] (KEGG), Chemical Entities of Biological Interest [43] (ChEBI) or the Human Metabolome Database [39] (HMDB). In addition to database identifiers, the metabolite structures were also represented using several formats including metabolite chemical tables (MDL MOL) that list all of the atoms in a molecule, as well as their coordinates and bonds [44]; the Simplified Molecular-Input Line-Entry System (SMILES), which uses a string of ASCII characters to describe the structure of a molecule [41]; or the International Chemical Identifier (InChI) developed by the IUPAC, which provides a standard representation for encoding molecular structures using multiple layers [40] as illustrated in *Figure S2*.

For a given metabolite, comparing different metabolic databases, one may obtain substantial structural diversity due to the inclusion of different isomers in the different sources. The fluxTrAM pipeline uses all of the aforementioned databases to obtain and ultimately select a single InChI for each metabolite. InChI was chosen due to its standard structure for encoding molecular information and it is a database independent representation [40]. fluxTrAM analyses all the InChI strings obtained from each source database assigning a score based on the criteria shown in **Table 1** to identify the metabolic structure that most closely resembles the metabolite described in the genome-scale reconstruction. The InChI for each metabolite is scored considering the chemical formula excluding hydrogen atoms, similarity with other databases, stereochemistry and charge in order to avoid loss of the predictive capacity of computer models, due to propagation of an inconsistent structures.

Table 1. InChI based comparison

Each InChI layer contains information that can be used to identify the metabolite structure that is most similar to the metabolite in the genome-scale reconstruction.

Concept	Score	Description
Chemical formula	0 or 10	The chemical formula indicated in the genome-scale model is compared with that obtained from the InChI. This feature is given more weight in order to keep the metabolite in the genome-scale model, where all reactions are stoichiometrically consistent and mass balanced. Hydrogen atoms were ignored in this comparison since they can be modified based on the charge (Figure S2).

Charge	0 or 1	The charge indicated in the genome-scale model is compared with the charge obtained from the source.
Stereochemical information	0 or 1	Indicates whether the InChI contains stereochemical information or not.
Standard	0 or 1	Indicates whether the InChI is standardised or not.
Similarity with other databases	0 or 1	The number of sources where the InChI strings are identical, divided by the total number of sources.
Main layer similarity	0 or 1	The number of sources where the main layers are identical, divided by the total number of sources.
InChI with more layers	0 or 1	InChI with more layers.

Letters in a formula that do not correspond to a chemical element, typically described with an R, represent any group of atoms attached to the rest of the molecule for example an alkyl group or hydrogen atom. To compare metabolite structures with R groups, these atoms are modified by replacing each non-chemical atom with hydrogen only for the InChI comparison (**Figure 3.1**). If the number of hydrogen atoms in the metabolite structure obtained from a database and the metabolite obtained from the genome-scale model are different, software (CXCALC [23]) is used to adjust the charge and number of hydrogen atoms of a metabolite based on the pH (**Figure 3.2**). To ensure database consistency, the molecular structures of the metabolites in the database were represented as either molecular graphs or hydrogen-suppressed molecular graphs (**Figure 3.3**). Finally, the results were presented as molecular structures in five different formats (metabolite chemical tables (MDL MOL) [44], the Simplified Molecular-Input Line-Entry System (SMILES) [41], the International Chemical Identifier (InChI), the InChIkey [40] and an image (JPEG file) containing a graphical representation of the metabolite structure (when CXCALC is installed).

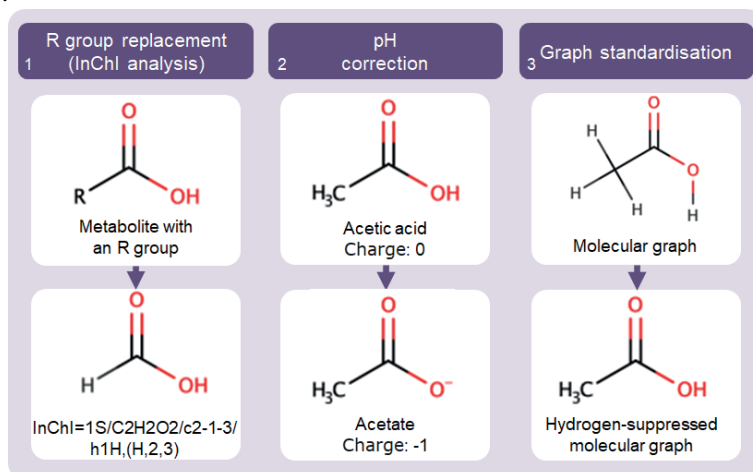


Figure 3. Example molecular graphs.

Metabolite structure represented in different forms, as well as how it is processed by the pipeline. (1) If an unspecified alkyl group attached to the carboxyl group is represented by a non-chemical atom (R), the R is replaced by a hydrogen to form a molecule that can be converted into an InChI. (2) The pH of the acetic acid molecule is changed in order to obtain the charge described in the model. (3) In order to achieve implicit hydrogen standardization, a molecular graph representing a metabolite's structural formula is converted to a hydrogen-suppressed molecular graph, which is a molecular graph with the hydrogen vertices removed.

3.2 Atomically resolved reactions

A reaction database was generated for all reactions where the corresponding metabolite structures were available, as shown in the example using a metabolic model, Recon3D [45] (Figure 4).

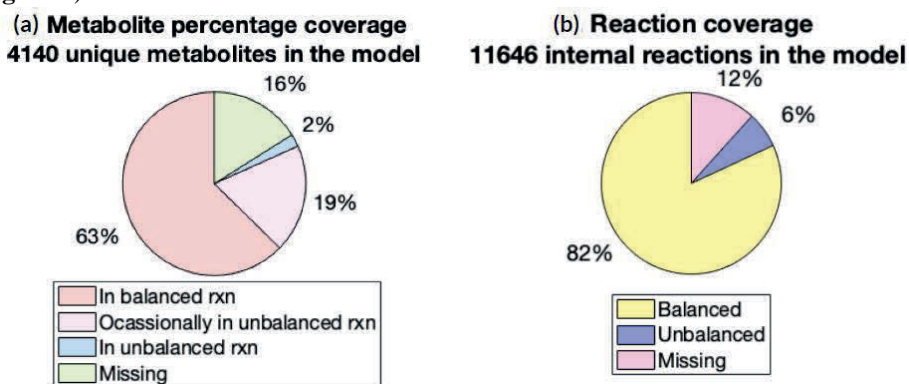


Figure 4. Coverage of metabolite structures and atom mapped reactions in the model case of Recon3D.

The fluxTrAM pipeline was used to collect 84% of the metabolite structures in Recon3D, while only 2% correspond to the metabolite structures that are always present in unbalanced reactions (a). The metabolite structures were used to atom-map 88% of the reactions. 12% of the reactions are missing because at least one metabolite structure is missing, and 6% are atomically unbalanced (b).

The obtained database of metabolite structures and reaction stoichiometries from the genome-scale model was then used to generate chemical tables for each reaction (MDL RXN format) and was atom mapped using the Reaction Decoder Tool algorithm [24], interfaced with the COBRA Toolbox [13]. Atom mapped metabolic reactions were represented in reaction chemical tables (MDL RXN [44]) and reaction SMILES, while unmapped metabolic reactions were represented in International chemical identifiers for reactions [46] (RInChI; see Figure S2). Additionally, the reactions were atom mapped to represent their reaction mechanism. To demonstrate the general utility of this software, we generated atomically resolved reaction databases for iDopaNeuroC model, as well as

several other species and community metabolic models, such as *E. coli* core [47], gut microbial organisms (AGORA2 [48] and Recon3D [45]).

4. Inference of metabolic fluxes

4.1 Isotopomer Network Compartmental Analysis of central carbon metabolism

To perform conventional ^{13}C metabolic flux analysis, a stoichiometric model of central carbon metabolism which included glycolysis, pentose phosphate pathway (PPP), tricarboxylic acid (TCA) cycle was extracted from the iDopaNeuroC model. First, this model was edited in a MATLAB-based ^{13}C metabolic flux inference software package, isotopomer network compartmental analysis (INCA, [16]), describing reaction stoichiometries and carbon transitions between substrate and products (*SM4. Table S2*). Then standardised MID data was imported into INCA to infer a steady-state metabolic flux distribution in a central carbon metabolic model. INCA employs a type of decomposition of an isotopomer network to simulate MIDs as a function of metabolic flux [49], then metabolic flux is inferred by minimising the lack-of-fit between experimentally measured and computationally simulated MIDs using a Levenberg-Marquardt optimisation algorithm. Flux inference was repeated 50 times from random initial metabolic flux values to search for a global minimum fit. To assess goodness-of-fit, we subjected flux results to a chi-square statistical test and calculated 95% confidence intervals for each estimated flux value by evaluating the sensitivity of the sum of squared residuals to parameter variations.

4.2 Inference of metabolic flux at genome-scale with moiety fluxomics

Previously [26], we provided a mathematical definition of a conserved moiety and demonstrated how identification of the complete set of conserved moieties for a given metabolic network leads to a novel *moiety graph decomposition* of a stoichiometric matrix. We applied moiety graph decomposition to obtain the complete set of conserved moieties for a genome-scale model from human stem cell-derived, midbrain-specific, dopaminergic neurons *in vitro*, specifically iDopaNeuroC as described elsewhere [29]. In a companion paper, we mathematically and computationally demonstrate how moiety graph decomposition enables the development of a computationally efficient constraint-based modelling method to infer metabolic fluxes from isotope labelling data for a using complete metabolic network at genome-scale [27]. We applied this moiety fluxomic method to infer metabolic reaction fluxes at genome-scale using the aforementioned standardised MID data and a genome-scale model of dopaminergic neuronal metabolism.

4.3 Prediction of metabolic flux at genome-scale

Two additional methods, neither of which used any tracer-based metabolomic data, were used to predict metabolic reaction flux in the genome-scale model of dopaminergic neuronal metabolism: (i) Flux Balance Analysis (FBA) [50], with maximisation of ATP consumption

(VMHID: ATPM) to simulate a high demand for energy of dopaminergic neurons [51], (ii) Entropic Flux Balance Analysis (EFBA) maximisation of the entropy of forward and reverse fluxes, a least biased flux prediction given the available data [52], which also ensures that predicted flux satisfies energy conservation and the second law of thermodynamics [29]. Visualisation of all relevant flux distribution maps was performed in the software VANTED (Visualization and Analysis of Networks containing Experimental Data), v2.1.0 [53].

Results

We present fluxTrAM, a semi-automated pipeline for quantitative flux inference at genome-scale, including modules for processing of raw tracer-based mass spectrometry data into standardised mass isotopologue distribution and for generation of a chemoinformatic database of standardised metabolite structures and atom-mapped reactions at genome-scale. We demonstrated the performance of these two modules using tracer-based metabolomics data from iPSC-derived midbrain-specific dopaminergic neurons and a corresponding neuronal metabolic model, respectively. Next, we utilised the intermediate results of the pipeline for conventional ^{13}C flux analysis with a central carbon metabolism model, and for moiety fluxomics analysis at genome-scale.

1. Tracer experiment

Intracellular ^{13}C -glucose increased rapidly after 5 minutes and began to stabilise within 5 hours (**Figure 5**). The neuronal culture system reached a metabolic steady state within 24 hours uptake of ^{13}C -glucose.

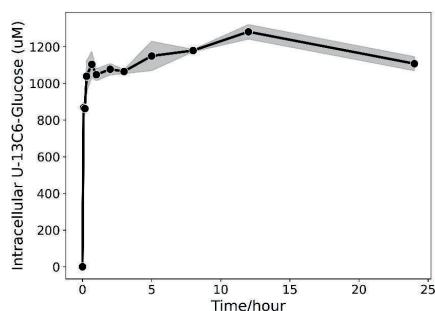


Figure 5. Progression toward metabolic steady state in differentiated dopaminergic neurons by uptake of U- $^{13}\text{C}_6$ -glucose.

The intracellular level of U- $^{13}\text{C}_6$ -glucose measured at 0min, 5min, 10min, 20min, 40min, 1h, 2h, 3h, 5h, 8h, 12h and 24h, constant level reached at 24h.

2. Tracer-based metabolomics data processing

2.1 Comparison for peak detection and extraction packages

Mass isotopologue peak integration using two automated software packages (mzMatch-ISO [7] and X¹³CMS [6]) and two manual peak picking software packages (EIMAVEN [34], Skyline [35]) were compared and the resulting isotopologue fractions for a set of 9 test metabolites are shown in **Figure 6**. The Pearson correlation of the isotopologue fractions between automated and manual is shown in **Table 2**. The test metabolites were representative of clear ion chromatographic peaks varied in peak width, intensity, and retention time. Given a list of well-established retention times and mass-to-charge ratios (m/z) for either respective metabolites monoisotopic peak in EIMAVEN or their mass isotopologues as well in Skyline, manual peak picking software still requires manual inspection across the integration results of every sample. Finally, EIMAVEN and Skyline showed comparable integration results for all test metabolites. The two automated packages differed in their peak integration performance. X¹³CMS returned isotopologue fractions that were less consistent with the integration results from the other packages. For example, no peak was extracted for phosphoenolpyruvate and compared to manual peak integration, there were low Pearson correlation coefficients for isotopologue fractions of aspartate and fructose 1,6-biphosphate. In contrast, for each of the test metabolites, mzMatch-ISO returned a similar isotopologue fraction to both of the manual software packages, which overall showed a high Pearson correlation coefficient above 0.95. Their respective statistical significance was below 0.002 (*SM4. Table S3*).

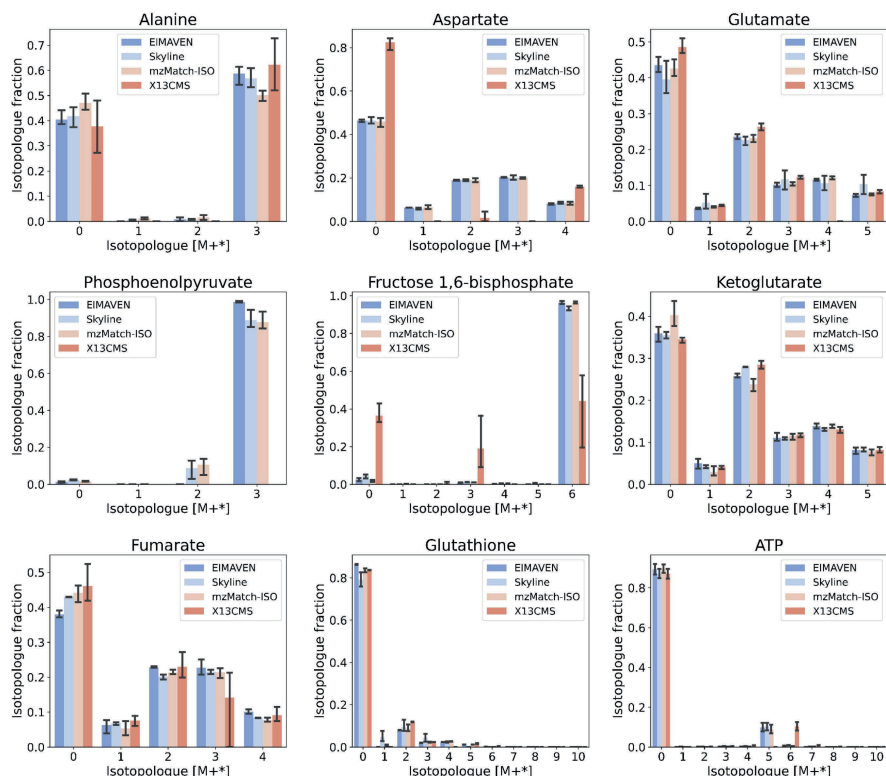


Figure 6. Comparison between the manual and automated peak detection and extraction results. The resulting metabolite isotopologue fractions of manual peak picking (EIMAVEN, Skyline) were compared to automated isotopologue peak integration (X¹³CMS, mzMatch-ISO) for the tested nine metabolites.

Table 2. Correlation analysis of integration results from automated packages and manual software.

Pearson correlation coefficients between automatically and manually collected isotopologue fractions for each of the tested nine metabolites. ND = not detected.

Metabolite	mzMatch-ISO vs Skyline	mzMatch-ISO vs EIMAVEN	X ¹³ CMS vs Skyline	X ¹³ CMS vs EIMAVEN
Alanine	0.979	0.969	0.971	0.984
Aspartate	0.997	0.998	0.872	0.87
Glutamate	0.984	1	0.959	0.954
Phosphoenolpyruvate	0.99	0.99	ND	ND
Fructose 1,6- bisphosphate	1	1	0.645	0.637
Ketoglutarate	0.975	0.989	0.998	0.989
Fumarate	0.995	0.985	0.899	0.852
Glutathione	0.996	1	0.995	0.998
ATP	1	1	0.985	0.985

2.2 Peak detection and extraction evaluation

To test the peak detection and extraction performance of the incorporated mzMatch-ISO [7] package within our pipeline, we next analysed mass isotopologue distribution of essential amino acids and non-essential amino acids in neurons from the pilot study set. The integration output of 14 amino acids was compared between groups of neurons treated with labelled glucose or unlabelled glucose, the result for nine amino acids is shown in **Figure 7**. For each amino acid, the statistical differences in the isotopic incorporation between labelled and unlabelled group were evaluated based on an external t-test examination (*SM4. Table S4*). Essential amino acids can only be taken up from diet and cannot be synthesised de novo. Non-essential amino acids can be synthesised, mainly from glucose. The isotopologue fractions of six essential amino acids showed a naturally labelled isotopologue pattern in labelled neurons and had no significant difference from unlabelled neurons, including methionine, threonine, leucine, isoleucine, phenylalanine, tryptophan. In contrast, five nonessential amino acids including alanine, serine, aspartate, asparagine, glutamate showed various labelling patterns in labelled neurons. Moreover, the calculated MID in *Table S4* showed high consistency across the three labelled or unlabelled sample replicates. Conditionally essential amino acids, proline, tyrosine, and glutamine, showed different preferences for synthesis from glucose in neurons. A significant labelling pattern from U- $^{13}\text{C}_6$ -glucose could be observed in proline. Meanwhile, glutamine and tyrosine showed little isotopic incorporation (**Figure 7**). The calculated MIDs were consistent among the labelled or unlabelled replicates.

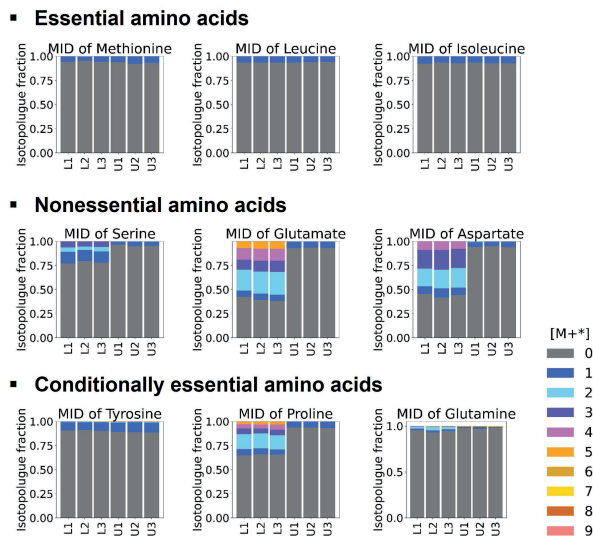


Figure 7. The mass isotopologue distribution (MID) of nine amino acids in the labelled neurons (n=3) and unlabelled neurons (n=3).

The labelled isotopomer pattern of methionine, leucine and isoleucine (essential amino acids), serine, glutamine, aspartate (nonessential amino acids) and tyrosine, proline, glutamine (conditionally essential amino acids) shown in both labelled and unlabelled neurons. Labelled neuron samples, abbreviated in L1, L2, L3: Three replicate samples in the group of cultured neurons with isotopic tracer. Unlabelled neuron samples, abbreviated in U1, U2, U3: Three replicate samples in the group of cultured neurons with no isotopic tracer. The color represents the different detected mass isotopologues as defined by the legend.

2.3 Data processing evaluation for a formal study set

To test the pipeline performance for processing a larger sample set, we further analysed the dynamic changes in mass isotopologue distribution of central carbon metabolites for neurons over a time course of 24 hours. A total of 36 samples for 10 metabolites (52 isotopologues) were processed automatically by fluxTram. The MID results can be found in *SM4. Table S5* and visualised in **Figure 8**. The labelling fractions of metabolites increased immediately after the initial time point. The glycolytic intermediates, phosphoenolpyruvate, pyruvate and lactate attained isotopic equilibrium within 5 hours. They showed high abundances of fully ^{13}C labelled states (M+3). The tricarboxylic acid cycle, including ketoglutarate, succinate, fumarate, malate, citrate and glutamate, took nearly 24 hours to reach an isotopic steady state. Each of them showed mass isotopologue distribution in multiple ^{13}C labelled states, ranging from one ^{13}C labelled to fully ^{13}C labelled.

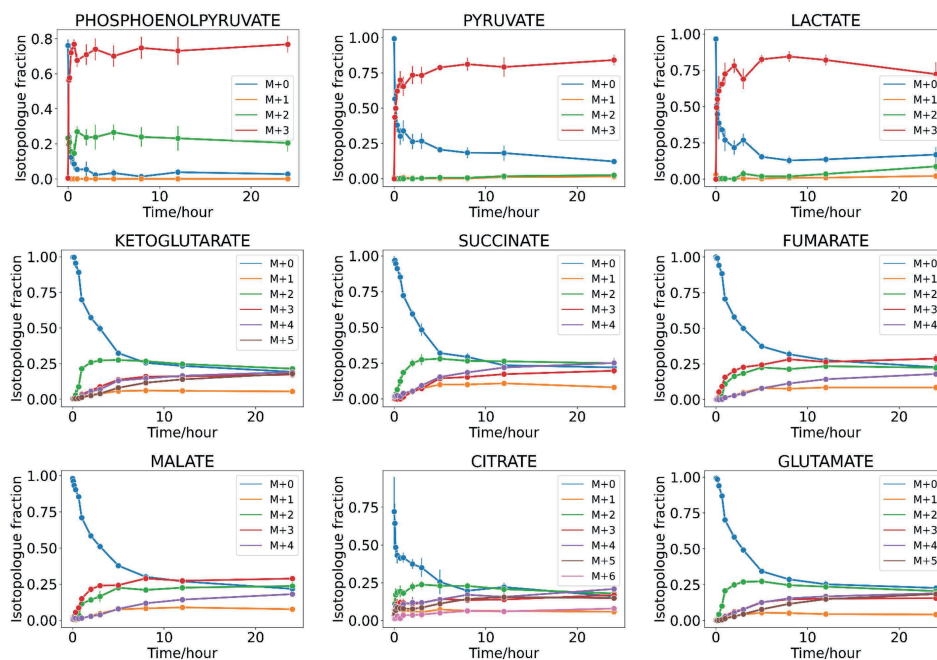


Figure 8. Evaluation of isotopic steady state in differentiated dopaminergic neurons by uptake of U-¹³C₆-glucose.

Mass isotopologue distributions as a function of time for intracellular metabolites within 24h of feeding isotopically labelled substrate, U-¹³C₆-glucose.

3. Databases of metabolite structures and atom mapped-reactions

3.1 Metabolite structures

Figure 9 shows a comparison of the identifiers in the iDopaNeuroC model (See **Table 1**). This comparison only reflects the specificity of the metabolite identifiers in the iDopaNeuroC model, not the quality of the databases consulted. The VMH database [37] contains the molecular structures that most closely resemble the metabolites described in the iDopaNeuroC model, providing the largest number of atomically balanced reactions. The more specific a metabolite structure is, the more likely it is to obtain a matched structure for a genome-scale metabolic network, as evidenced by **Figure 9 G**. The metabolite formula in the iDopaNeuroC model matched well with the formula from ChEBI [43], HMDB [39], KEGG [38], and PubChem [42] databases, however, the charge is inconsistent with the model, so they received a lower score in the InChI string analysis (**Figure 9 A, B, D and E**). On the other hand, the InChIs and SMILES identifiers in the model have high compatibility in the formula and charge, but they lack stereochemical information, reducing their specificity (**Figure 9 C and F**).

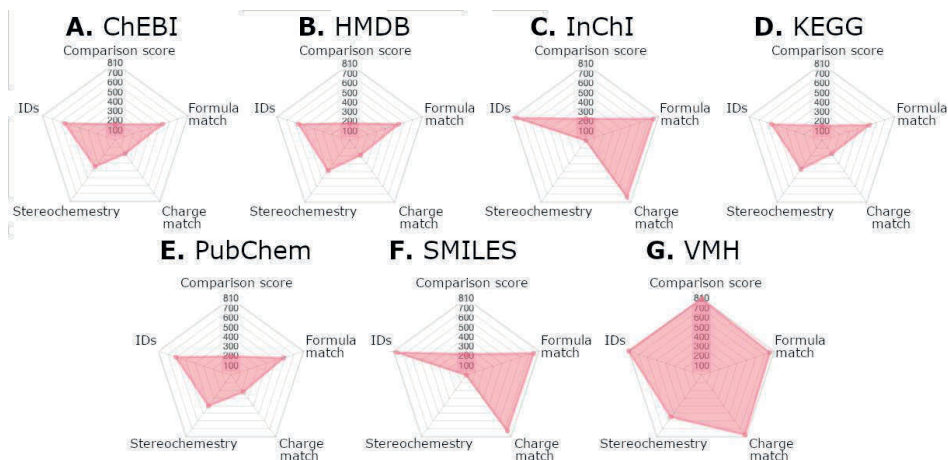


Figure 9. Comparison of metabolite structure identifiers in the iDopaNeuroC model.

Each of the metabolite identifiers evaluated in this work was compared using various criteria, including 1) IDs: the number of identifiers compared; 2) Comparison score: the number of times they received the best score; 3) Formula match: the number of times the chemical formula matched the metabolite formula in the iDopaNeuroC model (excluding the number of hydrogen atoms); 4) Charge match: the charge consistency with the model; and 5) Stereochemistry: the number of times stereochemical information was included.

3.2 Atomically resolved reactions

The genome-scale model of dopaminergic neuronal metabolism, iDopaNeuroC [29], was atomically resolved. We obtained almost all (810/818) structures corresponding to the metabolites in the iDopaNeuroC model. Of these, 677 metabolites were always present in atomically balanced reactions, 116 metabolites were occasionally present in atomically unbalanced reactions, and 15 metabolites were always present in atomically unbalanced reactions. Two molecular structures were not used, because at least one molecular structure was required to complete the reaction in which they were involved. Almost all (2,254/2,262) internal metabolic reactions in the iDopaNeuroC model could be atom-mapped, of which 2,155 were atomically balanced and 99 were unbalanced. 18 metabolic reactions could not be written, because at least one molecular structure was missing from the metabolite database. A list of the problematic reactions, along with an explanation of why each reaction was problematic, is provided in the supplementary information. **Table 3** provides a summary of the atomically resolved coverage of the iDopaNeuroC model as well as several additional species and community metabolic models.

Table 3. Atomically resolved coverage of metabolism in different models.

	iDopaNeuroC [29]	<i>E.coli</i> core [47]	AGORA2 [54]	Recon3D [45]
Metabolites in the database	810	53	1894	3534
Metabolites in balanced reactions	677	53	1510	2594
Metabolites occasionally in unbalanced reactions	116	0	260	789
Metabolites always in unbalanced reactions	15	0	66	92
Metabolites not used	2	0	58	59
Missing metabolites	8	1	1697	665
Reactions in the database	2254	71	4803	10279
Atom-mapped reactions	2254	71	4623	10279
Balanced reactions	2155	71	4583	9533
Unbalanced reactions	99	0	220	746
Missing reactions	18	3	1697	1367

4. Inference of metabolic fluxes

4.1 ^{13}C metabolic flux analysis of iPSC-derived midbrain-specific dopaminergic neurons

Steady-state flux inference was performed on the formal sample set collected at a 24-h time point on the basis of a stoichiometric model created in INCA covering 36 reactions (54 fluxes) from central carbon metabolism. As experimental constraints, the INCA flux analysis utilised uptake rates (glucose, glutamate), secretion rates (lactate), and ten standardised metabolite MIDs (glutamate, glutamine, ketoglutarate, succinate, fumarate, malate, citrate, lactate, pyruvate, and phosphoenolpyruvate). The final stationary ^{13}C flux distribution results in **Figure 10** showed glucose served as a primary nutrient to neurons compared to glutamine. Remarkably high glycolytic activity and relatively low metabolic activity in the tricarboxylic acid cycle were observed in neurons, whereas the pentose phosphate pathway showed almost no metabolic activity.

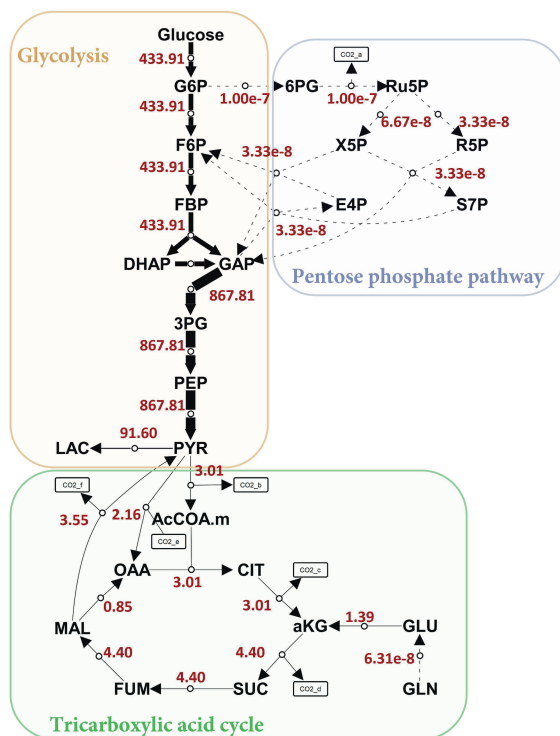


Figure 10. ¹³C metabolic flux analysis of differentiated dopaminergic neurons within central carbon metabolism network.

A steady-state flux distribution map covering glycolysis, tricarboxylic acid cycle, and pentose phosphate pathway for iPSC-derived midbrain-specific dopaminergic neurons. G6P: Glucose 6-phosphate; F6P: Fructose 6-phosphate; FBP: Fructose 1,6-bisphosphate; DHAP: Dihydroxyacetone phosphate; GAP: or G3P, Glyceraldehyde 3-phosphate; 3PG: 3-Phosphoglycerate; PEP: Phosphoenolpyruvate; PYR: Pyruvate; LAC: Lactate; AcCoA.m: Acetyl coenzyme A in mitochondria; OAA: Oxaloacetate; CIT: Citrate; aKG: alpha-Ketoglutarate; MAL: Malate; FUM: Fumarate; SUC: Succinate; GLN: Glutamine; GLU: Glutamate; 6PG: 6-Phosphogluconate; Ru5P: Ribulose 5-phosphate; R5P: Ribose 5-phosphate; X5P: Xylulose 5-phosphate; E4P: Erythrose 4-phosphate; S7P: Sedoheptulose 7-phosphate.

4.2 Genome-scale flux analysis

Flux balance analysis [50] and entropic flux balance analysis [29] predicted reaction fluxes in the iDopaNeuroC model without any constraints from isotope labelling data. The standardised MIDs (glutamate, glutamine, ketoglutarate, succinate, fumarate, malate, citrate, lactate, pyruvate, phosphoenolpyruvate) were used as new constraints to the iDopaNeuroC

model, and helped to generate a third metabolic flux solution with a newly developed moiety solver algorithm [27]. Three genome-scale flux solutions were compared to INCA flux within the same central carbon metabolism network in order to evaluate their flux rationality.

Regarding an accurate mapping of reaction flux at the genome scale to the corresponding reaction in the core model, we adhered to the rule of combining steady-state flux, as depicted in **Figure 11.A**. The self-defined central carbon metabolism model in INCA only describes the major carbon transitions from glucose without indicating other reaction substances and cofactors. However, metabolic reactions from the iDopaNeuroC model cover multiple reactions related to the same carbon transition and with diverse reaction substances or cofactor conversions involved. For instance, phosphoenolpyruvate can use different diphosphate-nucleotides as reactants and convert into pyruvate. In this sense, we merged the net fluxes of parallel reactions that share the same carbon transitions from the iDopaNeuroC model together. In another case, a simplified reaction was described in the INCA model to represent a series of reactions in the iDopaNeuroC model. For instance, the conversion from 3-phosphoglycerate into phosphoenolpyruvate is via the intermediate metabolite 2-phosphoglycerate. Therefore, the minimum flux of consecutive reactions was used to represent the simplified reaction flux for the iDopaNeuroC model. In a third case, if the intermediate metabolite receives net fluxes both from substrates A and C, the final flux representing conversion from A to C is considered to be zero. Based on the calculated flux distributions in the same core model (*SM4. Table S6*), a Spearman correlation analysis showed that the entropy and moiety flux solution and the INCA model flux solution had a relatively good correlation, however, the FBA flux solution had a poor correlation to any other flux solution (**Figure 11.B**).

In terms of the reaction directionality of the nutrient exchange, the entropy, moiety and INCA model flux solutions all showed the uptake of glucose, glutamate, glutamine, and the secretion of lactate and pyruvate in neurons, whereas the FBA flux solution showed the uptake of lactate and pyruvate and no uptake of glutamine. A comparison of internal reactions was then only focused on entropy, moiety, and INCA model flux solutions. Within the subsystem of glycolysis/gluconeogenesis, all relevant reactions share the same directionality between the three flux solutions. The flux value of the reaction converting pyruvate to lactate seen in the entropy and moiety flux solution fell within the INCA flux range. Several reactions of the pentose phosphate pathway showed in opposite directions to INCA model flux solutions, especially for moiety flux solution. They all, however, had low flux compared to glycolytic reactions. Generally, pyruvate can be converted into acetylCoA via pyruvate dehydrogenase (PDH) and join the tricarboxylic acid cycle. Besides, pyruvate

anaplerosis can convert pyruvate directly into oxaloacetate via pyruvate carboxylase (PC) to compensate for metabolite loss from tricarboxylic acid cycle due to biomass production [55]. Interestingly, the reaction flux of PDH and PC observed in the moiety flux solution both fell within the INCA flux range. Similar results can be also found in a few other reactions. Regardless of this, three reactions of the tricarboxylic acid cycle showed in opposite directions to INCA model flux solutions, as shown in **Figure 11.C**. A final steady-state flux distribution map based on entropy, moiety and INCA model flux solutions can be seen in **Figure 12**.

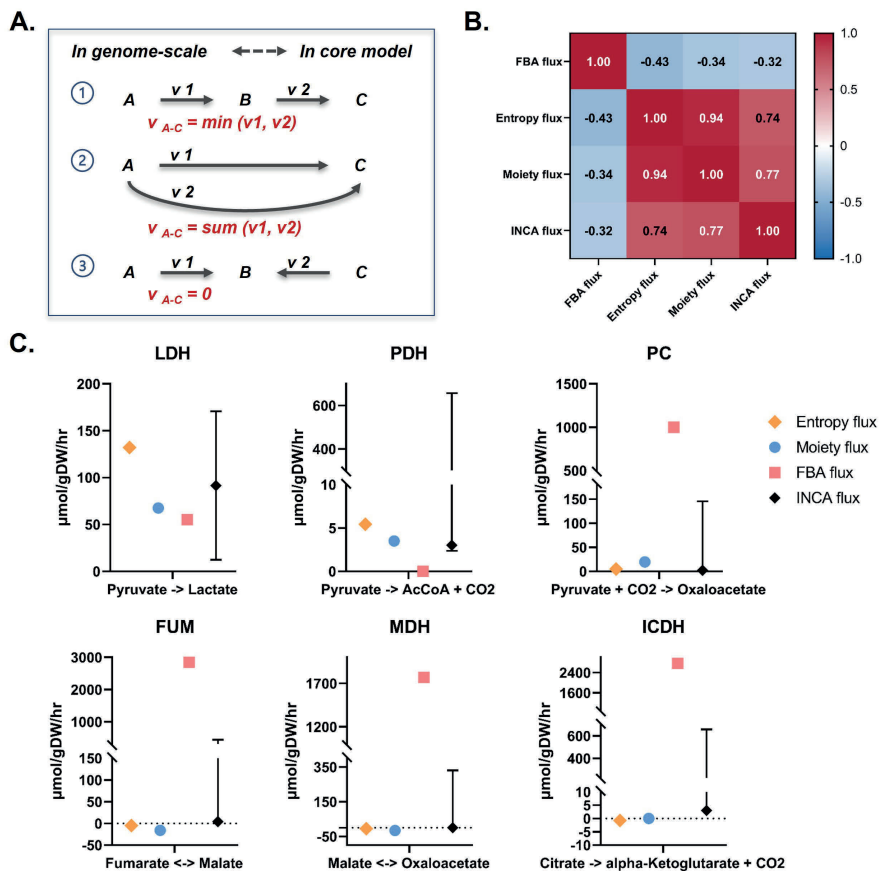


Figure 11. Flux comparison between FBA flux, entropy flux, moiety flux, and INCA model flux within the same central carbon metabolism network for iPSC-derived midbrain-specific dopaminergic neurons.

A. Illustration on mapping reaction fluxes at the genome scale to the corresponding reaction flux in the core model. B. Spearman correlation analysis between FBA flux, entropy flux, moiety flux, and INCA flux within the same network. C. Comparison of individual reaction fluxes from glycolysis and tricarboxylic acid cycle.

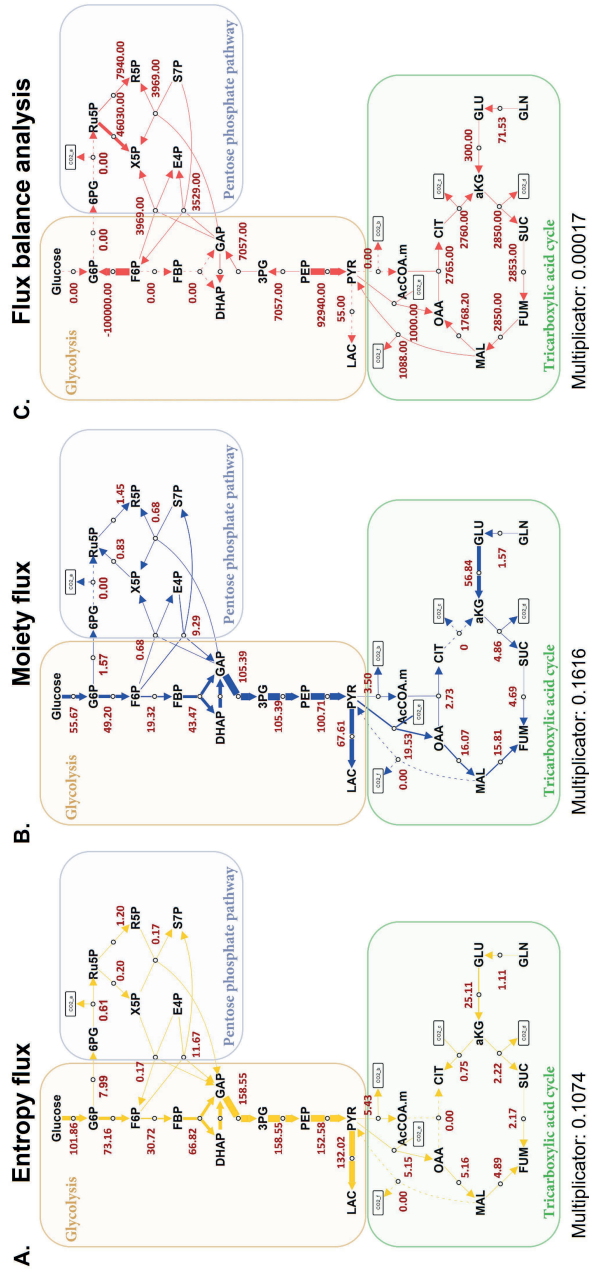


Figure 12. Genome-scale metabolic flux analysis of differentiated dopaminergic neurons projected within central carbon metabolism network.

A steady-state flux distribution map over glycolysis, tricarboxylic acid cycle, and pentose phosphate pathway for iPSC-derived midbrain-specific dopaminergic neurons based on entropy (A, shown in yellow), moiety (B, shown in blue), FBA (C, shown in red) flux solutions.

Besides, the top 15 active pathways within the genome-scale network based on entropic flux balance analysis were summarised in **Figure 13**. In comparison to the results of entropy flux, moiety flux solutions exhibited comparable average flux results in most of the subsystems. Higher flux activity can be found in the subsystems of fructose and mannose metabolism, oxidative phosphorylation, glutamate metabolism, and citric acid cycle, whereas lower flux activity was observed in the subsystem of glycolysis/gluconeogenesis.

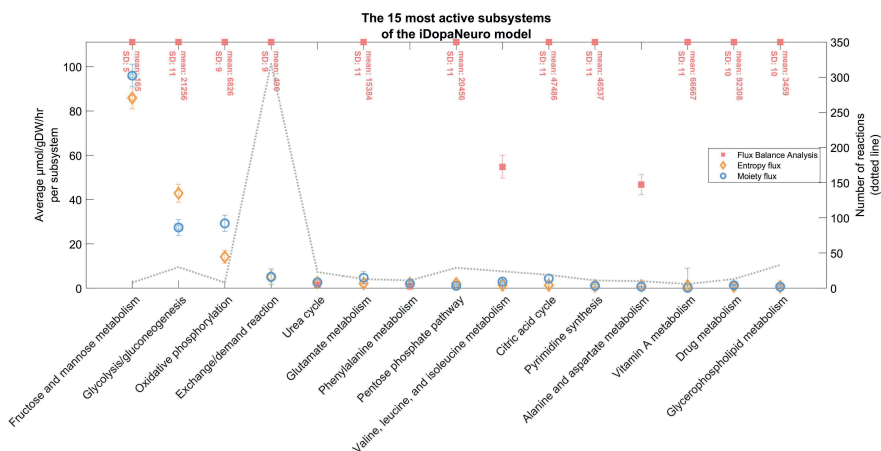


Figure 13. Subsystem activity.

Summary of top 15 active pathway subsystems in the iDopaNeuroC model based on the objective function of entropic flux balance analysis, and the correlated results with FBA flux (red), and moiety flux (blue) analysis.

Regarding the phenotypes for carbon source and energy production, entropy and moiety flux shared some similarities and showed a big difference from FBA flux. Notably, with moiety flux, the reaction of ATP synthase in mitochondria produced the most ATP, whereas phosphoglycerate kinase in the cytoplasm produced the most ATP with entropy flux. Both methods relied on glucose as their primary carbon source. (**Table 4**)

Table 4. Modelling phenotypes.

Comparison of energetic phenotypes obtained using various genome-scale modelling approaches.

	FBA flux	Entropy flux	Moiety flux
Carbon sources			
Metabolite#1	Bicarbonate	D-Glucose	D-Glucose
Flux	-4268 $\mu\text{mol/gDW/hr}$	-427.44 $\mu\text{mol/gDW/hr}$	-427.44 $\mu\text{mol/gDW/hr}$
Formula	CHO_3	$\text{C}_6\text{H}_{12}\text{O}_6$	$\text{C}_6\text{H}_{12}\text{O}_6$
Metabolite#2	D-Glucose	L-Arginine	L-Arginine
Flux	-440.40 $\mu\text{mol/gDW/hr}$	-29.35 $\mu\text{mol/gDW/hr}$	-27.77 $\mu\text{mol/gDW/hr}$
Formula	$\text{C}_6\text{H}_{12}\text{O}_6$	$\text{C}_6\text{H}_{15}\text{N}_4\text{O}_2$	$\text{C}_6\text{H}_{15}\text{N}_4\text{O}_2$
Metabolite#3	L-Threonine	Glycine	Glycine
Flux	-117.30 $\mu\text{mol/gDW/hr}$	-25.81 $\mu\text{mol/gDW/hr}$	-27.06 $\mu\text{mol/gDW/hr}$
Formula	$\text{C}_4\text{H}_9\text{NO}_3$	$\text{C}_2\text{H}_5\text{NO}_2$	$\text{C}_2\text{H}_5\text{NO}_2$
ATP production			
1st ATP source	Nucleotide interconversion	Phosphoglycerate Kinase	ATP synthase
Flux	$-1\text{e}10^5$ $\mu\text{mol/gDW/hr}$	-158.55 $\mu\text{mol/gDW/hr}$	110.88 $\mu\text{mol/gDW/hr}$
2nd ATP source	Succinate- Coenzyme A Ligase	ATP synthase	Phosphoglycerate Kinase
Flux	$-1\text{e}10^5$ $\mu\text{mol/gDW/hr}$	52.23 $\mu\text{mol/gDW/hr}$	-105.392 $\mu\text{mol/gDW/hr}$
3rd ATP source	ATP synthase	Pyruvate Kinase	Pyruvate Kinase
Flux	33370 $\mu\text{mol/gDW/hr}$	48.15 $\mu\text{mol/gDW/hr}$	-34.184 $\mu\text{mol/gDW/hr}$

5. Identification of conserved moieties and new tracer design

A list of 10 conserved moieties within the atomically resolved iDopaNeuroC model was identified (*SM4. Table S7*). Each conserved moiety corresponded to its own subnetwork. To predict the best conserved moieties to label in a future tracer-based metabolomic experiment, we first compared the coverage of internal reactions in every subnetwork. Conserved moiety #59 had the highest coverage of carrying internal reactions flux. Moreover, four of moiety-relevant subsystems were confirmed as top-15 active subsystems in entropy flux-based solution, and two of moiety-relevant subsystems were confirmed as top-15 active subsystems in moiety flux-based solution. Conserved moieties #5 and #56 showed about 50% internal reaction coverage. Nevertheless, they had no active subsystems hits and conserved moieties #56 was not found within any uptaken metabolite in the whole subnetwork. Overall, the conserved moiety #59 showed the most promising candidate because of its subnetwork activity. To further trace that conserved moiety within network through experiments, a partially $^{13}\text{C}_4$, D, $^{15}\text{N}_2$, ^{18}O -labelled thymidine can be designed as a new culture tracer (**Figure 14**).

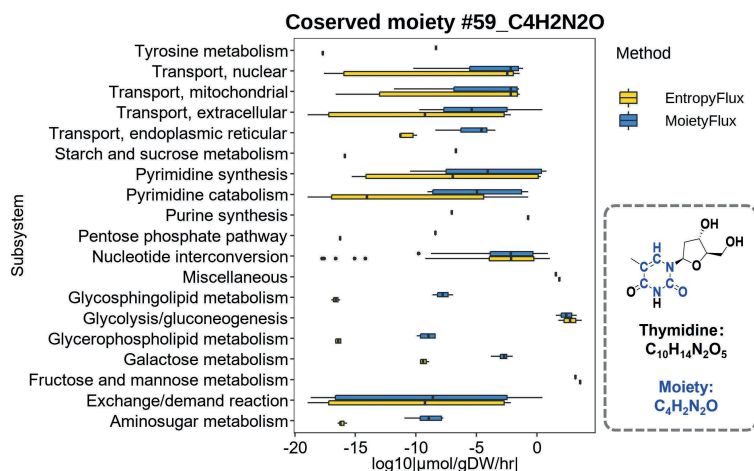


Figure 14. Conserved moiety #59_C4H2N2O

Overall reaction flux plot is classified by metabolic subsystem based on entropy flux and moiety flux predictions. Inside the dotted line illustrates a determined tracer that can be utilised in a new tracer-based metabolomic experiment.

Discussion

This work describes a semi-automated pipeline which streamlines and standardises the procedure for preparing an atomically resolved metabolic model and processing tracer-based metabolomics data to perform metabolic flux analysis at genome-scale.

Tracer-based metabolomics data processing

One part of fluxTrAM pipeline is focused on the standardised and high-throughput processing for stable isotope labelling data and ¹³C metabolic flux analysis. The accurate mass isotopologue distribution of the target metabolites depends on good peak detection and extraction. Based on our evaluation, mzMatch-ISO showed higher accuracy than X¹³CMS in collecting targeted isotopologue information. X¹³CMS is a package mainly designed for untargeted metabolomics [6], and mzMatch is a package for both untargeted and targeted metabolomics, mzMatch-ISO especially showed its unique advantage in isotopic labelling data analysis with a list of target analytes. The function of *peakDetector* based on the mzMatch-ISO package presented good consistency in the isotopologue fraction analysis for essential amino acids between the labelled and unlabelled groups while showing significant differences for non-essential amino acids. The automated connection between different packages guaranteed that no additional data format manipulation occurs, leading to a consecutive data processing workflow. This was demonstrated in the analysis of a time-course dataset from the formal study set. In addition, the pipeline is flexible in that it allows self-defined parameter settings, and the output result for each function step

can be freely exported. It is currently only applicable to processing LC-MS datasets due to the restriction of selected automated peak extraction package. When appropriate packages are developed by the metabolomics community, future development can be extended to LC-MS/MS and GC-MS datasets.

In the application of ^{13}C metabolic flux analysis for iPSC-derived dopaminergic neurons, reaction flux was obtained within a central carbon metabolism network model in INCA software. The experimental flux range within 95% confidence interval is valuable in reflecting the basic energy metabolism regulation on a healthy neuronal model. The net reaction flux map showed a very active glycolysis activity compared to the tricarboxylic acid (TCA) cycle and the pentose phosphate pathway. However, this model was built based on many assumptions to obtain a successful fit. Only a few nutrient transports (glucose, glutamine, glutamate) were described in the INCA model compared to 320 exchange reactions in the iDopaNeuroC model. Oxidative sources of unlabelled carbon such as amino acids and fatty acids in the TCA cycle were not considered in this model. The output carbon flux was limited to the secretion of lactate and pyruvate. Besides, metabolites were assigned in one single pool without a compartmental difference. Although the experimental flux solution was based on limited network size and many pre-defined assumptions, it still offers a flux solution that can indicate a feasible cellular activity with statistically approved goodness-of-fit and biological significance.

Metabolite structure and atom mapping databases

Obtaining metabolite identifiers is critical for expanding the database's coverage. Similarly, having a wide range of sources increases the probability of obtaining the metabolites that best represent those described in the genome-scale model. An InChI represents various metabolite structures depending on the level of detail included in it (see *Figure S1*). The main layer consists of layers 1 (standardised or not), 2 (chemical formula), 3 (atoms connectivity), and 4 (hydrogen atom connectivity), e.g., InChI=1S/C3H7NO2/c1-2(4)3(5)6/h2H,4H2,1H3,(H,5,6), which represents the alanine molecule; layer 5 adds the charges, e.g., adding p-1, representing the alaninate molecule; and finally, layer 6 indicates the stereochemistry, e.g., adding t2-/m0/s, representing the L-alaninate molecule. As the specificity of the metabolites increases, so does the number of atomically balanced reactions in the database. A high quality atomically resolved genome-scale metabolic model may have multiple applications, some of which were explored in this work. Among the applications are the estimation of fluxes in the metabolic network in combination with MID data [27], identifying conserved moieties in the metabolic network to optimise tracer-based experimental design [25,26], to calculate the potential energy in molecules [56] or to

identify the amount of enthalpy change associated with a metabolic reaction via bond enthalpies (See supplementary information).

Metabolite structures may be obtained in a variety of ways, including drawing based on the literature using chemoinformatic software [23] or obtained from metabolic databases either manually or computationally given various different identifiers. Different approaches exist to differentiate isomers in order to obtain a consistent representation of a metabolite structure from a biological system, such as the CAS Registry Number, a unique numerical identifier that is independent of any chemical nomenclature system and is widely used to identify chemical substances with a maximum capacity of 1 e9 identifiers [57]; or an InChI, representing a chemical structure in a standardised manner, allowing the generation of a unique identifier for a chemical structure [40], while other chemoinformatic formats such as SMILES [41] and chemical tables [44], may use different annotations to represent the same molecule. Nevertheless, assigning the correct identifier for a metabolite in a genome-scale model is a difficult task due to the various isomers that a molecule may have, and more work should be done in this area to avoid mismatches. This is the case of the metabolite nicotinamide adenine dinucleotide, which is represented in the iDopaNeuroC model [29] with the identifier CHEBI:15846 from the ChEBI database, whereas the consistent identifier based on the number of hydrogen atoms should be CHEBI:57540. Tools for mapping identifiers between different biological databases [58], such as BridgeDB [59], the chemical translation service [58,60] and MetaboAnnotator [61], can be useful to assigning metabolite identifiers in accordance with the genome-scale model.

Integrative metabolic flux analysis and new experimental tracer design

FBA was used to predict the steady-state flux distribution assuming maximization of neuronal ATP production. Entropic flux balance analysis does not maximise the flux of a single reaction but rather assumes the objective function is to maximise the entropy of every forward and reverse internal reaction flux and also predicts a thermodynamically feasible flux vector. In addition, the moiety fluxomics predicts a new genome-scale flux solution in the atomically resolved iDopaNeuroC model by integrating the labelled MID data as extra constraints. The latter two approaches outperformed the FBA method as evaluated by their higher correlations with the flux inference using conventional metabolic flux analysis with INCA while using a central carbon metabolism network model. Moiety flux inference [27] shares some similarities with the entropic flux balance analysis prediction in terms of metabolic phenotype. For instance, glucose was predicted as one of the primary carbon sources for dopaminergic neuron. Nevertheless, it also shows some inconsistencies with entropy modelling solution. Moiety flux predicted a very active ATP production via ATP synthase (four protons for one ATP) in mitochondria, while entropy flux predicted a major

ATP production from cytoplasm. While maintaining a comparable ATP production, incorporating labelled MID data reformed some active subsystems of the neuronal metabolism, shown as more active oxidative phosphorylation, glutamate metabolism, and citric acid cycle, and less active glycolysis/gluconeogenesis.

Tracer choice plays an important role in determining the precision of network flux estimation [62,63]. We applied U-¹³C₆-glucose as the tracer for iPSC-derived dopaminergic neurons, which is not an ideal tracer to elucidate flux through the pentose phosphate pathway. Although glucose is a major nutrient used for energy production, neurons can utilise multiple other nutrient sources as well. To improve the accuracy of genome-scale flux prediction, a validation experiment with a new tracer is further required. Identification of conserved moieties has strong potential for use in design of tracer-based metabolomic experiments [64]. By isotopically labelling any single atom in a conserved moiety, one can use the predict the reachable set reactions that could contain that isotopic label.

In our study, the results of the genome-scale flux prediction helped to determine optimal tracers by evaluating flux activity of candidate conserved moieties on intracellular metabolism. This will facilitate future study of particularly significant metabolic pathways in more detail. On the other hand, it also contributes to the systematic interaction between genome-scale modelling and experimental validation towards a more efficient level. The conserved moiety proposed in this study, present in the metabolite thymidine, was found in multiple subsystems making it a potential candidate for the design of novel labelled molecules for a tracer-based metabolomics experiments. Ikuno reported an increased level of thymidine in the plasma of prodromal Parkinson's disease mouse model, which can cause mitochondrial disorders characterized by mitochondrial DNA (mtDNA) depletion [65]. In Anandagopu *et al.* [66], the distribution of thymidine was found to be decreased in PINK1 mRNA *homo sapiens* sequences, a mutation associated with mitochondrial dysfunction and oxidative stress. Not all of the conserved moieties in the iDopaNeuroC were identified. This was hampered by the absence of metabolite structures for some reactants, e.g., lipids with R groups in the structure, as they precluded the atomic resolution of all reactions in the iDopaNeuroC model. However, it was possible to atom map the majority of internal reactions, which permitted the identification of the majority of conserved moieties [25,26] in the iDopaNeuroC model.

Conclusions

Unlike a snapshot of metabolic phenotypes reflected by metabolite concentration, metabolic fluxes offer a functional perspective on cellular metabolism. Current methods for flux inference are often restricted to use with small-scale metabolic networks and are rarely applicable at a genome-scale level. To standardise and streamline the implementation of

metabolic flux analysis at genome-scale, we developed a semi-automated pipeline, fluxTrAM, that enables the integration of tracer-based metabolomics data with atomically resolved metabolic networks for metabolic flux inference. The first module of fluxTrAM implemented automated processing of tracer-based LC-MS raw data into standardised MID data. The second module atomically resolves any given genome-scale metabolic model, and results in the creation of a chemoinformatic database of standardized and context-specific metabolite structures and atom-mapped reactions. We demonstrated the utility of this pipeline by integrating experimental mass isotopomer distribution data with an atomically resolved dopaminergic neuronal model using a novel moiety fluxomics method that enables flux inference at genome-scale. The fluxes inferred by moiety fluxomics showed good correlation with fluxes inferred using conventional ^{13}C flux solution obtained based on a central carbon metabolism network. To conclude on the relative merits of these approaches, further analyses are necessary with a genome-scale model that is suitable for both conventional and moiety fluxomic approaches to flux inference. Genome-scale flux inference has the potential to broaden the analysis of metabolic flux beyond central carbon metabolism and combined with the conserved moiety analysis, enables design of labelled tracer for new labelling experiments.

Data Availability:

The fluxTrAM pipeline can be found in the COBRA Toolbox v3.4 [13] (<https://github.com/opencobra/COBRA.tutorials/tree/master/analysis/tracerMetabolomics2atomResolvedModels>). The metabolite structures and atom-mapped reactions generated by the fluxTrAM pipeline from the genome-scale models iDopaNeuroC [29], E.coli core [47], AGORA2 [54] and Recon3D [45] can be found on GitHub (https://github.com/opencobra/COBRA.papers/2023_tracerMetabolomics2atomResolvedModels) and in the VMH database [37].

Scripts for running flux comparison analysis can be found on GitHub (https://github.com/opencobra/COBRA.papers/2023_tracerMetabolomics2atomResolvedModels)

Acknowledgments

This project has received funding from the European Union's Horizon 2020 research and innovation programme under grant agreement number 668738, the China scholarship council [No.201806210057], the Dutch National Institutes of Health (ZonMw) TKI-LSH Neuromet project (LSHM18092) and the Dutch Research Council (NWO) 'Investment Grant NWO Large' program, for the 'Building the infrastructure for Exposome research: Exposome-Scan' project (No. 175.2019.032).

References

- Basler G, Fernie AR, Nikoloski Z. Advances in metabolic flux analysis toward genome-scale profiling of higher organisms. *Bioscience Reports*. 2018;38: BSR20170224. doi:10.1042/BSR20170224
- Antoniewicz MR. A guide to metabolic flux analysis in metabolic engineering: Methods, tools and applications. *Metabolic Engineering*. 2021;63: 2–12. doi:10.1016/j.ymben.2020.11.002
- Jiang L, Shestov AA, Swain P, Yang C, Parker SJ, Wang QA, et al. Reductive carboxylation supports redox homeostasis during anchorage-independent growth. *Nature*. 2016;532: 255–258. doi:10.1038/nature17393
- McAtee Pereira AG, Walther JL, Hollenbach M, Young JD. 13C Flux Analysis Reveals that Rebalancing Medium Amino Acid Composition can Reduce Ammonia Production while Preserving Central Carbon Metabolism of CHO Cell Cultures. *Biotechnology Journal*. 2018;13: 1700518. doi:10.1002/biot.201700518
- Smith CA, Want EJ, O’Maille G, Abagyan R, Siuzdak G. XCMS: Processing Mass Spectrometry Data for Metabolite Profiling Using Nonlinear Peak Alignment, Matching, and Identification. *Anal Chem*. 2006;78: 779–787. doi:10.1021/ac051437y
- Huang X, Chen Y-J, Cho K, Nikolskiy I, Crawford PA, Patti GJ. X13CMS: Global Tracking of Isotopic Labels in Untargeted Metabolomics. *Anal Chem*. 2014;86: 1632–1639. doi:10.1021/ac403384n
- Chokkathukalam A, Jankevics A, Creek DJ, Achcar F, Barrett MP, Breitling R. mzMatch-ISO: an R tool for the annotation and relative quantification of isotope-labelled mass spectrometry data. *Bioinformatics*. 2013;29: 281–283. doi:10.1093/bioinformatics/bts674
- Bueschl C, Kluger B, Neumann NKN, Doppler M, Maschietto V, Thallinger GG, et al. MetExtract II: A Software Suite for Stable Isotope-Assisted Untargeted Metabolomics. *Anal Chem*. 2017;89: 9518–9526. doi:10.1021/acs.analchem.7b02518
- Zierer J, Menni C, Kastennüller G, Spector TD. Integration of ‘omics’ data in aging research: from biomarkers to systems biology. *Aging Cell*. 2015;14: 933–944. doi:10.1111/acer.12386
- Cisek K, Krochmal M, Klein J, Mischak H. The application of multi-omics and systems biology to identify therapeutic targets in chronic kidney disease. *Nephrology Dialysis Transplantation*. 2016;31: 2003–2011. doi:10.1093/ndt/gfv364
- Das T, Andrieux G, Ahmed M, Chakraborty S. Integration of Online Omics-Data Resources for Cancer Research. *Frontiers in Genetics*. 2020;11. Available: <https://www.frontiersin.org/articles/10.3389/fgene.2020.578345>
- Palsson BØ. *Systems Biology: Constraint-based Reconstruction and Analysis*. Cambridge University Press; 2015.
- Heirendt L, Arreckx S, Pfau T, Mendoza SN, Richelle A, Heinken A, et al. Creation and analysis of biochemical constraint-based models using the COBRA Toolbox v.3.0. *Nat Protoc*. 2019;14: 639–702. doi:10.1038/s41596-018-0098-2
- Pey J, Rubio A, Theodoropoulos C, Cascante M, Planes FJ. Integrating tracer-based metabolomics data and metabolic fluxes in a linear fashion via Elementary Carbon Modes. *Metabolic Engineering*. 2012;14: 344–353. doi:10.1016/j.ymben.2012.03.011
- Weitzel M, Nöh K, Dalman T, Niedenführ S, Stute B, Wiechert W. 13CFLUX2—high-performance software suite for 13C-metabolic flux analysis. *Bioinformatics*. 2013;29: 143–145. doi:10.1093/bioinformatics/bts646
- Young JD. INCA: a computational platform for isotopically non-stationary metabolic flux analysis. *Bioinformatics*. 2014;30: 1333–1335. doi:10.1093/bioinformatics/btu015
- Quek L-E, Wittmann C, Nielsen LK, Krömer JO. OpenFLUX: efficient modelling software for 13C-based metabolic flux analysis. *Microbial Cell Factories*. 2009;8: 25. doi:10.1186/1475-2859-8-25
- Foguet C, Jayaraman A, Marin S, Selivanov VA, Moreno P, Messegueur R, et al. p13CMFA: Parsimonious 13C metabolic flux analysis. *PLOS Computational Biology*. 2019;15: e1007310. doi:10.1371/journal.pcbi.1007310
- Kumar A, Maranas CD. CLCA: Maximum Common Molecular Substructure Queries within the MetRxn Database. *J Chem Inf Model*. 2014;54: 3417–3438. doi:10.1021/ci5003922
- Preciat Gonzalez GA, El Assal LRP, Noronha A, Thiele I, Haraldsdóttir HS, Fleming RMT. Comparative evaluation of atom mapping algorithms for balanced metabolic reactions: application to Recon 3D. *Journal of Cheminformatics*. 2017;9: 39. doi:10.1186/s13321-017-0223-1
- Huß S, Judd RS, Koper K, Maeda HA, Nikoloski Z. An automated workflow that generates atom mappings for large-scale metabolic models and its application to Arabidopsis thaliana. *The Plant Journal*. 2022;111: 1486–1500. doi:10.1111/tpj.15903
- O’Boyle NM, Banck M, James CA, Morley C, Vandermeersch T, Hutchison GR. Open Babel: An open chemical toolbox. *Journal of Cheminformatics*. 2011;3: 33. doi:10.1186/1758-2946-3-33
- Standardizer Transform | Chemaxon Docs. [cited 15 Jan 2023]. Available: <https://docs.chemaxon.com/display/docs/standardizer-transform.md>
- Rahman SA, Torrance G, Baldacci L, Martínez Cuesta S, Fenninger F, Gopal N, et al. Reaction Decoder Tool (RDT): extracting features from chemical reactions. *Bioinformatics*. 2016;32: 2065–2066. doi:10.1093/bioinformatics/btw096
- Haraldsdóttir HS, Fleming RMT. Identification of Conserved Moieties in Metabolic Networks by Graph Theoretical Analysis of Atom Transition Networks. *PLOS Computational Biology*. 2016;12: e1004999. doi:10.1371/journal.pcbi.1004999
- Ghaderi S, Haraldsdóttir HS, Ahooshoh M, Arreckx S, Fleming RMT. Structural conserved moiety splitting of a stoichiometric matrix. *Journal of Theoretical Biology*. 2020;499: 110276. doi:10.1016/j.jtbi.2020.110276

27. Fleming RMT, Haraldsdottir HS, Preciat G, Huang L, Thiele I, Harms A, et al. Conserved moiety fluxomics.
28. Hosseinkhani F, Huang L, Dubbelman A-C, Guled F, Harms AC, Hankemeier T. Systematic Evaluation of HILIC Stationary Phases for Global Metabolomics of Human Plasma. *Metabolites*. 2022;12: 165. doi:10.3390/metabo12020165
29. Preciat G, Moreno EL, Wegrzyn AB, Willacey CCW, Modamio J, Monteiro FL, et al. Mechanistic model-driven exometabolomic characterisation of human dopaminergic neuronal metabolism. *bioRxiv*; 2021. p. 2021.06.30.450562. doi:10.1101/2021.06.30.450562
30. Rahim M, Ragavan M, Deja S, Merritt ME, Burgess SC, Young JD. INCA 2.0: A tool for integrated, dynamic modeling of NMR- and MS-based isotopomer measurements and rigorous metabolic flux analysis. *Metabolic Engineering*. 2022;69: 275–285. doi:10.1016/j.ymben.2021.12.009
31. Reinhardt P, Glatza M, Hemmer K, Tsytsyura Y, Thiel CS, Höing S, et al. Derivation and expansion using only small molecules of human neural progenitors for neurodegenerative disease modeling. *PLoS One*. 2013;8: e59252. doi:10.1371/journal.pone.0059252
32. Moreno EL, Hachi S, Hemmer K, Trietsch SJ, Baumuratov AS, Hankemeier T, et al. Differentiation of neuroepithelial stem cells into functional dopaminergic neurons in 3D microfluidic cell culture. *Lab Chip*. 2015;15: 2419–2428. doi:10.1039/C5LC00180C
33. Chambers MC, Maclean B, Burke R, Amodei D, Ruderman DL, Neumann S, et al. A Cross-platform Toolkit for Mass Spectrometry and Proteomics. *Nat Biotechnol*. 2012;30: 918–920. doi:10.1038/nbt.2377
34. Agrawal S, Kumar S, Sehgal R, George S, Gupta R, Poddar S, et al. El-MAVEN: A Fast, Robust, and User-Friendly Mass Spectrometry Data Processing Engine for Metabolomics. In: D’Alessandro A, editor. *High-Throughput Metabolomics: Methods and Protocols*. New York, NY: Springer; 2019. pp. 301–321. doi:10.1007/978-1-4939-9236-2_19
35. MacLean B, Tomazela DM, Shulman N, Chambers M, Finney GL, Frewen B, et al. Skyline: an open source document editor for creating and analyzing targeted proteomics experiments. *Bioinformatics*. 2010;26: 966–968. doi:10.1093/bioinformatics/btq054
36. Millard P, Delépine B, Guionnet M, Heuillet M, Bellvert F, Létisse F. IsoCor: isotope correction for high-resolution MS labeling experiments. *Bioinformatics*. 2019;35: 4484–4487. doi:10.1093/bioinformatics/btz209
37. Noronha A, Modamio J, Jarosz Y, Guerard E, Sompairac N, Preciat G, et al. The Virtual Metabolic Human database: integrating human and gut microbiome metabolism with nutrition and disease. *Nucleic Acids Res*. 2019;47: D614–D624. doi:10.1093/nar/gky992
38. Kanehisa M, Sato Y, Kawashima M, Furumichi M, Tanabe M. KEGG as a reference resource for gene and protein annotation. *Nucleic Acids Research*. 2016;44: D457–D462. doi:10.1093/nar/gkv1070
39. Wishart DS, Feunang YD, Marcu A, Guo AC, Liang K, Vázquez-Fresno R, et al. HMDB 4.0: the human metabolome database for 2018. *Nucleic Acids Res*. 2018;46: D608–D617. doi:10.1093/nar/gkx1089
40. Heller SR, McNaught A, Pletnev I, Stein S, Tchekhovskoi D. InChI, the IUPAC International Chemical Identifier. *Journal of Cheminformatics*. 2015;7: 23. doi:10.1186/s13321-015-0068-4
41. Anderson E, Veith G, Weininger D. SMILES: a line notation and computerized interpreter for chemical structures. 1987. Available: <https://www.semanticscholar.org/paper/SMILES%3A-a-line-notation-and-computerized-for-Anderson-Veith/ae29190b303a24d6df28df571dd1631ad95e8af3>
42. Kim S, Thiessen PA, Bolton EE, Chen J, Fu G, Gindulyte A, et al. PubChem Substance and Compound databases. *Nucleic Acids Res*. 2016;44: D1202–D1213. doi:10.1093/nar/gkv951
43. Hastings J, de Matos P, Dekker A, Ennis M, Harsha B, Kale N, et al. The ChEBI reference database and ontology for biologically relevant chemistry: enhancements for 2013. *Nucleic Acids Res*. 2013;41: D456–463. doi:10.1093/nar/gks1146
44. Dalby A, Nourse JG, Hounshell WD, Gushurst AKI, Grier DL, Leland BA, et al. Description of several chemical structure file formats used by computer programs developed at Molecular Design Limited. *J Chem Inf Comput Sci*. 1992;32: 244–255. doi:10.1021/ci00007a012
45. Brunk E, Sahoo S, Zielinski DC, Altunkaya A, Dräger A, Mih N, et al. Recon3D enables a three-dimensional view of gene variation in human metabolism. *Nat Biotechnol*. 2018;36: 272–281. doi:10.1038/nbt.4072
46. Grethe G, Blanke G, Kraut H, Goodman JM. International chemical identifier for reactions (RInChI). *Journal of Cheminformatics*. 2018;10: 22. doi:10.1186/s13321-018-0277-8
47. Orth JD, Fleming RMT, Palsson BØ. Reconstruction and Use of Microbial Metabolic Networks: the Core *Escherichia coli* Metabolic Model as an Educational Guide. *EcoSal Plus*. 2010;4. doi:10.1128/ecosalplus.10.2.1
48. Heinken A, Hertel J, Acharya G, Ravcheev DA, Nyga M, Okpala OE, et al. Genome-scale metabolic reconstruction of 7,302 human microorganisms for personalized medicine. *Nat Biotechnol*. 2023; 1–12. doi:10.1038/s41587-022-01628-0
49. Young JD, Walther JL, Antoniewicz MR, Yoo H, Stephanopoulos G. An elementary metabolite unit (EMU) based method of isotopically nonstationary flux analysis. *Biotechnol Bioeng*. 2008;99: 686–699. doi:10.1002/bit.21632
50. Orth JD, Thiele I, Palsson BØ. What is flux balance analysis? *Nat Biotechnol*. 2010;28: 245–248. doi:10.1038/nbt.1614
51. Pissadaki EK, Bolam JP. The energy cost of action potential propagation in dopamine neurons: clues to susceptibility in Parkinson’s disease. *Front Comput Neurosci*. 2013;7: 13. doi:10.3389/fncom.2013.00013

52. Fleming RMT, Maes CM, Saunders MA, Ye Y, Palsson BØ. A variational principle for computing nonequilibrium fluxes and potentials in genome-scale biochemical networks. *Journal of Theoretical Biology*. 2012;292: 71–77. doi:10.1016/j.jtbi.2011.09.029
53. Rohn H, Junker A, Hartmann A, Grafahrend-Belau E, Treutler H, Klapperstück M, et al. VANTED v2: a framework for systems biology applications. *BMC Systems Biology*. 2012;6: 139. doi:10.1186/1752-0509-6-139
54. Heinken A, Acharya G, Ravcheev DA, Hertel J, Nyga M, Okpala OE, et al. AGORA2: Large scale reconstruction of the microbiome highlights wide-spread drug-metabolising capacities. *bioRxiv*; 2020. p. 2020.11.09.375451. doi:10.1101/2020.11.09.375451
55. Buescher JM, Antoniewicz MR, Boros LG, Burgess SC, Brunengraber H, Clish CB, et al. A roadmap for interpreting ¹³C metabolite labeling patterns from cells. *Curr Opin Biotechnol*. 2015;34: 189–201. doi:10.1016/j.copbio.2015.02.003
56. Wang L, Upadhyay V, Maranas CD. dGPredictor: Automated fragmentation method for metabolic reaction free energy prediction and de novo pathway design. *PLOS Computational Biology*. 2021;17: e1009448. doi:10.1371/journal.pcbi.1009448
57. Jacobs A, Williams D, Hickey K, Patrick N, Williams AJ, Chalk S, et al. CAS Common Chemistry in 2021: Expanding Access to Trusted Chemical Information for the Scientific Community. *J Chem Inf Model*. 2022;62: 2737–2743. doi:10.1021/acs.jcim.2c00268
58. Haraldsdóttir HS, Thiele I, Fleming RM. Comparative evaluation of open source software for mapping between metabolite identifiers in metabolic network reconstructions: application to Recon 2. *J Cheminform*. 2014;6: 2. doi:10.1186/1758-2946-6-2
59. van Iersel MP, Pico AR, Kelder T, Gao J, Ho I, Hanspers K, et al. The BridgeDb framework: standardized access to gene, protein and metabolite identifier mapping services. *BMC Bioinformatics*. 2010;11: 5. doi:10.1186/1471-2105-11-5
60. Wohlgemuth G, Haldiya PK, Willighagen E, Kind T, Fiehn O. The Chemical Translation Service—a web-based tool to improve standardization of metabolomic reports. *Bioinformatics*. 2010;26: 2647–2648. doi:10.1093/bioinformatics/btq476
61. Thiele I, Preciat G, Fleming RMT. MetaboAnnotator: an efficient toolbox to annotate metabolites in genome-scale metabolic reconstructions. *Bioinformatics*. 2022;38: 4831–4832. doi:10.1093/bioinformatics/btac596
62. Metallo CM, Walther JL, Stephanopoulos G. Evaluation of ¹³C isotopic tracers for metabolic flux analysis in mammalian cells. *J Biotechnol*. 2009;144: 167–174. doi:10.1016/j.jbiotec.2009.07.010
63. Antoniewicz MR. ¹³C metabolic flux analysis: optimal design of isotopic labeling experiments. *Current Opinion in Biotechnology*. 2013;24: 1116–1121. doi:10.1016/j.copbio.2013.02.003
64. Wiechert W. ¹³C Metabolic Flux Analysis. *Metabolic Engineering*. 2001;3: 195–206. doi:10.1006/mben.2001.0187
65. Ikuno M, Yamakado H, Amano I, Hatanaka Y, Uemura N, Matsuzawa S-I, et al. Mitochondrial dysfunction in a mouse model of prodromal Parkinson's disease: A metabolomic analysis. *Neurosci Lett*. 2021;765: 136267. doi:10.1016/j.neulet.2021.136267
66. Anandagopu P, Banu S, Li J. Low thymine content in PINK1 mRNAs and insights into Parkinson's disease. *Bioinformation*. 2010;4: 452–455. doi:10.6026/97320630004452

Supplementary Materials

1. Inconsistencies in atom mapping data

Not all of the metabolites from the HMDB database were collected, resulting in a low collection of metabolites. This was due to connection problems with the database, as shown by the The HyperText Transfer Protocol (HTTP) status 503, which indicates that the server is not ready to handle the request.

Inconsistent metabolites or reactions can cause unbalanced reactions. With the iDopaNeuroC model, 15 metabolites were always present in at least one of the 100 unbalanced reactions; of these metabolites, 9 have non-chemical atoms that are used to represent a variable metabolite pool or to highlight the reacting zone. Additionally, there are inconsistencies between the information from the sources and the information in the iDopaNeuroC model in 11 metabolites, such as metabolite 9E-elaidic acid, where the InChI with the highest score has a different chemical formula than the formula described in the iDopaNeuroC model, C₁₈H₃₄O₂ in all the sources and in the model C₃₉H₆₄N₇O₁₇P₃S. Furthermore, because the metabolites were obtained from open databases, the model's identifiers in some cases represent a molecule with no stereochemistry or charge, as demonstrated by the metabolite L-arginine, from which the VMH alone obtained the highest score. L-arginine is represented in on the VMH [31] as `arg_L`, in KEGG [39] as C00062 in PubChem [43] as 6322, in HMDB [40] as HMDB00517 and in ChEBI [44] as CHEBI:16467.

1.1 Inconsistencies caused by R groups

The R groups can cause inconsistencies because they represent a substructure that, because they are not defined, can result in unbalanced reactions, such as reaction sphingomyelin phosphodiesterase (VMH ID: HMR_0795).

Reaction	VMH ID	Formula
Glucosylceramidase	GBA	<code>h2o[c] + gluside_hs[c] -> glc_D[c] + crm_hs[c]</code>
Glucosylceramidase (lysosome)	GBA1	<code>h2o[l] + gluside_hs[l] -> crm_hs[l] + glc_D[l]</code>
S-Adenosyl-L-Methionine: Phosphatidylethanolamine N-Methyltransferase	HMR_0653	<code>amet[c] + pe_hs[c] -> 2 h[c] + ahcys[c] + M02686[c]</code>
Ceramide glucosyltransferase	HMR_0761	<code>crm_hs[c] + udpg[c] -> h[c] + udp[c] + gluside_hs[c]</code>
Sphingomyelin phosphodiesterase	HMR_0795	<code>h2o[c] + sphmyln_hs[c] -> h[c] + crm_hs[c] + cholp[c]</code>
Phosphatidic acid phosphatase	PPAP	<code>h2o[c] + pa_hs[c] -> pi[c] + dag_hs[c]</code>
Phosphatidylserine decarboxylase	PSDm_hs	<code>h[m] + ps_hs[m] -> co2[m] + pe_hs[m]</code>
Phosphatidylserine synthase	PSSA1_hs	<code>ser_L[c] + pchol_hs[c] <=> chol[c] + ps_hs[c]</code>
Phosphatidylserine synthase	PSSA2_hs	<code>ser_L[c] + pe_hs[c] <=> etha[c] + ps_hs[c]</code>
Psdm_Hsc	PSDm_hsc	<code>h[c] + ps_hs[c] -> co2[c] + pe_hs[c]</code>
Sphingomyelin synthase	SMS	<code>pchol_hs[c] + crm_hs[c] -> dag_hs[c] + sphmyln_hs[c]</code>

1.2 Inconsistencies caused by protons

Inconsistencies with protons are caused by metabolite pH, which changes the number of hydrogens, resulting in unbalanced reactions, such as reaction N-Acyl-Aliphatic-L-Amino Acid Amidohydrolase (VMH ID: RE2642C)

Reaction	VMH ID	Formula
Cardiolipin synthase	CLS_hs	<code>cdpdag_hs[c] + glylc_hs[c] -> h[c] + cmp[c] + clpn_hs[c]</code>
Glucosylceramidase	GBA	<code>h2o[c] + gluside_hs[c] -> glc_D[c] + crm_hs[c]</code>

Glucosylceramidase (lysosome)	GBA1	$h2o[l] + gluside_hs[l] \rightarrow crm_hs[l] + glc_D[l]$
S-adenosyl-L-methionine: phosphatidyl-N- dimethylethanolamine N- methyltransferase	HMR_0657	$amet[c] + M02758[c] \rightarrow ahcys[c] + pchol_hs[c]$
Ceramide glucosyltransferase	HMR_0761	$crm_hs[c] + udpg[c] \rightarrow h[c] + udp[c] + gluside_hs[c]$
Metabolism of LeuSerTrp (formation/degradation)	LEUSERTRPr	$2 h2o[c] + leusertrp[c] \Leftrightarrow ser_L[c] + leu_L[c] + trp_L[c]$
Lysophospholipase	LPASE	$h2o[c] + lpchol_hs[c] \rightarrow h[c] + Rtotal[c] + g3pc[c]$
Nicotinate D-ribonucleoside kinase	NICRNS	$atp[c] + nicrns[c] \rightarrow h[c] + adp[c] + nicrnt[c]$
Nucleotide phosphatase	NP1	$h[c] + nac[c] + r1p[c] \rightarrow pi[c] + nicrns[c]$
Phospholipase A2	PLA2_2	$h2o[c] + pchol_hs[c] \rightarrow h[c] + Rtotal2[c] + lpchol_hs[c]$
Phospholipase A2 (extracellular)	PLA2_2e	$h2o[e] + pchol_hs[e] \rightarrow h[e] + lpchol_hs[e] + Rtotal2[e]$
RE1266C	RE1266C	$o2[c] + 4mop[c] \rightarrow h[c] + co2[c] + CE2028[c]$
Aminoacid N-acetyltransferase	RE2031M	$accoa[m] + ala_L[m] \Leftrightarrow h[m] + coa[m] + CE1554[m]$
N-acyl-aliphatic-L-amino acid amidohydrolase	RE2642C	$h2o[c] + CE1554[c] \Leftrightarrow ac[c] + ala_L[c]$

1.3 Missing reactions

Finally, three of the missing reactions have stoichiometry that cannot be represented with integers, resulting in the failure to generate an MDL RXN reaction. Additionally, not all metabolites were present in the degradation (VMH id: HDL_HSDEG) and formation (VMH id: HDL_HSSYN) of HDL due to the limited information available about metabolites in the iDopaNeuroC model.

Reaction	VMH ID	Formula
Cytochrome C oxidase; mitochondrial complex IV	CYOOm3	$o2[m] + 7.92 h[m] + 4 focytc[m] \rightarrow 1.96 h2o[m] + 4 h[c] + 4 ficytc[m] + 0.02 o2s[m]$
Degradation of HDL	HDL_HSDEG	$h2o[e] + hdl_hs[e] \rightarrow 2 chsterol[e] + 2 pchol_hs[e] + Rtotal[e] + Rtotal2[e] + Rtotal3[e] + glyc[e] + HC00004[e] + HC00006[e] + HC00007[e] + HC00008[e] + HC00009[e]$
Formation of HDL	HDL_HSSYN	$2 chsterol[e] + 2 pchol_hs[e] + tag_hs[e] + HC00004[e] + HC00006[e] + HC00007[e] + HC00008[e] + HC00009[e] \rightarrow hdl_hs[e]$
HMR_0017	HMR_0017	$M02909[e] \rightarrow 0.125 octa[e] + 0.125 dca[e] + 0.125 but[e] + 0.125 C01601[e] + 0.125 M02108[e] + 0.125 M03117[e] + 0.125 M03134[e] + 0.125 caproic[e]$
Phosphate transport via Na+ symporter	Pit8	$1.5 na1[e] + pi[e] \Leftrightarrow pi[c] + 1.5 na1[c]$

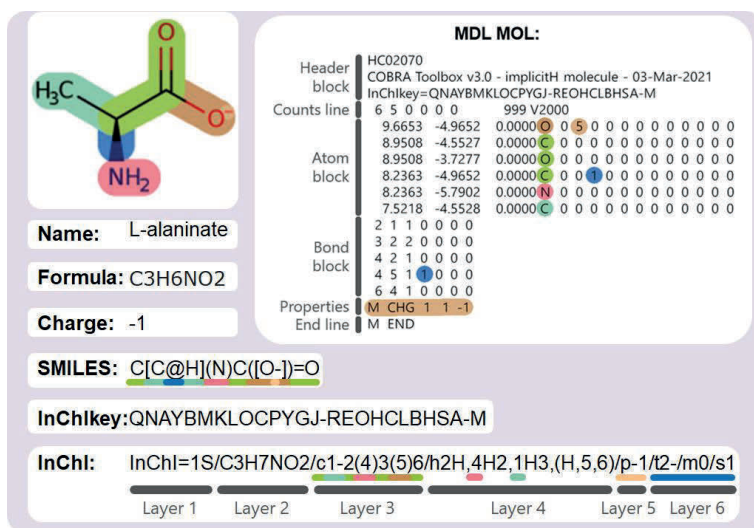


Figure S1. Comparison of metabolite structure formats.

An L-alaninate molecule represented by a hydrogen-suppressed molecular graph (implicit hydrogens). The main branch of the molecule can be seen in green; the additional branches can be seen in brown, pink and turquoise. The stereochemistry of the molecule is highlighted in blue, the double bond in dark green and the charges in light brown. The same colours are used to indicate where this information is represented in the different metabolite structure formats. The InChI is divided into layers, each of which begins with a lowercase letter, except for Layers 1 and 2. Layer 1 indicates if the InChI is standardised. Layer 2 shows the chemical formula in a neutral state. Layer 3 indicates the connectivity between the atoms (ignoring hydrogen atoms). Layer 4 demonstrates the connectivity of the hydrogen atom. Layer 5 indicates the charge of the molecule. Layer 6 shows the stereochemistry. Additional layers can be added, but they cannot be represented with a standard InChI.

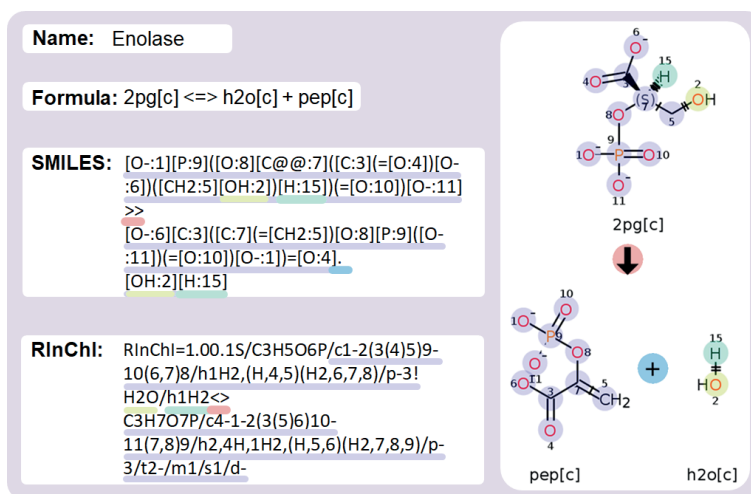


Figure S2. Chemoinformatic formats for chemical reactions.

Atom-mapped representation of enolase reaction in different chemoinformatic formats. The larger moiety in the reaction is shown in blue, the hydroxide moiety in yellow, the hydrogen atom in green, the sum sign in dark blue and the reaction sign in red.

Table S1. Metabolites targeted in the mass isotopologue distribution analysis by fluxTrAM

KEGG id	Name	Formula	LC-MS retention time
C00064	Glutamine	C5H10N2O3	9.952
C00025	Glutamate	C5H9NO4	9.206
C00074	Phosphoenolpyruvate	C3H5O6P	10.57
C00022	Pyruvate	C3H4O3	3.911
C00186	Lactate	C3H6O3	5.587
C00026	Ketoglutarate	C5H6O5	7.272
C00042	Succinate	C4H6O4	6.18
C00122	Fumarate	C4H4O4	8.049
C00149	Malate	C4H6O5	7.979
C00158	Citrate	C6H8O7	12.54

Table S2. List of reactions and atom transitions for the central carbon metabolism model created in INCA

ID	Equation
GLCt1r	glc_D.e (abcdef) -> glc_D (abcdef)
HEX1	glc_D (abcdef) -> g6p (abcdef)
PGI	g6p (abcdef) -> f6p (abcdef)
PFK	f6p (abcdef) -> fdp (abcdef)
FBA	fdp (abcdef) -> dhap (cba) + g3p (def)
TPI	dhap (abc) <-> g3p (abc)
GAPD/PGK	g3p (abc) <-> 3pg (abc)
PGM/ENO	3pg (abc) <-> pep (abc)
PYK	pep (abc) <-> pyr (abc)
LDH_L	pyr (abc) <-> lac_L (abc)
L_LACt2r	lac_L (abc) -> lac_L.e (abc)
G6PDH2r/PGL	g6p (abcdef) -> 6pgc (abcdef)
GND	6pgc (abcdef) -> ru5p_D (bcdef) + co2 (a)
RPI	ru5p_D (abcde) <-> r5p (abcde)
RPE	ru5p_D (abcde) <-> xu5p_D (abcde)
TALA	s7p (abcdefg) + g3p (hij) <-> e4p (defg) + f6p (abchij)
TKT2	xu5p_D (abcde) + e4p (fghi) <-> g3p (cde) + f6p (abfghi)
TKT1	xu5p_D (abcde) + r5p (fghij) <-> g3p (hij) + s7p (fgabcde)
PYRt2m/PDHm	pyr (abc) -> accoa (bc) + co2 (a)
CSm	accoa (ab) + oaa (cdef) <-> cit (fedbac)
ACONTm/ICDHxm	cit (abcdef) <-> akg (abcde) + co2 (f)
AKGDm/SUCOAS1m	akg (abcde) <-> succ (bcde) + co2 (a)
SUCD1m	succ (abcd) <-> fum (abcd)
FUMm	fum (abcd) <-> mal_L (abcd)
MDHm	mal_L (abcd) <-> oaa (abcd)
PCm	pyr (abc) + co2 (d) -> oaa (abcd)
GLUDxm	glu_L (abcde) <-> akg (abcde)
GLUVESSEC	glu_L.e (abcde) -> glu_L (abcde)
GLNtm/GLUNm	gln_L (abcde) <-> glu_L (abcde)
In_gln_L	gln_L.in (abcde) -> gln_L (abcde)
Out_Pyr	pyr (abc) -> pyr.out (abc)
ME	mal_L (abcd) -> pyr (bcd) + co2 (a)
In_CO2	co2.in (a) -> co2 (a)
Out_CO2	co2 (a) -> co2.out (a)
Out_gln_L	gln_L (abcde) -> gln_L.out (abcde)
In_Pyr	pyr.in (abc) -> pyr (abc)

Table S3. Correlation analysis of integration results from automated packages and manual software

Pearson correlation p values between automatically and manually collected isotopologue fractions for each of the tested nine metabolites. ND = not detected.

Metabolite	mzMatch-ISO _{vs} Skyline	mzMatch-ISO _{vs} & EIMAVEN	X¹³CMS _{vs} & Skyline	X¹³CMS _{vs} & EIMAVEN
Phosphoenolpyruvate	7.22E-10	6.77E-10	ND	ND
Fumarate	3.06E-14	3.18E-11	5.19E-06	5.54E-05
Ketoglutarate	6.29E-12	1.13E-14	8.45E-21	9.25E-15
Alanine	3.02E-08	2.09E-07	1.44E-07	8.31E-09
Aspartate	6.77E-16	1.02E-16	2.23E-05	2.48E-05
Glutamate	2.10E-13	8.95E-29	3.29E-10	8.17E-10
Fructose 1,6-bisphosphate	3.98E-31	1.33E-41	1.60E-03	1.91E-03
Glutathione	5.99E-34	9.49E-51	5.44E-33	1.89E-39
ATP	1.25E-53	1.61E-58	3.51E-25	2.08E-25

Table S4. The t-test examination over the automatically processed MID results of amino acids between labelled and unlabelled samples

class	metabolite	Isotopologue	Sample_L1	Sample_L2	Sample_L3	Standard deviation in Sample_L	Sample_U1	Sample_U2	Sample_U3	Standard deviation in Sample_U	statistic	p value	
Conditionally essential amino acid	Proline	0	0.65	0.66	0.66	0.01	0.94	0.93	0.93	0.00	-67.20	<0.00001*	
		1	0.07	0.06	0.05	0.01	0.06	0.07	0.07	0.00	-1.17	0.30582	
		2	0.15	0.16	0.15	0.00	0.00	0.00	0.00	0.00	0.00	59.87	<0.00001*
		3	0.06	0.05	0.06	0.01	0.00	0.00	0.00	0.00	0.00	16.68	0.00008*
		4	0.05	0.04	0.05	0.01	0.00	0.00	0.00	0.00	0.00	15.56	0.00010*
	Tyrosine	5	0.03	0.03	0.03	0.00	0.00	0.00	0.00	0.00	0.00	18.09	0.00005*
		0	0.91	0.91	0.90	0.01	0.89	0.89	0.88	0.88	5.44	0.00553*	
		1	0.09	0.08	0.09	0.01	0.10	0.10	0.11	0.11	0.00	-4.34	0.01222*
		2	0.00	0.01	0.00	0.00	0.01	0.00	0.00	0.01	0.00	-1.28	0.26843
		3	0.00	0.00	0.00	0.00	0.00	0.00	0.00	0.00	0.00	-4.28	0.01287*
Essential amino acid	Glutamine	4	0.00	0.00	0.00	0.00	0.00	0.00	0.00	0.00	4.97	0.00768*	
		5	0.00	0.00	0.00	0.00	0.00	0.00	0.00	0.00	-10.51	0.00046*	
		6	0.00	0.00	0.00	0.00	0.00	0.00	0.00	0.00	1.00	0.37390	
		7	0.00	0.00	0.00	0.00	0.00	0.00	0.00	0.00	4.61	0.00993*	
		8	0.00	0.00	0.00	0.00	0.00	0.00	0.00	0.00	1.00	0.37390	
	Methionine	9	0.00	0.00	0.00	0.00	0.00	0.00	0.00	0.00	0.00	1.00	0.37390
		0	0.95	0.93	0.94	0.01	0.98	0.97	0.98	0.98	0.01	-4.23	0.01342*
		1	0.02	0.02	0.02	0.00	0.01	0.02	0.02	0.01	0.01	1.75	0.15481
		2	0.00	0.00	0.00	0.00	0.00	0.00	0.00	0.00	0.00	5.52	0.00527*
		3	0.00	0.00	0.00	0.00	0.00	0.00	0.00	0.00	0.00	8.45	0.00107*
Threonine	Leucine	4	0.00	0.00	0.00	0.00	0.00	0.00	0.00	0.00	6.22	0.00340*	
		5	0.00	0.00	0.00	0.00	0.00	0.01	0.01	0.01	0.00	-9.65	0.00065*
		0	0.94	0.95	0.94	0.01	0.94	0.92	0.93	0.93	0.01	2.61	0.05955
		1	0.06	0.05	0.06	0.01	0.06	0.08	0.07	0.07	0.01	-2.79	0.04921*
		2	0.00	0.00	0.00	0.00	0.00	0.00	0.00	0.00	0.00	0.44	0.67992
	Isoleucine	3	0.00	0.00	0.00	0.00	0.00	0.00	0.00	0.00	0.00	1.00	0.37390
		4	0.00	0.00	0.00	0.00	0.00	0.00	0.00	0.00	0.00	0.00	0.00
		5	0.00	0.00	0.00	0.00	0.00	0.00	0.00	0.00	0.00	0.00	0.00
		6	0.00	0.00	0.00	0.00	0.00	0.00	0.00	0.00	0.00	0.00	0.00
		0	0.92	0.93	0.93	0.01	0.93	0.93	0.93	0.93	0.00	-0.21	0.84734
Phenylalanine	1	0.07	0.06	0.07	0.01	0.07	0.07	0.07	0.07	0.00	-0.14	0.89837	
	2	0.00	0.00	0.00	0.00	0.00	0.00	0.00	0.00	0.00	3.61	0.02346*	
	3	0.00	0.00	0.00	0.00	0.00	0.00	0.00	0.00	0.00	0.00	0.00	
	4	0.00	0.00	0.00	0.00	0.00	0.00	0.00	0.00	0.00	0.00	0.00	
	5	0.00	0.00	0.00	0.00	0.00	0.00	0.00	0.00	0.00	0.00	0.00	
	6	0.00	0.00	0.00	0.00	0.00	0.00	0.00	0.00	0.00	0.00	0.00	
	Phenylalanine	0	0.89	0.90	0.90	0.00	0.90	0.90	0.93	0.93	0.02	-1.52	0.20249
		1	0.10	0.09	0.10	0.00	0.09	0.09	0.07	0.07	0.02	1.32	0.25142
		2	0.01	0.01	0.00	0.00	0.00	0.00	0.00	0.00	1.45	0.22057	

Table S6. Comparison of four sets of flux distributions in the core model

Rxn_ID	Rxn_Name	Rxn_Formula	subSystems	INCA model Equation	EntropyFlux	MolecFlux	FluxFlux	FBAFlux	INC/Model	StdErr	I_B	UB
R1: Merge	Glucose Transport (Umpor)	glc_D[6] <=> glc_D[6]	Transport, extracellular	Glucose >= Glucose	427.4398	427.4396	440.0000	433.91	0.19	421.25	446.56	
R2: Reversed	Glucose Transport via Sodium Symport	na[1] + glc_D[6] <=> na[1] + glc_D[6]	Transport, extracellular	Pyr >= Pyr	530.6723	537.2800	10000.0000					
PR2R	Transport of Pyruvate Reversible via Proton Symport	hg[1] + pyr[6] <=> hg[1] + pyr[6]	Transport, extracellular	Pyr.in >= Pyr	6.9377	5.1566	-1.0000E+0000	774.60	0.47	660.74	896.96	
R3: GLN4	Transport of L-Glutamine via Sodium Symport, Reversible	na[1] + glc_L[6] <=> na[1] + glc_L[6]	Transport, extracellular	Gluc >= Gh	1.5147	2.1135	0.0000	6.31E-08	0.00	-1484.30	1228.80	
R4: Merge	Glutamate Transport via Na, H Symport, Acid K, Antiport	hg[1] + 3 na[1] + hg[1] + glc_L[6] <=> hg[1] + 3 na[1] + glc_L[6] + hg[1]	Transport, extracellular	Glu.in >= Glc	1.63E-07	1.63E-08	0.00	1.00E-07	0.00	2.73E-08	1328.30	
GLU6	Glutamate Secretion via Secretory Vesicle (ACT, DRAK1)	hg[1] + 3 na[1] + hg[1] + glc_L[6] <=> hg[1] + 3 na[1] + glc_L[6] + hg[1]	Transport, extracellular	Glu.in >= Glc.out	0.0000	0.0000	0.0000			0.00	1483.30	
GLU6SEC	Glutamate Intake by System Asct-1 Transporter	na[1] + glc_L[6] + pro_L[6] <=> na[1] + glc_L[6] + pro_L[6]	Transport, extracellular	Gluc >= Glu	2.2764	2.7179	100009.2040	1.39	0.06	1.24	1.55	
R5: Reversed	L-Lactate Reversible Transport via Proton Symport	hg[1] + hc_L[6] <=> hg[1] + hc_L[6]	Transport, extracellular	Glucose >= G6P	101.8607	55.6727	0.0001	433.91	0.19	421.25	446.56	
HEX1	Hexokinase (D-Glucose:ATP)	glc[6] + glc_D[6] >= hg[1] + adp[6] + g6p[6]	Glycolysis/gluconeogenesis	Glucose >= G6P	47.0870	22.6522	0.0001					
CHP1P	Catalanoyl Phosphate Phosphotransferase, Retention	hg[1] + glc_D[6] + g6p[6] >= na[6] + adp[6] + g6p[6]	Glycolysis/gluconeogenesis	Glucose >= G6P	0.0000	0.0004	0.0000					
0154	Hexokinase	hg[6] + glc_D[6] >= hg[6] + adp[6] + g6p[6]	Glycolysis/gluconeogenesis	Glucose >= G6P	4.6387	3.3390	0.0000					
0155	Hexokinase	hg[6] + glc_D[6] >= hg[6] + adp[6] + g6p[6]	Glycolysis/gluconeogenesis	Glucose >= G6P	50.1350	29.6811	0.0000					
R7: FGI	Glucose-6-Phosphate Isomerase	g6p[6] <=> f6p[6]	Glycolysis/gluconeogenesis	G6P >= F6P	73.1642	49.1976	-1.0000E+0000	433.91	0.70	421.25	446.56	
R8: FPK	Phosphofructokinase	f6p[6] + f6p[6] >= frp[6] + frp[6]	Glycolysis/gluconeogenesis	F6P >= FRP	30.7213	19.3229	0.0000	433.91	0.19	421.25	446.56	
R9: FBA	Fructose-Bisphosphate Aldolase	f6p[6] <=> dhap[6] + g3p[6]	Glycolysis/gluconeogenesis	FRP >= DHAP + GAP	66.8249	43.4680	0.0000	433.91	0.19	421.25	446.56	
R10: TPI	Triose Phosphate Isomerase	dhap[6] <=> g3p[6]	Glycolysis/gluconeogenesis	DHAP <=> GAP	78.6574	52.0826	-7.998E+0000	433.91	0.19	421.25	446.56	
R11: Merge	Glycerinaldehyde-3-Phosphate Dehydrogenase	pgl[6] + na[6] + p3p[6] <=> hg[6] + na[6] + 134p[6]	Glycolysis/gluconeogenesis	GAP <=> 3PG	158.5497	105.3870	-7057.0000	867.81	0.25	842.51	893.12	
PKD	Phosphopyruvate Kinase	na[6] + 3pg[6] <=> adp[6] + 134p[6]	Glycolysis/gluconeogenesis	3PG <=> PEP	-15.8397	-105.3920	7057.0000					
R12: Merge	Acylphosphatase	134p[6] + 134p[6] <=> hg[6] + 3pg[6]	Glycolysis/gluconeogenesis	3PG <=> PEP	158.5497	105.3936	-7057.0000	867.81	0.25	842.51	893.12	
RKM	Phosphopyruvate Kinase	3pg[6] <=> 3pg[6]	Glycolysis/gluconeogenesis	3PG <=> PEP	-15.8397	-105.3930	7057.0000					
ENO	Enolase	3pg[6] <=> b2pg[6] + p2p[6]	Glycolysis/gluconeogenesis	PEP <=> Pyr	158.5497	105.3940	-7057.0000					
R13: Merge	Pyruvate Kinase	hg[6] + adp[6] + p2p[6] >= pyg[6] + p2p[6]	Glycolysis/gluconeogenesis	PEP <=> Pyr	152.5825	100.7097	92940.0000	867.81	0.25	842.51	893.12	
PKK	DYATP Pyruvate O2-Phosphotransferase	hg[6] + adp[6] + p2p[6] >= pyg[6] + p2p[6]	Glycolysis/gluconeogenesis	PEP <=> Pyr	48.1342	34.1840	0.0000					
0113	DYATP Pyruvate O2-Phosphotransferase	hg[6] + adp[6] + p2p[6] >= pyg[6] + p2p[6]	Glycolysis/gluconeogenesis	PEP <=> Pyr	5.9925	4.0385	0.0000					
0120	DYATP Pyruvate O2-Phosphotransferase	hg[6] + adp[6] + p2p[6] >= pyg[6] + p2p[6]	Glycolysis/gluconeogenesis	PEP <=> Pyr	45.2266	26.0918	0.0000					
0122	GTP Pyruvate O2-Phosphotransferase	hg[6] + adp[6] + p2p[6] >= pyg[6] + p2p[6]	Glycolysis/gluconeogenesis	PEP <=> Pyr	6.6746	4.1498	0.0000					
0153	CTP Pyruvate O2-Phosphotransferase	hg[6] + adp[6] + p2p[6] >= pyg[6] + p2p[6]	Glycolysis/gluconeogenesis	PEP <=> Pyr	5.9884	4.8780	92940.0000					
0165	UTP Pyruvate O2-Phosphotransferase	hg[6] + adp[6] + p2p[6] >= pyg[6] + p2p[6]	Glycolysis/gluconeogenesis	PEP <=> Pyr	46.9792	27.3676	0.0000					
R14: Merge	L-Lactate Dehydrogenase	na[6] + hc_L[6] <=> hg[6] + na[6] + 134p[6]	Pyruvate metabolism	Pyr <=> Lac	132.0235	67.6056	55.0000	91.60	0.44	12.39	170.81	
LDR_Ln	Lactate Dehydrogenase	na[6] + hc_L[6] <=> hg[6] + na[6] + 134p[6]	Pyruvate metabolism	Pyr <=> Lac	0.1883	-0.0032	1200.0000					
0171	Lactate Dehydrogenase	na[6] + hc_L[6] <=> hg[6] + na[6] + 134p[6]	Glycolysis/gluconeogenesis	Pyr <=> Lac	-34.2120	-105.3920	7057.0000					
0173	5(2)-Lactate:NDP Oxidoreductase	na[6] + hc_L[6] <=> hg[6] + na[6] + 134p[6]	Glycolysis/gluconeogenesis	Pyr <=> Lac	158.5497	105.3930	-7057.0000					
R15: Merge	Glucose-6-Phosphate Dehydrogenase, Endoplasmic Reticulum	na[6] + g6p[6] <=> hg[6] + na[6] + g6p[6]	Pentose phosphate pathway	G6P >= 6PG	7.9932	1.5662	0.0000	1.00E-07	0.83	0.00	446.49	
GDHtrntr	Glucose-6-Phosphate Dehydrogenase, Endoplasmic Reticulum	na[6] + g6p[6] <=> hg[6] + na[6] + g6p[6]	Pentose phosphate pathway	G6P >= 6PG	0.0667	0.7647	-0.0366					
GDHtrZtr	Glucose-6-Phosphate Dehydrogenase, Endoplasmic Reticulum	na[6] + g6p[6] <=> hg[6] + na[6] + g6p[6]	Pentose phosphate pathway	G6P >= 6PG	0.2160	0.3325	0.0386					
GDHtrZtr	Glucose-6-Phosphate Dehydrogenase, Endoplasmic Reticulum	3 na[6] + g6p[6] <=> 3 hg[6] + 3 na[6] + 3 g6p[6]	Pentose phosphate pathway	G6P >= 6PG	7.7705	0.4489	0.0000					
PGI4tr	6-Phosphogluconate Kinase, Endoplasmic Reticulum	b2pg[6] + 6pg[6] >= hg[6] + 6pg[6]	Pentose phosphate pathway	6PG >= R6P	0.2227	1.1381	0.0000					
PGI4tr	6-Phosphogluconate Kinase, Endoplasmic Reticulum	3 b2pg[6] + 3 gpg[6] >= 3 hg[6] + 3 gpg[6]	Pentose phosphate pathway	6PG >= R6P	7.4600	0.6626	0.0000					
PGI4tr	6-Phosphogluconate Kinase, Endoplasmic Reticulum	b2pg[6] + gpg[6] >= hg[6] + gpg[6]	Pentose phosphate pathway	6PG >= R6P	0.8702	0.1328	0.0000					
R16: Merge	Phosphoethanolamine Dehydrogenase, Endoplasmic Reticulum	na[6] + epg[6] >= adp[6] + na[6] + epg[6]	Pentose phosphate pathway	6PG >= Ru5P - CO2	0.6909	1.95E-05	0.00E+0000	1.00E-07	0.83	0.00	446.49	
GDHtr	Phosphoethanolamine Dehydrogenase, Endoplasmic Reticulum	na[6] + epg[6] >= adp[6] + na[6] + epg[6]	Pentose phosphate pathway	6PG >= Ru5P - CO2	0.0000	0.0000	0.0000					

Table S7. A list of 10 conserved moieties identified within the atomically resolved iDopaNeuroC model

Index	Metabolites	Rxns	Moisty_formula	Mass	Minimal_mass_metabolite	Name	Formula	Mass_fraction	Internal reaction coverage	internal subsystem hits in flux-based active subsystems	internal subsystem hits in moiety flux-based top 15 active subsystems	Uptaken metabolite
28	59	228	'S'	31.9720707	'HC00250[c]'	'Hydrosulphide'	'HS'	0.96944123	40.80%	1	1	Cysteine
56	22	60	'C5HA2O5'	140.982398	'HC02056[c]'	'1,2-Diacylglycerol-Ld-Pc-Pool'	'C5HG05R2'	0.965490531	54.80%	0	0	
5	27	105	'C19H7N7O4'	397.055952	'fol[c]'	'Folate'	'C19HH18N7O6'	0.902129546	55.60%	0	0	Folate
59	60	294	'C4H2N2O'	94.0167127	'urs[c]'	'Uracil'	'C4HH4N2O2'	0.839230542	75.60%	4	2	Thymidine
27	44	125	'C5H3N2'	91.0296231	'im4act[c]'	'Imidazole-4-Acetaldehyde'	'C5H6N2O'	0.82718908	30.10%	0	0	Histidine
93	31	114	'C6H7O'	95.0496898	'4mop[c]'	'4-Methyl-2-Oxopentanoate'	'C6H9O3'	0.736504322	22.60%	1	1	Leucine
90	30	110	'C6H6O'	94.0418648	'3mop[c]'	'3-Methyl-2-Oxopentanoate'	'C6H9O3'	0.728695065	22.60%	1	1	Isoleucine
29	39	130	'C9H6N'	128.050024	'serm[c]'	'Serotonin'	'C10H13N2O'	0.723026586	27.00%	0	0	Tryptophan
25	37	148	'S'	31.9720707	'3mtp[c]'	'3-Methyl-Thio-Proprionate'	'C4H8OS'	0.307336327	44.30%	1	1	methionine
44	26	103	'CHN'	27.010899	'crtm[c]'	'Creatinine'	'C4H7N3O'	0.238909951	28.60%	1	1	Arginine

Chapter 6:

Conclusions and Perspectives

Conclusion

The progressive loss and degeneration of dopaminergic neurons in the mid-brain region is a major pathological hallmark of Parkinson's disease (PD). Due to poorly understood disease pathogenic mechanisms, current therapy is compromised and focused more on treating motor symptoms than slowing down the neurodegenerative process. The onset and progression of PD can be triggered by multiple risk factors, for instance genetic mutation, environmental exposure, and aging. Each of these factors may cause common or unique metabolic disturbances, ultimately converging into a complex metabolic disorder reflected in the diversity of clinical phenotypes. Through metabolome analysis, the full picture of the metabolic landscape depicting a biological system can be revealed. Metabolites function as key elements and direct read-outs of a system's functional status. Alterations in the metabolite concentrations are thus informative for inferring and understanding the underlying metabolic activity. Metabolites are typically characterized by significant physicochemical variability and wide concentration ranges. This diversity creates analytical challenges, and a single analytical platform rarely covers the full range of metabolites of interest [1]. It also makes it important to evaluate the platforms that can be utilized for metabolomics analysis, taking into account the sample type, sample volume, research questions, metabolite concentration, etc. Information derived from broad metabolic profiling can be very instructive in understanding biochemical changes resulting from perturbations. In addition, stable isotope labeling techniques coupled with metabolomics can bring us an extra dynamic vision of the metabolic landscape. Changes in the labeling patterns of metabolites help identify alterations with metabolic fluxes through pathways. For the analytical workflow to capture and process these alterations in metabolite labeling patterns, more analytical and computational developments are still required.

The aim of this thesis was to develop a comprehensive analytical strategy for characterizing the metabolic activity related to PD neurodegeneration, especially focused on the improvement in metabolome coverage and data quality, and facilitating use of stable isotope labeling in in-depth metabolism investigation. In this chapter, we summarize the multifaceted solutions for constructing our comprehensive analytical strategy in PD metabolomics research. The key solutions revolved around tackling the current analytical challenges faced in selecting an appropriate polar stationary phase used in polar metabolome analysis, advancing the analytical method for tracer-based metabolome analysis, and developing a computational workflow for metabolic flux analysis. These methods were applied to investigate metabolic dysregulation of dopaminergic neurons to genetic and environmental factors. The value and contribution of developed methodological

solution in this thesis, as well as the current limitations, are reviewed. Finally, we conclude by proposing opportunities for future research.

Polar metabolome analysis using LC-MS

The ultimate aim of metabolomics is to precisely identify and quantify all metabolites present in a specific biological sample. High-resolution mass spectrometry with an increasing mass resolving power, coupled with enhanced chromatographic resolution, has improved the metabolomics analysis towards broadened feature detection. It has been widely recognized that the combination of multiple analytical platforms in metabolomics is an appropriate strategy to increase global metabolite coverage. Reversed-phase liquid chromatography (RPLC) mainly targets the non-polar and mid-polar metabolome analysis, and hydrophilic interaction chromatography (HILIC) targets the polar metabolome analysis. The chromatographic separation is highly determined by the interaction of the metabolite with the stationary phase, followed by fine-tunings of solvents, pH, additives, column dimensions, and temperature. But due to the limited understanding of HILIC retention mechanisms and lack of guidance on HILIC method evaluation, HILIC is less widespread than RPLC for global metabolomics studies. Polar metabolites account for a large proportion of the metabolome and play important roles in regulating energy and biomass production (e.g. amino acids, carbohydrates, carnitines), interconnecting metabolic modules as a reflection of overall metabolic state (e.g. ATP, NAD(H), S-adenosylmethionine), and producing reporter metabolites in controlling and modulating the activity of signaling pathways (e.g. glycolytic intermediates) [2]. From this, it is reasonable to assume that the comprehensive analysis of polar metabolites involved in major biochemical pathways (e.g., glycolysis, the tricarboxylic acid (TCA) cycle, the pentose phosphate pathway, amino acid metabolism, nucleotide metabolism, neurotransmission, etc.) would allow for an extensive exploration of metabolic dysregulation related to neurodegeneration.

To accelerate the implementation of HILIC-MS analysis as a routine platform for large-scale clinical PD metabolomics studies, the analytical requirements of resolution, reproducibility, robustness, efficiency and result reliability have to be strictly evaluated. In **Chapter 2**, we provided guidance for systematically evaluating hydrophilic interaction chromatography column performance for global plasma metabolomics studies. Plasma was selected as the investigated biological matrix due to its ease of collection and high information content. First, a scoring system was designed to evaluate the chromatographic performance of representative standards involving the aspects of metabolite retention, peak sensitivity (signal-to-noise ratio), peak sharpness (peak height), and peak symmetry (tailing factor). Second, a simple linear regression model could be constructed to analyze the

relationship between metabolite polarity at different pH conditions and elution order, allowing for the investigation of the column retention mechanisms. Third, assessment of the matrix effect and particularly the ion suppression induced by salts helped to identify the vulnerable metabolite classes or the elution range affected by salt ions (clusters). Fourth, a repeatability test monitoring the retention time and peak area of spiked standards in plasma was used to evaluate the column stability for intra- or inter-batch analysis. Finally, a pilot study using an untargeted metabolomics analysis of test plasma from different phenotypes could be carried out to estimate the total metabolic feature coverage and feature retention distribution.

Following this systematic evaluation, we determined the ZIC-c HILIC column (zwitterionic stationary phase) operated at neutral pH was optimal for global polar metabolome analysis due to its superior performance for different classes of compounds, better isomer separation, good repeatability, and high metabolic coverage. We also specifically demonstrated the ion suppression caused by the sodium chloride in the plasma analysis. Thereby, it is recommended to restrict the introduction of salt ions, for instance anticoagulant counter cations (Na^+ from citrate in Na-citrate plasma and K^+ from K-EDTA in EDTA plasma), as reported by a previous study [3]. Additional difficulties arise because citrate and EDTA show some retention on the HILIC column and will induce ion suppression or enhancement effects on other co-eluting peaks. Considering these obstacles, heparin plasma is preferred for future HILIC-MS global analysis. This evaluation procedure can be selectively applied to any new HILIC column or new biomatrix test in the future. And as current HILIC columns are not yet fully robust, new HILIC columns can be expected to be developed and offered. The optimized HILIC-MS chromatographic method developed in **Chapter 2** served as the basis for the targeted metabolomics study in **Chapter 3**, and the mass spectrometric approach coupled with this separation method was further optimized for tracer-based metabolomics in **Chapter 4**.

Targeted metabolomics provides distinct advantages in the quantification of known metabolites belonging to certain compound classes or common metabolic pathways with a high level of confidence in the accuracy, precision, and repeatability, despite the limited number. To achieve a broad and known metabolite analysis with a wide dynamic range in our PD pathogenesis investigation, we adopted three analytical platforms for targeted profiling of 106 polar metabolites, 50 acyl-carnitines, and over 200 signaling lipids. By utilizing human iPSC-derived midbrain neuronal models, a new way for simulating PD metabolic disease brought on by specific genetic/environmental factors and their interacting contributions was presented. The methodological advancements enabled us to capture a comprehensive picture of metabolomic dysregulation in an in-vitro iPSC-derived midbrain

neuronal model of PD represented by the PINK1 mutation, mitochondrial complex I inhibitor (rotenone), and joint-factor intervention in **Chapter 3**. This gave us a chance to investigate into the hypothesis that genetic deficiency involved in mitochondrial-stress pathways could increase the susceptibility towards neurodegeneration in response to environmental toxins. Through comparative metabolomics analysis, we found similar metabolic dysregulation caused by rotenone and the PINK1 mutation seen in energy failure (reduced fueling by glucose, saturated fatty acids, and branched chain amino acids), impaired redox balance (blocked oxidation of NADH to NAD⁺), as well as different TCA cycle disturbances, all leading to impaired mitochondrial respiration. Moreover, oxidative damage was found in both the mutated and rotenone-exposed groups. However, the PINK1-mutated model showed a robust anti-oxidative and anti-inflammatory response, while a rather severely disturbed response was seen due to rotenone exposure. Neurons with the inherent PINK1 mutation interacting with exogenous rotenone stress resulted in a more complicated neurodegenerative metabolism. This study clearly unraveled the underlying molecular mechanism of mitochondrial dysfunction induced by a genetic or environmental toxin perturbation and explained the complexity of neurodegeneration from a metabolomics perspective. The supplementation of NAD⁺ or its precursors has been reported as a promising therapeutic strategy for future clinical PD treatment [4,5]. Targeting the same set of PD neuronal models, this study additionally demonstrated the limited efficacy of NAD⁺ treatment in ameliorating rotenone-related energy defects, and had no effectiveness for the PINK1 mutated group. Instead, it unexpectedly introduced dysregulation of polyunsaturated fatty acids to the joint-factor group. Overall, our study provides valuable insights into a deep understanding of parkinsonism pathogenesis.

In **Chapter 3**, the combination of multiple metabolomics platforms targeting specific polar and non-polar metabolites opened several windows that allowed us to specifically probe cellular metabolic activity in different metabolic pathway modules. Since just one patient cell line was used as the established neuronal model, a follow-up validation using more patient cell lines with the PINK1 mutation is still required. In the future, improved or novel drug treatments can be evaluated using the established neuronal models and targeted metabolomics platforms. Targeted metabolomics analysis can also be performed on plasma samples from patients in order to highlight the release of unique metabolite markers from neurons into the intravascular fluid. In addition, global plasma analysis will be a crucial and indispensable approach for identifying novel biomarkers with a strong correlation to neuronal alterations as well as a high level of significance, which is achievable by combining the established HILIC-MS method described in **Chapter 2** with the complementary RPLC-MS methods.

Use of Stable isotope labeling for in-depth metabolic flux investigations

The metabolomics study performed in **Chapter 3** to determine the probable changes in the metabolic network in neurons was helpful in identifying relevant biochemical pathways to follow up using stable isotope labeling. Therefore, we focused on central carbon metabolism and its connection to de novo nucleotide synthesis and glutathione metabolism pathways in an effort to capture the reaction changes from energy failure towards oxidative stress related to PD neurodegeneration. Current stable isotope enrichment analysis using mass spectrometry primarily records the total number of labeled atoms and the mass isotopologue distribution (MID) of the intact metabolite structure. Labeling information at the intact level can be used to probe pathway activity. Labeling information at the metabolite substructure (moiety) level also plays an important role in discovering novel pathways and estimating metabolic fluxes. A dissection at the moiety level can bring additional insights into pathway reconstruction, reaction connections, and relevant flux regulation [6–8]. However, there are still technological challenges in detecting intact metabolites and fragmented moiety isotopologues with strong specificity while maintaining high sensitivity and accuracy.

In **Chapter 4**, we developed a HILIC-Zeno MRM^{HR} method for structurally-resolved mass isotopologue distribution analysis, allowing simultaneous acquisition at MS¹ and MS² levels in a single analytical run. From an analytical perspective, this method successfully achieved accurate and reproducible MID quantification for intact metabolites as well as their fragmented moiety, with notably high sensitivity in the MS² fragmentation mode using Zeno trap pulsing, a system of trapping fragment ions prior to the Time-of-Flight (TOF) injection for duty cycle improvement. Compared to the conventional SWATH method, this method still preserved the relationship between labeled precursor and fragment ions, which was beneficial in accurately identifying the same labeled isotopologue with differential labeling positions. We demonstrated the case by distinguishing two different isotopomers (1,2-¹³C₂-glutamate and 3,4-¹³C₂-glutamate) that belong to the same isotopologue (¹³C₂-glutamate) but are produced by pyruvate anaplerosis (PDH) and pyruvate carboxylase (PC) activity, respectively, from a given D-¹³C₆-glucose tracer.

From an application perspective, the HILIC-Zeno MRM^{HR} method successfully identified flux regulations of glutathione metabolism in relation to rotenone-induced neurodegeneration. By interpreting the intact metabolite and moiety MID data, we first validated the pathway reconstruction of de novo glutathione synthesis in mid-brain neurons from isotopically labeled nutrient sources, separately using D-¹³C₆-glucose and L-¹⁵N₂-glutamine. Increased oxidation from basal and de novo synthesized glutathione pools under neuronal oxidative stress both contributed to the severely impaired anti-oxidative capability

caused by rotenone exposure. Furthermore, we demonstrated the decreased de novo glutathione synthesis was associated with altered activities of several key enzymes found in the glucose-derived glutamate supply and GSH synthetic reaction. The application of our approach was not limited to elucidating glutathione metabolism but also included studying de novo nucleotide metabolism connected with central carbon metabolism in response to rotenone perturbation. By considering the hypothesis of potentially changed enzyme activity along relevant pathways, the method allows for flexibility in selecting target metabolites for fragmentation. Identification of the key metabolic flux regulations within these metabolic pathways can further augment our understanding of disease mechanisms. Metabolite labeling patterns in conjunction with targeted metabolomics data are strongly effective in elucidating the cellular flux control of a specific metabolic pathway or reaction under selectively perturbed conditions [9]. This approach works well for hypothesis verification via revealing localized regulation [9,10]. To achieve comprehensive flux phenotyping for studied cell models on a network-wide scale, a quantitative approach to metabolic flux inference has been gradually developed, named fluxomics. This global monitoring approach shows promise for quickly identifying primary flux re-routing for accommodating diseased condition based on the changes of absolute fluxes over multiple metabolic pathways and contributes to new hypothesis generation. However, there is still a long way to go before it finally reaches its true potential for accurately characterizing mammalian cell metabolism at the broader scale. This heavily relies on the constant development and improvement of both analytical and computational methodologies covering reliable reconstruction of a cell type-specific metabolic model, accurate atom mapping in metabolic reactions, measurement of isotopomers encompassing labeled positional information, the development of standardized and high-throughput data processing and analysis pipelines, etc [11,12].

Chapter 5 presented our efforts in constructing a semi-automated pipeline in MATLAB, for computing **flux** with **Tracer-metabolomics in Atom-resolved Modelling (fluxTrAM)**. The first part of the fluxTrAM pipeline could process tracer-based LC-MS raw data and convert them into a standardized MID dataset. This involved multiple steps, including raw MS data format conversion, metabolite peak detection and integration, isotopologue peak correction with naturally occurring isotopic abundance, and basic summarization of metabolite MID results. The peak integration performance of both manual and automated software packages was rigorously assessed using the HILIC-MS method to measure multiple metabolite classes. The optimal package, mZMatch-ISO, was embedded into the pipeline and guaranteed accurate targeted isotopologue integration. Additionally, automated connections between various packages reduced the amount of data format

manipulation and enabled a sequential data processing workflow. The second part of the fluxTrAM pipeline focused on atomically resolving any given genome-scale metabolic model, where the results included a chemoinformatic database of standardized and context-specific metabolite structures and atom mapped reactions. In the final part of the fluxTrAM pipeline, experimental MID data could be exported into external ^{13}C flux analysis programs for flux estimation on a small network scale. Meanwhile, it could also be integrated into the atomically resolved genome-scale model for flux analysis at the genome-scale. The feasible flux distribution obtained from the small and generic central carbon metabolism model served as a good reference solution for determining the flux feasibility obtained from the neuron-specific genome scale model. On the other hand, the genome-flux solution revealed extensive metabolism regulation in the studied cell model that extended far beyond central carbon metabolism. Our work presented the first genome-scale flux solution of human dopaminergic neuronal metabolism based on experimental tracer-based metabolomics data. It helped in revealing many characteristic metabolic phenotypes of neuronal cells while also raising the necessity for studying more PINK1 patient-derived cell lines. In the future, follow-up verification of disease hypotheses generated from genome-flux solutions can be achieved using the combined targeted metabolomics (**Chapter 3**) and tracer-based metabolomics approaches (**Chapter 4**). In addition, new (tracer-based) metabolome data can be used as input for further refining the neuron-specific genome-scale model and predicting new flux distribution, as illustrated in the **Figure 6.1** (a, b, c, e, r1 and r2).

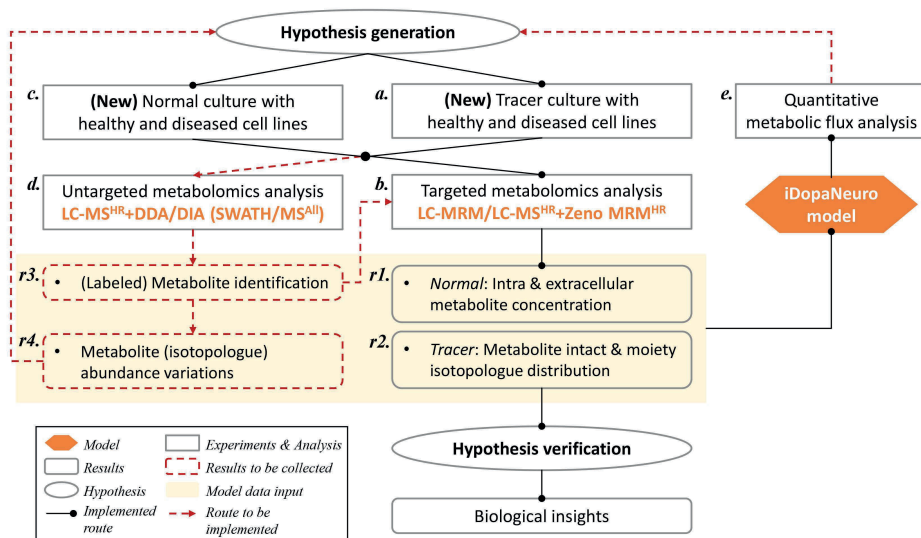


Figure 6.1. A schematic workflow for combining conventional metabolomics and tracer-based metabolomics approaches in the PD neuronal metabolism study. Tracer culture represents cells fed

with stable isotope-labeled substrates, while normal culture is provided with unlabeled substrates. The future implementations are labeled in red dotted lines and the expected results to be collected are labeled in red dotted boxes. a-e: cell culture, analytical experiments, and computational analysis. r1-r4: Metabolome results, as data input for the iDopaNeuro model.

Future perspectives

In this thesis, we demonstrated the capacity of our developed HILIC-MS method for global polar metabolome analysis (**Chapter 2**) and its subsequent application into targeted metabolomics analysis for a Parkinson's disease neuron metabolism study (**Chapter 3**), where relative quantification results were reported. Beyond this thesis with rigorous method validation, targeted absolute quantification so far has been achieved for 106 polar metabolites from nine classes, including amino acids, amines, sugars, sugar phosphates, nucleosides, nucleotides, acyl-carnitines, coenzyme A, and organic acids. By using the increasingly available reference standards and related internal standards, identification and characterization followed by adequate validation will allow to further expand the number of quantifiable targets. Two approaches can be generally followed for extending metabolite coverage. One is the pathway-wise inclusion strategy, which involves adding the missing metabolites from a pathway that is already covered or adding metabolite sets related to a newly given pathway. As an example, as discussed in **Chapter 4**, γ -glutamylcysteine should be added to the HILIC method because it is an important intermediate in the de novo synthesis of glutathione [13]. In addition, the UDP-GlcNAc synthetic pathway is an important pathway to investigate due to its position as a significant hub connecting glucose-, amino acid-, fatty acid-, and nucleotide-metabolism. UDP-GlcNAc is involved in O- and N-linked protein glycosylation, which is important for regulating nutrient sensing and responding to cellular stress [14,15]. The other strategy for prioritizing method extension is metabolite class-wise inclusion, which involves including as many metabolites as possible from a specific class. Growing evidence implies altered polyamine metabolism as a correlate of PD progression [16,17]. Our method has included some polyamine precursors and catabolites, such as L-ornithine and α -aminobutyric acid. Many polyamines, including 1,3-diaminopropane, putrescine, cadaverine, spermidine, spermine, agmatine, N-acetylputrescine, N-acetylspermine, and N-acetylspermidine, remain to be tested and should be given priority for inclusion in an extended method.

From a technical perspective, high resolution-based MS and MS/MS methods coupled to a chromatography method can be ideal tools for bridging the gap between untargeted metabolomics profiling and targeted metabolite quantification [18], further extending metabolite coverage in relative or absolute quantitative methods. In terms of large-scale

polar metabolomics quantification, the high-resolution TOF-MS approach can be more susceptible to interferences and have less selectivity than a typical multiple reaction monitoring (MRM) method. However, many QTOF mass spectrometers are able to perform data-dependent or data-independent acquisition (DDA or DIA), such as SWATH or MS^{All}, which allow for recording retention time, high-resolution m/z and MS/MS spectra within the same chromatographic run [19,20]. These three elements are valuable parameters and useful for constructing a comprehensive metabolite MS/MS library database, hence facilitating unknown feature identification in a new sample matrix, and comparing to existing (on-line) databases. Along with further enhanced dimensions in both chromatography and MS instrumentation, other advanced parameters including MS³ spectra, ion mobility-derived collision cross sections [21], and retention time matching using an orthogonal chromatography can be also recruited for metabolite identification. Newly identified metabolites can be incorporated for later targeted quantification, as illustrated in the left part of **Figure 6.1**. For overcoming the lack of selectivity in quantitative analysis, a high-resolution TOF-MS approach equipped with parallel reaction monitoring (PRM/MRM^{HR}) works as an ideal approach. A recent method coupling HILIC to the general PRM method in a positive/negative ion switching mode achieved simultaneous relative quantification for 237 polar metabolites [22]. Equipping the general PRM/MRM^{HR} method with Zeno trap pulsing could improve MS/MS sensitivity and extend the linear dynamic ranges even further. In Chapter 4, we showed how we used a HILIC-Zeno MRM^{HR} method to quantify 180 precursor isotopologue ions from 25 polar metabolites. This (HILIC-Zeno MRM^{HR}) method can also be easily modified to measure individual metabolites. Based on reduced elution overlap and a scheduled window design, it would have the advantages of providing a lower cycle time and higher method sensitivity for individual metabolite quantification.

The power of stable isotope tracer-based metabolomics, via leveraging additional labeling information to monitor individual reactions or pathway alterations within the interconnected metabolic networks, has been successfully demonstrated not only in our study but in many others as well. However, the potential of stable isotope tracing combined with high-resolution metabolomics technology for characterizing labeled metabolites in an untargeted manner has still not been fully explored. So far, most studies have focused on the targeted analysis of limited known metabolites from anticipated metabolic pathways. This is regarded as the most efficient and accurate way to answer the hypothesis-driven question, whereas a data-driven discovery based on isotope-enriched metabolome (isotopome) analysis can be of great value to a systematic investigation of metabolism and generate new hypothesis. Untargeted isotopome analysis is still quite challenging due to the complexity

of isotope labeled metabolomics data. The major bottleneck is the lack of an appropriate workflow to identify unknown labeled features and extract isotopologue information with good accuracy and reproducibility on a large scale.

Through the aforementioned high-resolution LC-MS/MS (DDA or DIA) analysis, metabolite annotation can be first carried out based on collected MS¹ and MS² data from unlabeled samples without tracer treatment. Following that, all present isotopologues of annotated metabolites present in labeled samples treated with tracer after a certain period can be extracted. This concept was successfully demonstrated in a recent study named "MetTracer". The study results showed high promise in the unbiased large-scale MID analysis of up to 830 ¹³C-labeled metabolites and 1725 ¹³C-labeled isotopologues, which covered 66 metabolic pathways in human embryonic kidney 293T cells [23]. Among the annotated 830 metabolites, each one is assigned three confidence levels. Level 1 means metabolites annotated through matching of retention time, high-resolution m/z and MS/MS spectra with the in-house metabolite database. Level 2 means metabolites annotated through matching high-resolution m/z and MS/MS spectra with public metabolite databases. Level 3 means metabolites annotated based on MS¹ and surrogated MS/MS match using in-house identification software. It should be noted that total annotated metabolite at levels 1 and 2 accounted for less than 50%. The use of in-house developed metabolite libraries still has its limits due to standards availability and cost issue. Additionally, it is prone to errors when using external metabolite databases, easily leading to ambiguity and low coverage of identification. To increase confidence in identification, labeled metabolites can provide valuable information on the possible numbers of certain atoms in the molecule. Besides, the metabolite labeling pattern may convey potential connections with other known labeled metabolites. A special effort has been made to analyze MID similarity for pathway contextualization of unidentified metabolites, which provides an alternative solution to further constrain database searches [24]. The proposed approach remains to be tested with LC-MS data and may provide higher metabolome coverage. Available software specializing in unknown labeled metabolite detection and extraction are often bespoke solutions developed to address specific project needs following specific analytical and culture workflows or data structures, for instance, having preconditions for selective ionization techniques, LC-MS or GC-MS, parallel labeling designs, joint analyses for native and highly isotope-enriched biological samples in a single run, etc [25–30]. This requires users to pre-evaluate suitable solutions applicable to their own scenario and tailor the tracer-based metabolomics workflow accordingly. In Chapter 5, we tested and incorporated mzMatch-ISO in fluxTrAM given its excellent capacity for targeted metabolite isotopologue extraction and integration. Future work can add unknown metabolite identification as a pre-

step before targeted processing, also complementing the automated demand of connecting Figure 6.1 d and Figure 6.1 r3. Candidate software can be tested for its performance in the following areas: speed of processing high-resolution LC-MS/MS (DDA or DIA) data, database matching accuracy, cell culturing cost, interoperability with other packages or manual curation, etc. This process can be time-consuming and cumbersome but will be long-term beneficial for future large-scale data analysis in studies involving multiple experimental conditions or serial time-points in dynamic monitoring.

One aspect that still needs to be addressed regarding stable isotope tracer-based metabolomics is the effective utilization of metabolite moiety MID data in metabolic flux analysis. For a localized pathway analysis, moiety MID from a key-node metabolite can be investigated in conjunction with intact metabolite MID to understand the enzymatic regulations of a series of connected reactions [7,8], as demonstrated in **Chapter 4**. For a global network analysis, moiety MIDs act as additional valuable inputs for improving the precision of metabolic flux prediction [31,32]. For instance, they were applied for shrinking the feasible flux solutions for the model of the cyanobacterium *Synechococcus* sp. PCC 7002 (59 reactions, 53 metabolites) [32]. It is highly promising that in future studies, we can incorporate both intact and moiety MIDs acquired by the HILIC Zeno MRM^{HR} method further into the established genome-scale model, iDopaNeuro, representing human dopaminergic neurons [33]. The computational approaches for performing genome-scale flux analysis assisted with intact and moiety MIDs can highly accelerate the process of biological inference and hypothesis generation for a new stable isotope tracing experiment. Current moiety MID analysis still requires a significant level of manual integration and calculation, once automated software tools are developed in the future, it will be possible to have them evaluated and integrated into the fluxTrAM pipeline.

Aiming at the ideal goal of fully comprehending cellular metabolism regulation in Parkinson's disease, there is still a long way ahead. With the recent analytical and computational developments in revealing metabolite concentrations and flux alterations, it becomes increasingly possible to address ambitious questions. Parallel efforts have been made on constructing the iPSC-derived microglial cell or astrocyte model using healthy and PINK1 mutant cell lines in our group. In the future, we can consider extending our metabolomics investigations into glial response to degenerative neurons. Activated microglial cells and reactive astrocytes are reported to exert both protective and detrimental effects in the neuronal extracellular environment [34,35]. To mimic the intercellular communication between glial cells and neurons and answer how these effects modulate neuronal degeneration, for instance, we can treat the patient-derived neurons with glial cell-conditioned media and perform our proposed tracer-based metabolomics analysis. After

more work is put into developing cellular models of co-cultures in an environment analogous to the human substantia nigra pars compacta, together with their corresponding interactive cellular genome-scale models based on multi-omics data, we expect to design new tracer-based metabolomics experiments to help determine the distinct role of each cell type in the neurodegenerative process. Overall, combining metabolomics profiling based on patient-derived cellular models with metabolic phenotype predictions via *in silico* genome-scale model analysis would constantly generate new hypotheses and allow us to perform validation or possible enzymatic treatment in a loop fashion. We believe that a better understanding of the metabolic dysregulation leading to PD pathogenesis may bring novel diagnostic and therapeutic approaches into clinical trials. On the other hand, our proposed strategy can also be used to examine any novel medications, providing additional indicators for drug preclinical evaluation. Combined efforts from the analytical, biological, and computational fields will be extremely valuable and will eventually contribute to the development of personalized treatments for Parkinson's disease patients, allowing them to live a high-quality elder life.

References

1. Dunn WB, Bailey NJC, Johnson HE. Measuring the metabolome: current analytical technologies. *Analyst*. The Royal Society of Chemistry; 2005;130:606–25.
2. Grüning N-M, Lehrach H, Ralser M. Regulatory crosstalk of the metabolic network. *Trends in Biochemical Sciences*. 2010;35:220–7.
3. Barri T, Dragsted LO. UPLC-ESI-QTOF/MS and multivariate data analysis for blood plasma and serum metabolomics: Effect of experimental artefacts and anticoagulant. *Analytica Chimica Acta*. 2013;768:118–28.
4. Brakedal B, Dölle C, Riemer F, Ma Y, Nido GS, Skeie GO, et al. The NADPARK study: A randomized phase I trial of nicotinamide riboside supplementation in Parkinson's disease. *Cell Metabolism*. 2022;34:396–407.e6.
5. Radenkovic D, Reason, Verdin E. Clinical Evidence for Targeting NAD Therapeutically. *Pharmaceuticals (Basel)*. 2020;13:247.
6. Jang C, Chen L, Rabinowitz JD. Metabolomics and Isotope Tracing. *Cell*. 2018;173:822–37.
7. Sun Q, Fan TW-M, Lane AN, Higashi RM. An Ion Chromatography–Ultrahigh-Resolution-MS 1 /Data-Independent High-Resolution MS 2 Method for Stable Isotope-Resolved Metabolomics Reconstruction of Central Metabolic Networks. *Anal Chem*. 2021;93:2749–57.
8. Fan TW-M, Sun Q, Higashi RM. Ultrahigh resolution MS1/MS2-based reconstruction of metabolic networks in mammalian cells reveals changes for selenite and arsenite action. *Journal of Biological Chemistry*. 2022;298:102586.
9. McAtee AG, Jazmin LJ, Young JD. Application of isotope labeling experiments and ¹³C flux analysis to enable rational pathway engineering. *Current Opinion in Biotechnology*. 2015;36:50–6.
10. Son J, Lyssiotis CA, Ying H, Wang X, Hua S, Ligorio M, et al. Glutamine supports pancreatic cancer growth through a KRAS-regulated metabolic pathway. *Nature*. Nature Publishing Group; 2013;496:101–5.
11. Emwas A-H, Szczepski K, Al-Younis I, Lachowicz JI, Jaremko M. Fluxomics - New Metabolomics Approaches to Monitor Metabolic Pathways. *Frontiers in Pharmacology [Internet]*. 2022 [cited 2022 Nov 9];13. Available from: <https://www.frontiersin.org/articles/10.3389/fphar.2022.805782>
12. Crown SB, Antoniewicz MR. Publishing ¹³C metabolic flux analysis studies: A review and future perspectives. *Metabolic Engineering*. 2013;20:42–8.
13. Huang L, Drouin N, Causon J, Wegrzyn A, Castro-Perez J, Fleming R, et al. Reconstruction of Glutathione Metabolism in the Neuronal Model of Rotenone-Induced Neurodegeneration Using Mass Isotopologue Analysis with Hydrophilic Interaction Liquid Chromatography-Zeno High-Resolution Multiple Reaction Monitoring. *Anal Chem [Internet]*. American Chemical Society; 2023 [cited 2023 Feb 6]; Available from: <https://doi.org/10.1021/acs.analchem.2c04231>
14. Gonzalez-Rellan MJ, Fondevila MF, Dieguez C, Nogueiras R. O-GlcNAcylation: A Sweet Hub in the Regulation of Glucose Metabolism in Health and Disease. *Frontiers in Endocrinology [Internet]*. 2022 [cited 2022 Dec 16];13. Available from: <https://www.frontiersin.org/articles/10.3389/fendo.2022.873513>

15. Liu X, Blaženović I, Contreras AJ, Pham TM, Tabuloc CA, Li YH, et al. Hexosamine biosynthetic pathway and O-GlcNAc-processing enzymes regulate daily rhythms in protein O-GlcNAcylation. *Nat Commun. Nature Publishing Group*; 2021;12:4173.
16. LeWitt PA, Li J, Wu K-H, Lu M. Diagnostic metabolomic profiling of Parkinson's disease biospecimens. *Neurobiology of Disease*. 2023;177:105962.
17. Saiki S, Sasazawa Y, Fujimaki M, Kamagata K, Kaga N, Taka H, et al. A metabolic profile of polyamines in parkinson disease: A promising biomarker. *Annals of Neurology*. 2019;86:251–63.
18. Zhou J, Yin Y. Strategies for large-scale targeted metabolomics quantification by liquid chromatography-mass spectrometry. *Analyst*. 2016;141:6362–73.
19. Chen S, Kong H, Lu X, Li Y, Yin P, Zeng Z, et al. Pseudotargeted Metabolomics Method and Its Application in Serum Biomarker Discovery for Hepatocellular Carcinoma Based on Ultra High-Performance Liquid Chromatography/Triple Quadrupole Mass Spectrometry. *Anal Chem*. 2013;85:8326–33.
20. van der Laan T, Boom I, Maliepaard J, Dubbelman A-C, Harms AC, Hankemeier T. Data-Independent Acquisition for the Quantification and Identification of Metabolites in Plasma. *Metabolites*. Multidisciplinary Digital Publishing Institute; 2020;10:514.
21. Paglia G, Williams JP, Menikarachchi L, Thompson JW, Tyldesley-Worster R, Halldórsson S, et al. Ion Mobility Derived Collision Cross Sections to Support Metabolomics Applications. *Anal Chem. American Chemical Society*; 2014;86:3985–93.
22. Zhou J, Liu H, Liu Y, Liu J, Zhao X, Yin Y. Development and Evaluation of a Parallel Reaction Monitoring Strategy for Large-Scale Targeted Metabolomics Quantification. *Anal Chem. American Chemical Society*; 2016;88:4478–86.
23. Wang R, Yin Y, Li J, Wang H, Lv W, Gao Y, et al. Global stable-isotope tracing metabolomics reveals system-wide metabolic alternations in aging *Drosophila*. *Nat Commun. Nature Publishing Group*; 2022;13:3518.
24. Weindl D, Cordes T, Battello N, Sapcariu SC, Dong X, Wegner A, et al. Bridging the gap between non-targeted stable isotope labeling and metabolic flux analysis. *Cancer & Metabolism*. 2016;4:10.
25. Capellades J, Navarro M, Samino S, Garcia-Ramirez M, Hernandez C, Simo R, et al. geoRge: A Computational Tool To Detect the Presence of Stable Isotope Labeling in LC/MS-Based Untargeted Metabolomics. *Anal Chem*. 2016;88:621–8.
26. Huang X, Chen Y-J, Cho K, Nikolskiy I, Crawford PA, Patti GJ. X13CMS: Global Tracking of Isotopic Labels in Untargeted Metabolomics. *Anal Chem. American Chemical Society*; 2014;86:1632–9.
27. Bueschl C, Kluger B, Neumann NKN, Doppler M, Maschietto V, Thallinger GG, et al. MetExtract II: A Software Suite for Stable Isotope-Assisted Untargeted Metabolomics. *Analytical Chemistry*. 2017;89:9518–26.
28. Chokkathukalam A, Jankevics A, Creek DJ, Achcar F, Barrett MP, Breitling R. mzMatch-ISO: an R tool for the annotation and relative quantification of isotope-labelled mass spectrometry data. *Bioinformatics*. 2013;29:281–3.
29. Hiller K, Metallo CM, Kelleher JK, Stephanopoulos G. Nontargeted Elucidation of Metabolic Pathways Using Stable-Isotope Tracers and Mass Spectrometry. *Analytical Chemistry*. 2010;82:6621–8.
30. Hoffmann F, Jaeger C, Bhattacharya A, Schmitt CA, Lisek J. Nontargeted Identification of Tracer Incorporation in High-Resolution Mass Spectrometry. *Anal Chem*. 2018;90:7253–60.
31. Rühl M, Rupp B, Nöh K, Wiechert W, Sauer U, Zamboni N. Collisional fragmentation of central carbon metabolites in LC-MS/MS increases precision of ¹³C metabolic flux analysis. *Biotechnol Bioeng*. 2012;109:763–71.
32. Jaiswal D, Prasannan CB, Hendry JI, Wangikar PP. SWATH Tandem Mass Spectrometry Workflow for Quantification of Mass Isotopologue Distribution of Intracellular Metabolites and Fragments Labeled with Isotopic ¹³C Carbon. *Analytical Chemistry*. 2018;90:6486–93.
33. Preciat G, Moreno EL, Wegrzyn AB, Willacey CCW, Modamio J, Monteiro FL, et al. Mechanistic model-driven exometabolomic characterisation of human dopaminergic neuronal metabolism [Internet]. *bioRxiv*; 2021 [cited 2022 Oct 15]. p. 2021.06.30.450562. Available from: <https://www.biorxiv.org/content/10.1101/2021.06.30.450562v1>
34. Vila M, Jackson-Lewis V, Teismann P, Choi D-K, Tieu K, Przedborski S. The role of glial cells in Parkinson's disease.
35. Iovino L, Tremblay ME, Civiero L. Glutamate-induced excitotoxicity in Parkinson's disease: The role of glial cells. *Journal of Pharmacological Sciences*. 2020;144:151–64.

Samenvatting

De hoge prevalentie van neurodegeneratieve ziekten onder de oudere bevolking is een almaar zorgwekkender probleem geworden. Dit vormt voor zowel individuele gezinnen als de gehele maatschappij een gezondheids- en economische last. Mensen bij wie de ziekte van Parkinson is vastgesteld hebben de gebruikelijke gebreken in motorisch handelen, die in een later stadium gepaard kunnen gaan met ontwikkeling van cognitieve- en gedragsstoornissen. De huidige beschikbare medicatie voor de ziekte van Parkinson helpt bij de symptomatische verlichting, maar is ineffectief in het vertragen van de ziekte. Daarom kan inzicht in de pathogene mechanismen van de ziekte baanbrekend zijn bij de behandeling. Gelukkig wordt er op dit gebied enorm veel onderzoek verricht in een poging om het ziekteverloop van Parkinson te verhelderen. De ontwikkeling van -omics-technieken voor het vinden van biomarkers gerelateerd aan Parkinson voor diagnose, prognose en behandeling, zijn met name in het laatste decennium in een stroomversnelling geraakt.

Metabolomics (metaboolanalyse) verwijst naar de systematische analyse van kleine biochemische moleculen in organismen. Het analyseren van het metabolisme kan een ideaal uitgangspunt zijn voor het begrijpen of interpreteren van systematische regulatie dat onder invloed staat van upstream veranderingen op genetisch of enzymatisch niveau. Dit kan bereikt worden door diverse analytische technieken, waarbij veranderingen in de metabolietenpoel of metabole response gekwantificeerd worden. Massaspectrometrie (MS) gecombineerd met vloeistofchromatografie (LC) is de meest gebruikte techniek vanwege haar voordelen: goede robuustheid, hoge verwerkingscapaciteit, groot dynamisch bereik en relatief eenvoudige monstervoorbewerking. Door regelmatig vernieuwing in kolommateriaalchemie en instrumentatie zullen LC-MS methoden alsmaar dichterbij het uiteindelijke doel van metabolomics komen: het nauwkeurig identificeren en kwantificeren van alle aanwezige metabolieten in een specifiek biologisch monster. Metabolomics gecombineerd met stabiele isotopenlabels is onmisbaar bij het bestuderen van metabole flux door metabole routes en netwerken. De huidige LC-MS methoden voor het meten van gelabelde metabolieten hebben echter hun beperkingen in het volledig vastleggen van de gelabelde informatie met hoge efficiëntie en gevoeligheid. Bovendien wordt de verdere benutting van informatie uit de gelabelde metabolieten voor de fluxinterpretatie beschouwd als een zeer rekenintensief en tijdrovend proces.

In het licht van de bovengenoemde uitdagingen, is de ontwikkeling van een passende strategie voor het bestuderen van het metabole landschap in relatie tot de pathogenese van de ziekte van Parkinson het belangrijkste doel van dit proefschrift. De door ons voorgestelde analytische strategie om metabole activiteit vast te stellen omvat twee analytische methoden en één dataverwerkingslijn. Deze kunnen vervolgens toegepast worden op het bestuderen van neuronale

modellen van het mesencephalon voortkomend uit geïnduceerde pluripotente stamcellen (iPSC) in toestand van gezondheid of tijdens de ziekte van Parkinson.

Analyse van het polaire metaboloom door middel van hydrofiele-interactievloeistofchromatografie (HILIC), die complementair is aan omgekeerde-fasevloeistofchromatografie (RPLC), is in populariteit gestegen dankzij de verbeterde chromatografische retentie en scheiding. Deze toepassing als routineplatform voor grootschalig klinisch breedvoerige metabolomics onderzoek wordt nog steeds onderschat vanwege een gebrek aan de systematische evaluatie van resolutie, reproduceerbaarheid, robuustheid, high-throughput en betrouwbaarheid van het resultaat. In **Hoofdstuk 2** hebben we richtlijnen opgesteld voor het systematisch beoordelen van het functioneren van hydrofiele-chromatografie kolommen voor breedvoerig bloedplasma metabolomics onderzoek. Deze evaluatie heeft betrekking op diverse eigenschappen van chromatografisch functioneren, waaronder, matrix effect, herhaalbaarheid van batch analyses en dekkingsgraad van metabole kenmerken. Onze resultaten laten zien dat de ZIC-c HILIC-kolom met zwitterionische stationaire fase bij neutrale pH bruikbaar is voor een uitgebreide polaire metaboliet profilering vanwege de superieure prestaties voor verscheidene stofklassen. Bovendien zorgt het voor betere isomeerscheiding, goede herhaalbaarheid en hoge dekkingsgraad van metabolieten. Deze beoordelingsprocedure kan selectief worden ingezet voor elke toekomstige test met een nieuwe HILIC-kolom of -biologische matrix. De ontwikkelde HILIC-MS-methode heeft een solide basis gevormd voor de analyse van doelgerichte polaire metabolieten in onze vervolgonderzoeken.

Om vervolgens metabole ontregeling te identificeren in humane iPSC afgeleide neuronale modellen onder individuele en gecombineerde invloed van Parkinson-gerelateerde genetische- en omgevingsfactoren, te weten PINK1 gen mutatie en rotenon blootstelling, hanteert **Hoofdstuk 3** meerdere doelgerichte metabolomics platformen. Deze platformen richten zich zowel op polaire metabolieten van het centrale koolstof- en acylcarnitinemetabolisme als op apolaire metabolieten van het meervoudig onverzadigde vetzuurmetabolisme. Bij deze uitgebreide analyse van metabolietniveaus is soortgelijke metabole ontregeling gevonden, veroorzaakt door rotenon en de PINK1 gen mutatie. Voorbeelden zijn onder andere falende energieproductie (vermindering van glucose, verzadigde vetzuren en vertakte keten aminozuren metabolisme), verstoorde redoxbalans (geblokkeerde oxidatie van NADH naar NAD⁺), evenals verschillende stoornissen van de citroenzuurcyclus, die allen leiden tot verminderde mitochondriale ademhaling. Bovendien vertoonden zowel de gemuteerde als de aan rotenon blootgestelde groepen oxidatieve schade, die relatief ernstiger was in de groep met rotenonblootstelling. Al met al wezen deze resultaten erop dat neuronen met een inherente PINK1 genmutatie gecombineerd met exogene rotenonstress zouden kunnen resulteren in een complexer neurodegeneratief metabolisme. Vervolgens hebben wij de metabole effecten van

NAD⁺-suppletie op neuronale modellen van de ziekte van Parkinson met PINK1 genmutaties en/of rotenonblootstelling geëvalueerd. Deze resultaten van de metabolomics toonden een beperkte werkzaamheid van de NAD⁺-behandeling wat betreft het verbeteren van rotenon-gerelateerde energietekorten en geen effect voor de PINK1-gemuteerde groep. In plaats daarvan bracht het een onverwachte ontregeling van meervoudig onverzadigde vetzuren in de joint-factor group. Over het geheel genomen biedt deze studie waardevolle inzichten en een diepgaand begrip voor de pathogenese van Parkinsonismen vanuit een metabolomics perspectief. Voor toekomstige studies bij PINK1 patiënten is het van wezenlijk belang om deze ontregelde metabolieten vroegtijdig als mogelijke diagnostische biomarkers te kunnen valideren met meerdere doelgerichte metabolomics platformen.

Vanwege het gebruik van stabiele isotopenlabels om metabole routes te traceren, zijn we in staat een extra laag van metabole regulering bloot te leggen in een dynamisch beeld. In navolging van de in **Hoofdstuk 3** ontdekte fluxregulatie van verstoorde metabole routes in het kader van neurodegeneratie, waar hoofdzakelijk is gekeken naar het centrale koolstofmetabolisme en de bijbehorende *de novo* nucleotidesynthese en glutathionmetabolismroutes, stelden wij in **Hoofdstuk 4** een nieuwe analysemethode voor. Deze HILIC methode koppelt aan hoge resolutie meervoudige reactie monitoring (MRM^{HR}) met Zeno-val, te weten HILIC-Zeno-MRM^{HR}. Hiermee bereikten wij nauwkeurige en reproduceerbare massa-isotopoloogkwantificering voor intacte metabolieten en het bijbehorende gefragmenteerde deel (substructuur), met vooral hoge gevoeligheid in de MS² fragmentatiemodus met ingeschakelde Zeno-valpulsing. Daarnaast behield de HILIC-Zeno-MRM^{HR} methode de relatie tussen gelabelde precursor- en fragmentionen. Dit hielp in het nauwkeurig onderscheiden van gelabelde isotopologen met verschillende labelposities. Vervolgens hebben wij deze methode toegepast op het bestuderen van een neuronaal model voor neurodegeneratie geïnduceerd door rotenon. Door de gegevens over isotopologen van intacte metabolieten en fragmentionen te interpreteren, valideerden wij eerst de reconstructie van de *de novo* glutathionsyntheseroute van neuronen in het mesencephalon aan de hand van voedingsbronnen met D-¹³C₆-glucose en L-¹⁵N₂-glutamine isotopenlabels. Onder neuronale oxidatieve stress droeg verhoogde oxidatie van zowel de basale als de *de novo* gesynthetiseerde glutathionpoel bij aan de ernstig verminderde antioxidatie capaciteit als gevolg van rotenonblootstelling. Voorts toonden wij aan dat de verminderde *de novo* glutathionsynthese gepaard ging met veranderde activiteit van verschillende sleutelenzymen van de glucose-afgeleide glutamaataanvoer en de glutathionsynthese. Het identificeren van belangrijke regulatoren van metabole flux, van falende energieproductie tot oxidatieve stress, heeft ons geholpen om de ziektemechanismen beter te begrijpen.

De identificatie van fluxregulering over gelokaliseerde metabole routes is voornamelijk een hypothesegestuurde benadering die gebruikt wordt voor karakterisatie van een specifiek

celmetabolisme. Een breedvoerige fenotypering van de metabole flux in het hele netwerk zou kunnen werken als een gegevensgestuurde aanpak voor vlotte identificatie van primaire fluxomleidingen onder ziekteomstandigheden die nieuwe hypothesen voortbrengen. Om dit doel te bereiken, introduceert **Hoofdstuk 5** een semi-geautomatiseerde lijn voor fluxberekeningen met tracer-metabolomics in modellering met atoomresolutie (fluxTrAM) in de technische softwareomgeving (MATrix LABoratory, MATLAB). Op basis van een in silico model op genoomschaal van dopaminerge neuronal stofwisseling (iDopaNeuroC) en verzamelde ^{13}C -gelabelde metabolomics gegevens uit in vitro iPSC-afgeleide neuronen van het mesencephalon, genereerde fluxTrAM automatisch experimentele ^{13}C -gelabelde massa isotopologen distributie (MID) gegevenssets van neuronen van het mesencephalon. Daaruit voortvloeiend genereerde fluxTrAM ook een chemo-informatica database van gestandaardiseerde en context specifieke metabolietstructuren en in-kaart-gebrachte atoomreacties voor het iDopaNeuroC model. Meerdere oplossingen voor de fluxproblematiek zouden kunnen worden geboden door middel van conventionele ^{13}C -gebaseerde metabole fluxanalyse op een kleine netwerkschaal. Bijvoorbeeld de voorspelling van fluxklassificatie, fluxbalansanalyse, en entropische fluxbalansanalyse op genoomschaal zouden een oplossing kunnen bieden. Dankzij een uitgebreide analyse- en vergelijking van fluxberekeningen kon de status beter worden vastgesteld van de fluxdistributie verkregen uit ons iDopaNeuroC model. fluxTrAM draagt ook bij aan het standaardiseren van high-throughput analyse van metabole flux op genoomniveau. De oplossing voor de flux op genoomschaal biedt een rekenkundige voorspelling van algemene metabole fenotypes voor gezonde menselijke neuronen van het mesencephalon, terwijl de noodzaak onderstreept wordt van het bestuderen van PINK1-cellijnen. Een vergelijkende analyse tussen PINK1- en isogene controlecellijnen zal ons in de gelegenheid stellen om belangrijke metabole ontregeling te onderscheiden. Voorspelde fenotypes kunnen kruislings worden gevalideerd en geïnterpreteerd aan de hand van de experimentele waarnemingen in **Hoofdstuk 3**. Deze kunnen gezamenlijk een extensief inzicht in ziektemechanismen voortbrengen.

Kortom, dit proefschrift heeft een analytische strategie ontwikkeld voor het bestuderen van het metabole landschap dat relevant is voor de pathogenese van de ziekte van Parkinson. Het vaststellen van de veranderingen in de metabole flux en metabolietconcentraties geeft een uitgebreid overzicht van metabole activiteit en helpt met het beter begrijpen van de ziektemechanismen van Parkinson. Een meer verfijnde en overtuigende modelreconstructie kan bereikt worden door toevoeging van compartimentele metabolietmetingen bij modelanalyse op genoomniveau. Wij hopen dat de identificatie van potentiële ziektemarkers wordt bespoedigd door de gecombineerde experimentele en rekenkundige aanpak en uiteindelijk zal bijdragen aan gepersonaliseerde behandelingen voor patiënten met de ziekte van Parkinson.

Curriculum vitae

Luojiao Huang was born on January 28th, 1993, in Yueqing, Zhejiang Province, China. In 2011, she obtained her high school diploma at Nanjing No. 1 Middle School. After her graduation, she was admitted to China Pharmaceutical University and studied traditional Chinese pharmacy. In her last year of bachelor study, she moved to the Institute of Materia Medica, Peking Union Medical College in Beijing, and started her bachelor's internship. She worked on the project of developing an LC-MS/MS method for the quantitative determination of 5-HMF (2-furfural) in traditional Chinese medicine injections. During her bachelor's study, she was awarded the China National Scholarship and university scholarships.

In September 2015, she started her master's study at Peking Union Medical College. She joined the group of Prof. Dr. Zeper Abliz and worked under the supervision of Dr. Jiuming He. Her master's project focused on using ambient mass spectrometry imaging techniques to perform molecular pathological diagnosis for thyroid tumors. Relevant research results were published in the journals *Analytica Chimica Acta* and *Molecules*. In 2016, she began her industrial internship at Beijing Ninesky Biomedical Technology and performed a preclinical pharmacokinetic study of dezocine. In June 2018, Luojiao obtained her master's degree, and her thesis was awarded the National Excellent Dissertation in Pharmacy.

In September 2018, she started her PhD work in the group of Prof. Dr. Thomas Hankemeier at Leiden University. Under the supervision of Dr. Amy Harms and Dr. Ronan Fleming, she focused on developing a tracer-based metabolomics methodology applied to investigating metabolic dysfunction in Parkinson's disease. Relevant research results were published in the journals *Analytical Chemistry* and *Metabolites*. In 2022, she gave a poster presentation at the Metabolomics Conference 2022 in Valencia, Spain. In 2023, she was invited to present her work at a webinar with SCIEX and Separation Science.

After her PhD, Luojiao is now working with Dr. Berta Cillero Pastor and Prof. Dr. Martijn van Griensven at Maastricht University. As a postdoctoral researcher, she is working on the development and application of mass spectrometry-based methods to characterize human infrapatellar fat pads for regenerative medicine using proteomics and mass spectrometry imaging.

List of publications

1. **L. Huang**, N. Drouin, J. Causon, A. Wegrzyn, J. Castro-Perez, R. Fleming, A. Harms, T. Hankemeier, Reconstruction of Glutathione Metabolism in the Neuronal Model of Rotenone-Induced Neurodegeneration Using Mass Isotopologue Analysis with Hydrophilic Interaction Liquid Chromatography-Zeno High-Resolution Multiple Reaction Monitoring, *Anal. Chem.* (2023).
2. F. Hosseinkhani*, **L. Huang***, A.-C. Dubbelman, F. Guled, A.C. Harms, T. Hankemeier, Systematic Evaluation of HILIC Stationary Phases for Global Metabolomics of Human Plasma, *Metabolites*. 12 (2022) 165.
3. **L. Huang**, A. Wegrzyn, V. Verschoor, F. R. Rosmasari, W. Yang, A. Kindt-Dunjko, J. C. Schwamborn, C. Klein, A. Harms, R. Fleming, T. Hankemeier, Unraveling the Metabolic Dysfunction Processes Fueling Parkinsonism Pathogenesis in Human iPSC-derived Mid-brain Neurons with PINK1 Mutation and Rotenone Exposure, In submission.
4. **L. Huang***, G. Preciat*, J. Alarcon-Gil*, E. L. Moreno, A. Wegrzyn, I. Thiele, E. Schymanski, A. Harms, R. Fleming, T. Hankemeier, fluxTrAM: Integration of tracer-based metabolomics data into atomically resolved genome-scale metabolic networks for metabolic flux analysis, In preparation.

Not part of this thesis

5. **L. Huang***, X. Mao*, C. Sun, T. Li, X. Song, J. Li, S. Gao, R. Zhang, J. Chen, J. He, Z. Abliz, Molecular Pathological Diagnosis of Thyroid Tumors Using Spatially Resolved Metabolomics, *Molecules*. 27 (2022) 1390.
6. X. Mao*, **L. Huang***, T. Li, Z. Abliz, J. He, J. Chen. Identification of Diagnostic Metabolic Signatures in Thyroid Tumors Using Mass Spectrometry Imaging. *Molecules*. 28 (2023) 5791.
7. Y. He, M. van Mever, W. Yang, **L. Huang**, R. Ramautar, Y. Rijksen, W.P. Vermeij, J.H.J. Hoeijmakers, A.C. Harms, P.W. Lindenburg, T. Hankemeier, A Sample Preparation Method for the Simultaneous Profiling of Signaling Lipids and Polar Metabolites in Small Quantities of Muscle Tissues from a Mouse Model for Sarcopenia, *Metabolites*. 12 (2022) 742.
8. **L. Huang***, X. Mao*, C. Sun, Z. Luo, X. Song, X. Li, R. Zhang, Y. Lv, J. Chen, J. He, Z. Abliz, A graphical data processing pipeline for mass spectrometry imaging-based spatially resolved metabolomics on tumor heterogeneity, *Analytica Chimica Acta*. 1077 (2019) 183–190.
9. J. He*, **L. Huang***, R. Tian, T. Li, C. Sun, X. Song, Y. Lv, Z. Luo, X. Li, Z. Abliz, MassImager: A software for interactive and in-depth analysis of mass spectrometry imaging data, *Analytica Chimica Acta*. 1015 (2018) 50–57.

10. C. Sun, T. Li, X. Song, **L. Huang**, Q. Zang, J. Xu, N. Bi, G. Jiao, Y. Hao, Y. Chen, R. Zhang, Z. Luo, X. Li, L. Wang, Z. Wang, Y. Song, J. He, Z. Abliz, Spatially resolved metabolomics to discover tumor-associated metabolic alterations, *Proc Natl Acad Sci U S A*. 116 (2019) 52–57.
11. J. He, C. Sun, T. Li, Z. Luo, **L. Huang**, X. Song, X. Li, Z. Abliz, A Sensitive and Wide Coverage Ambient Mass Spectrometry Imaging Method for Functional Metabolites Based Molecular Histology, *Advanced Science*. 6 (2019) 1802201.

* *Authors contributed equally*

Acknowledgements

The thesis marks the end of a long and wonderful journey full of challenges and surprises, pleasures and anxieties, changes and growths. I would like to express my deepest appreciation to all those who have accompanied me on this journey.

First and foremost, Thomas, I would like to look back with great enthusiasm on having worked with this diverse and dynamic team, always being encouraged by you to explore my own directions, and being provided freedom and unwavering support. Your enthusiasm and dedication to science have greatly inspired me to develop as a scientist. I appreciate every moment of our scientific discussion and the special moment you celebrated our progress with German sparkling wine.

Amy, your constructive criticism, insightful feedback, affirmation, and encouragement have been invaluable to my academic growth. I deeply appreciate the guidance and assistance you have provided. Ronan, your expertise and unique insights into the research fields have greatly broadened my scientific perspective and highly motivated me to work across fields. Aga, you have always been supportive, giving me solid advice and guidance during challenging times. I appreciate it very much.

My best students, Rosma and Jesus, I am fortunate to have you join my projects. Your curiosity, enthusiasm, and hard work have continuously fueled my passion for research. During this journey, it has also been a privilege for me to work with many fantastic scientists. Jason and Jose, our collaboration brought many inspirations to my method development. I am grateful for the precious feedback you provided on our work. Nicolas, You have always been generous in sharing your knowledge, experiences, and ideas with me. I enjoyed our scientific discussions, particularly those crazy drawings on our office door. Anne-Charlotte, It has been a pleasure to collaborate with you on our first HILIC paper; your constructive criticism has significantly enriched the quality of our work.

Many thanks go to all my past and present lovely colleagues. Farideh, German, Wei Yang, and Vincent, this thesis would not have been possible without your incredible collaborations. I appreciate all the sparkling moments during our discussion and our endeavors to improve our research. My dear officemates, Wei Zhang, Cornelius, Yupeng, Kanchana, and Congrou, thanks for bringing me so much daily laughter and positive vibes. I often miss it now. Loes, Ina, Cathy, and Ariadne, thank you for all the administrative work that makes our research more efficient. Gerwin, Tim, and Faisa, thank you for your dedication to maintaining our laboratory's infrastructure and equipment, always ensuring our lab work runs smoothly. Sabine, Daisy, and Nanda, thank you for sharing knowledge and offering help at the beginning of my PhD. Michael, thank you for your constant assistance in resolving many headache hardware and software issues. Alida, thank you for helping me navigate the

complexities of metabolomic data collection, interpretation, and statistical analysis. Hyung and Ida, thank you for your tremendous assistance with the Dutch summary of my thesis. Ahemd, thanks for arranging the focus group for writing and all the delicious meals afterward. Edinson, thank you for giving me the training and assistance in neuronal culture. I have learned a lot from your patience and self-discipline. Special thanks to my Chinese colleagues, Wei Zhang, Wei Yang, Zhengzheng, Xinyu, Yupeng, Bingshu, Pingping, Congrou, Mengle, Chunyuan, Yu, Lu, and Xiaoyue. Whether work-related or personal, you share with me much invaluable experience and lessons. Your companionship, encouragement, and incredible meals gave me home feelings, enabling me to endure pandemic periods. Babara, Madhu, Simon, Mariana, Manchu, Marlien, Marielle, Isabelle, Ischa, Laura, Paul, Maik, and Sam, you have made MAC a very inclusive and comfortable workplace. Thank you for all the enjoyable lunch talks, dancing clubs, borrels and parties, barbecues, pingpong competitions, etc. I truly enjoyed those beautiful moments with you. Yuqing, Yu Fu, Lu Chen, Liyan, Feiyan, Deyi, Chenguang, Zirui, Diyu, and Maria, my best buddies in Leiden since the beginning of my journey, have together experienced the beautiful Dutch landscape, cultural shocks, and multiple firsts. We have made unforgettable memories, and I wish you all the best in your future. Jiangshuo, Xiaoyu, Muyin, Jie, Hong, and Xinyue, although we live in different time zones, you can warm me up and give me the best support whenever I need it. Our friendship will last forever.

Binhao, Thank you for everything you have done for me, my best love!

Last but not least, my loved mom and dad, your open-mindedness and optimism give me the most confidence and perseverance to pursue my academic dream. Luoyi, Luojie, my dearest sister and brother, I am fortunate to have you in my life. Thank you for taking care of the family throughout this journey. I know that no matter what, you will unconditionally support me and remind me of the importance of health and laughter.